

# Systematic approach to geometrical calibration of X-ray computed tomography instruments



Massimiliano Ferrucci

Examination Committee:

Prof. dr. ir. J. Boydens, chair  
Prof. dr. ir. W. Dewulf, supervisor  
Prof. dr. ir. J-P. Kruth, co-supervisor  
Prof. S. Castagne, secretary  
Prof. dr. ir. B. Lauwers  
Dr. ir. F. Geuens  
Prof. R.K. Leach

Dissertation presented in partial  
fulfilment of the requirements  
for the degree of Doctor of  
Engineering Technology (PhD)

November 2018

© 2018 KU Leuven

Uitgegeven in eigen beheer, Massimiliano Ferrucci, Brussels, Belgium

Alle rechten voorbehouden. Niets uit deze uitgave mag worden vermenigvuldigd en/of openbaar gemaakt worden door middel van druk, fotokopie, microfilm, elektronisch of op welke andere wijze ook zonder voorafgaandelijke schriftelijke toestemming van de uitgever.

All rights reserved. No part of the publication may be reproduced in any form by print, photoprint, microfilm, electronic or any other means without written permission from the publisher.

# Table of contents

Acknowledgements .....	v
Abstract.....	ix
Beknopte samenvatting.....	x
List of abbreviations.....	xi
List of symbols.....	xii
Chapter 1 Introduction.....	1
1.1 Manufacturing and measurement.....	1
1.2 X-ray computed tomography for industry.....	1
1.3 Fundamentals of X-ray computed tomography.....	2
1.4 Measurement traceability .....	6
1.4.1 History.....	6
1.4.2 The standard unit of length .....	7
1.4.3 Achieving traceability of dimensional measurements .....	7
1.5 CT instrument scale.....	8
1.5.1 CT instrument geometry.....	10
1.6 Motivation of doctoral research.....	11
1.7 Objectives.....	11
Chapter 2 Literature review on the state-of-the-art.....	13
2.1 Parameterization of the instrument geometry .....	13
2.2 Measurement model.....	16
2.3 Methods to measure the CT instrument geometry.....	19
2.3.1 Scaling errors .....	19
2.3.2 Estimating CT instrument geometrical parameters.....	21
2.4 Summary and conclusion .....	38
Chapter 3 Sensitivity studies .....	45
3.1 Detector angular misalignments.....	45
3.1.1 Radiographic error model .....	46
3.1.2 Volumetric deviations.....	50
3.1.3 Radiographic correction.....	56
3.1.4 Discussion .....	58
3.2 Rotation stage errors .....	59
3.2.1 Test object .....	59

Table of contents

3.2.2	Parameterization of rotation stage errors.....	60
3.2.3	Simulation and data analysis .....	61
3.2.4	Results.....	62
3.2.5	Discussion .....	65
Chapter 4	Geometrical measurement procedure with implementation on simulated data .....	67
4.1	Reference object parameterization.....	67
4.2	Minimization of re-projection errors .....	69
4.3	Simulation of radiographic data acquisition.....	70
4.3.1	Perturbation of sphere center coordinates.....	72
4.3.2	Rotation stage error motions .....	72
4.3.3	Blur and noise.....	72
4.4	Analyzing the projection data .....	72
4.4.1	Estimating center projection coordinates .....	72
4.4.2	Tracking the spheres.....	74
4.4.3	Projected sphere overlaps.....	74
4.4.4	Error in observed center projection coordinates .....	74
4.5	Convergence to a global solution and parameter identifiability .....	75
4.6	Measured geometrical parameters.....	80
4.7	Instrument adjustment .....	82
4.8	Discussion .....	85
Chapter 5	Experimental validation of the geometrical measurement procedure .....	89
5.1	Reference object .....	89
5.2	Experimental CT instrument.....	90
5.3	Robustness testing.....	92
5.3.1	Number of projections .....	93
5.3.2	Continuous rotation .....	96
5.4	Instrument adjustment.....	100
5.5	Conclusion .....	103
Chapter 6	Uncertainty in the measured geometrical parameters .....	105
6.1	Monte Carlo framework.....	105
6.2	Input quantities.....	107
6.2.1	Sphere center coordinate uncertainty .....	107
6.2.2	Uncertainty in observed center projection coordinates.....	108
6.3	Estimation of uncertainty in geometrical parameter values.....	108
6.4	Discussion .....	114

Chapter 7 Conclusions.....	117
7.1 Contributions and conclusions.....	118
7.1.1 Literature review.....	118
7.1.2 Sensitivity studies.....	118
7.1.3 Development of geometrical measurement procedure.....	119
7.1.4 Experimental validation.....	120
7.1.5 Estimation of uncertainty in geometrical parameters.....	121
Appendix A.....	123
Appendix B.....	125
Doctoral publications.....	127
Curriculum Vitae.....	129



# Acknowledgements

The work presented in this doctoral thesis was funded sequentially from three sources. From November 2013 to November 2016, the doctoral research was funded by the European Commission's 7<sup>th</sup> Framework Programme FP7-PEOPLE Marie Curie Actions Initial Training Network INTERAQCT project, under grant agreement 607817. Prof. Wim Dewulf, Prof. Jean-Pierre Kruth, and Prof. Richard K. Leach are particularly considered for their contributions in preparing the proposal to the European Commission for funding what would eventually be the INTERAQCT project. During the first three years, the work was principally carried out at the Engineering Measurement Division of the National Physical Laboratory (NPL, United Kingdom) under the sequential supervision of Prof. Richard K. Leach, Dr. Claudiu L. Giusca, and Dr. Michael McCarthy, and the indirect, though continual, supervision of Prof. Wim Dewulf and Prof. Jean-Pierre Kruth (both at KU Leuven). Two secondments were performed at the Division of Production Engineering, Machine Design and Automation (Division PMA) of KU Leuven: the first was performed from June 2015 through August 2015 and the second from February 2016 through March 2016. Both secondments were performed under the supervision of Prof. Wim Dewulf. A third secondment was performed at the Department of Management and Engineering of the University of Padova from June 2016 to September 2016 under the supervision of Prof. Simone Carmignato.

From December 2016 to December 2017, the doctoral research was funded by the Belgian American Educational Foundation's (BAEF) Fellowship for Graduate Research in Belgium and carried out at the Division PMA of KU Leuven under the direct supervision of Prof. Wim Dewulf and Prof. Jean-Pierre Kruth. I would like to praise Dr. Emile Boulpaep for his excellent work in directing the BAEF and for his kind welcome upon the start of my one-year fellowship. From December 2017 until November 2018, the research was funded by the European Commission's Horizon 2020 Marie Curie Actions Individual Fellowship FlexCT project, under grant agreement 752672. I would like to recognize Dr. Tom Craeghs at Materialise NV, for his support and guidance in the final months of my doctoral thesis.

I would like to thank Prof. Wim Dewulf, the principal supervisor in the more than four years of my doctoral research. In addition to providing critical yet constructive feedback along the way, Prof. Dewulf motivated me by offering his trust. Of course, every so often he'd have to put his foot down but, in general, he trusted me with the ability to decide the direction of the research and the methodology with which it would be carried out. I would also like to express my gratitude to Prof. Richard K. Leach, Dr. Claudiu L. Giusca, and Dr. Michael McCarthy, who were my supervisors at NPL, for their support and contributions to the research. Prof. Leach is recognized for providing inspiration, motivation, and confidence for the tasks that stood before me. The discussions with Dr. Giusca and Dr. McCarthy helped to clarify the direction of the doctoral research and concretize the end-goal. Worthy of praise is also Prof. Alistair Forbes of NPL who, despite having no obligation to do so, listened attentively to my research concerns and provided suggestions that were incorporated into the research methodology. Furthermore, I am grateful to Prof. Simone Carmignato for reviewing each research article and for providing supervision during my secondment at the University of Padova.

I would like to recognize my role model in research.

Dr. Ted Doiron was my supervisor at the National Institute of Standards and Technology (NIST). He took me under his wing for what was my first full-time research position. Ted was very supportive. As long as I got those calibrations out of the way ("eat your vegetables first", he would say), I had the freedom to discover my niche in the research world. When I would occasionally take a bit too much freedom, he knew how to put me back on track ("why aren't you making me money?" he would say). Ted gave me the

## Acknowledgements

opportunity to pursue a Master's degree through a part-time program at the Johns Hopkins University. He not only insisted that I get the Master's, he also made sure it was fully funded. Going to work was never boring with Ted around: Ted's sense of humor and his human attitude towards work taught me that it's possible to do good work and enjoy it at the same time. Thank you for being you, Ted.

Family has been a beacon of support throughout my life.

My nonna Fedora showered me with unconditional affection. She made sure I never went hungry by feeding me conigliolo fritto, fiori di zucca fritti, maccheroni al sugo di cinghiale, and at least one mozzarella (she never forgot how much I love mozzarella). All the while, my nonno Franco hunted wild boar that his grandchildren would eat and harvested the grapes that would make the wine his grandchildren would drink (diluted with water, naturally). Otherwise, he would watch television and curse the heavens at the sight of unsavory celebrities and figures of spiritual authority. He knew how to make his grandchildren laugh. My grandpa George gave me the gift of passion and curiosity. He introduced me to photography—a passion of his—when he gave me my first camera: an Olympus OM-1. Grandpa was a self-taught cook. He ensured that was handed down as well every time he asked me to help him prepare a meal. My grandma Eunice is a well-spoken and elegant woman. She never let a grammatical mistake go unnoticed—something that has served me well in writing research articles and reviewing papers by others. I lived with my grandma and grandpa for several years. I was blessed to be exposed to their stories and their love. Shortly before starting my PhD, I met for the first time my great aunt Renie. She and I kept in contact throughout my doctoral studies by sending each other letters (yes, actual letters, since she is skeptical of computers). The kindness and positivity in her words helped me feel close to my family in the United States, despite the ocean separating us.

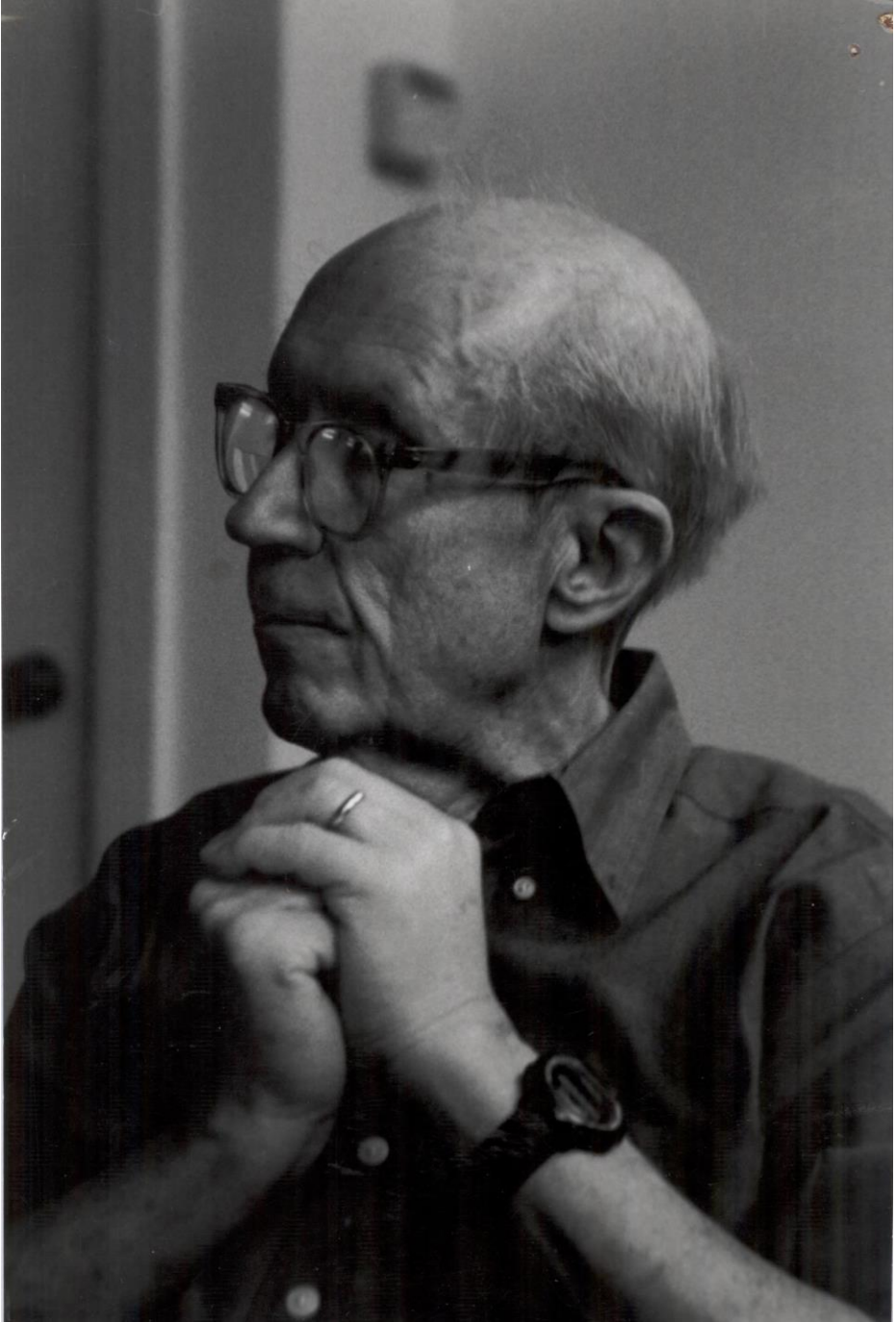
When the going would get tough, my babbo was always there to remind me not to take things too seriously. Throughout my doctoral studies, I was able to take short breaks to visit him in Tuscany. Besides bringing back loads of delicious salame, pecorino, vin santo, and olive oil, I also brought back a more relaxed attitude. My stepmother is a reflective soul, with whom I could discuss thoughts, emotions, and the quirks of both Italian and Anglo-Saxon cultures (the two cultures from which I hail). Conversations with my stepmother were rarely shallow in content and granted me moments of introspection.

My brother is my best friend. We grew up doing almost everything together, especially if it involved video games. He protected me when I was humiliated for my weight problems as an adolescent. He was always prepared to drop everything he was doing to come to my rescue. My brother now has a family of his own. Shortly after starting my PhD, my niece Alissa was born. A year and a half later, my nephew Matteo came to this world. My brother has opened his house to me every time I visited, something I cherish very much. It has been a wonderful experience being Uncle Massi to my brother's children.

My mother is a hardworking, humble, and high-minded woman. She raised me and my brother mostly on her own and her capacity as a mother is reflected in our achievements and in our contentment. We had a wonderful upbringing, filled with caring support and warm memories, and devoid of superfluous luxuries. My mother strived towards our self-reliance, and I am forever grateful to her for it. While my mother always encourages me to challenge myself, she frequently reminds me that she loves me for who I am.

I conclude my acknowledgments with a quote that reflects the loving atmosphere in which I grew up. In a letter written to me on my 23<sup>rd</sup> birthday, my grandpa George writes,

*"You have done many fine things for us, but the best of all has been just being yourself."*



Grandpa George Grier



# Abstract

This doctoral thesis addresses the issue of geometrical calibration of CT instruments. The term 'calibration' has a well-defined meaning in the field of metrology: measurement of a quantity by comparison to a traceable reference and assessment of uncertainty in that comparison. Therefore, instrument geometrical calibration refers to the measurement of the instrument geometry, defined by a set of geometrical parameters, by comparison to a traceable reference and assessment of uncertainty in the measured values. The doctoral journey has followed a relatively common path in the quest for developing standardized methods to measure the geometry of a measuring instrument. After realizing that standardized methods don't exist by way of a literature review, the sensitivity of measurements to various geometrical error sources is determined. Sensitivity analysis allows us to determine which error sources are negligible so that they may be put on the back burner of any research endeavor.

Dedicated procedures for the measurement of the CT instrument geometry by comparison to a traceable reference are developed and applied to simulated data. Implementation on simulated data provides us with ground truth, which we can use to evaluate the performance of the test procedures and adapt as necessary. The geometrical measurement procedure is applied to an experimental instrument. While ground truth is not available for the experimental implementation, i.e. we don't know the true instrument geometry, the efficacy of the developed procedures is validated by observing considerable reductions in measurement errors after compensation of the measured geometrical misalignments by instrument adjustment. The development of a Monte Carlo framework for assessing uncertainty in CT instrument geometrical parameters solved by minimization is discussed. However, application of the Monte Carlo framework is currently limited due to bias in the input data and coupling of the solvable parameters. The Monte Carlo framework and the limitations outlined provide a path for such future research endeavors. Furthermore, the Monte Carlo framework proposed here can be applied to evaluate uncertainty in any optimization-based measurement procedure.

# Beknopte samenvatting

Deze doctoraatsdissertatie behandelt het probleem van geometrische kalibratie van CT-toestellen. De term kalibratie heeft een precies gedefinieerde betekenis in het domein van de meettechniek. Deze luidt als volgt: kalibratie is de meting van een hoeveelheid door vergelijking met een traceerbare referentiewaarde met inbegrip van het bepalen van de onzekerheid op deze vergelijking. De geometrische kalibratie van een meetinstrument verwijst dus inherent naar de meting van de geometrie van dit instrument, omschreven door een set van geometrische parameters, door middel van vergelijking met een traceerbare referentie en de onzekerheidsbepaling hierop. Dit doctoraat heeft een generische aanpak gevolgd tijdens de zoektocht naar gestandaardiseerde methodes om de geometrie van zulk meetinstrument te meten. Tijdens het najagen van mogelijke standaard meetmethodes werd het duidelijk dat deze niet voor handen zijn in de literatuur. Daarom werd geopteerd de gevoeligheid van de metingen voor verscheidene geometrische foutenbronnen te bepalen. De gevoeligheidsanalyse stelt ons in staat te besluiten welke foutenbronnen verwaarloosbaar zijn en als dusdanig niet prioritair te behandelen zijn.

Dit onderzoek heeft geleid tot toegepaste procedures voor het meten van de geometrie van een CT-toestel in vergelijking met een traceerbare referentie. Deze procedures werden eerst uitgevoerd op gesimuleerde data. Deze implementatie op gesimuleerde data toont aan dat het principe valide is en dat de methode gebruikt kan worden om de prestaties van verdere testprocedures te evalueren en waar nodig bij te stellen. De geometrische meetprocedure werd vervolgens toegepast op een experimenteel CT-meettoestel. Omdat de ware geometrie van dit instrument steeds ongekend is, kan de uitkomst van deze experimentele implementatie niet rechtstreeks gevalideerd worden. De doeltreffendheid van de ontwikkelde procedures is daarom geratificeerd door observatie van aanzienlijke reducties in meetfouten na de compensatie van de gevonden geometrische uitrichtingsfouten via de machine-instellingen. De ontwikkeling van een structuur voor simulatie via Monte Carlo en het overzicht van de beperkingen zorgen voor een afbakening van verder onderzoek. Bovendien kan de simulatie-ontwikkeling via Monte Carlo die hier voorgesteld wordt, gebruikt worden om onzekerheid te evalueren in andere optimalisatiegebaseerde meetprocedures.

# List of abbreviations

CT	X-ray computed tomography
SPECT	Single-photon emission computed tomography
SDD	Source-to-detector distance
SRD	Source-to-rotation axis distance
AOR	Axis of rotation
SI	International System of Units
BIPM	International Bureau of Weights and Measures
VIM	International Vocabulary of Metrology
GUM	Guide to the expression of uncertainty in measurement
FDK	Feldkamp-Davis-Kress
CMS	Coordinate measuring system
CMM	Coordinate measuring machine
RMS	Root-mean-square
C2C	Center-to-center distance
M2C	Mean-to-center distance
CT <sup>2</sup>	Computed tomography calibration tube
CAD	Computer-aided design
TORATOM	Twinned Orthogonal Adjustable TOMograph
CET	Centre of Excellence Telč
MPE	Maximum permissible error

# List of symbols

$z_R$	Z-axis position of axis of rotation
$x_D$	X-axis position of detector geometrical center
$y_D$	Y-axis position of detector geometrical center
$z_D$	Z-axis position of detector geometrical center
$\theta$	Detector rotation about local X-axis (extrinsic)
$\varphi$	Detector rotation about local Y-axis (extrinsic)
$\eta$	Detector rotation about local Z-axis (extrinsic)
$\alpha$	Rotation stage angular index
$u$	Detector column position
$v$	Detector row position
$u_o$	Detector column position of principal point
$v_o$	Detector row position of principal point
$u_{obs}$	Observed detector column position of center projections
$v_{obs}$	Observed detector row position of center projections
$u_{mod}$	Modelled detector column position of center projections
$v_{mod}$	Modelled detector row position of center projections
$SSR$	Sum of squared residuals between observed and modelled center projections

# Chapter 1

## Introduction

This chapter is dedicated to establishing the motivation behind the research presented in this doctoral thesis. First, the chapter emphasizes the importance of measurement accuracy to the manufacturing industry. Then, X-ray computed tomography (CT) is presented in the context of its application to quality control of parts made by advanced manufacturing technologies. The role of metrology is presented in the context of establishing methods to determine accuracy of measurements; consequently, the concepts of traceability, calibration, and measurement uncertainty are introduced. Finally, the case is made for the importance of knowing the geometrical alignment of the CT instrument for ensuring accurate measurements.

The content in this chapter is mostly reproduced from [1-4].

### 1.1 Manufacturing and measurement

“You can only make as well as you can measure”. This phrase by 19th century engineer Joseph Whitworth embodies the importance and interconnectedness of manufacturing and measurement. The function of a manufactured part is often dependent on its physical characteristics, for example its dimensions, material composition, and mechanical properties. These characteristics are typically defined in the part’s engineering design and specifications. Manufacturers can use dedicated measuring instruments to perform quality control on the manufactured parts to determine whether the specific part or the batch, to which generalized single measured part or sample of measured parts belongs, are fit for their intended application, or whether they need to be reworked or scrapped. When choosing an appropriate measuring instrument, the manufacturer must consider what uncertainty in the measurement result (see section 1.4.3) is required to make a confident decision on the measured part’s conformance to specification.

### 1.2 X-ray computed tomography for industry

Advanced manufacturing techniques such as additive and composite manufacturing are gaining importance in industry because they provide several benefits over traditional production techniques. Benefits include more complex outer and inner geometrical features, and reductions in part mass. While advanced manufacturing techniques are still relatively slower and more expensive than traditional subtractive (e.g. turning and milling) manufacturing techniques, constant improvements to the technology and wider availability are making advanced manufacturing techniques more competitive. X-ray CT is currently the only method for non-destructive dimensional measurement of both inner and outer features and simultaneous non-destructive characterization of material properties such as density and porosity [5]. These capabilities make X-ray CT a promising solution for quality control of parts made by advanced manufacturing techniques.

In fact, X-ray CT is increasingly used for various industrial tasks, including testing of materials, analysis of fiber orientation and fracture dynamics in composite parts (e.g. in wind turbines), and localization of flesh, fat, and bone in pig carcasses for the meat industry. X-ray CT can be used for performing dimensional

measurements of a CT scanned object. Segmentation of the voxel-based attenuation map gives a 3D surface model (see section 1.3), which can be subsequently converted to a cloud of three-dimensional point coordinates by applying a surface sampling algorithm. The ability to extract both internal and external surface coordinates from scanned data has led many to consider CT as the third generation of coordinate measuring systems (CMSs), tabletop coordinate measuring machines (CMMs) being the first generation and portable CMSs—the second generation. Section 1.3 revisits the fundamentals of X-ray computed tomography.

However, the application of CT for inspection tasks with strict tolerance requirements is limited by lack of knowledge in the uncertainty of CT measurements. Hence, the words spoken by Mr. Whitworth in the 19th century still resonate today: without capable measurement technology, it is not possible to fully exploit the benefits of novel manufacturing methods. This is where the field of metrology—measurement science—plays a crucial role. In metrology, a certain level of confidence in the result of a measurement can be established when the result can be traced back to the definition of its corresponding unit and the uncertainty is assessed and stated alongside the measurement result. The general role of the metrologist is the standardization of measurements at all levels, be it international, national, or in-house (within a factory, research institute, or calibration laboratory). Standardization in this context includes defining the measurement unit, realizing the definition experimentally, and establishing traceability of measurements to that definition. The third category—establishing traceability—entails developing dedicated calibration procedures and assessing measurement uncertainty for a particular instrument. Section 1.4 introduces the concept of traceability particularly as it pertains to dimensional measurements.

### 1.3 Fundamentals of X-ray computed tomography

X-ray CT is an imaging technique that employs the attenuating properties of a medium as X-rays propagate through it. Since the early days of its commercialization, CT has been widely used in the medical field as a method to image inside the human body [6]. The technology was later adapted for industrial inspection of manufactured parts. A typical industrial CT instrument consists of an X-ray tube, a sample rotation stage, and an X-ray detector (figure 1.1). The workpiece is placed on the sample rotation stage. In the interest of conciseness, the principles of X-ray computed tomography are discussed briefly. References [7-9] provide an extensive overview of the principles of CT.

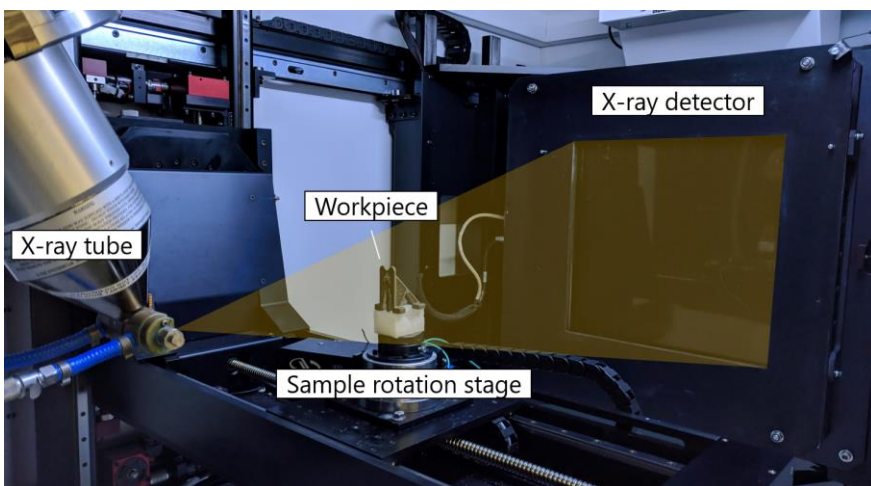


Figure 1.1. A typical industrial X-ray computed tomography instrument and its three main components: X-ray tube, sample rotation stage, and X-ray detector.

The CT measurement process begins with the generation of the X-ray radiation (figure 1.2). An X-ray tube consists of a cathode filament on one end and an anode on the opposite end. When the cathode filament is heated, electrons are released from the surface of the filament. A difference in electric potential between the cathode and the anode accelerates these 'free' electrons in the direction of the anode. As the accelerated electrons reach the anode, they are focused onto a target, where approximately 99 % of the energy is converted to heat and approximately 1 % is converted into X-ray photons [6]. The location on the target where X-rays are generated is known as the X-ray focal spot.

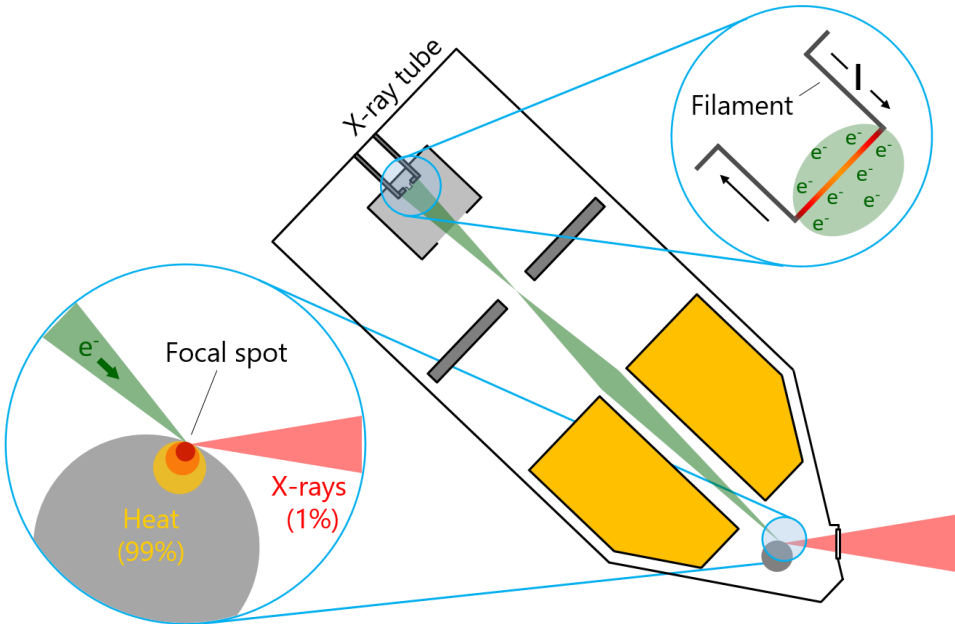


Figure 1.2. Technical diagram of a typical X-ray tube.

The generated photons are directed towards the workpiece, which is located on the sample rotation stage. As the X-rays travel through the workpiece, their intensity is attenuated. Attenuation occurs as a result of the interaction of the X-rays and the workpiece material, namely photoelectric absorption and Compton scattering [6], shown in figure 1.3. Photoelectric absorption occurs when the energy of an incoming X-ray photon is completely absorbed by an inner orbital electron of the workpiece atom. The energized inner orbital electron is ejected and the now empty inner orbital electron hole is filled by an outer orbital electron. The change in energy level of the electron from the outer orbital to the inner orbital results in the emission of a visible light photon. In Compton scattering, a high-energy ('hard') X-ray photon is partially absorbed by an outer orbital electron of the workpiece atom. The energized outer orbital electron is ejected, while the reduced-energy ('soft') X-ray photon is deflected along a direction different from its original incidence direction. The amount of attenuation through a specific material depends on the energy (wavelength) of the X-ray radiation and several characteristics of the material, such as its density, its element number, and the length of penetration of the X-rays through the material.

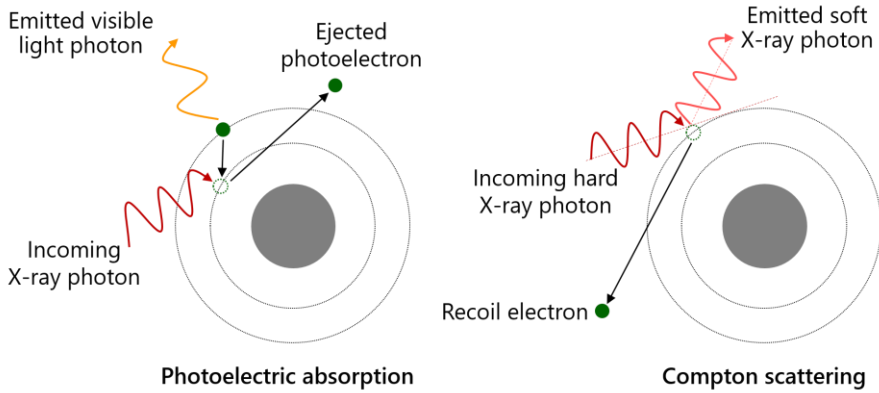


Figure 1.3. Attenuation of the X-rays by the workpiece is a result of photoelectric absorption and Compton scattering.

X-rays that are not completely attenuated by the object are transmitted to a detector, where they are measured (figure 1.4). In typical X-ray detectors, the incident X-rays are converted to visible light photons by a scintillator layer. Individual photodiode pixels convert the visible light photons into an electrical signal, which is then digitized as an intensity value. The intensity registered by each pixel is proportional to the energy of the X-rays incident upon it after having traversed the linear trajectory from the source to the respective pixel position on the detector. The collection of pixel intensities is stored as a radiographic image (also known as a radiograph). The total attenuation of the X-rays along a given path can be determined from the registered intensity values and the intensity of the non-attenuated X-rays. A radiograph, therefore, ideally represents the distribution of attenuated X-rays along the traversed volume. Radiographs are taken at multiple (typically thousands) object viewing angles from 0° to 360°, controlled by the sample rotation stage (figure 1.5).

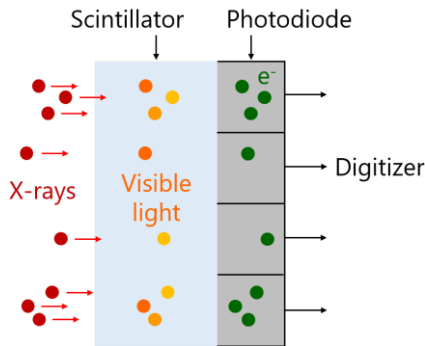


Figure 1.4. Typical X-ray detectors consist of a scintillator layer that converts X-ray photons into visible light photons. Photodiode pixels then convert the visible light photons into an electrical signal, which is digitized as an intensity value.

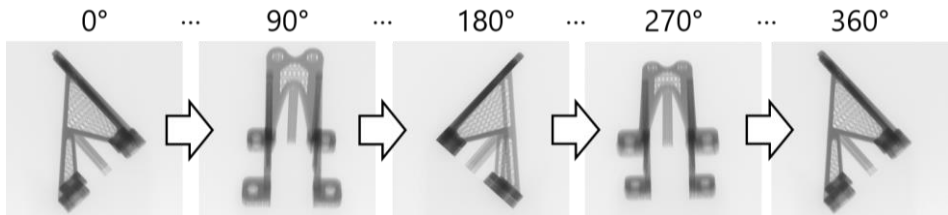


Figure 1.5. Radiographs of the workpiece are acquired at multiple viewing angles (typically thousands), controlled by the sample rotation stage.

A three-dimensional volumetric model of the workpiece can be generated by way of tomographic reconstruction on the set of radiographs. Just as an image is comprised of pixels, the volumetric model consists of three-dimensional voxels (volumetric pixels). Each voxel is characterized by a grey value corresponding to the local material attenuation at the voxel position within the measurement volume [10]. The grey value of the voxels can be used to extract surface information from the volumetric model. Since the grey values correspond to varying material properties, the edge between two materials can be defined by a transition in grey values. A surface model can be generated by detecting edges between features with different material attenuation by way of grey value thresholds. The concept of applying a grey value threshold to define a surface to the volumetric dataset is illustrated in figure 1.6. Subsequently, surface points can be extracted by defining a sampling interval on the surface model. The resulting surface points can then be used for dimensional analysis of the workpiece.

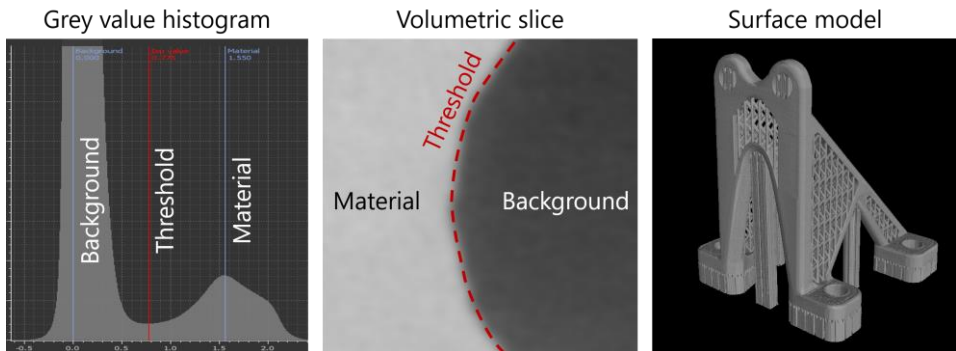


Figure 1.6. A surface model can be defined from the volumetric dataset by applying a grey value threshold.

As CT is adopted by manufacturers and other industrial users, there is a strong demand for methods to determine the measurement performance of the instrument. In particular, the assessment of measurement uncertainty is critical to the application of CT for traceable coordinate measurements [11,12]. The uncertainty of coordinate measurements made on a CT system is a result of various influence factors in the measurement procedure [13]; a simplified diagram of influence factors is shown in figure 1.7.

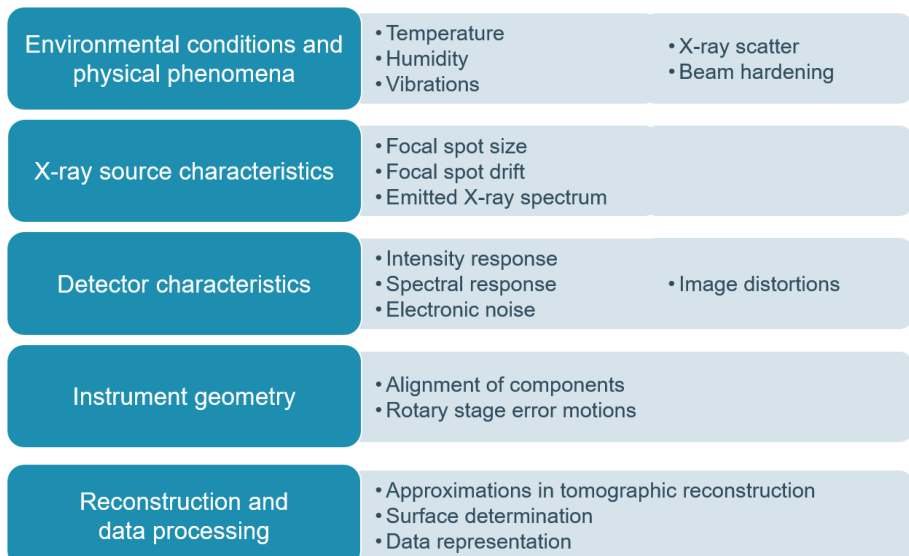


Figure 1.7. Influence factors in X-ray CT measurements

A subset of influence factors are related to the CT instrument geometry. Inconsistencies between the actual CT instrument geometry and the geometry assumed by the tomographic reconstruction algorithm can be detrimental to the quality of coordinate measurements. For this reason, it is important that users are provided with a procedure they can use to measure the geometry of their CT system. The focus of this doctoral thesis is the development of such a procedure.

## 1.4 Measurement traceability

The International Vocabulary of Metrology (VIM [14], abbreviated from the French equivalent) defines traceability as the

“property of a measurement result whereby the result can be related to a reference through a documented unbroken chain of calibrations, each contributing to the measurement uncertainty.”

Measurement traceability provides a certain level of confidence about the validity of a result. This confidence is achieved by establishing a relationship between the result of a measurement and a common reference. Achieving traceability of measurements can be an arduous task. Traceability is an important property of a measurement and has several economic and practical implications, particularly in manufacturing and in commerce. For this purpose, the significant efforts needed to establish traceability of measurements can be justified. A look into the history of traceability provides context for its importance today.

### 1.4.1 History

The concept of traceability was born out of the need to standardize measurements [2]. The industrial revolution of the 18<sup>th</sup> and 19<sup>th</sup> centuries brought about influential breakthroughs in measurement technology as a result of a newly introduced paradigm in manufacturing: the adoption of interchangeable components. Products that were once individually custom-made by a skilled craftsman and in a single manufacturing process could now be made in separate but parallel manufacturing steps by relatively lower skilled technicians; the final product was achieved by assembly. This new paradigm significantly increased production rates. Also, there was no longer the need to have a skilled craftsman who knew how to make all components of a final product. The elimination of skilled labor meant cost-saving for the manufacturer.

Interchangeability means that any component chosen at random from the same manufacturing step will fit the final assembly. However, the delegation of production to separate manufacturing steps introduced a new challenge: ensuring that all the components indeed fit in the final assembly of the product. Each technician had to ensure that their components conformed to their specifications. In order to achieve this conformance, measurements performed during quality control needed to be uniform among all manufacturing processes. In other words, all measurements needed to be consistent with a common reference. Traceability was introduced as a property of a measurement to demonstrate this consistency.

The increasingly global nature of manufacturing and trade during the 19th century meant that the issue of traceability was no longer limited to a single factory or manufacturing chain. Representatives from several industrialized states agreed on the need for international uniformity of measurements. The *Metre Convention* of 1875 established the International Bureau of Weights and Measures (BIPM, abbreviated from the French equivalent), which was tasked with defining and disseminating the International System

of Units (SI) [15]. The definition of each SI unit of measurement serves as the ultimate reference for traceable measurements of the corresponding physical quantity throughout the world.

### 1.4.2 The standard unit of length

The international reference for dimensional measurements is the SI unit of length—the meter. The definition of the meter and the method with which it is practically realized have changed several times in history. The first internationally accepted meter was defined in 1889 as the length between two lines marked on a physical object: the International Prototype Platinum-Iridium meter bar (figure 1.8). The original prototype meter bar is stored in Breteuil, a location south of Paris.



Figure 1.8. The International Prototype Platinum-Iridium meter bar. Image courtesy of NIST.

In 1960, the meter was re-defined in terms of the wavelength of light emitted by the excitation of krypton-86 atoms. The definition of the meter in terms of a physical constant—in this case, the wavelength of light—meant that the standard unit of length could be realized in any laboratory by way of interferometric methods [16]. The most recent definition of the meter was accepted in 1983 and is given by the

“length of the path travelled by light in vacuum during a time interval of  $1/299\,792\,458$  of a second.” [15]

This definition sets the speed of light in vacuum as a constant and ties the definition of the meter to the definition of the SI unit of time—the second. In practice, this definition meant that the realization of the standard unit of length by interferometric methods was no longer limited to light emitted by krypton-86. The BIPM provides a list of recommended sources of light that provide a stable wavelength with narrow bandwidth. Helium-neon (He-Ne, wavelength  $\lambda_{\text{He-Ne}} \approx 632.8$  nm) lasers are one of the more commonly used light sources for interferometry. A further re-definition of the meter is expected in the near future.

### 1.4.3 Achieving traceability of dimensional measurements

The measurement result is linked to the physical realization of the meter by one or more calibrations. *Calibration* is the measurement of a physical quantity, such as the length of a feature on a test object or the distance between indications on a test instrument, by comparison to a traceable reference. The path of calibrations linking a measurement result to the definition of the meter is known as the *traceability chain*. An example of a traceability chain for CT measurements is illustrated in figure 1.9, including how the various calibration steps are realized. Each calibration step contributes to uncertainty in the final measurement, which must be assessed for the measurement to be considered traceable.

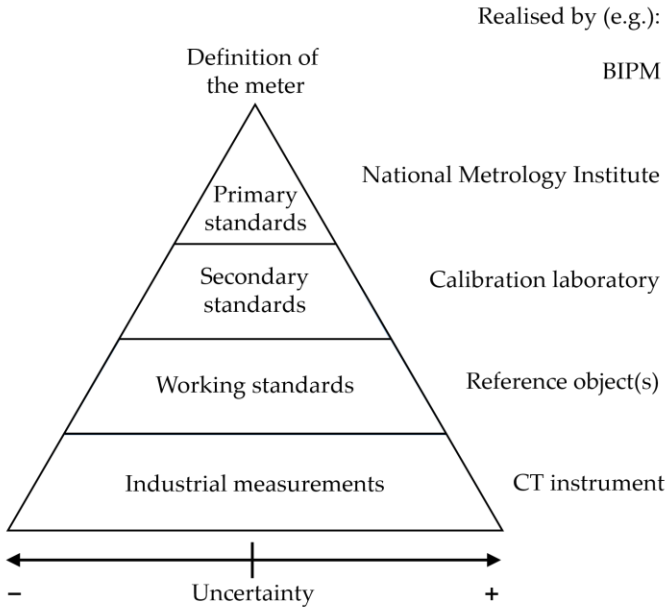


Figure 1.9. Sample traceability chain for CT measurements.

The result of a measurement is an estimate of the quantity being measured, i.e. the measurand, and *measurement uncertainty* is the degree of confidence with which the estimate can be attributed to the measurand. Consistent with its formal definition in the VIM, uncertainty  $U$  in the measurement of  $Y$  is expressed as a dispersion of values about the measurement result  $y$ , i.e.  $Y = y \pm U$ . A common misconception is that a measurement can be “more traceable” if there are fewer calibration steps separating it from the definition of the unit or if its uncertainty is comparatively lower. Traceability is a nominal property [14] of measurement and, therefore, does not have a magnitude. A measurement is either traceable or it is not traceable, irrespective of the number of calibration steps linking it to the definition of the SI unit or its uncertainty.

A measuring instrument serves as the reference for establishing traceability of its measurements. The reference is typically provided by the instrument scale, for example the length indications on Vernier calipers and micrometers. In these simple cases, instrument calibration refers to comparing the positions of instrument’s indications to a traceable reference and assessing the uncertainty in the comparison step. Gauge blocks are commonly used reference objects for calibrating the scales of simple one-dimensional end-to-end measuring instruments [17]. Calibration of more complicated measuring systems, such as X-ray CT, requires a thorough understanding of how the scale is realized in the instrument.

## 1.5 CT instrument scale

To understand how traceability of CT measurements can be achieved, it is necessary to understand how the instrument scale is realized and transferred to the measured object as a set of surface coordinates. CT measurements differ from measurements by other CMSs in that the coordinates of a surface point are not directly given by the indexed position of the instrument’s kinematic axes [2]. The imaging nature of the radiographic data acquisition step is further complicated by the tomographic reconstruction of the measurement volume and subsequent thresholding to convert the volumetric data to surface coordinates.

The measurement volume is defined as a three-dimensional distribution of voxels centered at the intersection of the magnification axis and the axis of rotation (see figure 1.10). The shape of the voxels is typically cuboid but not necessarily cubic. For simplicity, measurement volumes with cubic voxels are discussed here. The length of the voxel's sides, namely the voxel size  $vox$ , is generally a function of detector pixel size  $pix$  and the magnification factor  $M$ , as shown in equation 1.1:

$$vox = \frac{pix}{M} \quad (1.1)$$

where  $M$  is given by the ratio of the source-to-detector distance  $SDD$  and the source-to-rotation axis distance  $SRD$ , as shown in equation 1.2:

$$M = \frac{SDD}{SRD}. \quad (1.2)$$

Substituting equation 1.2 into equation 1.1,

$$vox = pix \left( \frac{SRD}{SDD} \right). \quad (1.3)$$

It should be noted that the relationship provided in equation 1.3 is only a general rule; the physical size and shape of the voxels can be specified differently in the tomographic reconstruction step.

The goal of tomographic reconstruction is to populate the voxel space with values proportional to the X-ray attenuation incurred within the volumetric extent of each voxel. The measured X-ray intensity at each pixel is back projected as a linear trajectory from the corresponding pixel position to the X-ray focal spot. Each trajectory traces a path through the measurement volume and intersects a series of voxels along that path (figure 1.10). Attenuation values for each voxel are calculated from the collection of radiographic intensities whose back projected trajectories intersect that voxel for all angular positions of the volume. Accurate reconstruction of the measurement volume therefore relies on accurate knowledge of the instrument geometry. The measurement of the CT instrument geometry is the topic of doctoral research in this thesis.

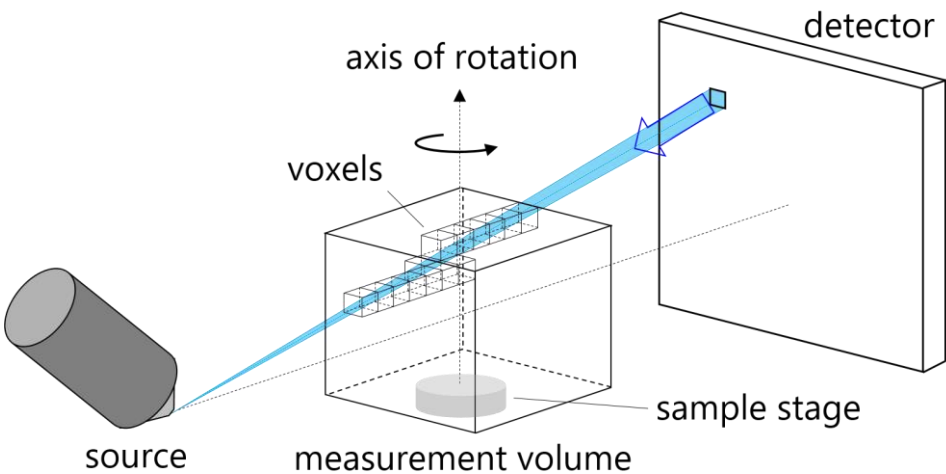


Figure 1.10. Schematic diagram of the backprojection concept in tomographic reconstruction.

### 1.5.1 CT instrument geometry

Conventional tomographic reconstruction algorithms rely on a nominal alignment of the CT instrument. Furthermore, sample stage rotation is assumed free from error motions. In practice, the actual CT instrument geometry will deviate from its nominal state and the sample stage will exhibit error motions. Deviations from the conditions assumed by conventional tomographic reconstruction algorithms will result in errors of CT measurements. Cone-beam X-ray CT instruments are discussed here, although the concepts can be extended to other instrument architectures given appropriate modifications.

The geometry of a cone-beam CT instrument is defined by the relative position and orientation of X-ray source focal spot, axis of object rotation (AOR), and detector. The diagram in figure 1.11, which illustrates a typical cone-beam CT instrument, supplements the following description of the coordinate convention. A right-handed global Cartesian coordinate system is fixed with its origin at the X-ray source focal spot  $S$ . The  $Y$  axis is parallel to the AOR, while the  $Z$  axis is coincident with the line from  $S$  that intersects the AOR orthogonally. The  $X$  axis subsequently follows the right-hand screw rule. In an aligned instrument, the detector rows are parallel to the global  $X$  axis, while the detector columns are parallel to the  $Y$  axis. The  $Z$  axis ideally intersects the detector at its geometrical center. The  $U$  and  $V$  axes of the detector coordinate frame correspond to the indexing axes for the detector column and rows, respectively.

The position of the AOR is given by  $\mathbf{R} = (0, 0, z_R)$ , corresponding to the coordinate position of its intersection with the  $Z$  axis. Rotation of the sample stage is parameterized by the angle  $\alpha$ . The position of the detector center is parameterized by the point  $\mathbf{D} = (x_D, y_D, z_D)$ . Detector orientation is defined by three extrinsic rotations performed about local axes that are parallel to the axes of the coordinate system and whose origin is the detector center: tilt  $\theta$  about the local  $X$ -axis, slant  $\phi$  about the local  $Y$ -axis, and skew  $\eta$  about the local  $Z$ -axis. Rotations are applied in the following sequence:  $\eta$ ,  $\phi$ , then  $\theta$ . The angular displacement of the sample rotation stage with respect to a starting position is given by  $\alpha$ . The parameterization of a cone-beam CT instrument is therefore given by 8 parameters, which are summarized in table 1.1. The CT instrument parameterization presented here is not unique, as will be shown in the literature review (chapter 2).

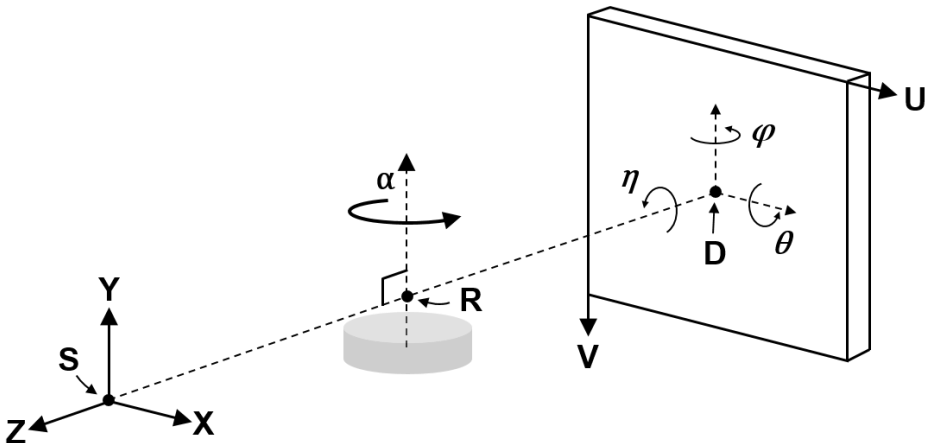


Figure 1.11. Parameterization of CT instrument geometry.  $S$  is the position of the X-ray source focal spot,  $R$  is the position of the axis of rotation, and  $D$  is the position of the detector geometrical center. Detector orientation is given by three extrinsic rotations in the order  $\eta$ ,  $\phi$ , and  $\theta$ . The rotation angle of the sample stage is given by  $\alpha$ .

Table 1.1. Parameters of cone-beam CT instrument geometry.

Component	Feature	Parameters
X-ray focal spot	Position	$\mathbf{S} = (0,0,0)$
AOR	Position	$\mathbf{R} = (0,0,z_R)$
Detector	Position	$\mathbf{D} = (x_D, y_D, z_D)$
Detector	Orientation	$(\eta, \varphi, \theta)$
Rotation stage	Angular position	$\alpha$

Error motions of the rotation stage in X-ray CT instruments can also affect the quality of measurements performed on the acquired data. The stage with which the measured sample is rotated can have indexing errors and rotational error motions. Parameterization and sensitivity analysis of rotation stage errors are covered in section 3.2, where their influence on CT measurements is deemed negligible for common “macro” CT instruments. Other factors that can be considered geometrical are planar distortions of detector, focal spot drift, and focal spot size. The measurement of these factors is covered briefly in [1]; however, they are not addressed further in this thesis.

## 1.6 Motivation of doctoral research

Geometrical misalignments can be partially compensated by instrument adjustment, i.e. physically positioning the components to their aligned state, or by adapting the tomographic reconstruction algorithm to the actual instrument geometry. Both compensation strategies rely on the measurement of the instrument geometry. Currently, measurement and compensation of CT instrument misalignments are generally proprietary to instrument manufacturers. The research presented in this thesis concerns the development and implementation of a robust method to measure the geometry of a cone-beam CT instrument. A critical objective in this doctoral research is the development of a method that can be easily implemented by any user of CT instruments. The users would be able to use the output of the geometrical measurement procedure to inform the compensation of instrument misalignments.

## 1.7 Objectives

The objectives listed below corresponds directly to the topics discussed in the chapters presented in this doctoral thesis.

- Identify significant geometrical error sources by way of sensitivity studies (chapter 3)
- Develop robust and effective method for measuring the CT instrument geometry (chapter 4)
- Apply the geometrical measurement procedure on an experimental CT instrument and validate its effectiveness on the subsequent adjustment of the instrument and CT measurement of a validation object (chapter 5)
- Present a method for assessing uncertainty in the measured geometrical parameters and discuss its implications. (chapter 6)

## References

- [1] Ferrucci M, Leach RK, Giusca CL, Carmignato S, Dewulf W (2015) Towards geometrical calibration of X-ray computed tomography systems - A review. Measurement Science Technology 26, 92003. doi:10.1088/0957-0233/26/9/092003

## Chapter 1

- [2] Ferrucci M (2017) Towards traceability of CT dimensional measurements. In: Carmignato S, Dewulf W, Leach RK, editors. *Industrial X-Ray Computed Tomography* (Springer-Verlag: Berlin, Germany)
- [3] Ferrucci M, Hermanek P, Ametova E, Carmignato S, Dewulf W (2018) Measurement of the X-ray computed tomography instrument geometry by minimization of reprojection errors—implementation on simulated data. *Precision Engineering* 54, 7-20
- [4] Ferrucci M, Heřmanek P, Ametova E, Sbettega E, Vopalensky M, Kumpova I, et al. (2018) Measurement of the X-ray computed tomography instrument geometry by minimization of reprojection errors—implementation on experimental data. *Precision Engineering* 54, 107-117
- [5] De Chiffre L, Carmignato S, Kruth J-P, Schmitt R, Weckenmann A (2014) Industrial applications of computed tomography. *CIRP Annals - Manufacturing Technology* 63, 655–677 doi:10.1016/j.cirp.2014.05.011
- [6] Kruth JP, Bartscher M, Carmignato S, Schmitt R, Chiffre L De, Weckenmann A (2011) Computed tomography for dimensional metrology. *CIRP Annals - Manufacturing Technology* 60, 821–842 doi:10.1016/j.cirp.2011.05.006
- [7] Hsieh J (2015) *Computed Tomography: Principles, Design, Artifacts, and Recent Advances* 3<sup>rd</sup> edition (SPIE Press: Bellingham, USA)
- [8] Buzug T (2008) *Computed Tomography: From photon statistics to modern cone-beam CT* (Springer-Verlag: Berlin, Germany) doi:10.1007/978-3-540-39408-2
- [9] Carmignato S, Dewulf W, Leach RK, editors (2018) *Industrial X-Ray Computed Tomography* (Springer International Publishing: Cham, Switzerland). doi:10.1007/978-3-319-59573-3
- [10] Müller P (2012) *Coordinate metrology by traceable computed tomography*. PhD Thesis (Technical University of Denmark)
- [11] Carmignato S (2012) Computed tomography as a promising solution for industrial quality control and inspection of castings. *Metallurgical Science and Technology* 30 (1), 5–14
- [12] Angel J, De Chiffre L (2014) Comparison on computed tomography using industrial items. *CIRP Annals - Manufacturing Technology* 63 (1), 473–476 doi:10.1016/j.cirp.2014.03.034
- [13] Verein Deutscher Ingenieure (2008) *VDI/VDE 2630 Part 1.2 Computer tomography in dimensional metrology – Factors influencing the measurement result and recommendations for dimensional computed tomography measurements*
- [14] BIPM JCGM 200 (2012) *International vocabulary of metrology – Basic and general concepts and associated terms (VIM) 3<sup>rd</sup> edition* (Geneva: International Organization for Standardization)
- [15] BIPM (2006) *The International system of units (SI), 8<sup>th</sup> edition “The SI Brochure.”* (Geneva: International Organization for Standardization)
- [16] National Bureau of Standards (1975) *The International Bureau of Weights and Measures 1875–1975, translation of the BIPM centennial volume*. NBS Special Publication 420, 77–85
- [17] Doiron T, Beers J (2005) *The gauge block handbook*. NIST Monograph 180

# Chapter 2

## Literature review on the state-of-the-art

This chapter provides a review of the literature dedicated to understanding the effects of geometrical errors on CT dimensional measurements and on methods to measure these errors. The contents of this chapter are reproduced from the more comprehensive literature review published at the beginning of my doctoral research [1]. The parameterization of the CT instrument geometry varies among the reviewed works. A temporary parameterization is presented in this chapter to improve legibility and comprehension of the presented studies. The role of measurement models to determine the sensitivity of CT measurements to various influence factors is introduced and several studies are presented in which such measurement models are applied. Then, analytical and numerical (minimization) methods based on imaging a reference object for determining the CT instrument geometry are reviewed. A discussion is provided on the nature of CT as both an imaging and a mechanical technology. Reference instruments such as interferometers and electronic levels can be used to measure the mechanical error motions of the sample stage kinematic axes. A full geometrical mapping of the instrument relies on the combination of both imaging and mechanical methods. These concepts are considered in the summary and conclusions section of the literature review and suggestions for future work are provided.

### 2.1 Parameterization of the instrument geometry

Most studies parameterize the CT instrument geometry from the perspective of the imaging system, thereby introducing concepts such as the magnification axis and the detector principal point. This parameterization differs from the more ‘mechanical’ parameterization presented in chapter 1 and used in the geometrical measurement procedure presented in this thesis. Furthermore, some studies define the coordinate axes of the global frame with respect to the detector, as opposed to the source/rotation axis coordinate axes defined in chapter 1. The word ‘gantry’ sometimes mentioned in this chapter denotes the source and detector assembly and is a term often used in medical CT, where the source and detector rotate about a fixed patient. We introduce a temporary parameterization to improve legibility of the presented studies. Note that the following parameterization is only relevant within the confines of this chapter.

Global coordinate axes are defined for the purpose of describing the ideal system geometry (figure 2.1). The magnification axis, also the Z axis, is given by the linear path from the center of the X-ray source to the detector. The Y axis is parallel to the rotation axis. The X axis is orthogonal to both the Y and Z axes, thus forming a Cartesian coordinate system. For a fixed position of the rotation stage, a cone-beam CT system is considered aligned when it satisfies the following conditions (figure 2.2):

- (i) the intersection of the magnification axis with the detector (also known as the principal point – a term used in geometrical modelling of cameras [2]) is coincident with the center of the detector,
- (ii) the magnification axis is normal to the detector,
- (iii) the magnification axis intersects the axis of rotation and the angle between the two axes is  $90^\circ$ , and
- (iv) the projection of the axis of rotation is parallel to the detector pixel columns.

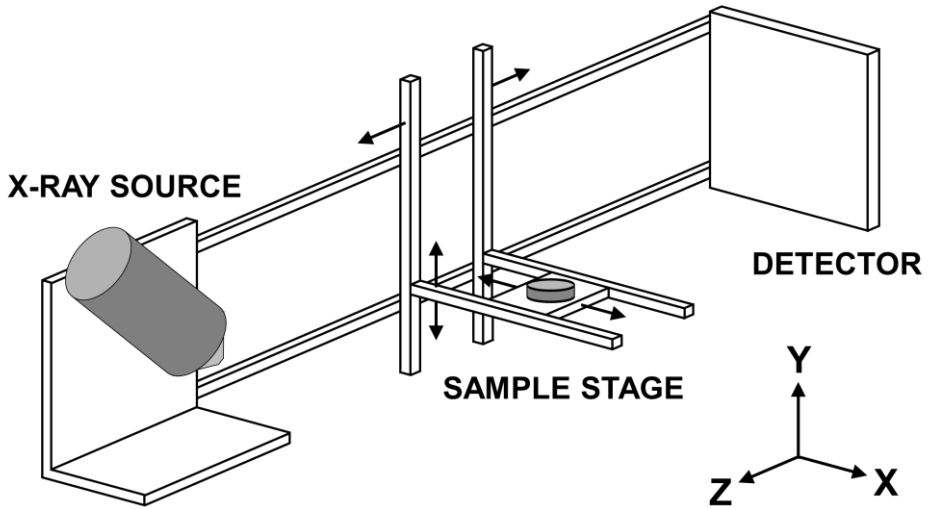


Figure 2.1. The dotted line from the X-ray source to the detector defines the magnification axis. The Y axis is parallel to the rotation axis. The X axis is orthogonal to both the Y and Z axes, forming a Cartesian coordinate system. A flat panel detector, which corresponds to cone-beam CT systems, is shown. This diagram shows one type of construction of CT systems; however, other architectures are possible.

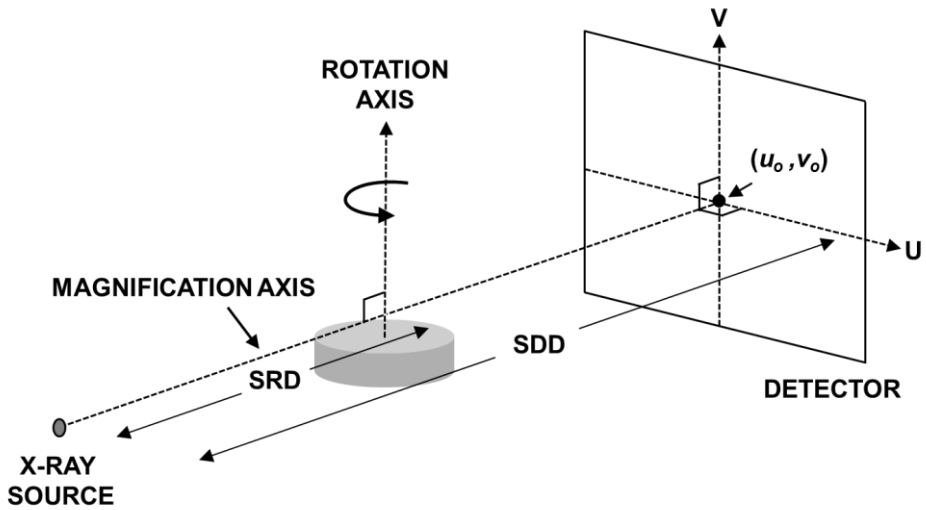


Figure 2.2. An aligned cone-beam CT system satisfies a series of conditions shown in this diagram. Any deviation from these ideal conditions is considered a geometrical influence factor.

Any deviations from these ideal conditions are considered misalignments and can contribute to errors in dimensional measurements. Deviations from condition (i) can be described by the pixel position  $(u_0, v_0)$  of the principal point. Deviations from condition (ii) are described by two out-of-plane rotations  $\theta$  and  $\varphi$  of the detector (figure 2.3a and figure 2.3b, respectively). If the magnification axis does not intersect the rotation axis (condition (iii)), the rotation axis is said to have an X offset  $m$ . The parameter  $m$  is used in the literature and corresponds to a 'mechanical offset' of the rotation axis, not to be mistaken with the magnification factor  $M$ . Generally, a Y offset of the rotation axis is only of consequence for scans that require translation of the stage along Y (fan-beam CT). If the rotation axis is not orthogonal to the

magnification axis, the rotation axis is said to have a tilt  $\theta_R$  about the X-axis (figure 2.3c). A deviation from condition (iv) is an in-plane rotation of the detector  $\eta$  (figure 2.3d). Additionally, the distance from X-ray source to rotation axis, SRD, and the distance from X-ray source to detector, SDD, are assumed to be accurately known. Any discrepancy between assumed and actual distances will result in a global scaling error. Rotation of the sample throughout a scan is given by the angular index  $\alpha$ . The parameters that describe the geometry of a CT system for a fixed rotation stage position are shown in table 2.1.

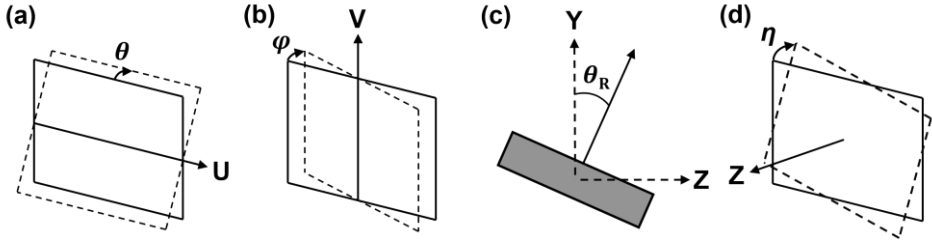


Figure 2.3. Some of the geometrical influence factors in cone-beam CT systems include (a) detector tilt  $\theta$ , (b) detector slant  $\varphi$ , (c) rotation axis tilt  $\theta_R$ , and (d) detector in-plane rotation  $\eta$ .

Table 2.1. The geometry of a cone-beam CT system for a fixed kinematic position of the rotation stage can be described by the set of parameters shown here.

Parameter	Description
$SRD$	Source-to-rotation axis distance
$SDD$	Source-to-detector distance
$u_o$	Detector offset (X)
$v_o$	Detector offset (Y)
$\theta$	Detector tilt (out-of-plane)
$\varphi$	Detector slant (out-of-plane)
$\eta$	Detector skew (in-plane)
$m$	Rotation axis offset (X)
$\theta_R$	Rotation axis tilt (about X)
$\alpha$	Angular index of rotation axis

The position of the sample rotation stage can be controlled by way of kinematic positioning axes, which are known to have errors [3]. Rotation stage translation is achieved by way of precision guide-ways; linear encoders or other distance sensors monitor the position of the rotation stage on each kinematic axis separately. Offsets between linear indexed position and actual position are considered positioning errors. Squareness errors between axes and straightness errors can also exist in the kinematic axes. These errors directly affect the parameters describing the linear position and angular orientation of the rotation axis with respect to the source/detector assembly. For example, positioning errors of the Z axis as well as squareness and straightness errors of the X and Y axes along the Z direction (generally associated with Abbe offsets) will result in an error in SRD. Alternatively, positioning errors of the X axis as well as squareness and straightness errors of the Y and Z axes along the X direction will result in an error of  $m$ . Errors along the Y direction are only considered if translation of the rotation stage along the Y axis is required, such as for fan-beam systems. Kinematic axes can also exhibit rotational behaviors (roll, pitch, and yaw) as a function of axis position, which translate to tilts and shifts of the rotation stage with respect to the fixed gantry ( $\theta_R$  and  $\eta$ ). If these kinematic errors are not mapped, the instrument geometry as parameterized in table 2.1 would need to be newly determined with every new position of the sample stage.

## 2.2 Measurement model

A useful step in trying to understand the performance of a measurement system is by way of a measurement model. The behavior of a particular system can be described by mathematical expressions that relate influence factors in the measurement procedure to the final measurement result [4]. Each influence factor will have a corresponding parameter within the model. In the case of coordinate measurement systems, the model parameters correspond to the behaviors of the various mechanisms that allow the instrument to make a coordinate measurement. For example, contact-probe CMMs make three-dimensional measurements by translating a touch-probe along mechanical axes. In an ideal Cartesian system, the axes are orthogonal to each other and do not exhibit any positioning, straightness, or tilt errors [5]. Assuming no environmental factors, e.g. temperature variations from the specified reference (usually 20 °C) or vibrations, the model of such an ideal system would simply be defined by a Cartesian coordinate system with inputs X, Y, and Z, corresponding to the position along each translation axis. The surface coordinates of a sample (the output) would be a collection of the input coordinates for each probing point. However, in practice, mechanical axes can have myriad error motions. In the presence of these motions, the actual position of a touch probe deviates from the intended position. In order to map the behavior of the mechanical axes, parameters that correspond to the possible error motions are introduced in the CMM model. Once the error motions have been experimentally measured (see e.g. [6-9]), the parameters in the measurement model are populated with their corresponding quantities. If the measurement model accurately describes the behaviors of a specific test system, the results of a simulation should be very close to the results that the test system would provide given the same measurement task. The difference between model output and test results is often used as criteria to evaluate how well the model describes a test system. Measurement models have also been applied to laser trackers [10] and laser scanners [11].

CT is an imaging technology and, as such, a CT model is an imaging model. In particular, concepts from projective geometry are applicable in describing how X-rays are projected from the source, through the sample, and onto the detector. The geometrical relationships between the three main components of a CT system are incorporated into the parameters of a projective geometry model. Given a set of geometrical parameters, the model maps the three-dimensional space of the sample onto the two-dimensional radiograph for each rotation position or 'pose' of the system. However, due to the fact that CT systems also incorporate kinematic parts, the imaging model needs to allow for changes in geometry as a result of changes in the kinematic configuration. Therefore, the mechanical models and principles often used in modelling CMMs are applicable to CT systems together with projection models [12].

One of the benefits of having a measurement model is the ability to evaluate the sensitivity of a measurement to each influence factor. Such a study can be performed either by analytical derivation of the mathematical expressions relating the measurement output to each influence factor [13] or by performing simulations in which the measurement results are observed as the various parameters are changed [14]. A model can also be applied to determine the influence quantities of a test system. In this method, the model is fit to a set of experimentally observed results; the parameters in the model are allowed to change until the simulated results resemble the observed results. This section will discuss the application of models to sensitivity studies. The 'inverse' application of the model to determine influence quantities will be covered more thoroughly in section 2.3.1 on imaging methods.

A study by Kumar et al. [15] simulated the effects of tilts and positioning errors on the measurement of sphere-to-sphere distances for ball bars of various lengths. In this study, an error model was developed to consider errors in the Z positions of the X-ray source, rotation stage and detector. The error model also incorporates angular errors of the detector, such as tilt, slant and in-plane rotation. The ball bars

were measured in different regions of the detector and at different orientations. The value of each error parameter was controlled individually and the effect on sphere-to-sphere distances was observed.

Results from the simulation indicate that certain error sources affect measurement error more strongly than others. Figure 2.4 shows the measurement error on a 2 mm ball bar as a function of errors in source position (a), rotation stage position (b), detector position (c), in-plane rotation of the detector (d), tilt of the detector (e), and slant of the detector (f). Errors in source and rotation stage positioning had a larger effect on measurement error than positioning errors of the detector. This difference in sensitivity is noted by the fact that, in order to attain the same measurement errors, the largest detector positioning error is thirty five times larger than both source and rotation stage positioning errors. As shown in figures 2.4a-c, measurements made at high magnification (effectively smaller voxel size) were more sensitive to positioning errors than measurements made at low magnification (effectively larger voxel size). The sensitivity is evaluated as the ratio of measurement error to voxel size. A source positioning error of 100  $\mu\text{m}$  resulted in a 0.5 % length measurement error. Rotation stage positioning errors of 100  $\mu\text{m}$  also resulted in a length measurement error of 0.5 %. An error in detector positioning of 3500  $\mu\text{m}$  yielded a 0.0035 % length measurement error, which is well below the noise level of general CT measurements (see chapter 5). The plots also indicate that measurement errors due to positioning errors did not have a strong dependence on ball bar orientation and position in the area of the detector. This is shown by the overlapping of the different plot lines. Thus, it can be deduced that positioning errors result in global scaling errors throughout the measurement volume.

The maximum in-plane rotation ( $0.4^\circ$ ) results in length measurement errors up to 0.1 %. The plot shows that errors from in-plane rotation increase as the ball bar is positioned away from the center of the detector. The presence of detector out-of-plane tilt has a significant effect on the measurement of vertical lengths and very little effect on horizontal lengths. The opposite is true for detector slant; horizontal lengths were measured to have higher errors than vertical lengths. For both tilt and slant, misalignments of  $10^\circ$  resulted in errors up to 1.5 % of the measured length, depending on the position and orientation of the ball bar. The author explains that in-plane rotation can be easily corrected by software and is, therefore, not a critical alignment. On the other hand, the author suggests that detector tilt and slant should be aligned to within  $1^\circ$  to  $2^\circ$  from nominal. However, the findings in chapters 4 and 5 of this thesis indicate that detector out-of-plane rotations of less than  $1^\circ$  from nominal have significant effects on measurement errors.

A study by Wenig et al. [16] also simulated the effects of geometrical errors on a reference object. In this study, the authors observed the effects of detector tilt, slant and in-plane rotation. Each of the angles was individually offset by  $1^\circ$  from their ideal alignment. The average measurement error for a set of seven dimensional features on an alloy object (figure 2.5) was observed as a result of each misalignment separately. The results show that in-plane rotation of the detector caused the largest average error in the measurement of the seven features (about 3.5 % relative measurement error). The errors as a result of detector tilt and slant were barely noticeable.

The authors also looked at the influence of misalignments in the rotation axis of the rotation stage. The seven features on the same object were measured and the influence of each error source was determined. A lateral shift of the rotation axis along the X-axis of 700  $\mu\text{m}$ , which corresponded to a shift of two pixels on the detector, led to an average relative measurement error of about 2.5 %. A  $1^\circ$  tilt of the rotation axis about the X-axis resulted in a relative measurement error of about 0.5 % over all features of the object.

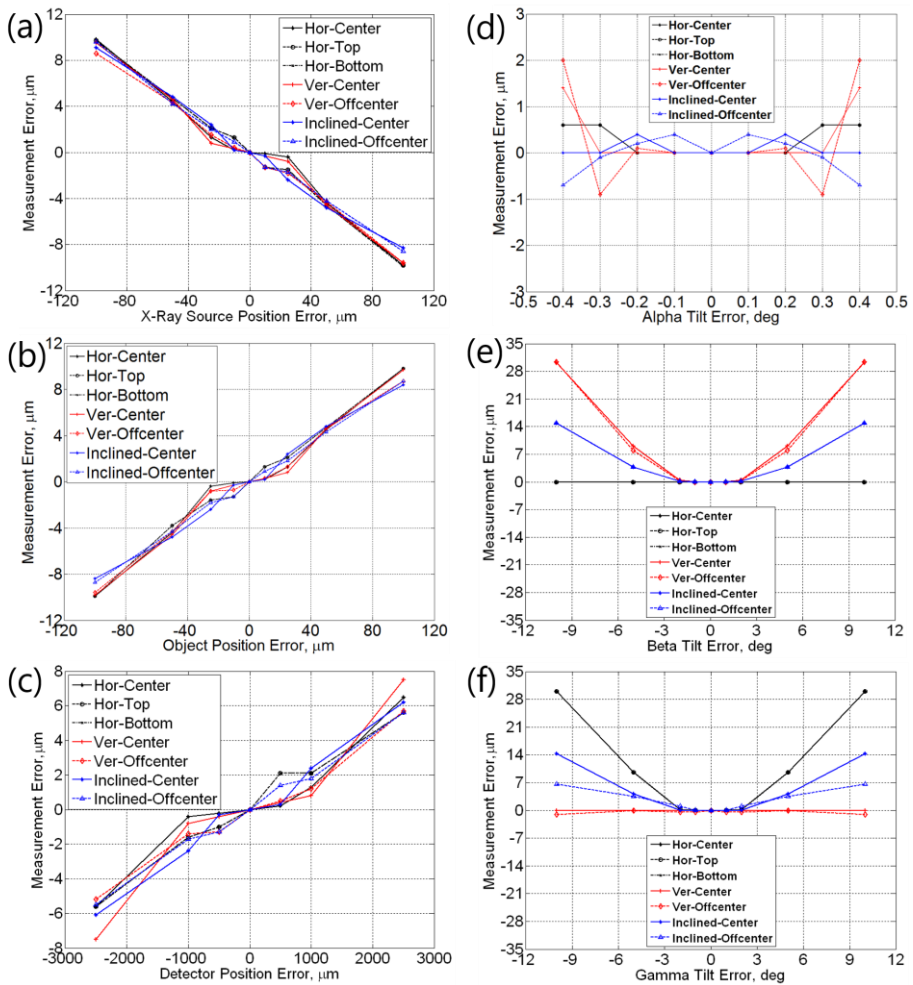


Figure 2.4. The error in measuring a 2 mm ball bar at various positions and orientations is plotted as a function of (a) X-ray source position error, (b) object position error, (c) detector position error, (d) in-plane rotation of the detector, (e) tilt of the detector, and (f) slant of the detector. Figures reproduced from reference [15] with permission.

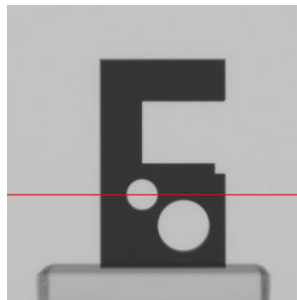


Figure 2.5. A study [16] simulated the influence of detector tilt, slant, and in-plane rotation, as well as tilt and lateral offset of the rotation axis on the measurement of seven features of a simulated object. Figure reproduced from reference [16] with permission.

It is interesting to compare the results of detector misalignment in this study to the results shown in reference [15]. In reference [16] it is concluded that, for equal angle misalignment of  $1^\circ$ , in-plane rotation had the largest effect on measurement error. On the other hand, the simulation study in reference [15] limits the in-plane rotation to  $0.4^\circ$  while changing tilt and slant by  $10^\circ$ . It is then concluded that tilt and slant have larger effects on measurement error than in-plane rotation. Also, the test object in reference [16] includes various dimensional features (outer edges, inner edges, circle-to-circle distance, and circle diameter), whereas reference [15] performed the simulation on a ball bar at various orientations and positions. It is important to note that the measurands in reference [16] suffer from edge offsets, which are caused by thresholding errors. The measurands in reference [15], on the other hand, do not suffer from edge offsets [17]. It should be noted that the observations made on the sensitivity of measurement error to various error sources are highly dependent on the measurement setup (e.g. magnification position, pixel size).

## 2.3 Methods to measure the CT instrument geometry

The general principle in the measurement of the CT instrument geometry is the analysis of radiographic or voxel data to estimate some or all parameters describing the instrument geometry. Most of these imaging methods consist of imaging reference object(s) placed in the instrument's field of view. There are some imaging methods that do not require a dedicated object; these methods are often known as 'on-line' methods [1]. The guiding principle behind 'on-line' methods is the improvement in image and reconstruction quality rather than determining dimensional accuracy. Still, these 'on-line' methods can provide insight into geometrical calibration of CT systems. However, for purposes of conciseness, only imaging methods that utilize dedicated reference objects will be covered in this review.

In general, imaging methods take advantage of concepts from projective geometry. A projective imaging model describes the relationship between the three-dimensional coordinates  $(x, y, z)$  of an object placed in the system's field of view and the coordinates of its projected image (1D for fan-beam CT and 2D for cone-beam CT). This relationship is dependent on the geometry of the imaging system. Imaging methods exploit this dependence to inversely determine system geometry from projection data, given some a priori information about the object or the system. It should be noted that some studies presented here were developed for single-photon emission computed tomography (SPECT) systems; this is of no consequence since the principles presented are also relevant to CT systems. Also, in this section both simulation and experimental studies are presented; the order in which the literature is presented does not separate the two types of studies. Thus, the topics will alternate frequently between simulation and experimental studies.

Section 2.3.1 highlights a commonly applied technique employed by researchers to measure and compensate scaling errors in CT instruments. Then, section 2.3.2 presents the various methods that have been developed—overwhelmingly from the field of medical physics—to estimate the geometrical parameters of the CT instrument. While many of the methods were developed for CT instruments that employ a rotating gantry about a fixed stage, these methods provide insight into future development of procedures for industrial CT systems.

### 2.3.1 Scaling errors

It is appropriate to start the discussion with those methods that have been widely accepted by researchers in the field of industrial CT [18]. A common procedure is to compensate for errors between registered and effective magnification factor, *i.e.* the ratio of *SDD* and *SRD*. The general practice for these 'scale correction' methods is to scan a reference object, which has a series of calibrated length segments, and

to subsequently re-scale the voxels given the difference between the lengths measured by CT and their corresponding calibrated values. In reference [19], a carbon-fiber plate with twenty-five ruby spheres arranged in a regular grid pattern is used as a reference object (figure 2.6a). The distances between sphere centers (for all possible sphere pairs) were calibrated on a CMM. Subsequent to scanning the reference object and performing volumetric reconstruction, the distance between each pair of sphere centers is measured by CT. The authors calculate the deviation (measurement error) of each CT length measurement from its calibrated reference value. The collection of sphere distance errors are plotted against their corresponding calibrated values in figure 2.6b. A linear regression fit is applied to the sphere distance errors and the slope of the fit line,  $a$ , is used to correct the voxel scale *via* equation 2.1.

$$s_{\text{vox}} = \frac{1}{a + 1} \quad (2.1)$$

where  $a$  is the slope of the sphere distance error data and  $s_{\text{vox}}$  is the correction factor to be applied to the original voxel scale. The voxels were consequently corrected and the residual sphere distance errors were plotted against their corresponding calibrated values (figure 2.6b). The effect of the scale correction procedure is noticeable in the residual sphere distance errors.

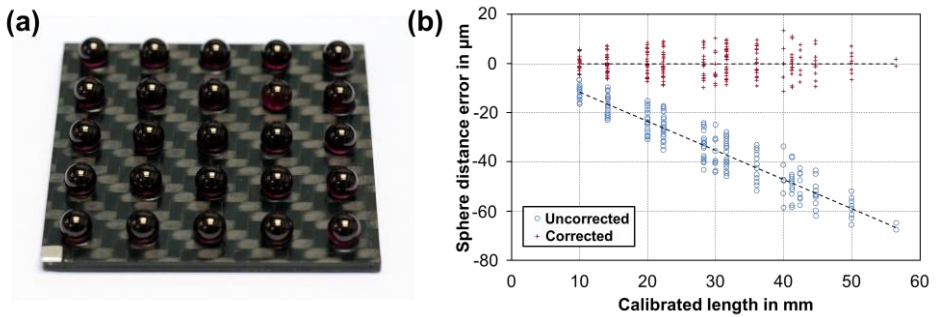


Figure 2.6. (a) A ruby sphere plate is used as a reference object for compensating errors in effective magnification factor. The center-to-center distances between spheres (sphere distance) are calibrated on a reference instrument. (b) The error in sphere distance is plotted against the corresponding calibrated length. The slope of the plotted errors is used to correct the voxel scale. Figures reproduced from reference [19] with permission.

Other studies [20–26] on scale correction methods were performed and were based on the same principle of recalculating voxel scale from the measurement of calibrated features on a variety of reference objects. In reference [20], the authors performed scale correction multiple times over a period of a few months and observed a change in scale correction factor; the scaling factors ranged from approximately 1.005 to approximately 1.00675. For this reason, and due to poor repeatability in the positioning of the rotation stage, the authors recommend that the scale correction methods be carried out either immediately before or immediately after the test scan. On the other hand, if the kinematic positioning is shown to be stable over time, then repeated scale correction might not be necessary. Additionally, instabilities in the position of the X-ray source (focal spot drift) during a scan result in a drift of the effective magnification factor between radiographs. This change in scale between radiographs can be detrimental to the quality of the reconstructed volume.

Scale correction is shown to provide significant improvement in measurement error. However, because of poor repeatability in the kinematic assembly of the system, it is necessary to perform scale correction for each test measurement. It should be noted that the studies mentioned so far apply an error correction to the entire volume of the model, that is, a correction to the effective magnification factor. Dimensional errors can also be non-uniform, *i.e.* they differ from voxel to voxel. In reference [26], a clear difference is shown in dimensional errors along a vertical cross section of the volumetric model. The authors measured

a stack of spheres oriented vertically (figure 2.7a). The sphere-to-sphere distance is measured for each pair of adjacent spheres and the error in distance is plotted against reference values (figure 2.7b). The trend in measurement error for subsequent sphere distances confirms that a systematic non-uniform error exists along the vertical cross section of the volumetric model. Non-uniform errors can exist as a result of various factors, including tilt and slant of the detector, tilt of the rotation stage about the horizontal axis, and distortions along the detector plane (such as dissimilar pixel sizes). In the presence of non-uniform errors, a simple scale correction procedure does not suffice [15].

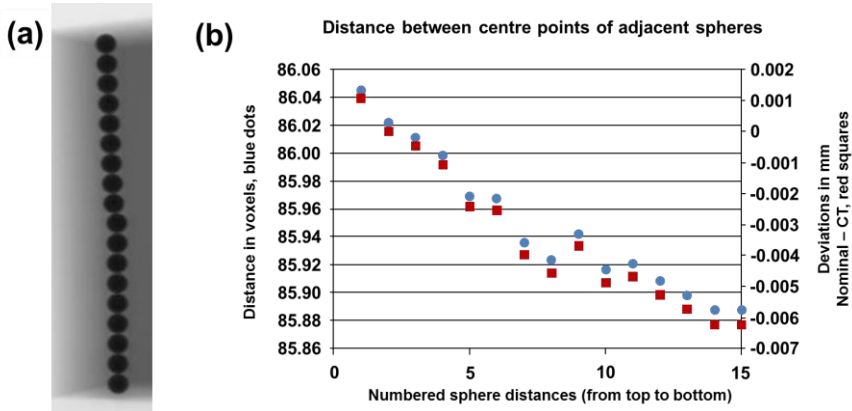


Figure 2.7. (a) A vertical stack of spheres was imaged and the sphere distance between adjacent spheres was compared to the reference measurement. (b) A clear trend in the measurement error as a function of vertical position in the volumetric model confirms the existence of non-uniform errors. Figures reproduced from reference [26] with permission.

### 2.3.2 Estimating CT instrument geometrical parameters

The imaging methods in this section are mainly from the field of medical physics. In general, these methods are based on reference objects consisting of one or more circular or spherical markers. The centers of the spherical markers are used to represent point coordinates in both the 3D object space and on the projected image. The term 'point markers' will be used to denote such markers. Most reference objects consist of a particular arrangement of point markers. Reference objects consisting of several roughly positioned markers, often in an approximately linear array, provide a simple solution to the problem since they do not require accurate alignment. However, the disadvantage of these simple methods is the reliance on assumptions about the system geometry. For example, most of the imaging methods based on simple reference objects require projections to be taken at various rotation positions. An assumption that is often made is that the rotation axis is perfectly stable, i.e. no tilt or positioning error motions as a function of rotation angle. Other imaging methods, on the other hand, employ reference objects with a structured arrangement of point markers, e.g. circular orbits and orthogonal structures. The advantage of these methods is the ability to determine system geometry from one rotation position, thereby avoiding assumptions on the rotational stability. In fact, these methods can be applied to evaluate system geometry as a function of rotation angle and, subsequently, to characterize instabilities in the rotation.

Methods based on imaging of point markers can be distinguished by the process with which the geometrical parameters are determined from projection data [1]. Two of the more prominent processes are numerical optimization (also known as iterative fitting) and analytical evaluation (also known as direct determination). Numerical optimization methods determine geometrical parameters by way of iteratively fitting simulated projections from an imaging model to the observed projections from a test system. An objective function is defined as the difference between simulated and observed projection coordinates.

As the parameters of the imaging model are iteratively changed, the value of the objective function will also change. When the objective function is minimized, the parameters of the imaging model should be closest to those of the test system. A shortcoming of optimization methods is the presence of local minima in the objective function; in this case, the minimization of the objective function has been satisfied but the resolved set of parameters might not be representative of the test system. Thus, to ensure an accurate solution, it is essential that the initial parameter values in the model be reasonably close to the true values. This can be achieved by first obtaining rough estimates of some or all of the parameters by other methods. Alternatively, analytical methods determine geometrical parameters by directly solving a set of equations that relate projection data to the system geometry. Analytical methods do not suffer from the shortcomings encountered in optimization methods. However, analytical methods often require a priori information about the reference object or about the system geometry.

It should be noted that the methods in this section are not organized by the type of analysis performed. Instead, the studies are presented in the context of the error parameters considered in the proposed methods. The first studies are based on imaging a reference object at limited positions and rotations of the stage. The second category of studies consists of methods based on the circular, that is, ideal, rotation of the stage. Finally, methods that consider rotational instabilities of the stage are presented.

#### *Methods based on fixed or limited positions of the rotation stage*

A study from 1993 by Sire et al. [27] proposes a set of procedures to analytically determine misalignments and offsets in cone-beam systems using a grid-plate with regularly distributed holes. Each hole is identified sequentially by a number  $i = 1$  to  $N$  (figure 2.8a). When the grid is imaged, the center of each projected hole  $P_i$  is denoted by  $(u_i, v_i)$  in the coordinate frame of the detector (figure 2.8b). One of the first steps in aligning the system involves ensuring that the magnification axis is centered on the detector. To resolve the principal point, the grid-plate is imaged at two magnification positions (figure 2.8c). The normal to the grid plate should be parallel to the Z axis; this assumes the magnification and Z axes are roughly parallel to each other. As the grid-plate is moved from the first magnification position to the second, the pixel coordinate of each hole will move from  $P_{i,1}$  to  $P_{i,2}$ . By definition, the projection of the X-ray source will not experience a change in pixel coordinates between magnifications. The authors provide an equation for calculating  $(u_0, v_0)$  from the set of hole coordinates  $P_{i,1}$  and  $P_{i,2}$ .

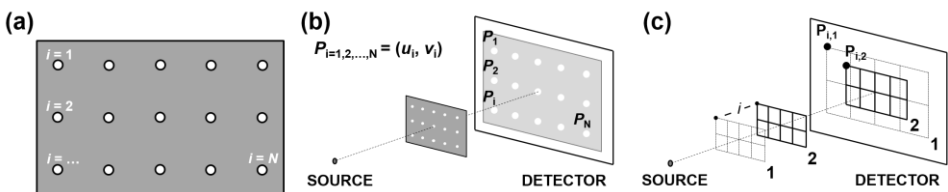


Figure 2.8. (a) Misalignments are determined in reference [27] by way of imaging a grid-plate with regularly distributed holes. Each hole is assigned an identifier  $i$  from 1 to  $N$ . (b) The projection of each hole is assigned an identifier  $P_i$ , where the subscript  $i$  corresponds to the respective hole identifier on the grid-plate. (c) The principal point of the system can be determined by imaging the grid-plate at two magnification positions. The authors provide a mathematical relationship between the principal point and pixel coordinates of the imaged holes at multiple magnifications. Figures adapted from reference [27] with permission.

In an ideal system, the rotation axis of the stage is parallel to the columns of the detector. An angular deviation of the rotation axis about the normal to the detector is equivalent to an in-plane rotation of the detector  $\eta$ . To determine the in-plane rotation of the detector, the grid-plate is imaged at two rotation angles  $180^\circ$  apart. The projected hole centers at the  $0^\circ$  and  $180^\circ$  position are identified as  $P_{i,0}$  and  $P_{i,\pi}$ , respectively. Again, the grid-plate is positioned such that its normal is parallel to the Z axis at the  $0^\circ$  position. If the rotation axis is parallel to the detector columns, the  $v$  coordinate of each imaged hole will

remain the same between rotations, *i.e.*  $v_{i,0} = v_{i,\pi}$ . If this is not the case, a mathematical relationship is provided to calculate the tilt between the axis of rotation and the detector columns (figure 2.9a). Also, the rotation axis should ideally intersect the magnification axis, *i.e.* the projection of the rotation axis should intersect the principal point on the detector plane. The grid-plate is imaged at two rotation angles  $180^\circ$  apart (figure 2.9b). For each hole, the center of mass between the two rotation positions along the U axis,  $u_{i,0}$  and  $u_{i,\pi}$ , is calculated. The U position of the rotation axis,  $u_R$ , is given by the average center of mass of all hole centers. If the rotation axis indeed intersects the principal point, then  $u_R$  should be equal to  $u_0$ . Otherwise, the rotation axis is offset from the magnification axis.

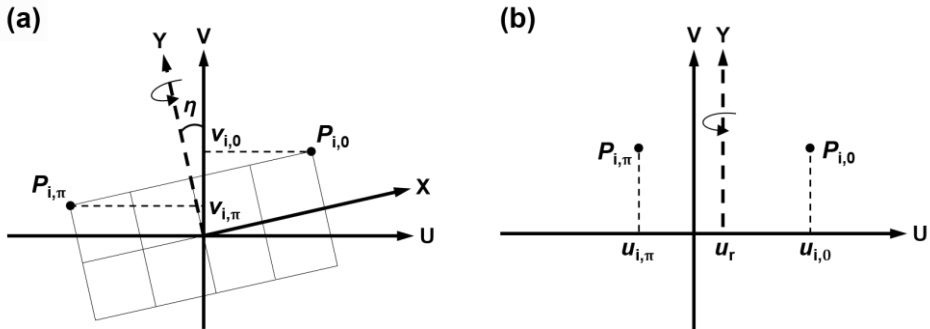


Figure 2.9. (a) A tilt of the rotation axis about the normal to the detector can be determined by imaging the grid-plate at  $0^\circ$  and  $180^\circ$  rotation positions. The relationship between corresponding pixel coordinates for each hole can be used to determine in-plane rotation,  $\eta$ . (b) Similarly, an offset of the rotation axis from the magnification axis can be determined by imaging the grid-plate at  $0^\circ$  and  $180^\circ$  rotation positions and performing analyses on the projected hole coordinates. Figures adapted from reference [27] with permission.

The authors of reference [27] provide a way of calculating *SRD* from pixel coordinates of the hole centers at two or more known magnification positions. If two magnification positions are used, the principal point must be known in addition to the distance between the two positions. If three magnification positions are used, only the distance between the positions is necessary. Additionally, pixel size (the term ‘sampling step’ is used in the study) can be calculated from the hole-to-hole distances, *e.g.* measured by optical CMM.

The study in reference [27] also evaluates geometrical distortions in the plane of the detector. The method involves imaging the grid-plate parallel to the plane of the detector and fitting polynomial functions to the projection of the grid. Any distortions in the plane of the detector will result in distortions of the structure in the projected grid. Global distortions are fit by quadratic equations, whereas local distortions are fit by higher-order polynomial equations for each triangular area defined by lines connecting three adjacent holes.

Another purely analytical method is proposed by Sun et al. in reference [28] using a square plate with four point markers at each of the four corners (figure 2.10). The length between two point markers  $l$  is measured in advance. The authors convert offsets and misalignments in the X-ray source and rotation axis to a set of six parameters in the detector coordinate frame. Analytical expressions are provided that describe the conversion of X-ray source position errors ( $\Delta x_S, \Delta y_S, \Delta z_S$ ), rotation axis position errors ( $\Delta x_R, \Delta y_R, \Delta z_R$ ), rotation axis tilt about the X-axis  $\theta_R$ , and rotation axis skew  $\eta_R$  (about the Z-axis) to the “global” error parameters in detector position ( $\Delta x, \Delta y, \Delta z$ ) and detector orientation ( $\theta, \varphi, \eta$ ). Additionally, consideration is given to the fact that detector tilt, slant and in-plane rotation may not be centered along the middle row, column, and pixel, respectively. Despite the fact that rotation axis tilt and skew are considered, the authors suggest aligning the rotation axis prior to performing the parameter evaluation. The method involves first evaluating the two out-of-plane rotations of the detector  $\theta$  and  $\varphi$  then

calculating  $\Delta z$ . Given the calculated parameters, the detector coordinates are tilted and twisted accordingly to compensate for the out-of-plane rotations. Additionally, the coordinates of the detector are modified to account for  $\Delta z$ . The rotated and translated coordinates are then used to evaluate the in-plane rotation of the detector  $\eta$ . Finally,  $\Delta x$  and  $\Delta y$  can be evaluated.

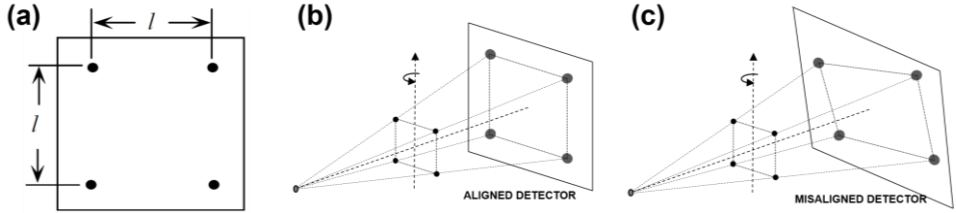


Figure 2.10. In reference [28], the system geometry is defined by a set of six detector parameters. (a) A square plate with four embedded point markers is proposed as a reference object. The point markers are positioned at each of the corners of the plate. (b) In the case of an aligned detector, the line segments between point markers will form a square. (c) Any misalignment in the detector will result in the line segments being imaged in a non-square arrangement. Figures reproduced from reference [28] with permission.

The quality of parameter estimation is determined by simulating the method on several misaligned geometries. In the first simulation, the authors applied misalignments to the X-ray source position, while keeping the rotation axis and detector perfectly aligned. The simulation was performed similarly for misalignments in the rotation axis position and detector. Then, a second set of simulations held one component aligned while applying misalignments to the other two components. A final simulation applied misalignments to all three components. Given the analytical expressions relating X-ray source and rotation axis misalignments to the detector misalignments, the authors provide the equivalent misalignments of the detector when misalignments are applied to the other two components. According to the results, the lateral positioning offsets  $\Delta x$  and  $\Delta y$  and in-plane rotation of the detector  $\eta$  were determined accurately for every combination of misalignments. On the other hand, the estimation accuracy of  $\Delta z$ ,  $\theta$ , and  $\varphi$  differed depending on the applied misalignments. The largest estimation error in  $\Delta z$  (0.132 mm),  $\theta$  (0.3154°), and  $\varphi$  (0.1408°) occurred for the simulation in which both source and detector were misaligned. Large errors are observed in the estimation of out-of-plane detector rotations  $\theta$  (-0.2412°) and  $\varphi$  (0.1267°) for the simulation in which all components were misaligned. It is interesting to note that, for the same simulation, there were no errors in the estimation of  $\Delta z$ .

It should be noted that the previous results were evaluated for perfectly acquired point projection coordinates. The authors investigated the effects of errors in the point projection coordinates on parameter estimation. In the simulation only detector misalignments were applied since the method was able to evaluate the parameters exactly. The coordinates of each projected point marker were systematically perturbed by 1/10, 1/3, 1/2, and 1 pixel(s) sequentially. At each pixel perturbation, the parameters were evaluated. The error in estimating out-of-plane rotations degraded substantially with increasing point coordinate errors. An error in point coordinates of 1 pixel yielded estimation errors of 0.3798° in  $\theta$  and -0.3246° in  $\varphi$ . The errors on other parameters were negligibly small. The authors of reference [28] applied the results of their parameter estimation procedure to modify the reconstruction algorithm in a subsequent study [29]. In this study, it was found that translational errors and in-plane rotation of the detector affect reconstruction quality more severely than out-of-plane rotations.

#### *Methods based on ideal rotation of the stage*

In these studies, reference objects consisting of one or more point markers, *e.g.* small spheres or balls, are imaged at multiple rotation positions. The methods are designed with the assumption that the rotation stage behaves ideally. Early studies [30,31] evaluate system geometry by imaging a single point

marker at various angular positions of the rotation stage (figure 2.11); the authors apply numerical optimization methods. In reference [30] the procedure is presented for a fan-beam system defined by the parameters  $SRD$ ,  $SDD$ , principal point, and X-offset of the rotation axis from the magnification axis  $m$ . This method was subsequently adapted to a cone-beam system in reference [31]; in this study on a cone-beam system, the axis of rotation is assumed perpendicular to and coincident with the magnification axis, therefore the geometry is defined by  $SRD$ ,  $SDD$ , and the principal point.

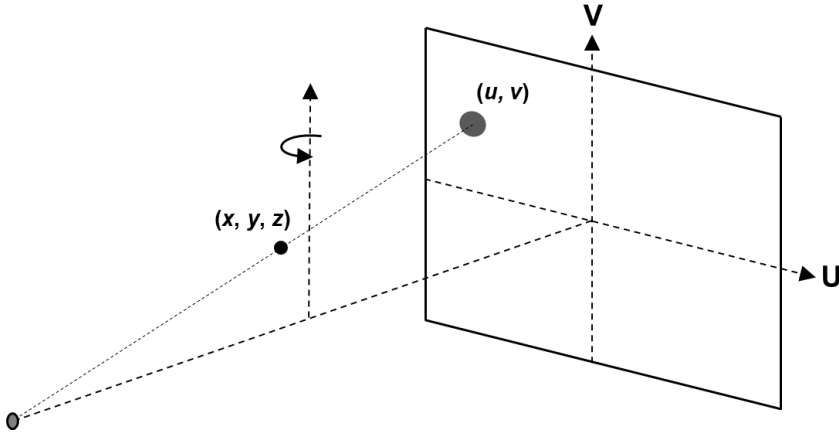


Figure 2.11. Projective geometry is used to model the projection of a point marker from three-dimensional object space  $(x, y, z)$  to two-dimensional detector space  $(u, v)$ .

An analytical approach is presented in reference [32]. Two point objects are placed off the rotation axis and on opposite sides of the system's mid-plane (figure 2.12a). The distance between the two point objects must be known accurately. When the rotation stage performs a complete revolution, each of the point objects ideally traces a circular trajectory in object space (figure 2.12b). This circular trajectory will be imaged by the detector as an ellipse. Depending on the distance of the point object from the mid-plane, *i.e.* its position in  $Y$ , the geometrical properties of the projected ellipse will differ (see figure 2.15, for example).

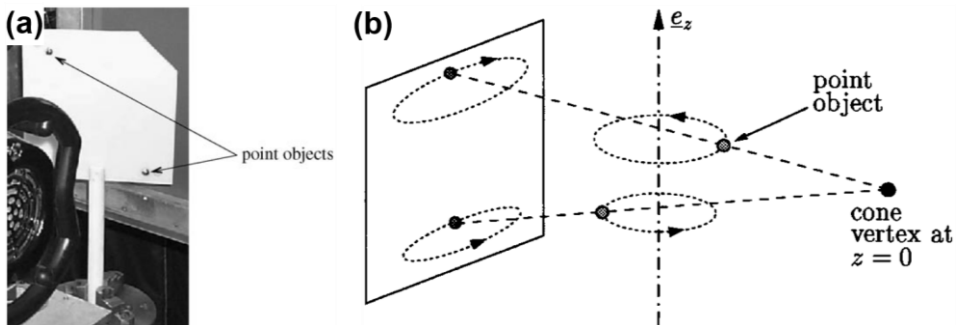


Figure 2.12. In reference [32] the geometry of the system is defined by a set of seven parameters. (a) The method involves imaging two point objects as they revolve around the rotation axis. (b) The circular trajectories traversed by the point objects in physical space are imaged on the radiograph as ellipses. The authors explain that a series of geometrical analyses can be performed on the imaged ellipses to extract geometrical information about the system [32]. © Institute of Physics and Engineering in Medicine. Reproduced from reference [32] by permission of IOP Publishing. All rights reserved.

The properties of the two ellipses are subsequently used to solve for the geometry of the system, which is defined by a set of seven parameters:  $SRD$ ,  $SDD$ ,  $\theta$ ,  $\varphi$ ,  $\eta$ , and principal point.  $SDD$  is defined in reference [32] as the shortest distance between the source and the detector plane, not necessarily along the magnification axis. The method assumes that the detector has no tilt ( $\theta = 0^\circ$ ); the authors ensured this condition with a spirit level before implementing the procedure. Parameters were evaluated for  $N = 6, 12$ , and 120 equally-spaced rotation positions over a full revolution of the rotation axis (table 2.2). The results from different number of rotation positions exhibited only small variations in the estimated parameters, indicating that the method is robust. It is interesting to note that, for the estimation of  $SRD$  and  $SDD$ , the values increased with increasing rotation positions; this trend was not observed for the other parameters.

Table 2.2. The authors of reference [32] evaluated the system parameters for  $N = 6, 12$ , and 120 rotation positions. There were only small deviations in the estimated parameters, indicating a robust method. © Institute of Physics and Engineering in Medicine. Reproduced from reference [32] by permission of IOP Publishing. All rights reserved.

$N$	$SRD$ /mm	$SDD$ /mm	$u_0$ /mm	$v_0$ /mm	$\varphi$ /°	$\eta$ /°
6	377.88	553.49	150.92	202.08	-1.611	-0.304
12	377.90	553.56	151.25	202.08	-1.650	-0.299
120	378.09	553.82	150.88	202.10	-1.607	-0.305

The authors suggest that the accuracy of the parameter estimates strongly depends on the accuracy of locating the center coordinate of the projected point markers. In order to evaluate the sensitivity of parameter estimation to errors in projection coordinates, the authors apply a 0.1 pixel error to all measured point coordinates. This error corresponds to an error associated with using the centroid function on the projection data to approximate the center of the point marker. Given the analytical expressions relating each parameter to the set of point coordinates  $(u_i, v_i)$ , the error in estimated parameters as a result of the coordinate error can be calculated. These error values are presented in table 2.3. The authors suggest that more than two point objects should be imaged for a complete evaluation of system parameters, *i.e.*  $\theta \neq 0^\circ$ .

Table 2.3. Applying a 0.1 pixel error to the measured projection coordinates of each point marker resulted in an error of the various parameter estimates. © Institute of Physics and Engineering in Medicine. Reproduced from reference [32] by permission of IOP Publishing. All rights reserved.

$N$	$\Delta SRD$ /mm	$\Delta SDD$ /mm	$\Delta u_0$ /mm	$\Delta v_0$ /mm	$\Delta \varphi$ /°	$\Delta \eta$ /°
6	1.093	2.012	2.228	0.497	0.223	0.077
12	1.074	1.936	2.201	0.472	0.221	0.077
120	1.163	2.065	2.133	0.511	0.211	0.083

Studies [33,34] were performed to determine the optimal number and arrangement of point markers. In reference [33], the authors confirmed the suggestion made in reference [32] that a minimum of three point markers is required for providing a unique geometrical solution. It should be noted that this study was performed on a SPECT system, which has a focal point (pinhole aperture) located between the detector and the axis of rotation. The distance between the point markers should be known *a priori*. The authors observe that the robustness of parameter estimation is strongly dependent on noise in the projections and any errors in the measurement of distance between point markers. A study of covariance uncovered cross correlations in parameters. The authors found that X-offset of translation axis  $m$  was highly correlated to  $u_0$ , detector tilt  $\theta$  was highly correlated to  $v_0$ , and  $SRD$  was highly correlated to  $SDD$ . In-plane rotation of the detector  $\eta$  was the only parameter found to have no clear correlation to other parameters. Detector slant  $\varphi$  was not considered.

In reference [34], the authors use parameter robustness as criteria to determine the optimal configuration of the three point markers. For each configuration, the authors evaluate the variation in estimated

parameters as a result of (i) noise in the projection data and (ii) errors in the distances between point markers. The analytical expressions in projection geometry relate the geometrical parameters to the point marker locations  $(x_i, y_i, z_i)$  and their projected coordinates  $(u_i, v_i)$ . The authors use these expressions to calculate the deviation in parameter values as a result of noise in the projected point coordinates and errors in the point marker locations. The standard deviation of parameter estimates from their mean is evaluated. The optimal point marker configuration will exhibit the smallest variation in parameter estimates.

The set of possible point marker configurations is given by a spherical grid, the cross section of which is shown in figure 2.13a. The authors systematically iterate through the various point marker configurations, each time evaluating the standard deviation of parameter estimates. The authors found two optimal point marker configurations, one which minimized the parameter deviation as a result of noisy projections (figure 2.13b) and the second minimizing the parameter deviation as a result of errors in the point marker distances (figure 2.13c). Both optimal setups are shown in the X-Y plane, with the dashed line representing the axis of rotation.

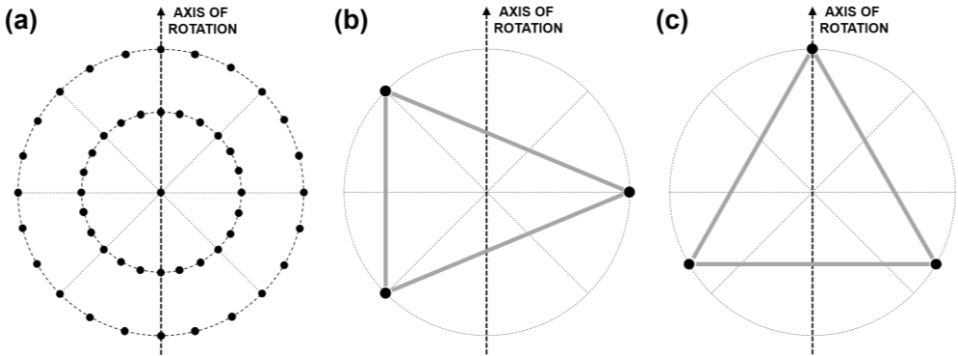


Figure 2.13. Optimal point marker configurations were investigated in reference [34]. (a) The possible point marker positions were distributed within a spherical grid. Here a cross section of the grid is shown together with the rotation axis. (b) A particular configuration of point markers minimized the effects of noise in the projections. (c) Another configuration minimized the effects of errors in the distances between point markers. © 2005 IEEE. Reprinted, with permission, from reference [34].

In reference [35] the analytical approach seen in reference [32] based on imaging circular trajectories is revisited. In this simulation study, twelve point markers were aligned along a line roughly parallel to the axis of rotation and imaged at 180 positions, *i.e.*  $2^\circ$  angular increments of the rotation axis. Six detector parameters ( $\theta$ ,  $\varphi$ ,  $\eta$ ,  $SDD$ , and principal point) were resolved by performing Fourier analysis on the low-frequency components of the elliptical projection coordinates. The method does not require *a priori* spatial information about the point objects; however,  $SRD$  must be known in advance. The parameters were evaluated for each point marker independently. The averaged parameters were compared to the true values from the model used for simulation. To evaluate the stability of the proposed method, the authors applied Gaussian noise to the simulated projection data. The variance in the twelve sets of estimated parameters is taken as the uncertainty of the averaged parameter estimates. The simulation was performed for various levels of noise, denoted by the standard deviation  $\sigma$  of the Gaussian noise: 0.01 pixels, 0.1 pixels, 0.2 pixels, and 0.4 pixels. The deviations of each parameter from true value are shown in table 2.4. While it is clear that the uncertainty in the parameter estimates increases with an increase in the added noise, there is no consistent trend for parameter deviations as a function of added noise.

Table 2.4. The authors of reference [35] evaluated the robustness of their method by simulating various levels of noise in the projection coordinates of the point markers; values were calculated from 50 simulations. Table adapted from reference [35] with permission.

Parameter	True value	Gaussian noise with standard deviation $\sigma$ /pixels			
		0.01	0.1	0.2	0.4
$\theta$ /°	-1.200	$-0.003 \pm 0.019$	$-0.121 \pm 0.219$	$0.225 \pm 0.617$	$-0.083 \pm 0.816$
$\varphi$ /°	1.500	$0 \pm 0.012$	$-0.040 \pm 0.117$	$-0.092 \pm 0.265$	$0.137 \pm 0.352$
$\eta$ /°	-1.000	$0 \pm 4 \times 10^{-4}$	$-0.001 \pm 0.003$	$-0.004 \pm 0.010$	$-0.005 \pm 0.017$
$SDD$ /mm	701.2	$0 \pm 0.3$	$0.4 \pm 2.2$	$-0.4 \pm 2.8$	$-4.3 \pm 5.6$
$u_o$ /mm	1.50	$0 \pm 1 \times 10^{-5}$	$0 \pm 1.4 \times 10^{-4}$	$0 \pm 4.2 \times 10^{-4}$	$0 \pm 6.2 \times 10^{-4}$
$v_o$ /mm	1.30	$0 \pm 5 \times 10^{-3}$	$-0.03 \pm 0.07$	$-0.01 \pm 0.12$	$-0.02 \pm 0.18$

The authors then evaluated the geometry of a test system. As in the simulation study, the geometry is evaluated for each point marker independently and then averaged over the number of point markers. The variance in each parameter is taken to be a measure of uncertainty. The authors note that the uncertainty (characterized by  $\sigma$ ) associated with the estimation of out-of-plane rotations  $\theta$  and  $\varphi$  is as high as 50 % of the estimated value. A possible reason for this, the authors argue, is the residual distortions in the plane of the detector that result in an erroneous pixel size.

It is interesting to note in table 2.4 that the uncertainty in estimated out-of-plane rotations increases rapidly with increasing noise in the simulated projections. However, the authors suggest that the effect of out-of-plane rotations to the quality of reconstructed images is small when compared to the same effect caused by an in-plane rotation. The estimated value of  $SDD$  in both experimental tests is about one half of a centimeter from the reference  $SDD$ . Erroneous pixel size could also result in this offset of the estimated value. Additionally, the authors argue that the reference  $SDD$  is difficult to measure accurately as there is some ambiguity as to where the X-ray focal spot is and where the X-rays are absorbed in the detector.

Subsequent to the observations made in reference [35], the analytical method presented in reference [36] assumes that both out-of-plane rotations of the detector are negligible. The authors support this assumption by evaluating the error in projected point coordinates as a result of out-of-plane rotations. It was shown analytically that an out-of-plane rotation of  $2^\circ$  results in a maximum pixel coordinate error of 1 %. In contrast to the method in reference [35], the authors of reference [36] do not require  $SRD$  to be known *a priori*; it is acknowledged that there is an ambiguity in the exact measurement of this distance. As a result, the method requires a rough estimate of the distance between two point markers. Thus, the method determines the other five parameters ( $SRD$ ,  $SDD$ ,  $\eta$ , and principal point). An approximately linear set of balls is imaged at multiple rotation positions and the projected elliptical trajectories are analyzed. The angular readout of the rotation axis (figure 2.14a) for each projection is used to identify 'radial pairs', *i.e.* pair of point marker projections separated by a rotation angle of  $180^\circ$  (figure 2.14b). The distance between projected point markers within each radial pair is calculated.

The point marker projections that correspond to the radial pairs with the maximum and minimum distances are designated 'benchmark points' and are used for analysis. It should also be noted that the lines connecting point markers within each radial pair intersect at the projected center of the circular trajectory in object space. The accuracy of the proposed method was evaluated by simulation. The authors applied varying levels of Gaussian noise ( $\sigma = 0.1, 0.2, 0.4$ , and  $1.0$  pixels) to the center coordinates of the point projections and observed the resulting deviation in the estimated parameters. Simulations were performed ten times and the standard deviation in parameter estimates was taken to be a measure of uncertainty.

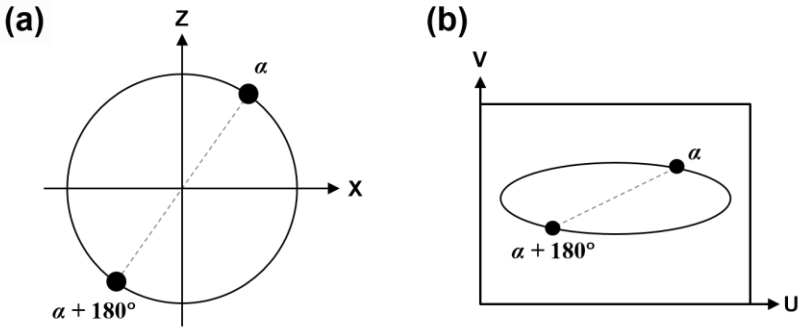


Figure 2.14. The concept of radial pairs is applied in reference [36]. The distance between two markers in a radial pair on the projected image is greatest when the length segment between the two markers is parallel to the X axis. Alternatively, the shortest distance between two markers in a radial pair on the projected image occurs when the length segment between the two markers is parallel to the Z axis. Figures adapted from reference [36] with permission.

This method is applied in reference [37] to provide an initial estimate of the same five parameters. Numerical optimization is then used to solve for detector out-of-plane rotations. In the fitting process, the initial five parameters are also allowed to vary, thus refining their solutions. Table 2.5 shows the comparison of the results from reference [37] to those from reference [36] with a Gaussian noise of  $\sigma = 0.4$  pixels on projected point coordinates.

Table 2.5. The authors of reference [37] propose a method that uses numerical optimization to determine out-of-plane rotations and to refine the parameters that were initially estimated using the method from reference [36]. The results for data with Gaussian noise ( $\sigma = 0.4$  pixels) is compared to the results from reference [36]. Table adapted from reference [37] with permission.

Parameter	True value	Reference [36]	Reference [37]
$u_o$ /pixel	1005	$1005.9 \pm 0.3$	$1005.0 \pm 0.0$
$v_o$ /pixel	480	$480 \pm 1$	$479.90 \pm 0.15$
$\eta$ /°	-1	$-0.99 \pm 0.03$	$-1.0001 \pm 0.0002$
SRD /mm	150	$150.2 \pm 0.5$	$149.62 \pm 0.06$
SDD /mm	400	$401 \pm 1$	$399.99 \pm 0.06$
$\theta$ /°	1.2	Not determined	$1.1961 \pm 0.0116$
$\varphi$ /°	1.5	Not determined	$1.5018 \pm 0.0046$

In reference [38], an analytical method is provided to determine the in-plane rotation  $\eta$  independently of  $\theta$  and  $\varphi$ . The authors exploit the dependence of the projected ellipse to the Y position of the point marker. When the point object is at  $Y = 0$  (on the mid-plane), its trajectory is imaged as a line (figure 2.15a). The detector in-plane rotation  $\eta$  can be calculated from the slope of this line in the detector coordinate frame. The authors argue that, theoretically, only one point object is required if that point object is exactly positioned on the mid-plane. However, this condition is very difficult to satisfy; therefore, the authors provide a method to determine the slope of this line from a minimum of two objects placed away from the mid-plane. This method is based on principles from perspective geometry, namely the presence of a converging point in the projection of lines that are parallel in the object space. In particular, the authors circumscribe the circular trajectories with a square, the sides of which are parallel in object space (figure 2.15b). In the projected ellipse, the parallel sides of the circumscribed square in object space converge to a point (figure 2.16a,b). Analytical expressions reveal system parameters from the extracted converging point information.

By simulating a Gaussian perturbation ( $\sigma = 0.1$  pixel) of the point projection coordinates, the authors compared the average estimated  $\eta$  from a set of 50 simulations to the true value. The standard deviation of the 50 estimated  $\eta$  values is also calculated. The simulations were repeated for different out-of-plane rotations and the authors confirmed that the quality of the estimated  $\eta$  is independent of the values of  $\theta$  and  $\varphi$ . It was observed that the standard deviation of the estimated  $\eta$  decreased with increasing rotation positions  $N$ .

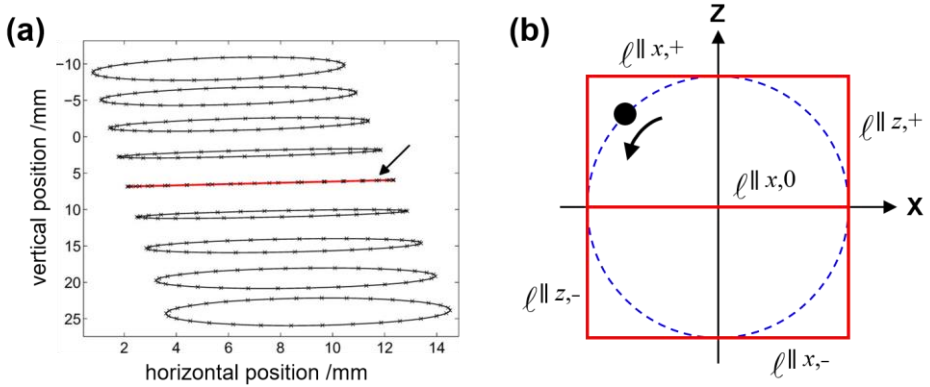


Figure 2.15. (a) The trajectory of a point marker located on the mid-plane will be imaged as a line. The slope of this line can be used to determine the in-plane rotation  $\eta$  of the detector [38]. (b) In the absence of a point marker on the mid-plane, two or more point markers located off the mid-plane can be used. The authors first define a set of parallel lines in object space by circumscribing the marker trajectory with a square. Opposing pairs of the square are parallel to each other. © 2012 IEEE. Reprinted, with permission, from reference [38].

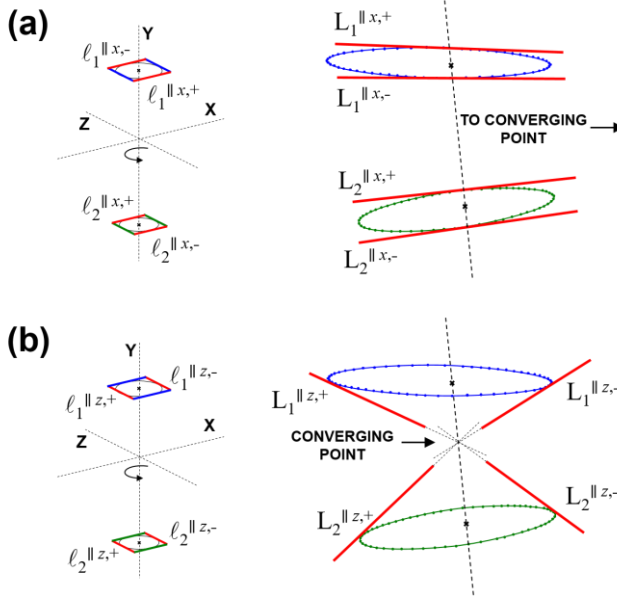


Figure 2.16. The method proposed in reference [38] exploits a principle from perspective geometry, which states that the projections of parallel lines in object space converge to a point. From the trajectories of two point markers placed on opposite sides of the mid-plane the authors extract two converging points. The converging point in (a) corresponds to the projection of lines parallel to the X axis, while the converging point in (b) corresponds to the projection of lines parallel to the Z axis. © 2012 IEEE. Reprinted, with permission, from reference [38].

The method proposed in reference [38] is extended to determine the other six parameters ( $SRD$ ,  $SDD$ ,  $\theta$ ,  $\phi$ , and principal point) in reference [39]. After determining  $\eta$ , the projection data is rotated to remove the in-plane rotation, which then simplifies the determination of the other six parameters. In both references [38,39] a bias is observed in the parameters estimated from noisy projections. The authors suggest that this bias is most likely a result of errors from the center determination of finite point markers, as well as systematic errors in the ellipse fitting algorithm. In reference [39] the effect of applying different fitting algorithms is investigated. The authors found that the bias in the estimated parameters varied between fitting algorithms, citing Taubin's ellipse fitting method [40] as the most effective in reducing the observed bias. Any residual bias was observed to depend on the size of the point markers; an increase in point marker size resulted in an increase of bias.

A numerical optimization method was applied to a newly developed bench-top CT system in reference [41]. In particular, the bench-top system allows the mechanical control of the position and orientation of source, rotation stage, and detector (figure 2.17). It should be noted that the variables used in reference [41] to denote the various translations and rotations are different from the variables used here. In an effort to determine errors in the mechanical movements of the system, the authors image five spherical objects over two hundred equally-spaced rotation positions. For each applied mechanical translation or rotation, the system parameters are fit to the observed projection data. In this study, a model for axis translations and rotations is provided, including parameters for errors in axis scaling and squareness. To evaluate the effectiveness of the method, the authors determined the geometrical parameters for a series of applied movements from a given 'home' geometry of the CT system. For each axis of movement, the authors applied multiple distinct motions. The authors evaluate the average residuals between simulated and observed projections from the numerical optimization procedure for each mechanical movement of the CT system as well as the standard deviations of the residuals. The results suggest that the proposed imaging methods are robust for a variety of system geometries.

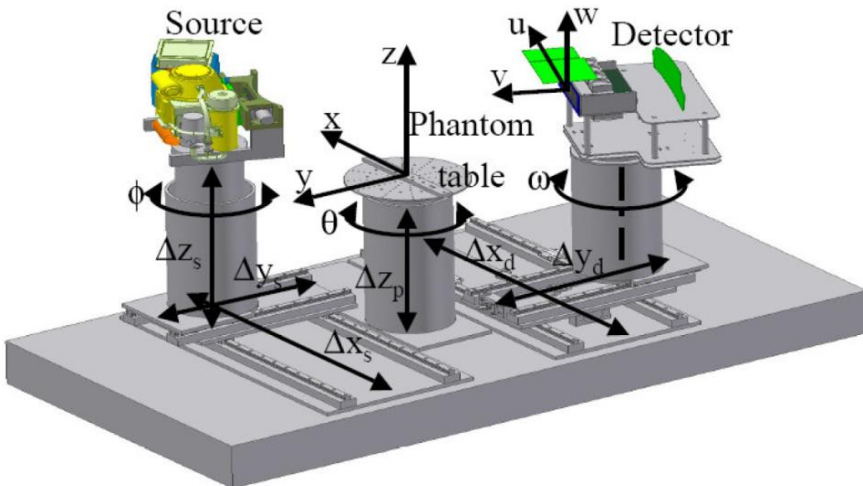


Figure 2.17. A bench-top CT system allows for the translation and rotation of source, rotation stage, and detector. © 2007 IEEE. Reprinted, with permission, from reference [41].

In reference [42] a cube with twenty-six spheres at known three-dimensional positions is used to solve for  $SDD$ ,  $\theta$ ,  $\eta$ , rotation angle ( $\alpha$ ), principal point, and source position (in the coordinate frame of the reference object) by way of numerical optimization. A drawback of the cubic object is the high potential for overlap of sphere projections. The same authors subsequently compared the reference object in [42] to a new object in reference [43]. This new object consists of a helical arrangement of spheres (figure

2.18a). The authors tested the effectiveness of multiple helical arrangements (figure 2.18b), which differ in the number of spheres and the pitch of the helix; the cubic arrangement from reference [42] was also tested for comparison. The authors applied Gaussian noise ( $\sigma = 0.25$  pixels) to 1000 simulated projections of the point markers. The standard deviation of the residuals from numerical optimization on the noisy projections is used as the criterion for determining the effectiveness of the arrangements. The authors found that a helix with higher pitch and more spheres (bottom left of figure 2.18b) provided the lowest standard deviation. In both references, the detector is compensated for planar distortions prior to performing the parameter evaluation.

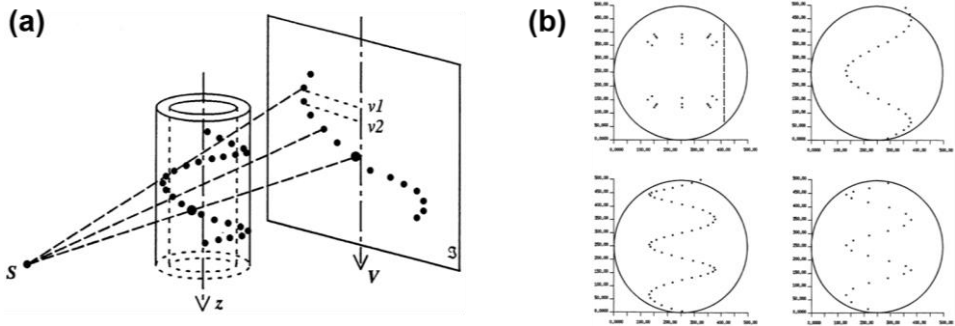


Figure 2.18. (a) A helical arrangement of point markers is proposed to reduce the occurrence of marker overlap in the projected image. (b) In reference [43] the effectiveness of various helical arrangements was compared to the cubic arrangement (top left) from reference [42]. The standard deviation of residual values from numerical optimization was used as the criterion; the authors found that a helix with more spheres and highest pitch provided the best results (bottom left). Figures reproduced from reference [43] with permission.

#### *Methods considering rotational error motions*

The imaging methods presented up to this point rely on a critical assumption: point objects perform a circular trajectory as they are rotated. This implies that the rotation axis is without error motions. In the presence of rotational error motions, the methods presented previously could provide erroneous results. In reference [44], numerical optimization was performed on projections of three rotating point markers. After minimization of the objective function, the authors observed systematic residuals between the simulated and observed projections (figure 2.19a). The authors suggest that the presence of systematic residuals is an indication that the model is not accounting for all behaviors in the test system. Two parameters were subsequently added to model a sinusoidal variation in the detector tilt as a function of rotation angle (figure 2.19b). These parameters are  $\Delta\theta$  and  $\beta$ , which correspond to the amplitude of the tilt oscillation and the phase shift, respectively. Residuals after minimization were reduced as a result of these additional modelled parameters (figure 2.19c). The results indicate that the added terms in the imaging model succeeded in detecting a sinusoidal change in detector tilt as a function of rotation angle.

The amplitude of tilt oscillation  $\Delta\theta$  was consistently estimated at  $0.3^\circ$ , while the phase shift  $\beta$  was between  $-0.6^\circ$  and  $0.0^\circ$ . Table 2.6 presents the estimated parameters with and without tilt oscillation in the model. It should be noted that this study was performed on a SPECT system. The addition of oscillation amplitude and phase shift in the model resulted in a change of other estimated parameters. For example, estimates of  $SDD$  and  $SRD+SDD$  (distance from detector to rotation axis) increased after including tilt oscillation. At the same time, the mechanical offset of the rotation axis  $m$  and  $\eta$  were both reduced. The value of  $u_0$  shifted from a negative value to a positive value. Changes in the estimates of  $\theta$  and  $v_0$  were not consistently in the same direction. It should be noted that, given a fixed detector, the results in reference [44] are most likely indicative of instabilities in the rotation axis.

Table 2.6. The parameters estimated with and without tilt oscillation parameters in the model are compared. The estimation was performed twice for each case. It should be noted that this study was performed on a SPECT system. SRD is replaced with SRD+SDD, which is the distance from the detector to the rotation axis. The focal point in a SPECT system is located between the detector and the axis of rotation [44]. © 2004 IEEE. Reprinted, with permission, from reference [44].

$SDD$ /mm	$SDD+SRD$ /mm	$m$ /mm	$u_o$ /mm	$v_o$ /mm	$\theta$ /°	$\Delta\theta$ /°	$\beta$ /°	$\eta$ /°
<b>Without tilt oscillation</b>								
198.3	241.8	1.4	-6.0	2.3	2.04	0.00	0.00	-0.34
199.8	243.5	0.9	-2.2	-0.6	1.28	0.00	0.00	-0.20
<b>With tilt oscillation</b>								
200.6	244.7	0.2	0.8	3.2	1.11	0.31	-0.09	-0.19
201.6	245.7	0.1	2.3	3.3	1.36	0.31	-0.01	-0.12

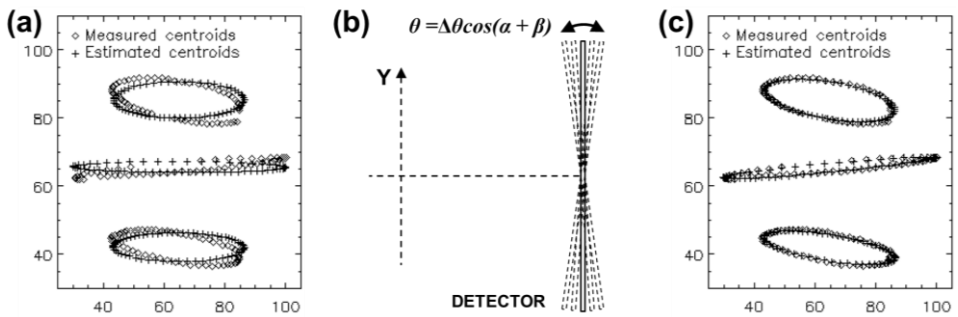


Figure 2.19. (a) The presence of residual values between simulated and measured point markers projections after numerical minimization is an indication that not all behaviors are considered by the imaging model. (b) The authors adapted their model to consider a sinusoidal variation in detector tilt  $\theta$ . (c) The optimization procedure was repeated; the residuals decreased as a result of the new tilt parameters. © 2004 IEEE. Reprinted, with permission, from reference [44].

The issue of non-ideal rotation is also addressed in reference [45]. The author argues that the parameterization in reference [44] is not adequate to capture small and unpredictable error motions of the geometry. A method is therefore proposed that applies small perturbations to a set of initial parameters, which were estimated assuming ideal rotation. In particular, the perturbations are applied to the parameters that describe the position and orientation of the detector with respect to the rotation axis. These parameters are defined in reference [45] as a translation vector  $\mathbf{T} = [t_x, t_y, t_z]$  and the three rotation angles  $[\theta, \varphi, \eta]$ . The objective of this numerical optimization method is a further reduction of the objective function (between observed and estimated projections of three rotating point markers  $i = 1, 2, 3$ ) by applying small perturbations to the estimated parameters.

To evaluate the effectiveness of their method, the authors applied the concept to simulated data. At each of the 64 equally spaced angular positions ( $\alpha = 1, 2, \dots, 64$ ), a pseudo-randomly generated perturbation was applied independently to each translation  $[t_x, t_y, t_z]$  and rotation  $[\theta, \varphi, \eta]$  of the detector. The perturbations ranged from 0.5 mm to 3 mm for translations and from  $0.5^\circ$  to  $5^\circ$  for the rotations. Given these perturbations, the exact point projection coordinates for each of the three markers ( $u_{i,\alpha}^{\text{exact}}, v_{i,\alpha}^{\text{exact}}$ ) are calculated. The authors then apply Gaussian noise ( $\sigma = 0.2$  pixels) to the exact coordinates, yielding a new set of coordinates ( $u_{i,\alpha}^{\text{obs}}, v_{i,\alpha}^{\text{obs}}$ ). These steps are performed on a set of 110 simulated geometries. Given the set of observed point projection coordinates, the authors performed their refined method to estimate the geometrical parameters of the simulated system ( $u_{i,\alpha}^{\text{est}}, v_{i,\alpha}^{\text{est}}$ ). For comparison, the authors also estimate the parameters using the method in reference [33], which assumes ideal rotation. The root-

mean-square error between estimated and exact projection coordinates over 110 simulated geometries is calculated for each method using equation 2.2.

$$\langle E \rangle = \sqrt{\frac{1}{192} \sum_{i=1}^3 \sum_{\alpha=1}^{64} (|u_{i,\alpha}^{est} - u_{i,\alpha}^{exact}|^2 + |v_{i,\alpha}^{est} - v_{i,\alpha}^{exact}|^2)} \quad (2.2)$$

Figure 2.20a presents these errors for each method individually. Each point on the plot corresponds to one of 110 simulated geometries. The points are plotted in order of increasing error for both methods. Figure 2.20b shows the estimated and observed projections superimposed onto the detector for both the ideal rotation method (left) and the refined method (right).

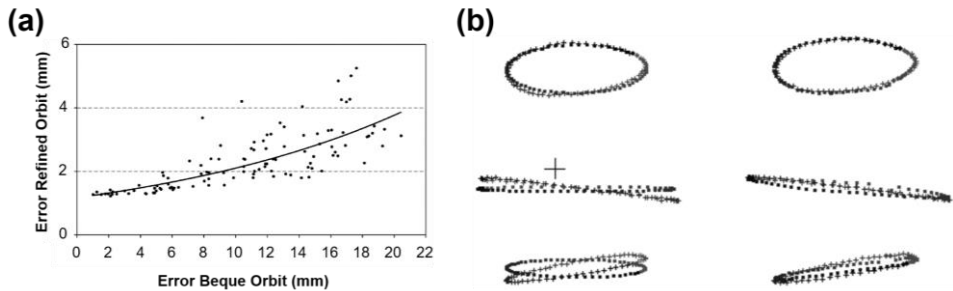


Figure 2.20. The authors of reference [45] propose a 'refined' method to determine instabilities in the rotation of the stage. The method applies perturbations to the parameters describing the position and orientation of the rotation axis with respect to the gantry. The system parameters are then determined by numerical optimization given a set of noisy ( $\sigma = 0.2$  pixels) point projection coordinates. (a) The root-mean-square error between estimated and exact point coordinates is presented for the proposed method and for the method in reference [33], which assumes an ideal rotation. (b) The estimated point projection coordinates for the method assuming ideal rotation (left) and for the refined method (right) are superimposed onto the exact coordinates. © 2008 IEEE. Reprinted, with permission, from reference [45].

The influence of rotational instabilities on the evaluation of system geometry is avoided by the method described in reference [46]. A reference object incorporates a total of twenty-four balls in two circular arrangements within a cylindrical casing (figure 2.21a). The relative positions between balls must be known accurately. Whereas in references [30-39,41,44,45] the reference objects are imaged at multiple rotation positions and, in some cases, must perform a full revolution, the method in reference [46] allows the geometry of the system to be resolved from one pose. Thus, any instability in the rotation of the stage is of no consequence to the determination of geometrical parameters. The parameters in this study are: source position  $(x_S, y_S, z_S)$ , detector position  $(x_D, y_D, z_D)$ , detector rotations  $(\theta, \phi, \eta)$ , principal point, and angle of rotation of the rotation stage (with respect to a chosen datum). The position and rotation parameters are evaluated with respect to a coordinate frame in the reference object. While all other parameters are evaluated analytically, out-of-plane rotations of the detector are estimated by nonlinear root finding (optimization).

The error in the proposed method is evaluated experimentally. Parameter estimation is performed subsequently after accurate offsets are applied to the test system. The newly-measured parameters are then compared to the applied offsets. The error in measuring the displacement in X-ray source was  $80 \mu\text{m}$  in the X and Y directions and  $800 \mu\text{m}$  in the Z direction. On the other hand, the error in detector displacement was  $60 \mu\text{m}$  in X and Y directions. The experimentally observed errors are summarized in table 2.7.

Table 2.7. The authors evaluated the effectiveness of their proposed method on a set of accurate displacements of the X-ray source and detector. The error between estimated and applied displacements is presented here. Table based on data from reference [46].

$\Delta x_D / \text{mm}$	$\Delta y_D / \text{mm}$	$\Delta x_S / \text{mm}$	$\Delta y_S / \text{mm}$	$\Delta z_S / \text{mm}$
0.060	0.060	0.080	0.080	0.800

Another advantage of this method is the ability to characterize non-ideal behaviors of the rotation axis. By measuring source and detector positions as a function of rotation position, the authors were able to observe instabilities in the axis of rotation (see figure 2.21b). According to the results, the authors observed precession in the rotation axis of about  $0.0115^\circ$ . This wobble occurred three times within a full revolution of the rotation stage. Error in determining rotation angle was found to be no larger than  $0.05^\circ$ . The rotation angle measurements were compared with the angular encoder readout.

The authors argue that the quality of parameter estimation can suffer from errors in the physical position of the markers (fabrication errors) and from errors in the determination of the projected marker center. Thus, the sensitivity of parameter estimation is evaluated in the presence of 0.1 pixel error in the pixel coordinate of the projected point marker center. Sensitivity analysis is performed by taking the first derivative of each parameter with respect to the pixel coordinates. Then, given a difference in pixel coordinate of 0.1 pixels, the resultant change in parameter value can be determined. The analysis is repeated for multiple reference objects, each with different numbers of point markers. The authors note that an average reduction of 30% in the change of source position, detector position, and detector angles occurred when the number of point markers increased from 16 to 32. Additionally, the authors evaluate the sensitivity in detector rotations and magnification factor as a function of increasing out-of-plane rotations (figure 2.22). At  $\theta = \varphi = \pm 40^\circ$ , the error in rotation angle estimation was less than  $0.05^\circ$  for  $\theta$  and  $\varphi$ , and  $0.005^\circ$  for  $\eta$ . The error in magnification factor was 0.5 % for the highest out-of-plane rotations.

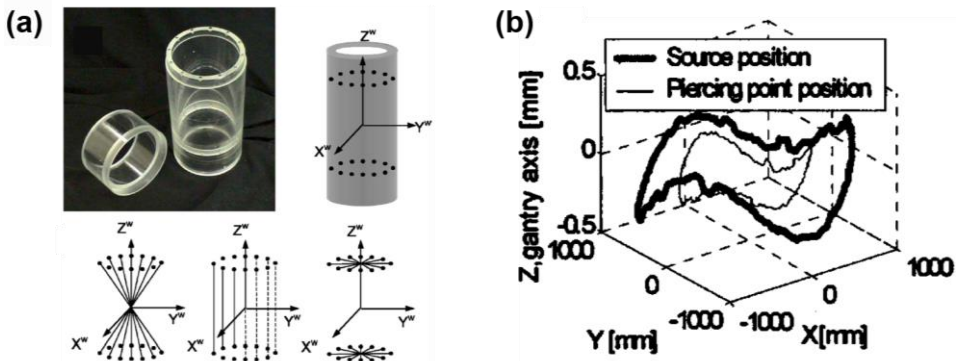


Figure 2.21. (a) In reference [46], the authors propose a reference object with static circular trajectories, thus removing the need to rotate the object. (b) By evaluating system geometry as a function of rotation angle, the authors in reference [46] observed instabilities of the rotation stage. In this plot, the  $Z$  axis corresponds to the rotation axis, while the  $X$  axis corresponds to the magnification axis. Figures reproduced from reference [46] with permission.

The authors suggest that the reference object could also prove useful in determining temporal instabilities (e.g. focal spot drift, mechanical vibrations) by observing changes in the system geometry over a given period of time. It should be noted that, since the system geometry evaluated from a coordinate frame fixed to the reference object, some of the observed instabilities as a function of rotation position could be a result of misalignment between the cylindrical axis of the reference object and the axis of rotation.

The authors suggest that changing the coordinate frame of the parameter estimates to one that is not fixed to the reference object could resolve this problem.

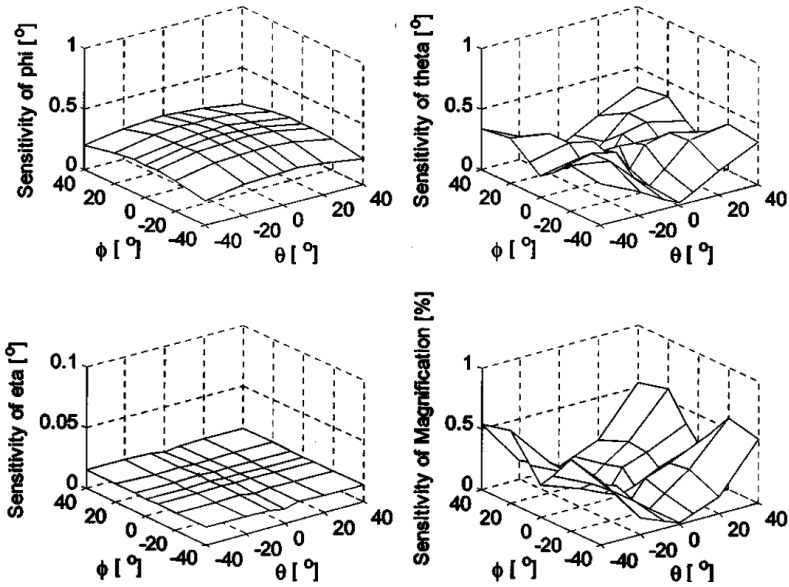


Figure 2.22. The sensitivity of detector rotations and magnification (due to 0.1 pixel error) was evaluated as a function of out-of-plane rotations. The estimation error of  $\theta$  and magnification factor increased with increasing out-of-plane rotations. On the other hand, the opposite behavior is observed for the estimation of  $\phi$  – the error decreased with increasing out-of-plane rotations. Estimation of  $\eta$  is shown to have little sensitivity to out-of-plane rotations. Figures reproduced from reference [46] with permission.

The authors of reference [47] investigate the change in coordinate frame suggested in reference [46]. The authors performed the initial parameter estimation from the coordinate frame of the reference object according to reference [46]. Given the source positions at various rotation angles, the center of source trajectory (iso-center) and the orientation of the rotation axis were determined. The authors then evaluate a translation vector  $\mathbf{T} = [t_x, t_y, t_z]$  and two rotations  $(\alpha, \beta)$  that describe the transformation from the coordinate frame of the reference object to the new source trajectory frame, which is aligned to the observed axis of rotation and has its origin at the iso-center. By re-evaluating the parameters in the new frame, the authors suggest that the parameter estimates are no longer influenced by positioning of the reference object.

Indeed, a simulation study [47] confirmed the reduction of the parameter variation when changing coordinate frames. The authors observe that, given the new coordinate frame, the source and detector positions were found to within 100  $\mu\text{m}$  from true. Detector rotations and rotation axis angle were found to within 0.05°, while the principal point was found to within 0.4 pixels. Additionally, the position of the reference object with respect to the iso-center and its orientation with respect to the rotation axis were found to within 50  $\mu\text{m}$  and 0.1°, respectively.

The advantage of the new coordinate frame is also observed experimentally. The source and detector positions are measured in the reference object coordinate frame and subsequently re-calculated in the iso-center coordinate frame. Figure 2.23a shows source and detector trajectories plotted in the object coordinate frame, whereas figure 2.23b shows the same trajectories in the iso-center coordinate frame. The apparent tilt of the trajectories in the object frame is removed in the iso-center frame. However, a closer look at the detector and source trajectories uncovered an offset of the trajectory centers in the X-

Z plane (figure 2.23c). The authors determined that this offset was a result of imprecisions in the point marker positions. To solve this problem, the reference object was rotated by  $180^\circ$  about its cylindrical axis and the parameter estimation is repeated. After averaging the parameters from the two scans, the authors found that the X-Z offset in trajectory centers was greatly reduced (figure 2.23d). It should be noted that a Y offset remained, for which the authors suggest an additional test.

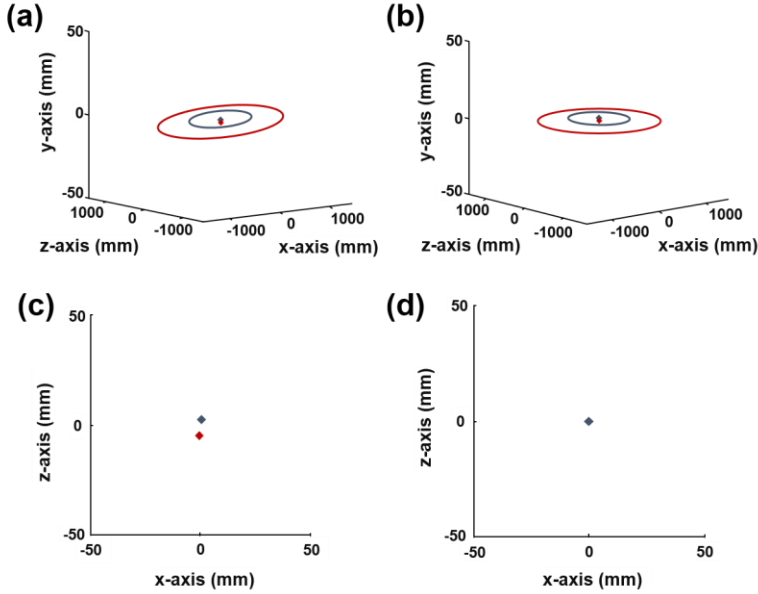


Figure 2.23. (a) The positions of the source and detector in the reference object coordinate frame are plotted as functions of rotation angle. A tilt in the trajectories is visible. (b) Once the positions were re-calculated in the iso-center coordinate frame, the tilt is removed. (c) Upon closer inspection along the X-Z plane, an offset between the center of source trajectory and the center of detector trajectory was observed. (d) The test scan was repeated with a rotated orientation of the reference object ( $180^\circ$  about cylindrical axis). Averaging each estimated trajectory over the two scans removed the offset in the X-Z plane. Figures reproduced from reference [47] with permission.

In other studies, point markers are arranged such that they form orthogonal features. For example, in reference [48], thirteen point markers are aligned along three orthogonal lines, with one of the markers serving as a common 'origin' point between the lines. The markers are equally spaced and the distance is known a priori. Figure 2.24 depicts the orthogonal arrangement, albeit with seven point markers. A set of intermediate parameters are calculated from the projected point coordinates; these parameters are then used to determine the geometry of the system by way of analytical expressions. The system is defined by  $SDD$ , principal point  $(u_o, v_o)$ , source position  $(x_s, y_s, z_s)$ , and detector rotations  $(\theta, \varphi, \eta)$  with respect to the axes of the reference object. A scan of the proposed object was simulated to determine the efficacy of their method. The imaging model incorporates a sinusoidal variation of the source and the system parameters were evaluated for each rotation position of the reference object. The authors found that the parameters were estimated to within 0.5 % of true value.

A slightly modified reference object was presented in a subsequent study [49]. A total of six markers are arranged to form three orthogonal lines without a common marker at their intersection. The method requires the reference object to be positioned such that three of the markers are above the mid-plane while the other three are below. In particular, the triangles traced by each set of three markers should ideally be parallel to the mid-plane. This arrangement reduces the chance of overlap between imaged markers, which can have detrimental effects to the quality of parameter estimation. The authors suggest

that decreasing the size of the markers and increasing their spacing can also reduce likelihood of overlap. Simulations were performed on the proposed reference object: one assumed a circular trajectory of the X-ray source (stable rotation) while the other allowed for small and random perturbations of the geometry. Additionally, the simulations assumed that the reference object was not perfectly aligned. In both cases, the authors evaluated the accuracy of the parameter estimates. *SDD* and principal point were estimated to within 1 mm. Source position was found to be within 0.5 mm along the X and Z directions and within 0.1 mm along the Y direction. Out-of-plane rotations of the detector were within  $0.1^\circ$ , while in-plane rotation was estimated to within  $0.02^\circ$  from true. In the case of large deviations in the rotation axis, there is an increased possibility of overlap between imaged balls. The authors of reference [50] therefore suggest incorporating two additional spheres oriented diagonally (in addition to twelve spheres along three orthogonal lines) to compensate for any overlapping that may occur. In this study, the estimated detector and source positions were also found to within 0.5 mm. Detector out-of-plane rotation angles were estimated to within  $0.05^\circ$ , while the in-plane rotation was also found to within  $0.02^\circ$ . The authors noticed a bias in their estimated *SRD* and *SDD* of 0.1 mm; this is believed to be a result of using centroids to define the center projections of point markers. The topic of identifying the projection of the sphere center is discussed in more detail in other publications [51-53].

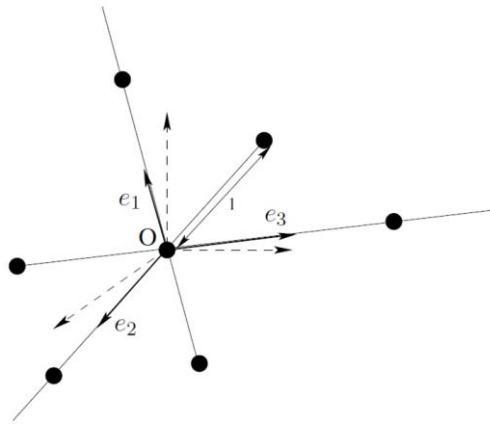


Figure 2.24. Point markers are arranged such that the lines connecting each set of three form an orthogonal set. © 2005 IEEE. Reprinted, with permission, from reference [48].

## 2.4 Summary and conclusion

In this chapter a review of the research efforts that contribute to the development of a geometrical calibration procedure for CT systems is provided. The geometrical construction of an industrial cone-beam CT system was described and the various offsets and misalignments that affect the quality of measurements (geometrical influence factors) were outlined. The application of measurement models to simulation studies is discussed. Then, methods to estimate geometrical errors are presented. Imaging methods, which are based on the imaging of reference objects, are ideal for evaluating fixed imaging geometries. The role of measurement models is critical in understanding how geometrical errors affect the quality of measurements. In particular, models allow the parameterization of geometrical errors, which can be useful for evaluating sensitivity coefficients and parameter correlation. In this way, geometrical errors that have a critical impact on measurements can be prioritized in any future calibration procedure. Additionally, measurement models can be applied 'inversely' for the development of experimental test procedures to map the geometry of an actual measuring instrument. In this review, this principle was observed in section 2.3.

The literature from the industrial CT community [19-25] indicates that current practice only considers global scaling errors in the measurement. Certain geometrical influence factors result in non-uniform errors (as shown in reference [26]) as well as reconstruction errors; therefore, global scale error compensation does not account for all geometrical misalignments. A particular group of imaging methods (overwhelmingly from the field of medical physics) are based on reference objects consisting of point markers [28,30-39,41-43]. Some imaging methods evaluated the system geometry by directly solving analytical expressions, while other methods iteratively solved for geometrical parameters by fitting simulated projections to a set of experimentally acquired projections. More recent imaging methods [44-50] have been designed to account for instabilities of the rotation axis, such as tilt error motion or positional drifts. However, a disadvantage of imaging methods is that they are only applicable for fixed kinematic configurations of the rotation stage. Thus, imaging methods would have to be performed every time the position of the rotation stage is changed.

The authors of imaging studies consistently found that the accuracy of parameter estimation strongly depended on the ability to accurately locate point projection coordinates in the radiographs. In fact, correct identification of the centers of point objects from their projections is a topic of other research [51-53]. Also, it is shown in reference [47] that imaging methods can suffer from non-ideal placement of the reference object, as well as inaccuracies in the measured point marker positions within the object.

The kinematic axes are critical to users who want to measure objects of varying sizes. It has been shown [3] that kinematic error motions, such as positioning errors, lack of squareness between axes, straightness errors, and rotational errors (roll, pitch, and yaw) can be measured. One of the issues with the methods used to determine kinematic error motions is the requirement for reference instruments. In this case, high-precision instruments such as laser interferometers were used. While these instruments are common place in research laboratories, they may not be practical for all users of X-ray CT.

In order to achieve the goal of establishing traceability of measurements made on CT systems, it is important that users are equipped with the knowledge to evaluate the necessary measurement uncertainty. Typically, measurement uncertainty can be assessed through a systematic evaluation of all influence factors in a measurement procedure. Methods to determine geometrical influence factors, *i.e.* influence factors particularly related to the system geometry, have been presented in this review. However, these methods are limited in their practical application by users of CT systems. Determination of mechanical error motions of the kinematic axes requires the use of expensive reference instruments, the operators of which require training. On the other hand, imaging methods can be an easier and cheaper solution since their application only requires the imaging of a reference object. However, a drawback of imaging methods is that they can only be applied to determine the system geometry for a single position of the rotation stage. Imaging methods in their current state require a significant amount of image processing. Additionally, compensation of reconstruction errors from geometrical offsets and tilts, *i.e.* errors that cannot be compensated by applying corrections to the radiographic or voxel data, require access to the reconstruction algorithm; many users of commercial CT systems do not have this access.

Future research should be dedicated to the development of methods that are practical for users of CT systems. Such methods should not be time consuming, nor should they require the use of expensive equipment. A possible solution includes the use of reference objects, which is in line with the imaging methods presented in this review. The first step in designing effective geometrical calibration and correction methods involves determining the sensitivity of measurements to each geometrical parameter. The sensitivity analysis will inform the development of geometrical calibration procedures by identifying the critical parameters to be measured in the system. The next step is to design suitable reference objects and test procedures to allow users to measure the geometry of their instrument. To ensure metrological

traceability of the geometrical calibration results, the reference object should incorporate one or more calibrated features, such as the distance between sphere centers. Also, the procedure should provide guidelines for propagating uncertainty in the calibrated features to uncertainty in the measured geometry.

## References

- [1] Ferrucci M, Leach RK, Giusca CL, Carmignato S, Dewulf W (2015) Towards geometrical calibration of X-ray computed tomography systems - A review. *Measurement Science and Technology* 26, 92003 doi:10.1088/0957-0233/26/9/092003
- [2] Hartley R, Zisserman A (2004) *Multiple view geometry in computer vision*, 2<sup>nd</sup> edition. (Cambridge University Press: Cambridge, UK) doi:10.1017/CBO9781107415324.004
- [3] Welkenhuyzen F (2016). Investigation of the accuracy of an X-ray CT scanner for dimensional metrology with the aid of simulations and calibrated artifacts. PhD Thesis (KU Leuven)
- [4] Quarteroni A (2009) *Mathematical models in science and engineering*. Notices of the AMS 56 (1), 10–19
- [5] Cox M, Forbes AB, Harris P, Peggs G (1998) Determining CMM behaviour from measurements of standard artefacts. NPL Report CISE 15/98
- [6] Sartori S, Zhang GX (1995) Geometric error measurement and compensation of machines. *CIRP Annals* 44 (2), 599-609
- [7] Kruth JP, Vanherck P, De Jonge L (1994) Self-calibration method and software error correction for three-dimensional coordinate measuring machines using artefact measurements. *Measurement* 14, 157-167
- [8] Kruth JP, Zhou L, Van den Bergh C, Vanherck P (2003) Method for squareness error verification on a coordinate measuring machine *The International Journal of Advanced Manufacturing Technology* 21, 874–878
- [9] Balsamo A, Franke M, Trapet E, Waldele F, De Jonge L, Vanherck P (1997) Results of the CIRP-Euromet intercomparison of ball plate-based techniques for determining CMM parametric errors. *Annals of the CIRP* 46 (1), 463-466
- [10] Muralikrishnan B, Sawyer D, Blackburn C, Phillips S, Borchardt B, Estler W (2009) ASME B89.4.19 Performance evaluation tests and geometric misalignments in laser trackers. *Journal of Research of the National Institute of Standards and Technology* 114, 21–35
- [11] Muralikrishnan B, Ferrucci M, Sawyer D, Gerner G, Lee V, Blackburn C et al. (2015) Volumetric performance evaluation of a laser scanner based on geometric error model. *Precision Engineering* 40, 139–150 doi:10.1016/j.precisioneng.2014.11.002
- [12] Welkenhuyzen F, Kiekens K, Pierlet M, Dewulf W, Bleys P, Kruth J-P, Voet A (2009) Industrial computer tomography for dimensional metrology: Overview of influence factors and improvement strategies 4<sup>th</sup> International Conference on Optical Measurement Techniques (Antwerp, Belgium)
- [13] BIPM JCGM 100 (2008) *Evaluation of Measurement Data—Guide to the Expression of Uncertainty in Measurement*. (Geneva: International Organization for Standardization)
- [14] Cox MG, Siebert BRL (2006) The use of a Monte Carlo method for evaluating uncertainty and expanded uncertainty. *Metrologia* 43, S178–188 doi:10.1088/0026-1394/43/4/S03

- [15] Kumar J, Attridge A, Wood PKC, Williams MA (2011) Analysis of the effect of cone-beam geometry and test object configuration on the measurement accuracy of a computed tomography scanner used for dimensional measurement. *Measurement Science Technology* 22, 35105 doi:10.1088/0957-0233/22/3/035105
- [16] Wenig P, Kasperl S (2006) Examination of the measurement uncertainty on dimensional measurements by X-ray computed tomography. *European Conference on Non-Destructive Testing* (Berlin, Germany)
- [17] EN 16016-4 (2011) Non destructive testing — Radiation methods — Computed tomography Part 4 : Qualification (Brussels: European Committee for Standardization)
- [18] Kruth JP, Bartscher M, Carmignato S, Schmitt R, Chiffre L De, Weckenmann A (2011) Computed tomography for dimensional metrology. *CIRP Annals - Manufacturing Technology* 60, 821–842 doi:10.1016/j.cirp.2011.05.006
- [19] Müller P (2012) Coordinate metrology by traceable computed tomography. PhD Thesis (Technical University of Denmark)
- [20] Bartscher M, Wäldele F (2004) Computed Tomography – a highly potential tool for industrial quality control and production near measurements. 8<sup>th</sup> International Symposium on Measurement and Quality Control in Production, (Erlangen, Germany)
- [21] Kasperl S, Hiller J, Krumm M (2009) Computed tomography metrology in industrial research & development. *Materialprüfung* 51, 405–411
- [22] Hiller J, Kasperl S, Hilpert U, Bartscher M (2007) Coordinate measuring with industrial X-ray computed tomography. *Technisches Messen* 74 (11), 553–564
- [23] Lifton JJ, Malcolm AA, McBride JW, Cross KJ (2013) The application of voxel size correction in X-ray computed tomography for dimensional metrology. *Singapore International NDT Conference & Exhibition* (Singapore)
- [24] Kiekens K, Welkenhuyzen F, Tan Y, Bleys P, Voet A, Kruth J-P (2011) A test object with parallel grooves for calibration and accuracy assessment of industrial computed tomography (CT) metrology. *Measurement Science and Technology* 22, 115502 doi:10.1088/0957-0233/22/11/115502
- [25] Carmignato S, Dreossi D, Mancini L, Marinello F, Tromba G, Savio E (2009) Testing of x-ray microtomography systems using a traceable geometrical standard. *Measurement Science and Technology* 20, 084021 doi:10.1088/0957-0233/20/8/084021.
- [26] Dewulf W, Kiekens K, Tan Y, Welkenhuyzen F, Kruth J-P (2013) Uncertainty determination and quantification for dimensional measurements with industrial computed tomography. *CIRP Annals - Manufacturing Technology* 62, 535–538 doi:10.1016/j.cirp.2013.03.017.
- [27] Sire P, Rizo P, Martin M (1993) X-ray cone beam CT system calibration. *Proceedings of the SPIE* 2009, 229–39
- [28] Sun Y, Hou Y, Zhao F, Hu J (2006) A calibration method for misaligned scanner geometry in cone-beam computed tomography. *Independent Nondestructive Testing and Evaluation International* 39 (6), 499–513 doi:10.1016/j.ndteint.2006.03.002.
- [29] Sun Y, Hou Y, Hu J (2007) Reduction of artifacts induced by misaligned geometry in cone-beam CT. *IEEE Transactions on Biomedical Engineering* 54, 1461–1471 doi:10.1109/TBME.2007.891166.
- [30] Gullberg GT, Edgerton ER, Tsui MW, Crawfordb CR (1987) Geometrical Parameters for Fan Beam Tomography 32, 1581–1594

## Chapter 2

- [31] Gullberg GT, Tsui BMW, Crawford CR, Ballard JG, Hagius JT (1990) Estimation of geometrical parameters and collimator evaluation for cone beam tomography. *Medical Physics* 17, 264–272 doi:10.1118/1.596505
- [32] Noo F, Clackdoyle R, Mennessier C, White TA, Roney TJ (2000) Analytic method based on identification of ellipse parameters for scanner calibration in cone- beam tomography. *Physics in Medicine and Biology* 45, 3489–3508 <http://dx.doi.org/10.1088/0031-9155/45/1>.
- [33] Bequé D, Nuyts J, Bormans G, Suetens P, Dupont P (2003) Characterization of pinhole SPECT acquisition geometry. *IEEE Transactions on Medical Imaging* 22, 599–612 doi:10.1109/TMI.2003.812258.
- [34] Bequé D, Nuyts J, Suetens P, Bormans G (2005) Optimization of geometrical calibration in pinhole SPECT. *IEEE Transactions on Medical Imaging* 24, 180–190 doi:10.1109/TMI.2004.839367.
- [35] von Smekal L, Kachelrieß M, Stepina E, Kalender WA (2004) Geometric misalignment and calibration in cone-beam tomography. *Medical Physics* 31, 3242–3266 doi:10.1118/1.1803792.
- [36] Yang K, Kwan ALC, Miller DF, Boone JM (2006) A geometric calibration for cone-beam CT systems. *Medical Physics* 33, 1695–1706
- [37] Johnston SM, Johnson GA, Badea CT (2008) Geometric calibration for a dual tube/detector micro-CT system. *Medical Physics* 35, 1820–1829 doi:10.1118/1.2900000
- [38] Xu J, Tsui BMW (2012) A graphical method for determining the in-plane rotation angle in geometric calibration of circular cone-beam CT systems. *IEEE Transactions on Medical Imaging* 31, 825–33
- [39] Xu J, Tsui BMW (2013) An analytical geometric calibration method for circular cone-beam geometry. *IEEE Transactions on Medical Imaging* 32, 1731–44
- [40] Taubin G (1991) Estimation of planar curves, surfaces, and nonplanar space curves defined by implicit equations with applications to edge and range image segmentation. *IEEE Transactions on Pattern Analysis and Machine Intelligence* 13 (11), 1115–1138
- [41] Bequé D, Harrison DD, Basu SK, Fitzgerald PF (2007) Geometric model, control & calibration of universal benchtop CT system. *IEEE Nuclear Science Symposium Conference Record* 4, 2980–2984 doi:10.1109/NSSMIC.2007.4436760
- [42] Rougee A, Picard C, Ponchut C, Troussset Y (1993) Geometrical calibration of x-ray imaging chains for three-dimensional reconstruction. *Computerized Medical Imaging and Graphics* 1993 17, 295–300 doi:10.1016/0895-6111(93)90020-N
- [43] Rougee A, Picard CL, Troussset YL, Ponchut C (1993) Geometrical calibration for 3D x-ray imaging. *Proceedings of the SPIE 1897 Medical Imaging 1993: Image Capture, Formatting, and Display* doi:10.1117/12.146963
- [44] Bequé D, Vanhove C, Andreyev A, Nuyts J, Defrise M (2004) Correction for imperfect camera motion and resolution recovery in pinhole SPECT. *IEEE Nuclear Science Symposium Conference Record* 4, 2507–2510 doi:10.1109/TMI.2003.812258
- [45] Defrise M, Vanhove C, Nuyts J (2008) Perturbative refinement of the geometric calibration in pinhole SPECT. *IEEE Transactions on Medical Imaging* 27, 204–214 doi:10.1109/TMI.2007.904687
- [46] Cho Y, Moseley DJ, Siewerdsen JH, Jaffray DA (2005) Accurate technique for complete geometric calibration of cone-beam computed tomography systems. *Medical Physics* 32, 968–83 doi:10.1118/1.1869652

- [47] Ford JC, Zheng D, Williamson JF (2011) Estimation of CT cone-beam geometry using a novel method insensitive to phantom fabrication inaccuracy: Implications for isocenter localization accuracy. *Medical Physics* 38, 2829–2840 doi:10.1118/1.3589130
- [48] Mennessier C, Clackdoyle R (2005) A simple analytic method for cone beam calibration. *IEEE Nuclear Science Symposium Conference Record* 5, 2743–2746 doi:10.1109/NSSMIC.2005.1596904
- [49] Mennessier C, Clackdoyle R (2008) Automated geometric calibration and reconstruction in circular cone-beam tomography. *IEEE Nuclear Science Symposium Conference Record*, 5081–5085 doi:10.1109/NSSMIC.2008.4774380
- [50] Mennessier C, Clackdoyle R, Noo F (2009) Direct determination of geometric alignment parameters for cone-beam scanners. *Physics in Medicine and Biology* 54, 1633–1660 doi:10.1088/0031-9155/54/6/016
- [51] Clackdoyle R, Mennessier C (2011) Cone-beam calibration using small balls: Centroids or ellipse centers? *IEEE Nuclear Science Symposium Conference Record*, 2763–2767
- [52] Desbat L, Clackdoyle R, Grezes-Besset L, Mennessier C, Bricault I (2006) Cone-beam imaging of delta functions. *IEEE Nuclear Science Symposium Conference Record* 5, 2859–2863 doi:10.1109/NSSMIC.2006.356473
- [53] Clackdoyle R, Mennessier C (2011) Centers and centroids of the cone-beam projection of a ball. *Physics in Medicine and Biology* 56, 7371–7391 doi:10.1088/0031-9155/56/23/003



# Chapter 3

## Sensitivity studies

Prior to the development of methods to quantify error sources, it is worthwhile to determine the sensitivity of measurements to each error source. If a measurement procedure can be described by an analytical function, the sensitivity study can (in the case of no parameter correlation) simply consist of determining sensitivity coefficients by taking the partial derivative of the function with respect to each input parameter. In the absence of an analytical function, numerical methods and simulation can be employed to determine the effects of error sources to a measurement result. In this chapter, the sensitivity of CT measurements to detector angular misalignments and to rotation stage errors is investigated by simulation.

### 3.1 Detector angular misalignments

In this section, the effects of angular misalignments of a flat-panel detector on volumetric measurements made by CT are studied. The content of this section is reproduced from [1]. First, the geometry of a typical cone-beam X-ray CT system is briefly revisited. Then, a forward projection model [2] is adapted to generate radiographic distortion maps for various detector angular misalignments. It is shown by simulation that detector angular misalignments result in systematic dimensional errors of the reconstructed volume. The simulation study is briefly discussed and the volumetric errors are presented for various detector misalignments. The distortion model is then applied inversely to correct the radiographs from each simulated detector misalignment. A new, corrected volume is reconstructed with the corrected radiographs. The deviations from ideal geometry in the corrected volumes are compared to the deviations in the corresponding uncorrected volumes.

The nominal alignment of the detector is as follows (figure 3.1a). The magnification axis (Z) is normal to the plane of the detector. The vertical axis of the detector (V) is antiparallel to the Y-axis, while the horizontal axis of the detector (U) is parallel to the X-axis. The flat panel detector consists of M by N pixels, where M is the number of rows and N is the number of columns (figure 3.1b). Ideally, the pixels are equally-sized and equally-spaced in the plane of the detector; the variables  $\Delta u$  and  $\Delta v$  correspond to the pixel width and height, respectively. The center of each pixel in the detector is assigned column ( $u$ ) and row ( $v$ ) indices. The  $(u, v) = (1, 1)$  position is at the top left corner of the detector screen; the columns increase rightward (+X direction in the system coordinate frame), while the rows increase downward (-Y direction in the system coordinate frame). The variables  $u_o$  and  $v_o$  are the pixel column and row coordinates, respectively, corresponding to the intersection of the magnification axis and the detector; this feature is also known as the principal point – a term commonly found in camera calibration for machine vision [3]. In the case of an ideally aligned detector, the principal point is located at the geometrical center of the detector plane. Depending on the number of pixel rows and columns (even or odd), the center of the detector can fall on a pixel or on the edge between adjacent pixels, *i.e.*  $u_o$  and  $v_o$  can be non-integer values.

Angular misalignments of the detector are described by three rotations: detector tilt  $\theta$  about the X-axis (figure 3.2, left), detector slant  $\varphi$  about the Y-axis (figure 3.2, center), and detector skew  $\eta$  about the Z-axis (figure 3.2, right). Tilt  $\theta$  and slant  $\varphi$  are known as out-of-plane rotations, while skew  $\eta$  is an in-plane rotation. Detector rotations, in practice, are not constrained to occur about the central axes of the detector plane [4]; such rotations can be modelled as a combination of detector translation and rotation. A detector can be misaligned by more than one rotation angle simultaneously. Various established conventions may be used for rotating three-dimensional coordinates [5]; these conventions differ by the axes about which the rotations are performed and the sequence in which the axes are rotated. In general, the application

of different conventions will not generate equivalent final three-dimensional rotations. The convention used here is chosen to agree with the convention used to simulate a rotation of the detector in the analytical (ray-tracing) simulation software Scorpius XLab<sup>®</sup>. More information on Scorpius XLab<sup>®</sup> can be found in the literature [6]. All rotations are extrinsic and are performed about the fixed X, Y, and Z axes of the global coordinate frame. The positive direction of rotation is given by the right-hand screw rule (see figure 3.2).

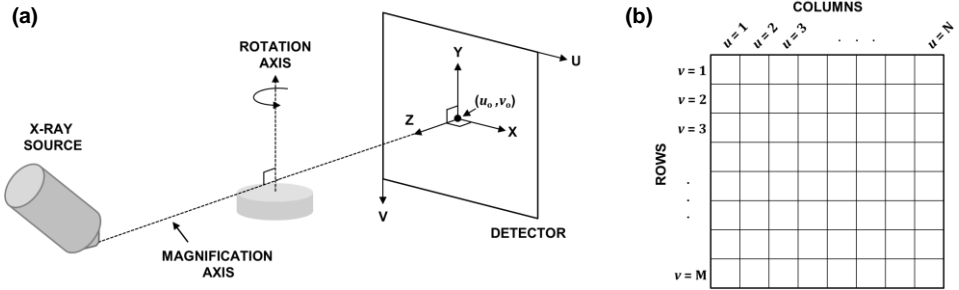


Figure 3.1. (a) The ideal geometrical alignment of a typical industrial cone-beam X-ray CT system. (b) The pixel column indices increase rightward, while the pixel row indices increase downward. The pixel position  $(u, v) = (1, 1)$  is located at the top left corner of the detector.

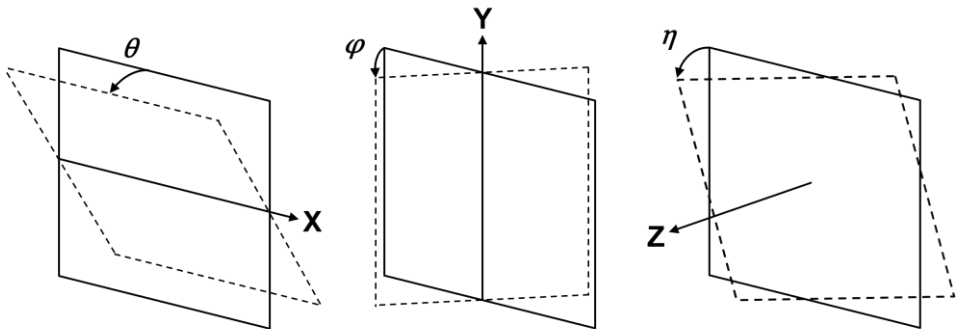


Figure 3.2. Potential detector angular misalignments include tilt  $\theta$  (left), slant  $\varphi$  (middle), and in-plane skew  $\eta$  (right). Positive rotations are illustrated.

The effects of positional misalignments of the detector are not investigated here to allow for in-depth analysis of angular misalignments. The principal point is therefore located at the detector center. It should be noted, however, that the radiographic error model presented here includes parameters for positional misalignments of the detector. Positional misalignments in X and Y can be modelled by adapting the principal point  $(u_0, v_0)$ , whereas a misalignment in Z is modelled by adapting the source-to-detector distance SDD.

### 3.1.1 Radiographic error model

Radiographic or pixel distortion is defined as the shift in the pixel coordinates assigned to registered point intensities (X-ray photons) from the image plane of an aligned detector to the image plane of a misaligned detector. The intensity of incident X-rays is registered by pixel  $(u, v)$  in the aligned detector. On a misaligned detector, the same X-ray intensity is registered by pixel  $(u_R, v_R)$ , as depicted in figure 3.3.

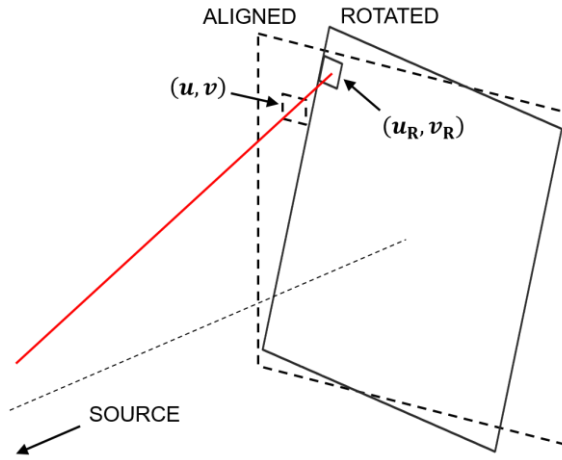


Figure 3.3. An incident X-ray photon will be registered at different pixel coordinates on the aligned and rotated detectors  $((u, v)$  and  $(u_R, v_R)$ , respectively). In this diagram, the rotated detector is a result of multiple rotations.

The difference in registered pixel position from the aligned detector plane to the misaligned detector plane corresponds to the pixel distortion for the pixel  $(u, v)$  in the aligned detector plane and is given by the equation 3.1.

$$du = u_R - u, \quad dv = v_R - v \quad (3.1)$$

Principles of forward projection may be adapted to evaluate the pixel distortion in the presence of various representative detector rotations. Similarly to the derivation provided by Yang et al. [4], the calculation of  $du$  and  $dv$  is achieved by the following steps. First, the  $(x, y, z)$  coordinates of each pixel center in the aligned detector are determined. Then, a set of straight lines from the X-ray focal spot center (given by a point) to the coordinates of each pixel center are generated. The intersections of the straight lines with the now misaligned detector plane are subsequently determined. For each intersection point on the rotated detector, the corresponding column and row indices  $(u_R, v_R)$  are extracted. Finally,  $du$  and  $dv$  are evaluated for each pair of  $(u_R, v_R)$  and  $(u, v)$ .

Distortion maps may be generated for various out-of-plane rotations  $\theta$  and  $\varphi$  and in-plane rotations  $\eta$ . It is important to note that the magnitude of detector rotations studied in this section is significantly larger than experimentally observed rotations in test systems (see chapter 5). Nevertheless, the magnitudes are chosen to clearly present the geometrical behavior in the radiographic distortions. The values of other non-varying geometrical input parameters used in the model are given in table 3.1. The magnitude of the total distortion, *i.e.*  $\sqrt{du^2 + dv^2}$ , is plotted in colour for each pixel. The direction of the distortion vector is given by the superimposed arrows (decimated by 80 for clarity). Distortion statistics are presented for each applied rotation in table 3.2.

Table 3.1. The non-varying geometrical parameters describing the CT system.

Geometrical parameter	Value
Detector size	400 mm $\times$ 400 mm
Number of pixels ( $M \times N$ )	2000 $\times$ 2000
Pixel size ( $\Delta u \times \Delta v$ )	0.2 mm $\times$ 0.2 mm
SRD	350 mm
SDD	1700 mm

*Out-of-plane rotations  $\theta$  and  $\varphi$*

Distortion maps are presented for  $\theta = +5^\circ, +10^\circ$  in figure 3.4 and for  $\varphi = +5^\circ, +10^\circ$  in figure 3.5. In the case of a detector tilt  $\theta$ , distortion increases for rows further from mid-plane (row  $v_0$ ). Distortion is, to first approximation, constant for all  $u$  in a given  $v$ . Note that the trend of distortion increase for rows away from  $v_0$  is not symmetrical about  $v_0$ . Further, the general trend for constant distortion across a row is modified by the local minimum, which is evident on the vertical centerline of the distortion plot for each test rotation in figure 3.4. The pixel distortions point towards the local minimum for pixel rows occupying the same image half as the local minimum. Equal and opposite rotations have mirrored distortions about the horizontal center line in the case of detector tilt  $\theta$  and about the vertical center line in the case of detector slant  $\varphi$ . Due to the simplified nature of the modelled geometry, distortions due to detector slant  $\varphi$  can be expected to correspond to distortions for tilts  $\theta$ , but mirrored in the line  $u = v$ .

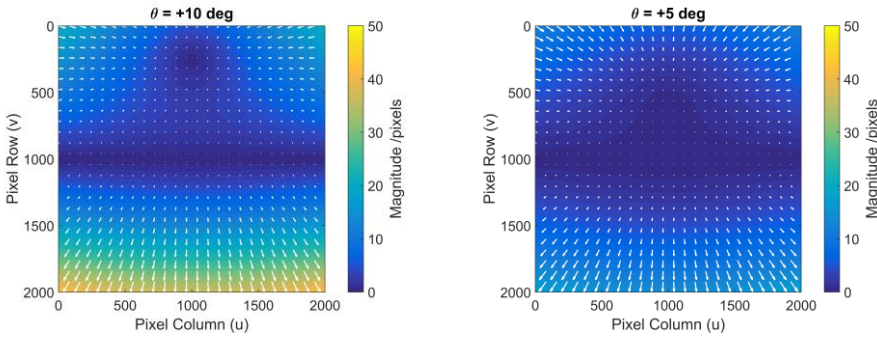


Figure 3.4. Distortion maps for varying values of  $\theta$ . Note the direction of U and V.

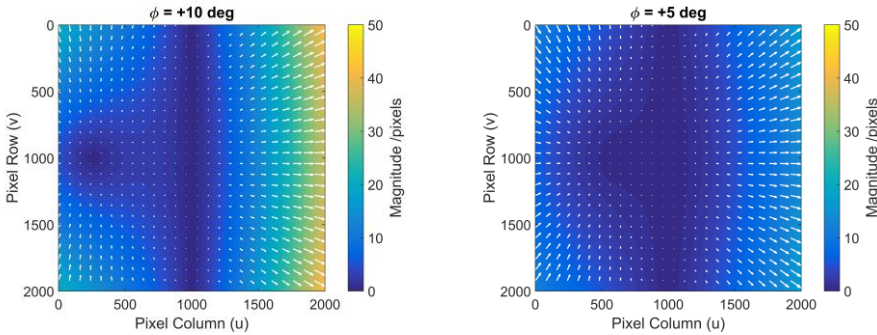


Figure 3.5. Distortion maps for varying values of  $\varphi$ . Note the direction of U and V.

The presence of local minima along the image center lines can be explained by the diagram in figure 3.6a, in which an X-ray path to a detector with tilt  $\theta$  is shown on the YZ plane. The X-ray path from the source intersects the rotated detector at  $v_R$  and the ideal detector at  $v$ . The dotted arc has a radius of  $v$  and connects the two pixel row positions  $v_R$  and  $v$ . Therefore,  $v_R = v$  and the pixel row distortion  $dv = 0$ . Also, since the diagram is on the YZ plane,  $du = 0$  (see figure 3.4). Therefore, the total distortion for that particular pixel row is zero. The row position of this minimum changes with the magnitude of  $\theta$ , as is shown by the diagonal zero line in figure 3.6b. In this figure, the horizontal zero line corresponds to the X-axis and the vertical zero line is the distortion when  $\theta = 0$ .

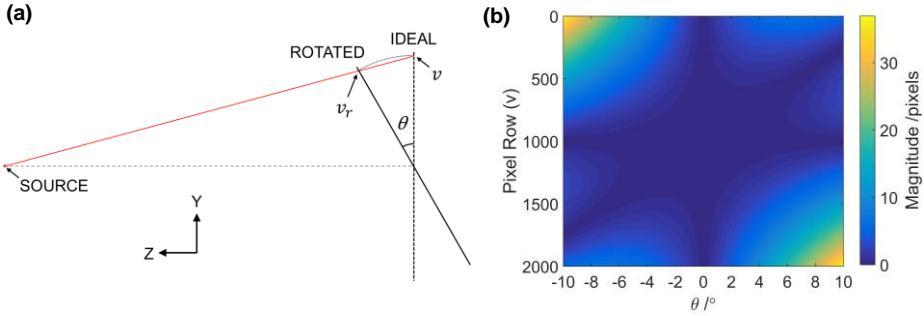


Figure 3.6. (a) X-ray path diagram along YZ plane. Given detector tilt  $\theta$ , there exists an X-ray path that will be registered by the same pixel coordinate in both the ideal and rotated detectors. (b) The pixel row position for this occurrence depends on the value of  $\theta$ , as is shown by the diagonal zero line.

### In-plane rotation $\eta$

Distortion maps in the presence of in-plane rotation  $\eta = +1^\circ, +2^\circ$  are presented in figure 3.7. The magnitude of distortions increases with increasing distance from the detector center. As expected, the distortion direction at any pixel position is tangent to the radial direction; that is, the distortions follow a circular trajectory with the detector center at the trajectory center. Table 3.2 summarizes the magnitude of the distortion for various detector rotations.

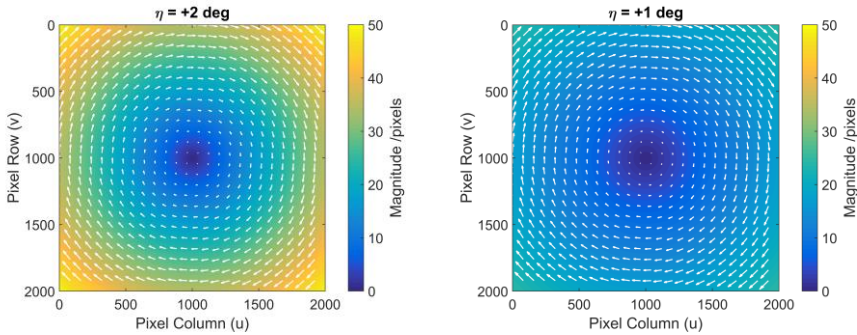


Figure 3.7. Distortion maps for varying values of  $\eta$ . Note the direction of U and V.

Table 3.2. Maximum, mean, and standard deviation  $\sigma$  of the distortion magnitudes in the presence of various detector rotations.

Rotation		Distortion magnitude (pixels)		
		Maximum	Mean	$\sigma$
$\theta$ or $\varphi$	$\pm 10^\circ$	42.5	10.9	10.0
	$\pm 5^\circ$	17.6	4.7	4.0
$\eta$	$\pm 2^\circ$	49.3	26.7	9.9
	$\pm 1^\circ$	24.7	13.4	5.0

The distortions in the presence of  $\eta = \pm 1^\circ$  and  $\eta = \pm 2^\circ$  are larger than the distortions in the presence of  $\theta = \varphi = \pm 5^\circ$  and  $\theta = \varphi = \pm 10^\circ$ , respectively. The sensitivity of distortion magnitude to rotation angle is depicted by figure 3.8, in which maximum and mean distortion magnitude is plotted as a function of rotation angle.

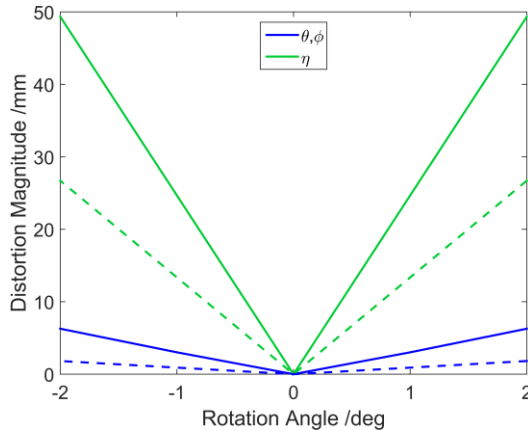


Figure 3.8. Maximum (solid line) and mean (dotted line) pixel distortion magnitude as a function of rotation angle for  $\theta$ ,  $\phi$ , and  $\eta$ .

### 3.1.2 Volumetric deviations

The effects of angular misalignments of the detector are studied on simulated CT scans of a test object. A cone-beam CT system is simulated using Scorpius XLab<sup>®</sup>. The system geometry is characterized by the parameters in table 3.1. The current of the X-ray source is set to 0.1 mA and the voltage is set to 100 kV. The test object is a computer-modelled cylindrical array of aluminum spheres (figure 3.9). 125 spheres are separated into 5 layers along the cylindrical axis. Each layer consists of 24 spheres arranged in three concentric circles and 1 additional sphere located at the common center. The diameter of the modelled spheres is 5 mm.

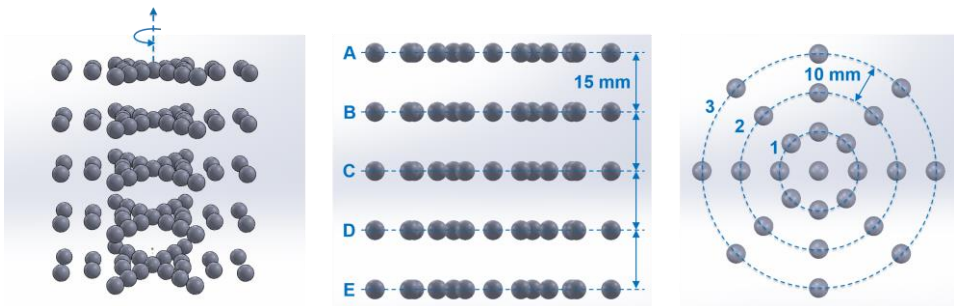


Figure 3.9. A cylindrical array of aluminium spheres was modelled for the purpose of sampling the measurement volume. (Left) 3D view, (center) lateral view, (right) top-down view.

The test object is placed within the system such that its cylindrical axis is coincident with the axis of rotation and its center (the central sphere of layer C) is coincident with the intersection of the rotation and magnification axes. In this position and orientation, the third layer of spheres is centered on the mid-plane (XZ); thus, two of the layers are below this mid-plane and two are above it. To isolate the effects of geometrical errors, other influence factors, such as finite X-ray focal spot size, focal spot drift, and electronic noise and MTF of the detector, were not simulated. The test object is imaged at 3600 equally spaced rotation positions over a range of 360°; the number of projections was chosen to reduce the effects of insufficient projection data. Subsequent to collecting the full set of radiographs, the volume is reconstructed by filtered backprojection (Feldkamp type) algorithms [7] included in the simulation software. Default settings for performing reconstruction in Scorpius XLab<sup>®</sup> were used. Prior to the

backprojection step, a Shepp-Logan filter [8] is applied to the radiographic data. Bilinear interpolation [9] is performed in the backprojection step. The number of voxels in the reconstructed volume are 1999, 2000, and 1999 along X, Y, and Z, respectively. Voxel dimensions are 40.9  $\mu\text{m}$  along X and Z, and 36.4  $\mu\text{m}$  along Y.

Surfaces in the three-dimensional voxel model are determined by applying a grey value threshold between the material of interest (aluminium) and the background (air). Advanced (local) thresholding on VGStudio MAX 2.2 (Volume Graphics GmbH, Germany) with a search distance of 0.15 mm is performed on a starting grey value, which was chosen to provide a single continuous surface for each sphere object. The surface is subsequently converted to a three-dimensional point cloud by way of sampling the isosurface at intervals of 0.08 mm along all three coordinate directions (using the surface extraction feature in VGStudio MAX). For each sphere object in the point cloud, the center of mass (centroid) of all surface points is calculated. It should be noted that sphere fitting is not used in determining the centroid of the sphere object; it is shown later in this chapter that certain detector orientations resulted in form deviations of the scanned spheres. For this purpose, the form of the reconstructed spheres is also used to understand the effects of detector misalignments. Other studies [10] use the volumetric grey value data to evaluate the centroid of the sphere objects. This method eliminates the surface determination step, thereby removing the effects of thresholding [11] on the centroid results. Here, surface data is used as it is necessary to evaluate the form of the reconstructed spheres. Spheres are linear least-squared fit to each object and the root-mean-square (RMS) value of sphere fit residuals is used as the criterion for form deviation. It should be noted that other definitions for sphere form exist. The centroid and form deviation evaluated under each detector misalignment are compared to the same features obtained under ideal system geometry. Feldkamp artifacts due to insufficient radon data, i.e. backprojected intensity information, at large cone-beam angles [12] could affect the centroid calculation. Given that both misaligned and ideal scan data are affected by Feldkamp artifacts, their influence is not considered.

#### *Detector tilt, $\theta$*

The following tilts of the detector about the X-axis are simulated:  $\theta = +10^\circ$ ,  $+5^\circ$ ,  $-5^\circ$ , and  $-10^\circ$ . In figure 3.10, centroid deviations are presented as vectors superimposed on the nominal centroid positions (dark circles). The deviation vectors are scaled by a factor of 20 for visualization in the measurement volume. Centroid deviations are not symmetrical about the XZ mid-plane. A local minimum is evident above the mid-plane for positive tilt angles and below the mid-plane for negative tilts. This behavior corresponds to the local minimum observed in figure 3.4. The data in table 3.3 confirms the non-symmetrical behavior about the mid-plane. Deviations due to equal and opposite rotations are mirrored about the XZ plane.

Table 3.3. Mean centroid deviation magnitude by sphere layer in the presence of detector tilt  $\theta$ .

$\theta$	Mean centroid deviation magnitude /mm				
	Layer A	Layer B	Layer C	Layer D	Layer E
$+10^\circ$	0.29	0.19	0.01	0.38	0.99
$+5^\circ$	0.19	0.07	0.01	0.14	0.38
$-5^\circ$	0.38	0.14	0.01	0.07	0.19
$-10^\circ$	0.99	0.38	0.01	0.19	0.29

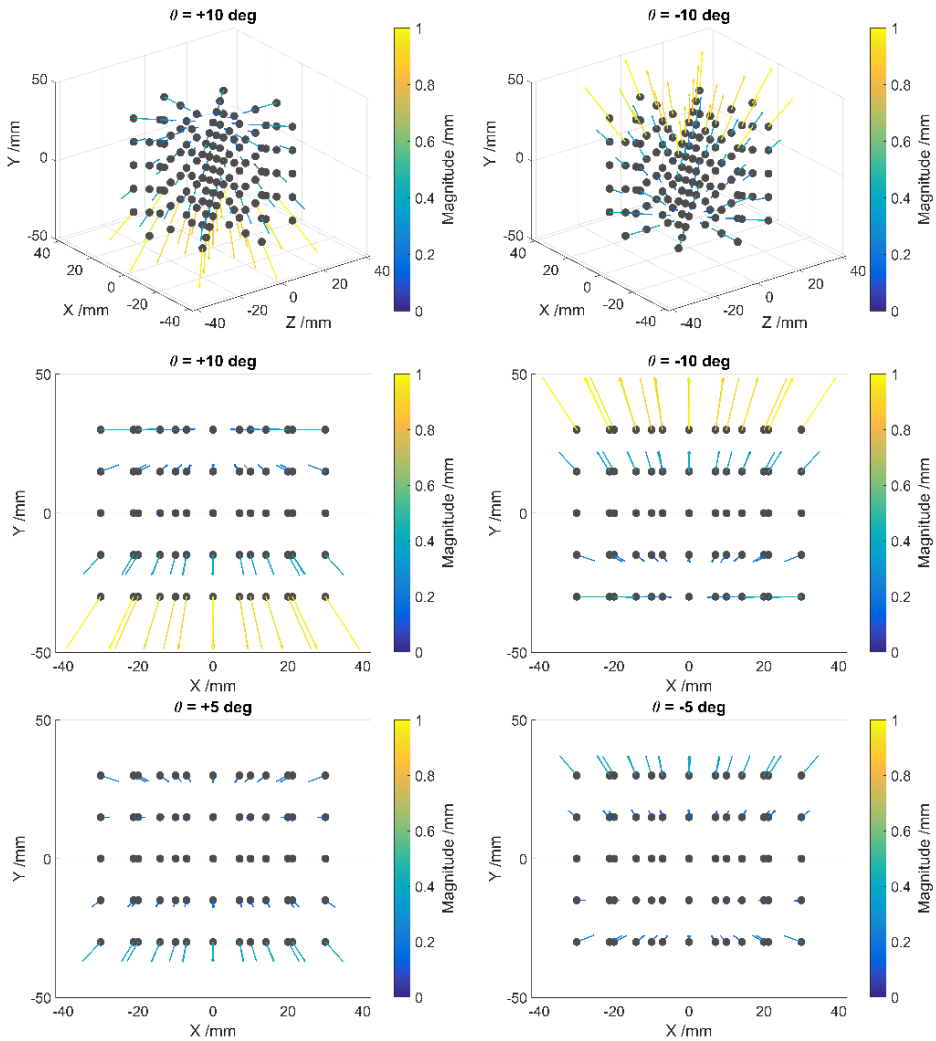


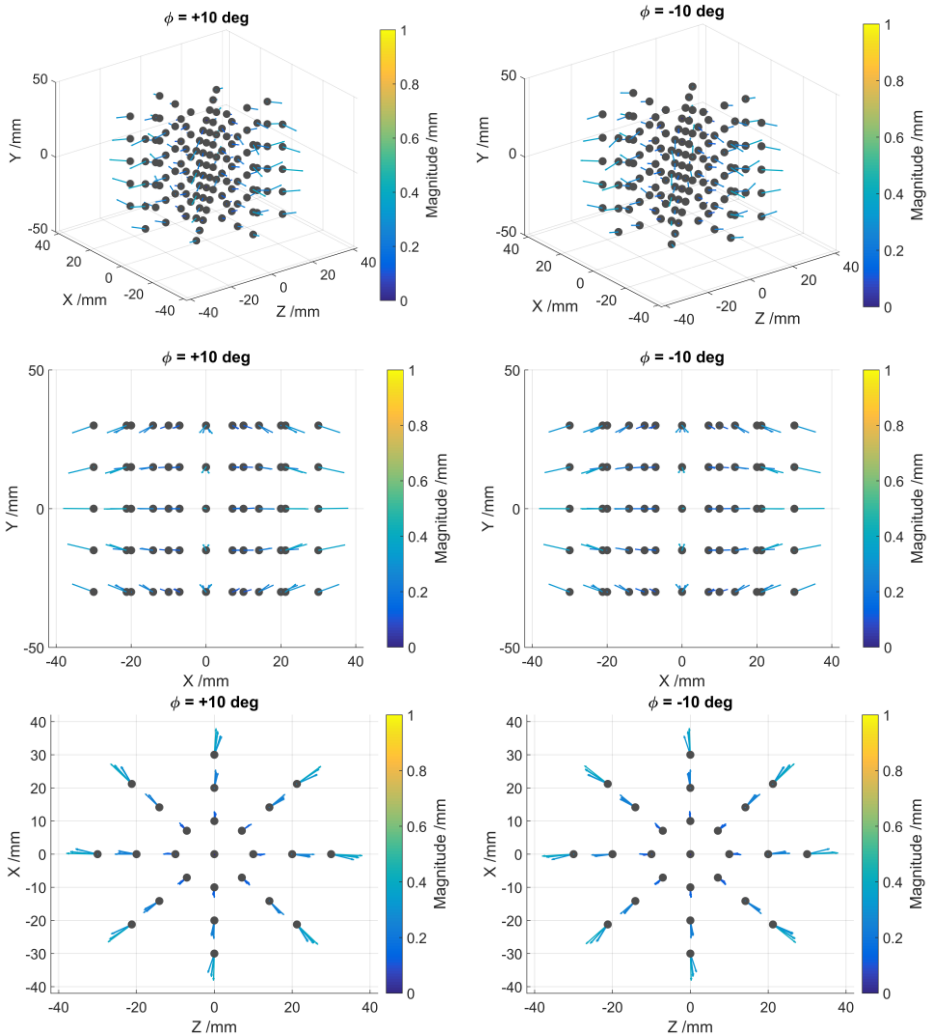
Figure 3.10. Centroid deviations in the presence of detector tilt  $\theta$ . Deviation vectors are scaled by a factor of 20 for visualization. Centroid deviations are presented as vectors superimposed on the nominal centroid positions (dark circles).

### Detector slant, $\varphi$

The following slants of the detector about the Y-axis are simulated:  $\varphi = +10^\circ$ ,  $+5^\circ$ ,  $-5^\circ$ , and  $-10^\circ$ . The deviations in centroid coordinates for the cases  $\varphi = +10^\circ$  and  $\varphi = -10^\circ$  are plotted in figure 3.11; centroid deviations are presented as vectors superimposed on the nominal centroid positions (dark circles). The magnitude of plotted deviations is scaled by a factor of 20 for visualization in the measurement volume. The results for  $\varphi = \pm 5^\circ$  exhibit the same behavior as the  $\varphi = \pm 10^\circ$  cases, respectively, only at smaller magnitudes; for this reason, the  $\varphi = \pm 5^\circ$  plots are not presented. Horizontal (XZ) deviations are radially outward, *i.e.* away from axis of rotation and vertical (Y) deviations point towards the mid-plane (figure 3.11, center). The magnitude of deviations generally increases with increasing distance of the sphere from the axis of rotation; this behavior is evident from the data in table 3.4.

Table 3.4. Mean centroid deviation magnitude by distance from rotation axis in the presence of detector slant  $\varphi$ .

$\varphi$	Mean centroid deviation magnitude /mm			
	Center	Ring 1	Ring 2	Ring 3
+10°	0.01	0.13	0.26	0.34
+5°	0.02	0.04	0.06	0.08
-5°	0.01	0.04	0.06	0.08
-10°	0.01	0.13	0.26	0.34

Figure 3.11. Centroid deviations in the presence of various detector slants  $\varphi$ . Deviation vectors are scaled by a factor of 20 for visualization. Centroid deviations are presented as vectors superimposed on the nominal centroid positions (dark circles).

The following skews of the detector about the Z-axis are simulated:  $\eta = +2^\circ, +1^\circ, -1^\circ,$  and  $-2^\circ$ . The centroid deviation diagram is not shown for detector skew since the deviation vectors were not noticeable at a scaling factor of 20. Instead, the statistics for centroid deviation due to each detector rotation are summarized in table 3.5.

Table 3.5. Maximum, mean, and standard deviation of centroid deviation magnitude for all sphere objects in the presence of detector rotations.

Rotation		Centroid deviation magnitude /mm		
		Maximum	Mean	$\sigma$
$\theta$	$+10^\circ$	1.05	0.37	0.34
	$+5^\circ$	0.42	0.16	0.13
	$-5^\circ$	0.42	0.16	0.13
	$-10^\circ$	1.04	0.37	0.34
$\varphi$	$+10^\circ$	0.40	0.23	0.10
	$+5^\circ$	0.10	0.06	0.02
	$-5^\circ$	0.10	0.06	0.02
	$-10^\circ$	0.40	0.23	0.10
$\eta$	$+2^\circ$	0.11	0.04	0.03
	$+1^\circ$	0.04	0.02	0.01
	$-1^\circ$	0.04	0.01	0.01
	$-2^\circ$	0.11	0.04	0.03

A closer look at the reconstructed volume suggests that centroid deviation is not the most suitable criterion for determining the effects of detector skew. The reconstructed volumes in the presence of detector tilt  $\theta = +10^\circ$ , detector slant  $\varphi = +10^\circ$ , and detector skew  $\eta = +2^\circ$  are presented, respectively, in figure 3.12 top, center, and bottom. On the left, a grey-value slice along the XY plane (prior to the application of a surface threshold) is shown. A magnified portion of the grey-value image is shown in the center of figure 3.12; in the presence of detector slant and skew, the sphere object is reconstructed as two overlapping sphere objects, each individually having a lower material attenuation value than the overlapping section. An appropriate grey-value threshold is applied to generate a surface for the overlapping portion, as this section has comparable grey-values to the ideally-reconstructed sphere objects. A three-dimensional view of the reconstructed sphere objects after grey-value thresholding is presented in figure 3.12, right. As a result of the behavior observed in figure 3.12 and the magnitude of centroid deviations in table 3.5, form deviation seems to be a more appropriate criterion to determine the complete effects of detector slant  $\varphi$  and detector skew  $\eta$ . Given the symmetrical behavior observed in table 3.5, form deviation statistics (table 3.6) are only shown for positive rotation angles. The results support the sensitivity statements made in sections 3.1.1 and 3.1.2. Also, detector slant contributes more strongly to form deviations than detector tilt.

Table 3.6. The root-mean-square of the sphere fit residuals over all spheres in the volume is used as criterion for form deviation. Here the mean and standard deviation  $\sigma$  of the RMS are shown for positive values of each detector angle. Maximum values are omitted due to the presence of noise particles, which result in outliers of the surface data.

Rotation		RMS of sphere fit residuals /mm	
		Mean	$\sigma$
$\theta$	$+10^\circ$	0.02	0.02
	$+5^\circ$	0.01	$2.66 \times 10^{-3}$
$\varphi$	$+10^\circ$	0.10	0.06
	$+5^\circ$	0.05	0.04
$\eta$	$+2^\circ$	0.23	0.07
	$+1^\circ$	0.13	0.04

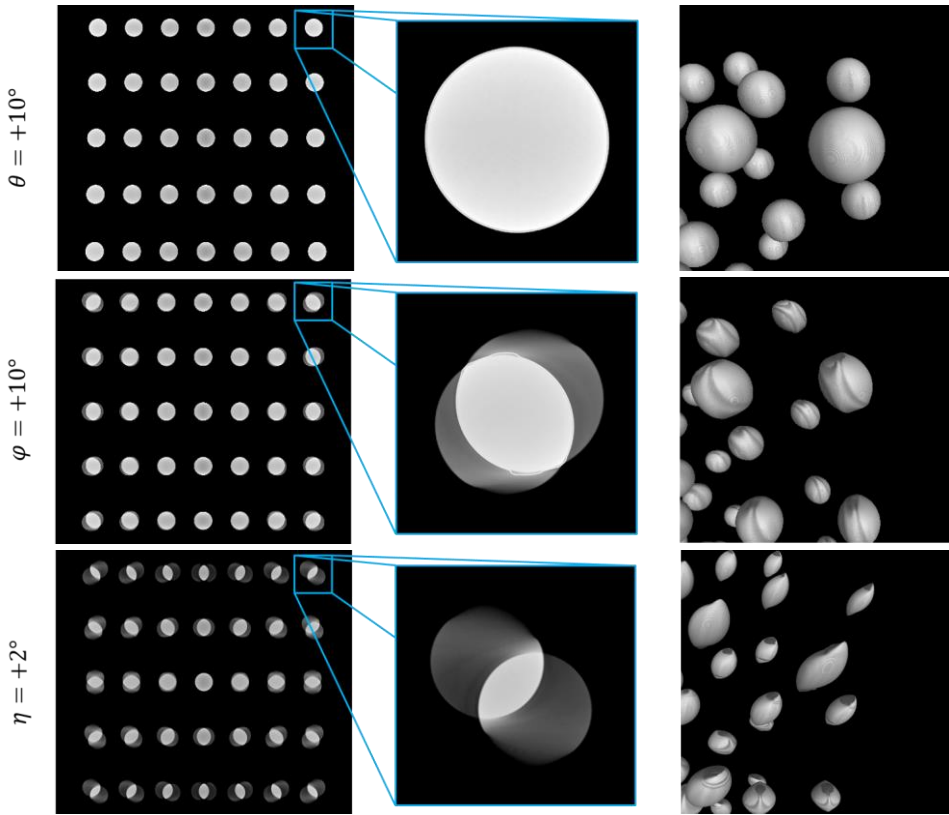


Figure 3.12. Reconstructed volume in the presence of detector tilt  $\theta = +10^\circ$ , detector slant  $\varphi = +10^\circ$ , and detector skew  $\eta = +2^\circ$ . Left: grey-value slice along XY-plane before grey-value thresholding. Center: magnified portion of grey-value image. Right: three-dimensional view of the reconstructed sphere objects after applying grey-value thresholding.

### Multiple rotations

CT scans in the presence of multiple detector rotations are simulated. The first three combinations included rotations about two axes, while the last two combinations included rotations about all three axes. Negative rotations are covered in the final three-axis combination.

$$(\theta, \varphi, \eta) = (+5, +5, 0); (+5, 0, +1); (0, +5, +1); (+5, +5, +1); (-5, -5, -1)$$

The statistics for centroid and form deviations due to multiple rotations are summarized in table 3.7. The effect of detector skew on the reconstructed sphere form is noted by the increase in the RMS of sphere fit residuals.

Table 3.7. Centroid deviation and form deviation statistics in the presence of multiple rotations.

Rotation			Centroid deviation magnitude /mm			RMS of sphere fit residuals /mm	
$\theta$	$\varphi$	$\eta$	Maximum	Mean	$\sigma$	Mean	$\sigma$
+5°	+5°		0.44	0.16	0.13	0.06	0.03
+5°		+1°	0.42	0.16	0.13	0.13	0.04
	+5°	+1°	0.21	0.08	0.05	0.13	0.05
+5°	+5°	+1°	0.63	0.19	0.17	0.12	0.05
-5°	-5°	-1°	0.44	0.16	0.12	0.15	0.05

### 3.1.3 Radiographic correction

The authors of reference [13] observed an improvement in tomographic image quality after correcting for geometrical errors in the radiographic data. Here, the approach of correcting radiographic data prior to reconstruction is evaluated quantitatively and in the context of reducing dimensional measurement errors. Since the approach is applied to simulated data, the angular misalignments of the detector are known precisely. In a test system, detector misalignments can be measured either with reference instruments or by imaging a reference object. Uncertainty in the experimental measurements would result in an uncertainty of the applied correction.

Distortion correction maps were generated for each simulated detector misalignment and applied to the corresponding radiographic data. Correcting the radiograph consists of shifting the pixel position assigned to an intensity value by an amount corresponding to the distortion correction at that pixel position. The *imwarp* function in MATLAB's image processing toolbox is used to perform the re-binning of intensity data for all radiographs. The function includes options for interpolating the shifts between pixels; linear interpolation was used in this study. As an example, a radiograph taken with a detector skew  $\eta = +2^\circ$  is shown in figure 3.13 (left); the imaged cylindrical array is slightly tilted. To ensure that the border pixels are preserved after the correction procedure, the radiographic images were initially padded by 50 pixels on each side with repeated border intensity values. The result of not padding the image data prior to correction is shown in figure 3.13 (center). The intensities from the original border pixels are shifted inward towards the center of the image. Since there is no data to replace the border pixels, they are automatically assigned a zero intensity value. As a result of the padding step, it is important that the border pixels only include background (air) intensity data. Subsequent to padding the image and applying the pixel shifts, the image is cropped back to its original size (figure 3.13, right).

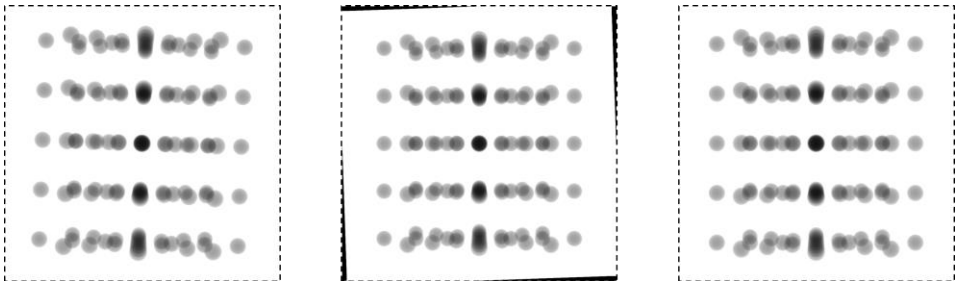


Figure 3.13. The pixel positions assigned to intensity values in the original radiograph are shifted according to the distortion correction map for the given detector misalignments. Left: The original radiograph in the presence of a skew  $\eta = 2^\circ$ ; notice the tilted orientation of the imaged cylindrical array. Center: Without padding the radiograph beforehand intensity values for border pixels are shifted inward, while there are no intensity values to replace to occupy the original pixels—thus, those ‘empty’ border pixels are assigned zero intensity. (Right) The result of shifting the pixels after padding and subsequent cropping.

New volumes are reconstructed from the corrected radiographs. The same procedures defined in section 3.1.2 for determining centroid and form deviations are used here.

#### *Individual rotations*

The statistics for centroid deviation in the corrected volumes are presented for individual rotations in table 3.8. Form deviation statistics are summarized for positive individual rotations in table 3.9. The percentage change from the uncorrected form deviation is also presented.

Table 3.8. Maximum, mean, and standard deviation  $\sigma$  of centroid deviation magnitude for individual rotations after radiographic correction. The percent change from the uncorrected deviation values is also shown.

Angles		Centroid deviation after correction /mm					
		Maximum	Change	Mean	Change	$\sigma$	Change
$\theta$	+10°	$5.73 \times 10^{-2}$	-94.5%	$1.76 \times 10^{-2}$	-95.3%	$1.42 \times 10^{-2}$	-95.8%
	+5°	$2.39 \times 10^{-2}$	-94.3%	$9.64 \times 10^{-3}$	-93.9%	$4.27 \times 10^{-3}$	-96.7%
	-5°	$2.21 \times 10^{-2}$	-94.8%	$9.55 \times 10^{-3}$	-93.9%	$3.72 \times 10^{-3}$	-97.1%
	-10°	$5.37 \times 10^{-2}$	-94.9%	$1.65 \times 10^{-2}$	-95.5%	$1.37 \times 10^{-2}$	-96.0%
$\varphi$	+10°	$3.28 \times 10^{-2}$	-91.8%	$1.34 \times 10^{-2}$	-94.2%	$6.32 \times 10^{-3}$	-93.9%
	+5°	$1.97 \times 10^{-2}$	-80.8%	$9.14 \times 10^{-3}$	-84.4%	$3.83 \times 10^{-3}$	-83.9%
	-5°	$2.70 \times 10^{-2}$	-74.1%	$9.61 \times 10^{-3}$	-83.7%	$4.35 \times 10^{-3}$	-82.4%
	-10°	$3.13 \times 10^{-2}$	-92.2%	$1.34 \times 10^{-2}$	-94.2%	$5.73 \times 10^{-3}$	-94.5%
$\eta$	+2°	$7.19 \times 10^{-2}$	-36.2%	$3.70 \times 10^{-2}$	+3.0%	$1.27 \times 10^{-2}$	-55.6%
	+1°	$2.61 \times 10^{-2}$	-30.8%	$1.32 \times 10^{-2}$	-14.1%	$5.26 \times 10^{-3}$	-30.8%
	-1°	$2.67 \times 10^{-2}$	-33.4%	$1.32 \times 10^{-2}$	-11.3%	$5.03 \times 10^{-3}$	-31.0%
	-2°	$6.72 \times 10^{-2}$	-38.8%	$3.70 \times 10^{-2}$	+3.1%	$1.30 \times 10^{-2}$	-55.9%

Table 3.9. Mean and standard deviation  $\sigma$  of the RMS of sphere fit residuals over all spheres for individual rotations after radiographic correction. The percent change from the uncorrected RMS values is also shown.

Angles		RMS of sphere fit residuals after correction /mm			
		Mean	Change	$\sigma$	Change
$\theta$	+10°	$2.82 \times 10^{-3}$	-82.8%	$6.59 \times 10^{-4}$	-96.0%
	+5°	$2.58 \times 10^{-3}$	-59.3%	$3.85 \times 10^{-4}$	-85.5%
$\varphi$	+10°	$2.77 \times 10^{-3}$	-97.1%	$6.03 \times 10^{-4}$	-99.0%
	+5°	$2.44 \times 10^{-3}$	-94.7%	$2.91 \times 10^{-4}$	-99.2%
$\eta$	+2°	$2.48 \times 10^{-3}$	-98.9%	$3.92 \times 10^{-4}$	-99.4%
	+1°	$2.44 \times 10^{-3}$	-98.1%	$3.16 \times 10^{-4}$	-99.3%

### Multiple rotations

The statistics for centroid deviation in the corrected volumes are presented for multiple rotations in table 3.10. Sphere form statistics are summarized for positive multiple rotations in table 3.11. The percentage change from the uncorrected sphere form is also presented.

Table 3.10. Maximum, mean, and standard deviation  $\sigma$  of centroid deviation magnitude for multiple rotations after radiographic correction. The percent change from the uncorrected deviation values is also shown.

Angles			Centroid deviation after correction /mm					
$\theta$	$\varphi$	$\eta$	Maximum	Change	Mean	Change	$\sigma$	Change
+5°	+5°		$2.51 \times 10^{-2}$	-94.3%	$1.13 \times 10^{-2}$	-92.8%	$4.61 \times 10^{-3}$	-96.4%
+5°		+1°	$3.03 \times 10^{-2}$	-92.7%	$1.12 \times 10^{-2}$	-92.9%	$4.90 \times 10^{-3}$	-96.1%
	+5°	+1°	$3.27 \times 10^{-2}$	-84.5%	$1.41 \times 10^{-2}$	-82.5%	$6.31 \times 10^{-3}$	-87.2%
+5°	+5°	+1°	$2.30 \times 10^{-2}$	-96.4%	$1.11 \times 10^{-2}$	-94.1%	$4.10 \times 10^{-3}$	-97.6%
-5°	-5°	-1°	$4.64 \times 10^{-2}$	-89.4%	$1.60 \times 10^{-2}$	-90.0%	$8.44 \times 10^{-3}$	-93.2%

Table 3.11. Mean and standard deviation of the RMS of sphere fit residuals over all spheres for multiple rotations after radiographic correction. The percent change from the uncorrected RMS values is also shown.

Angles			RMS of sphere fit residuals /mm			
$\theta$	$\varphi$	$\eta$	Mean	Change	$\sigma$	Change
+5°	+5°		$2.58 \times 10^{-3}$	-95.8%	$3.32 \times 10^{-4}$	-98.9%
+5°		+1°	$2.55 \times 10^{-3}$	-98.0%	$3.89 \times 10^{-4}$	-99.1%
	+5°	+1°	$2.58 \times 10^{-3}$	-98.1%	$3.57 \times 10^{-4}$	-99.3%
+5°	+5°	+1°	$2.66 \times 10^{-3}$	-97.7%	$4.62 \times 10^{-4}$	-99.1%
-5°	-5°	-1°	$2.78 \times 10^{-3}$	-98.2%	$4.49 \times 10^{-4}$	-99.1%

### 3.1.4 Discussion

A forward projection model [2] is adapted to evaluate distortions in the pixel coordinates assigned to X-ray intensity data due to angular misalignments of a detector. It is observed in this study that the magnitude of pixel distortions is more sensitive to detector rotations about the Z-axis (skew,  $\eta$ ) than about the X- or Y-axes. For example, in the presence of detector tilt  $\theta = 10^\circ$  (about the X-axis) or detector slant  $\varphi = 10^\circ$  (about the Y-axis), the maximum distortion was 42.5 pixels; a detector skew  $\eta = 2^\circ$  resulted in a maximum distortion of 49.3 pixels. Similarly, the average distortion over the entire  $2000 \times 2000$  pixel image space was 10.9 pixels in the presence of detector tilt  $\theta = 10^\circ$  or detector slant  $\varphi = 10^\circ$ ; the average distortion in the presence of detector skew  $\eta = 2^\circ$  was 26.7 pixels.

Commercial software Scorpius XLab<sup>®</sup> is used to simulate CT scans of a computer generated cylindrical array of aluminum spheres. Scans are simulated under ideal geometry and in the presence of various detector misalignments. Centroid position and sphere form in the reconstructed volumes are used as criteria for evaluating the effects of detector misalignments on the measurement volume. It is shown that tilts of the detector about the X axis contributed mostly to centroid deviations; these deviations increased with increasing distance of the sphere from the mid-plane. On the other hand, detector slants about the Y axis contributed significantly to both centroid and sphere form deviations; the effects of detector slant increased with increasing sphere distance from the rotation axis. Detector skew about the Z axis contributed mostly to sphere form deviation; the effects of detector skew increased with increasing distance from the center of the volume. Systematic deviations observed in the volumetric data can be used to inform the development of dedicated reference objects for estimating detector misalignments in a test system.

The distortion model is applied inversely to correct radiographic data from a misaligned detector. New volumes are reconstructed from the corrected radiographs and the centroid and form deviations are compared to the uncorrected values. After distortion correction, deviations in centroid position in the presence of detector tilt were reduced by 93 % to 97 %, while deviations due to detector slant were reduced by 74 % to 94 %. On the other hand, deviations in centroid position due to detector skew are reduced by 30 % to 40 %. The RMS of sphere fit residuals was reduced by 95 % to 99 % in the presence of detector slant and skew, while it was reduced by 50 % to 80 % in the presence of detector tilt. Similar reductions were observed for the data in the presence of multiple detector rotations. The observation of such reductions validates the efficacy of the radiographic distortion model presented in this study.

The methodology presented here can be useful for a user to correct for detector rotations in their CT system, without requiring involvement from the instrument manufacturer. However, several limitations exist. For example, the proposed method assumes the values of the detector rotations are known in advance. Some methods to determine detector position and orientation exist in the literature [14]. Additionally, to enable corrections, measurements should be avoided at the extremities of the reconstructed volume; that is, the projection of the measured object should not occupy the border pixels of the radiographic image (see section 3.1.3). Finally, the radiographic correction procedure has been validated under strictly-controlled, e.g. noiseless, simulation conditions. There is concern that pixel

interpolation used in the re-binning of radiographic intensities (the MATLAB function *imwarp*, in this study) could result in loss of valuable projection data. An alternative method to correct for known geometric misalignments involves modifying the geometrical parameters used in the backprojection step of the reconstruction algorithm [15].

## 3.2 Rotation stage errors

The stage with which the measured sample is rotated can have indexing errors and rotational error motions [14]. Methods to measure rotary stage error motions using reference instruments are well defined and are often applied by the stage manufacturer to ensure the product meets specified tolerances prior to making it commercially available. A control report indicating the measured rotation stage errors for the particular product is typically provided to the customer. Discrepancies between the actual position and orientation of the measured sample and the position and orientation of the voxel space assumed in the backprojection step can result in dimensional errors of the reconstructed volumetric data. The sensitivity of dimensional measurements to rotation stage indexing errors and error motions is studied here for simulated CT data of a test object. Acquisitions are repeated for several magnification positions and the test object is appropriately scaled to preserve the test object-to-voxel size ratio between scans. This scaling of the test object allows us to scale the dimensional measurements to approximate the size of typical test objects imaged at the given magnification position; magnitude of rotation stage errors do not change with magnification position. The content of this section is reproduced from [16].

### 3.2.1 Test object

The test object consists of 27 spheres arranged in a helical trajectory of two helical turns at a fixed radius from a common cylindrical axis (figure 3.14). Such an object can be manufactured, for example, by attaching highly X-ray absorptive spheres (e.g. steel or zirconia) to a cylindrical support with significantly lower X-ray absorption (e.g. a carbon fiber tube), as shown in [17]. In this simulation study, the test object is modelled as a set of spheres ‘floating’ in space to remove the influence of absorption and scatter (see e.g. [18]) from other objects on dimensional measurements. Spheres are numbered sequentially from the top of the helix to the bottom. The positions of the spheres are defined in cylindrical coordinates: radius  $r$ , angular position  $\beta$  about the cylindrical axis, and height  $h$  along cylindrical axis.

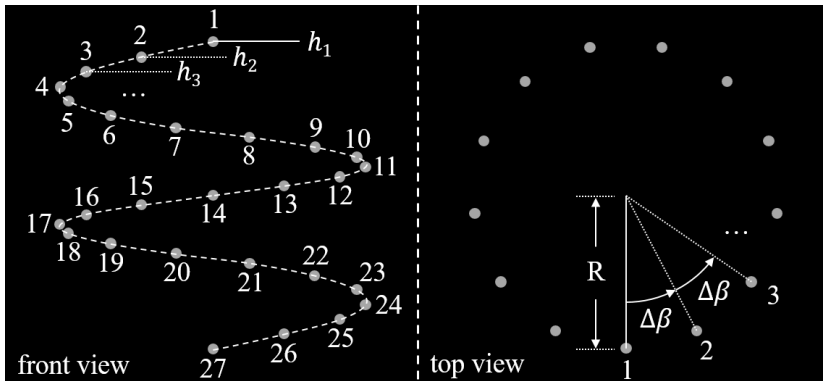


Figure 3.14. The test object and geometrical parameterization.

The following dimensions are specified for the sphere positions and diameter at a magnification of 1 in the simulated CT instrument. The test object dimensions for each simulated magnification position are given by the following values divided by the respective magnification factor. The diameter of the spheres is 9.416 mm. All spheres are located at a fixed radius  $r = R$  from the cylindrical axis, where  $R = 105.304$

mm. The angular spacing between adjacent spheres  $\Delta\beta$  is constant, where  $\Delta\beta = (720/26)^\circ$ . Spheres 1, 14, and 27 are located at angular positions  $\beta_1 = 0^\circ$ ,  $\beta_{14} = 360^\circ$ , and  $\beta_{27} = 720^\circ$ , respectively. Angular spacing does not change with magnification. The height  $h$  of each sphere is defined with respect to sphere 1; these values are shown in table 3.12.

Table 3.12. Height along cylindrical axis from sphere 1 of each sphere in the test object at a magnification of 1 for the CT instrument simulated in this study. The scaled heights for simulated magnification positions are given by the values in this table divided by the respective magnification factor.

<b>Sphere</b>	<b>1</b>	<b>2</b>	<b>3</b>	<b>4</b>	<b>5</b>	<b>6</b>	<b>7</b>	<b>8</b>	<b>9</b>
Height /mm	0.00	15.54	30.60	45.20	59.32	73.44	85.21	95.10	104.99
<b>Sphere</b>	<b>10</b>	<b>11</b>	<b>12</b>	<b>13</b>	<b>14</b>	<b>15</b>	<b>16</b>	<b>17</b>	<b>18</b>
Height /mm	114.88	124.29	133.71	143.12	152.54	161.96	171.37	180.79	190.20
<b>Sphere</b>	<b>19</b>	<b>20</b>	<b>21</b>	<b>22</b>	<b>23</b>	<b>24</b>	<b>25</b>	<b>26</b>	<b>27</b>
Height /mm	200.09	209.98	219.86	231.63	245.76	259.88	274.48	289.54	305.08

### 3.2.2 Parameterization of rotation stage errors

The global coordinate system introduced in chapter 1 is recalled. The X-ray source focal spot is the origin of the global coordinate frame. The Z axis is coincident with the magnification axis, which is defined as the line from the source focal spot that intersects the detector perpendicularly to its plane. The Y axis is parallel to the sample stage axis of rotation and the X axis follows the right-handed screw rule, i.e.  $(X \times Y) = Z$ . Rotation stage errors in CT are unintended changes in position and orientation of the sample stage as a function of rotation position  $n$ . It should be noted that zero-order rotation stage errors, i.e. errors that are constant as a function of rotation position  $n$ , do not affect CT measurements; therefore, only higher order rotation stage errors are modelled. The following parameterization of rotation stage errors is accompanied by the diagrams in figure 3.15. The functions and magnitudes of the modelled rotation stage errors are shown in table 3.13 and correspond to the observed behaviors and acceptance limits, respectively, in the technical specification of a Newport RVS80CC rotation table employed in a Nikon 225kV CT system.

Indexing error  $\delta$  is the error between the assumed rotation angle  $\alpha_{\text{index}}$  and actual rotation angle  $\alpha_{\text{actual}}$  about the sample stage axis of rotation. In this study, indexing error is modelled as a first order harmonic component and a smaller, superimposed random component. Axial error motion  $\tau_Y$  is a translation of the sample stage along its axis of rotation. Radial error motion is a translation of the sample stage along a plane orthogonal to the sample stage axis of rotation. Two parameters,  $\tau_X$  along the global X axis and  $\tau_Z$  along the global Z axis, are used to parameterize radial error motion. Axial and radial error motions are randomly sampled from uniform distributions. Tilt error is a tilt of the sample stage surface normal with respect to the sample stage axis of rotation. This error motion is parameterized by two angles:  $\xi$  denotes the direction of the unit vector along the XZ plane about which the tilt error motion occurs and  $\gamma$  denotes the magnitude of the tilt. Tilt error is intrinsic to the rotating frame of the sample stage; therefore,  $\xi$  rotates with the axis of rotation from an initial position  $\xi_0$ . Modelling of tilt magnitude  $\gamma$  consists of two systematic components: a half order harmonic tilt (repeats once every  $720^\circ$  of stage rotation) and a thirteenth order harmonic tilt due to e.g. imperfect ball bearings between stage stator and rotor. These behaviors were chosen to correspond to the behaviors observed in the control report of the previously mentioned Newport RVS80CC rotation stage. The modelled center of rotation for tilt error motion is located at the center of the rotation stage stator assembly.

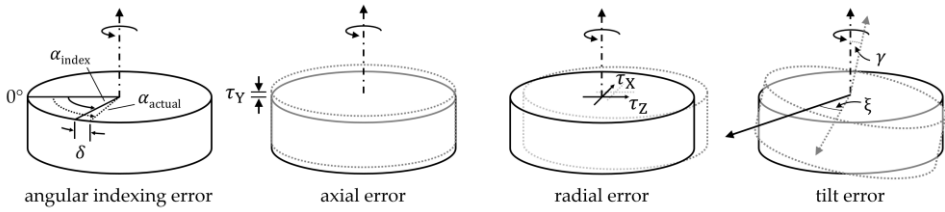


Figure 3.15. Rotation stage errors are unintended shifts and tilts of the sample rotation stage that vary with rotation position  $n$ . In this simulation study, the following rotation stage errors are modelled: angular indexing error, axial and radial error motions, and tilt error.

Table 3.13. Functions and magnitudes for the modelled rotation stage errors. 'Random' denotes random sampling from a uniform distribution, the interval  $[-a, +a]$  of which is given by the values in the corresponding magnitude column. The magnitude for harmonic error components corresponds to the maximum and minimum intensity of the corresponding waveform.

Rotation error	Parameter	Function	Magnitude
Indexing error	$\delta_1(n)$	First order harmonic	$\pm 0.0027$ degrees
	$\delta_R(n)$	Random	$\pm 0.0003$ degrees
Tilt error motion	$\gamma_{1/2}(n)$	Half-order harmonic	$\pm 18$ $\mu$ radians
	$\gamma_{13}(n)$	Thirteenth-order harmonic	$\pm 2$ $\mu$ radians
	$\xi(n)$	Linear	$\xi(n) = \xi_0 + \alpha(n)$
Radial error (X)	$\tau_X(n)$	Random	$\pm 2$ $\mu$ m
Radial error (Z)	$\tau_Z(n)$	Random	$\pm 2$ $\mu$ m
Axial error	$\tau_Y(n)$	Random	$\pm 2$ $\mu$ m

### 3.2.3 Simulation and data analysis

Analytical (ray-tracing) software Scorpius XLab<sup>®</sup> [6] is used to simulate the radiographic acquisition and tomographic reconstruction of the test object. The constant geometrical parameters of the simulated CT system are shown in table 3.14, where SDD is the source-to-detector distance. Six CT acquisitions are simulated, each at a different position of the sample stage along the magnification axis. The source-to-rotation axis distance (SRD) and corresponding magnification for each simulated acquisition are shown in table 3.15. Magnification positions were chosen to highlight the measurement domain for which modelled rotation stage errors have a significant effect. Filament current and X-ray tube acceleration voltage were chosen for each acquisition to provide similar contrast and brightness in the simulated radiographs among all acquisitions.

Table 3.14. Constant parameters of the simulated CT system.

Parameter	Value
Detector size	400 mm $\times$ 400 mm
Number of pixels	2000 $\times$ 2000
Pixel size	0.2 mm $\times$ 0.2 mm
SDD	1177 mm
Projections	720

Table 3.15. Source-to-rotation axis distance and magnification for six simulated acquisitions. Magnification positions were chosen to indicate the measurement domain for which modelled rotation stage errors have a significant effect.

Acquisition	1	2	3	4	5	6
SRD	250 mm	25 mm	12.5 mm	6 mm	4.5 mm	3 mm
Magnification	4.71	47.08	94.16	196.17	261.56	392.33

For each acquisition, the test object is scaled such that the ratio of test object (sphere size and sphere positions) to voxel size is constant among all acquisitions. Each acquisition is simulated once under ideal rotation of the sample stage and once in the presence of rotation stage errors. Each simulated dataset is then tomographically reconstructed by a filtered backprojection (Feldkamp type) algorithm [7] in Scorpion XLab<sup>®</sup>. The built-in reconstruction applies a Shepp-Logan filter [8] to the radiographic images prior to backprojection into the volume, in which bilinear interpolation [9] is used. Reconstructed volumes consist of 1999 (X) × 2000 (Y) × 1999 (Z) voxels. Voxel sizes and the size of measurement volumes are shown for each acquisition in table 3.16.

Table 3.16. Parameters of the reconstructed volumes, surface determination search distance, and surface sampling interval for all acquisitions.

Acquisition		1	2	3	4	5	6
Voxel size / $\mu\text{m}$	X	41.90	4.19	2.10	1.01	0.75	0.50
	Y	35.36	3.54	1.77	0.85	0.64	0.42
	Z	41.90	4.19	2.10	1.01	0.75	0.50
Measurement volume /mm	X	83.76	8.38	4.20	2.02	1.50	1.00
	Y	70.72	7.08	3.54	1.70	1.28	0.84
	Z	83.76	8.38	4.20	2.02	1.50	1.00
Local surface determination search distance		4 voxels					
Surface sampling interval (X × Y × Z)		1 × 1 × 1 voxels					

Processing of the volumetric datasets is performed in VGStudio MAX 3.0 (Volume Graphics GmbH, Germany). Surfaces are generated from the volumetric models by applying advanced (local) surface determination to automatically-determined isosurface grey values. The local deviation search distance in the advanced surface determination is set to the default 4 voxels. The surface model is converted to three-dimensional point coordinates by applying surface sampling at 1 voxel intervals along each coordinate direction. Point coordinates corresponding to each sphere in the test object are isolated and a sphere is least-squares fit. The parameters of the fit spheres namely sphere center, radius, and residuals are analyzed in the following section.

### 3.2.4 Results

Measured results from the acquisition with rotation stage errors are compared to the same results from acquisition with ideal rotation. Since the size of the measured features vary among acquisitions, errors (differences) between the datasets are presented as percent of the features measured under ideal rotation. The following results indicate that, as can be expected, the sensitivity of dimensional measurements given constant rotation stage errors increases with magnification. The scope of this study is to investigate the relationship between the modelled rotation stage errors and measurements made at the upper magnification limits of the simulated instrument. A typical measurand in objects consisting of multiple spheres is the error in sphere center-to-center distances from a chosen reference sphere to all

other spheres. However, error in the position of the chosen reference sphere will be present in all center-to-center distance errors, thereby shedding doubt on the exemplariness of the measurand to describe general length errors in the measurement volume. An alternative is to calculate distances to sphere centers from a new reference point, defined by the mean coordinates over all spheres in a given dataset. These distances are hereby referred to as mean-to-sphere center distances (M2C). Errors in M2C as a result of rotation errors are shown as percent of the measured length from ideal rotation in figure 3.16. M2C errors do not exceed one tenth of a percent with respect to the measured distances under ideal rotation. M2C errors indicate sensitivity to rotation stage errors starting at acquisition 2, corresponding to a voxel size of approximately  $4\ \mu\text{m}$ . The maximum observed error in acquisition 2 is one fortieth of a percent, which corresponds to a maximum expected length measurement error (from one end of the volume to the opposite) of approximately  $4\ \mu\text{m}$ . Maximum expected length measurement errors over the reconstructed volumes for acquisitions 3, 4, 5, and 6 are approximately  $3\ \mu\text{m}$ ,  $2\ \mu\text{m}$ ,  $3\ \mu\text{m}$ , and  $1.8\ \mu\text{m}$ , respectively.

Errors in sphere fit radii due to rotation errors are presented in figure 3.17 as percent of the radii measured with ideal rotation. Noticeable effects appear by acquisition 4, corresponding to a voxel size of approximately  $1\ \mu\text{m}$ . These effects increase with magnification to approximately 1.5 % error at acquisition 6. Sphere fit radius errors are similar for all spheres within a given acquisition. Maximum observed radius errors for acquisitions 4, 5, and 6 are  $0.084\ \mu\text{m}$  on  $24\ \mu\text{m}$  radii,  $0.09\ \mu\text{m}$  on  $18\ \mu\text{m}$  radii, and  $0.18\ \mu\text{m}$  on  $12\ \mu\text{m}$  radii, respectively. Form errors in the reconstructed spheres can be discerned by observing the residuals between surface points and the corresponding fit sphere. These residuals are shown as percent of sphere radii measured with ideal rotation in histogram form in figure 3.18. Results are shown separately for acquisitions with ideal rotation and acquisitions with rotation errors, albeit side by side for comparison. The Y axis in the histograms corresponds to relative frequency; therefore, no units are shown. The 2.5 % and 97.5 % quantiles are shown in table 3.17, corresponding to the lower and upper limits, respectively, for the central 95 % of all residual values in a given dataset. The results indicate that noticeable differences in sphere form due to rotation errors appear from acquisition 3, corresponding to a voxel size of approximately  $2\ \mu\text{m}$ .

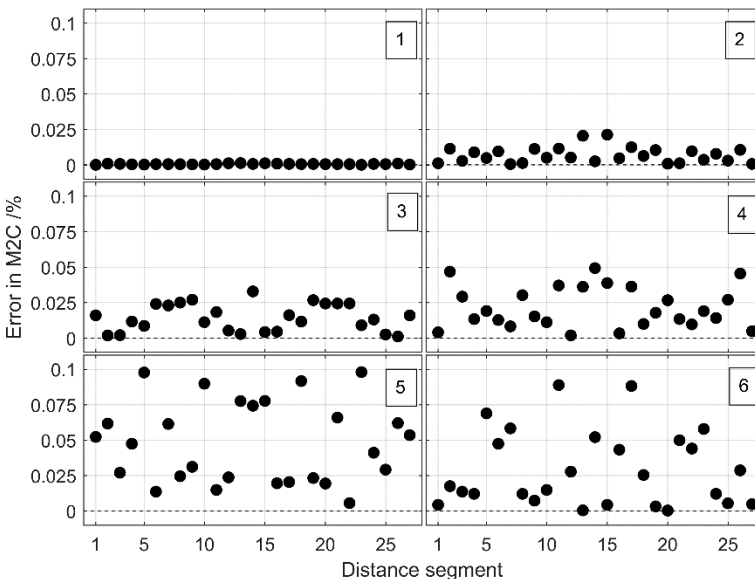


Figure 3.16. Error due to rotation error motions in mean-to-sphere center distances (M2C) as percent of measured M2C under ideal rotation for acquisitions 1 to 6. Noticeable errors in M2C appear in acquisition 2, corresponding to a magnification factor of approximately 50.

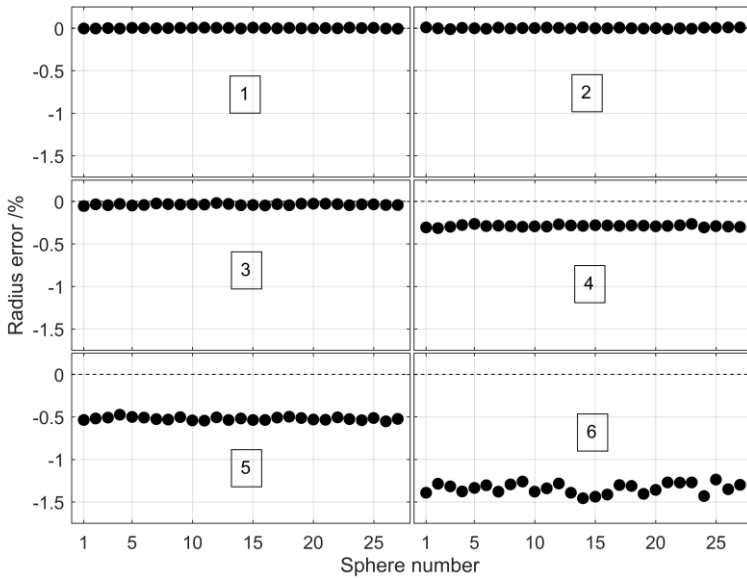


Figure 3.17. Radius errors due to rotation error motions as percent of measured radii under ideal rotations for acquisitions 1 to 6. Noticeable radius errors appear in acquisition 4, corresponding to a magnification factor of approximately 200.

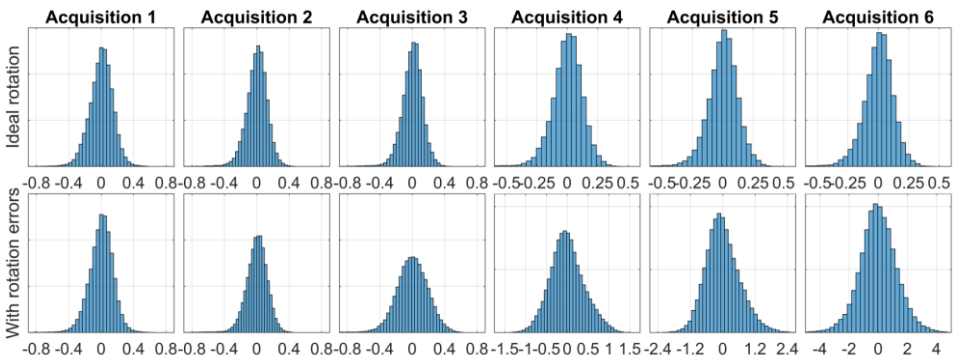


Figure 3.18. Histograms for residuals between reconstructed sphere surface points and sphere fit as percent of measured radii under ideal rotation for acquisitions 1 to 6.

Table 3.17. Distribution of sphere fit residuals as percent of measured radii under ideal rotation. The distribution is indicated by the 2.5 % and 97.5 % quantiles, corresponding to the lower and upper limits, respectively, for 95 % of observed residuals.

Sphere fit residuals / %		Acquisition					
		1	2	3	4	5	6
Ideal rotation	2.5 %	-0.30	-0.27	-0.27	-0.26	-0.26	-0.27
	97.5 %	0.27	0.23	0.24	0.23	0.23	0.22
With rotation errors	2.5 %	-0.30	-0.27	-0.38	-0.75	-1.11	-2.52
	97.5 %	0.27	0.24	0.36	0.86	1.36	2.59

### 3.2.5 Discussion

The results in this study indicate that the error behaviors as indicated by the specifications of the rotation stage employed in a Nikon 225kV CT system introduce noticeable effects on CT measurements for magnifications above 50, corresponding to voxel sizes below 4  $\mu\text{m}$  (see figure 3.16). For the CT system in this study, these magnifications correspond to measurement volumes below 8 mm  $\times$  8 mm  $\times$  8 mm, where maximum expected measurement errors were approximately equivalent to the length of one voxel. Sphere radius and form errors were noticeable at magnifications of approximately 100 and 200, respectively (see figure 3.17). In this measurement domain, effects due to the finite size of the focal spot are overwhelmingly larger than the observed effects due to rotation stage errors. Understanding the sensitivity of measurements to certain error sources can help users prioritize error mapping of their measuring instrument. In this simulation study, it is shown that the effects of rotation stage errors are relatively small for measurements made on “macro” CT instruments, such as the one modelled here. A similar study should be extended to rotation stage errors in micro- and nano-CT systems.

### References

- [1] Ferrucci M, Ametova E, Carmignato S, Dewulf W (2015) Evaluating the effects of detector angular misalignments on simulated computed tomography data. *Precision Engineering* 45, 230-241 doi:10.1016/j.precisioneng.2016.03.001
- [2] Yang K, Kwan ALC, Miller DF, Boone JM (2006) A geometric calibration for cone-beam CT systems. *Medical Physics* 33 (6), 1695–1706
- [3] Hartley R, Zisserman A (2004) *Multiple view geometry in computer vision*, 2<sup>nd</sup> edition (Cambridge University Press: Cambridge, UK) doi:10.1017/CBO9781107415324.004
- [4] Sun Y, Hou Y, Zhao F, Hu J (2006) A calibration method for misaligned scanner geometry in cone-beam computed tomography. *Independent Nondestructive Testing and Evaluation International* 39 (6), 499–513 doi:10.1016/j.ndteint.2006.03.002
- [5] Weisstein E Euler Angles. From MathWorld--A Wolfram Web Resource <http://mathworld.wolfram.com/EulerAngles.html> (accessed June 15, 2015).
- [6] Hiller J, Reindl LM (2012) A computer simulation platform for the estimation of measurement uncertainties in dimensional X-ray computed tomography. *Measurement* 45, 2166–2182 doi:10.1016/j.measurement.2012.05.030
- [7] Feldkamp LA, Davis LC, Kress JW (1984) Practical cone-beam algorithm. *Journal of the Optical Society of America* 1 (6), 612–619
- [8] Shepp LA, Logan BF (1974) The Fourier reconstruction of a head section. *IEEE Transactions on Nuclear Science* NS-21, 21–43
- [9] Buzug T (2008) *Computed Tomography: From photon statistics to modern cone-beam CT* (Springer-Verlag: Berlin, Germany) doi:10.1007/978-3-540-39408-2
- [10] Kumar J, Attridge A, Wood PKC, Williams MA (2011) Analysis of the effect of cone-beam geometry and test object configuration on the measurement accuracy of a computed tomography scanner used for dimensional measurement. *Measurement Science and Technology* 22, 35105 doi:10.1088/0957-0233/22/3/035105
- [11] Ontiveros S, Yagüe JA, Jiménez R, Brosed F (2013) Computer tomography 3D edge detection comparative for metrology applications. *Procedia Engineering* 63, 710–719 doi:10.1016/j.proeng.2013.08.263

### Chapter 3

- [12] Grass M, Köhler T, Proksa R (2000) 3D cone-beam CT reconstruction for circular trajectories. *Physics in Medicine and Biology* 45, 329–347
- [13] Stevens GM, Saunders R, Pelc NJ (2001) Alignment of a volumetric tomography system. *Medical Physics* 28, 1472-1481 doi:10.1118/1.1382609
- [14] Ferrucci M, Leach RK, Giusca CL, Carmignato S, Dewulf W (2015) Towards geometrical calibration of X-ray computed tomography systems - A review. *Measurement Science and Technology* 26, 92003 doi:10.1088/0957-0233/26/9/092003
- [15] Ametova E, Ferrucci M, Chilingaryan S, Dewulf W (2018) Software-based compensation of instrument misalignments for X-ray computed tomography dimensional metrology. *Precision Engineering* 54, 233-242
- [16] Ferrucci M, Ametova E, Probst G, Craeghs T, Dewulf W (2018) Sensitivity of CT dimensional measurements to rotation stage errors. 8<sup>th</sup> Conference on Industrial Computed Tomography (Wels, Austria)
- [17] Hermanek P, Ferrucci M, Dewulf W, Carmignato S (2017) Optimized reference object for assessment of computed tomography instrument geometry. 7<sup>th</sup> Conference on Industrial Computed Tomography (Leuven, Belgium)
- [18] Lifton JJ, Carmignato S (2017) Simulating the influence of scatter and beam hardening in dimensional computed tomography. *Measurement Science and Technology* 28, 104001

# Chapter 4

## Geometrical measurement procedure with implementation on simulated data

Methods for measuring the CT instrument geometry typically consist of solving a set of geometrical parameters by radiographically imaging a reference object and analyzing the acquired projection data. The most common type of reference object consists of several radiographically opaque, *i.e.* high X-ray absorption, spherical markers. Calibration of the CT geometry demands the comparison of the measured geometrical parameters to a traceable reference. It is therefore critical that the reference features in the imaged object, in this case the three-dimensional coordinate positions of the sphere centers, be calibrated. Furthermore, error sources in the geometrical calibration procedure must be quantified and propagated to uncertainty in the geometrical parameters.

In this study, we propose a method to measure the geometry of a cone-beam CT instrument using a traceable reference object. Geometrical parameters are determined by minimizing the difference between observed and modelled projection data of the reference object. Practical considerations are provided for the analysis of radiographic data and for the robust implementation of the minimization technique. The proposed method is applied on simulated radiographic data of the Computed Tomography Calibration Tube (CT<sup>2</sup>) reference object (see figure 4.3) [1]. Uncertainty in the reference object features and error motions of the rotation stage are included to approximate the simulated environment to what can be expected in experimental data (see section 4.3). The application of the geometrical measurement procedure to simulated data allows us to compare the measured geometrical parameter values to the actual simulated values. The luxury of knowing the ‘true’ values, however, is not afforded in experimental implementation of the proposed method. Furthermore, application of the proposed method on simulated data is a critical first step to validate the implementation on experimental data. For this reason, discussions are provided throughout this chapter to address this discrepancy and suggestions are made for eventually implementing the method on the measurement of experimental CT geometries. Finally, a discussion on error sources in the proposed method is provided in the context of assessing uncertainty in the measured geometrical parameters, which is required for calibration of the CT instrument geometry.

### 4.1 Reference object parameterization

The geometry of a cone-beam CT instrument is defined in chapter 1. Since a reference object is used in the geometrical estimation, its position and orientation must also be defined with respect to the components of the CT instrument. The diagram in figure 4.1, which illustrates a typical cone-beam CT instrument, supplements the following description. The parameterization of the reference object in the CT geometry is given by the position of its local origin and the orientation of its local axes with respect to the global origin and coordinate axes of the CT geometry, respectively, at the  $\alpha = 0^\circ$  position of the rotation stage. The position of the local origin in the global frame is given by the point  $\mathbf{P} = (x_p, y_p, z_p)$  and the orientation of the local axes is given by three extrinsic rotations, performed sequentially in the order (1)  $\rho_y$ , (2)  $\rho_z$ , and (3)  $\rho_x$ . The reference object rotation sequence was chosen to correspond to the sequence in the simulation software. These parameters are considered ‘nuisance’ parameters, as they do not describe the CT geometry, yet are necessary for solving the minimization problem. Furthermore, these

nuisance parameters eliminate the need to know accurately the position and orientation of the reference object in the global coordinate frame. The CT geometry can therefore be defined by 13 geometrical parameters: 7 instrument parameters ( $x_D, y_D, z_D, \eta, \varphi, \theta, z_R$ ) and 6 object 'nuisance' parameters ( $x_P, y_P, z_P, \rho_X, \rho_Y, \rho_Z$ ) $_{\alpha=0^\circ}$ .

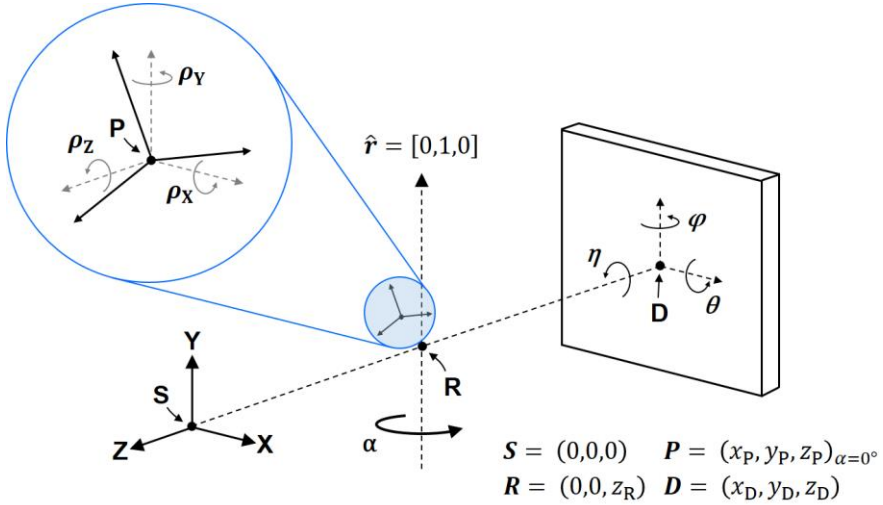


Figure 4.1. CT geometry with reference object position and orientation.

The geometry of a CT instrument can be determined by imaging a dedicated reference object at  $N$  angular positions of the rotation stage from  $0$  to  $360^\circ$ ; in this study, angular positions are equally spaced, though it is not a requirement. The rotation angle of each rotation position  $n = 1, 2, \dots, N$  is given by  $\alpha_n$ . The acquired projection images can then be used to estimate the CT imaging geometry by way of dedicated analyses [2]. Most commonly used reference objects consist of several high-absorption spherical markers distributed in a particular arrangement on a cylindrical structure. This structure is typically made from a relatively low absorption material to ensure high contrast of the projected markers in the radiographs. Each sphere  $m$ , where  $m = 1, 2, \dots, M$  and  $M$  is the total number of spheres, is defined by a three-dimensional coordinate position of its center  $(x, y, z)_m^{\text{local}}$  in the local (object) coordinate frame. The sphere center coordinates in the global coordinate frame and at the rotation position  $\alpha = 0^\circ$  of the rotation stage  $(x, y, z)_m^{\text{global}}$  are given by applying the three rotations ( $\rho_X, \rho_Y, \rho_Z$ ) and the three translations ( $x_P, y_P, z_P$ ) to the sphere center coordinates in the local coordinate frame. This operation is conceptualized in equation 4.1 below.

$$(x, y, z)_{m, \alpha=0^\circ}^{\text{global}} = f(x_m^{\text{local}}, y_m^{\text{local}}, z_m^{\text{local}}, \rho_X, \rho_Y, \rho_Z, x_P, y_P, z_P, \alpha = 0^\circ) \quad (4.1)$$

In the projection image of the reference object, the set of  $M$  projected sphere center coordinates  $(u_{\text{obs}}, v_{\text{obs}})_m$ —henceforth referred to as center projection coordinates—are determined utilizing the image analysis procedure described in section 4.4.

For each angular position  $n$  of the rotation stage, the global sphere center coordinates are rotated by the corresponding angle  $\alpha_n$ , thereby providing a new set of sphere center coordinates  $(x, y, z)_{m,n}^{\text{global}}$ . Analysis of the newly acquired projection image provides estimates of the corresponding set of center projection coordinates  $(u_{\text{obs}}, v_{\text{obs}})_{m,n}$  (figure 4.2). The complete scan of the reference object and subsequent image analysis provides a set of  $M \times N$  sphere center coordinates  $(x, y, z)_{m,n}^{\text{global}}$  and a corresponding set of  $M \times N$  center projection coordinates  $(u_{\text{obs}}, v_{\text{obs}})_{m,n}$ .

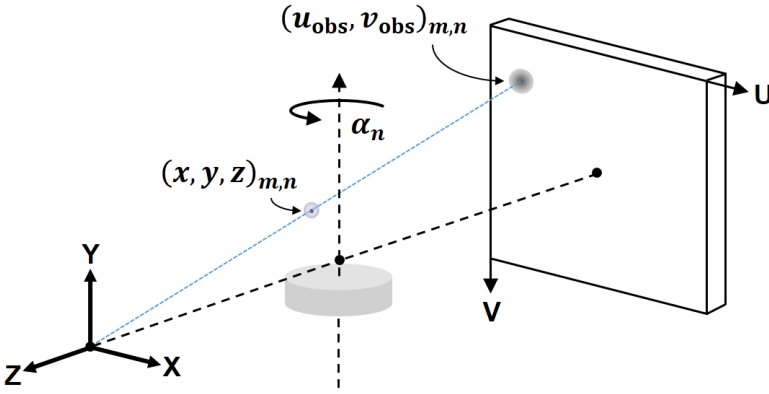


Figure 4.2. Analysis of each radiograph provides  $M$  center projection coordinates. A complete data acquisition of  $N$  radiographs and subsequent analysis provide a set of  $M \times N$  center projection coordinates  $(u_{obs}, v_{obs})_{m,n}$ .

Geometrical parameters can be determined analytically, that is by solving discrete equations relating the sphere center coordinates  $(x, y, z)_{m,n}$  in the global coordinate frame and observed center projection coordinates  $(u_{obs}, v_{obs})_{m,n}$  to the set of instrument parameters  $p_i$ , where  $i = 1, 2, \dots, 7$ . Analytical methods typically rely on the accurate alignment of the reference object, i.e. on the prior knowledge of the 6 reference object nuisance parameters, thereby making the accuracy of the solved parameters dependent on the accuracy of this alignment [2]. This requirement makes analytical methods unwieldy.

## 4.2 Minimization of re-projection errors

Minimization methods consist of finding the set of modelled geometrical parameters that minimize the error between modelled and observed center projection coordinates, known as the re-projection error [3]. A ray-tracing model is used to calculate the center projection coordinates for a reference object with known sphere positions given an initial set of geometrical parameter values. The set of modelled center projection coordinates  $(u_{mod}, v_{mod})_{m,n}$  are compared to the set of observed center projection coordinates  $(u_{obs}, v_{obs})_{m,n}$  from analysis of acquired radiographs. The sum of squared residuals (SSR) between modelled and observed center projection coordinates, shown in equation 4.2, is used as the objective function to be minimized.

$$SSR = \sum_{n=1}^N \sum_{m=1}^M \left( \sqrt{(u_{mod}(m, n) - u_{obs}(m, n))^2 + (v_{mod}(m, n) - v_{obs}(m, n))^2} \right)^2 \quad (4.2)$$

It should be noted that the objective function can take other algebraic forms, for example keeping the  $u$  and  $v$  components of the center projection residuals separate prior to summing instead of summing in quadrature. The implications of other objective functions on the performance of the minimization is covered in Annex A of this doctoral thesis.

The fundamental principle of minimization methods is to iteratively adapt—or ‘solve’—the geometrical parameters of the ray-tracing model to minimize the reprojection error. If the minimization procedure is implemented correctly, the solved parameters that provide the lowest reprojection error should correspond to the parameters of the test instrument with which the observed coordinates were acquired. A shortcoming of minimization methods is the possibility of solving to a local minimum, which would provide an erroneous set of solved parameters. Global optimization tools can be used to reduce the

occurrence of solving to local minima and generally consist of repeating the minimization procedure under different initial values of the solvable parameters. The Global Optimization Toolbox in MATLAB (Mathworks Inc., USA) provides several such solutions, e.g. *Global Search* [4] and *Multi Start* [5]. In these global optimization functions, the user must define constraints for the search range of initial parameter values. Preliminary studies of both functions on simulated data indicate that the *Global Search* function provided more consistent convergence in comparison to the *Multi Start* function. However, coupling between solvable parameters remains a limitation to the accuracy of measured results irrespective of global optimization tools and is discussed in section 4.5 on convergence testing.

The reference object used in this study is based on the prototype described in [1], in which 49 opaque (steel) spheres of 2.5 mm diameter are arranged in four helices, each performing one full helical turn along the outer circumference of a carbon fiber cylindrical support. Spheres at the top and bottom of the helices perform a full circular trajectory to allow static determination of the instrument geometry, as described in [6]. In this study, only the spheres are simulated (i.e. the carbon fiber structure is not included in the CAD file when generating radiographs) to allow the focus of the investigation to be on the minimization procedure. Each sphere is defined by the coordinate position of its center in a local coordinate frame (figure 4.3). In this study, the sphere center coordinate positions are given by their nominal values in the CAD file plus random perturbations to account for uncertainty in calibrated sphere coordinates expected in experimental implementation (see section 4.3.1).

The coordinate position of each sphere center both in the physical reference object and on the projection image constitute corresponding data points. Overlaps between projected spheres can occur, particularly for reference objects with a relatively large number of spheres. If not properly considered, these overlaps can introduce errors in the estimation of the center projections and, ultimately, can compromise the effective implementation of geometrical estimation. The CT<sup>2</sup> was designed to reduce sphere overlaps in the projections while maintaining the number of spheres that was deemed optimal in [7]. For a sample data set, the CT<sup>2</sup> object resulted in less than 1 % of data points having overlaps.

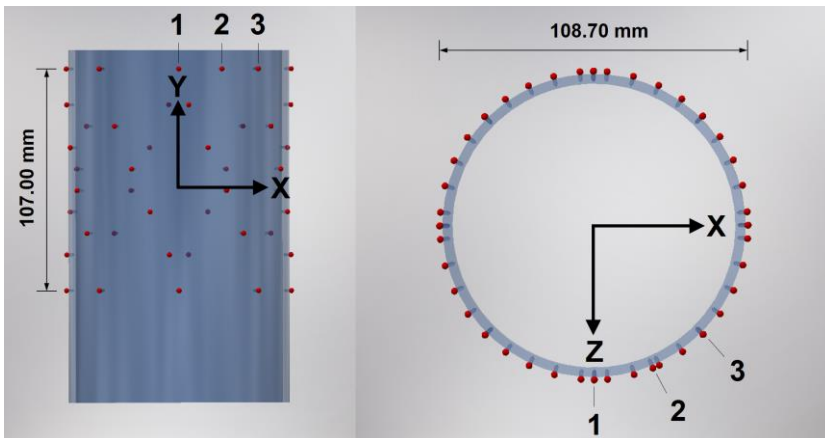


Figure 4.3. CAD model of the 49-sphere CT<sup>2</sup> reference object with local coordinate frame. Left: Side view. Right: Top-down view. Spheres 1, 2, and 3 are indicated for orientation.

### 4.3 Simulation of radiographic data acquisition

Scorpius XLab® (Fraunhofer IIS, Germany) is used for generating radiographs of the set of  $M$  spheres at  $N$  rotation positions. Radiographs were generated in the presence of various geometrical misalignments

of the reference object, the rotation stage, and detector. The magnitude of each misalignment was randomly chosen from a uniform distribution, the intervals of which correspond to what could be realistically expected, but not readily noticeable, misalignments in CT instruments. The unvaried settings used in all simulated acquisitions are provided in table 4.1. The nominal and perturbed instrument geometrical parameters are shown in table 4.2, while the nominal and perturbed reference object geometrical parameters are shown in table 4.3. Ten simulations ( $s = 1$  to 10) in the presence of perturbed parameters are performed. Simulated acquisitions are adapted to approximate expected conditions in experimental implementation. The simulated sphere center coordinates were perturbed from their nominal values to consider the effects of uncertainty in reference object calibration. Furthermore, perturbations were applied to the sphere center coordinates as a function of rotation position to approximate the effects of rotation stage error motions.

Table 4.1. Parameters in the simulated acquisition of radiographs.

Parameter	Value
Acceleration voltage	100 kV
Filament current	0.1 mA
Number of projections	720 (from 0° to 359.5° in increments of 0.5°)
Pixel size	0.2 mm × 0.2 mm
Detector size	2000 × 2000 pixels

Table 4.2. Simulated values for instrument geometrical parameters.

Simulation $s$	$x_D$ /mm	$y_D$ /mm	$z_D$ /mm	$z_R$ /mm	$\theta$ /°	$\varphi$ /°	$\eta$ /°
Nominal	0	0	-1177	-400	0	0	0
1	1.2590	-1.3700	-1175.4430	-402.5450	-0.6756	-0.0989	-0.7867
2	1.6230	1.8820	-1181.6430	-402.6760	0.5886	-0.8324	0.9238
3	-1.4920	1.8290	-1173.5090	-399.8150	-0.3776	-0.5420	-0.9907
4	1.6540	-0.0590	-1172.6600	-398.3250	0.0571	0.8267	0.5498
5	0.5290	1.2010	-1175.2130	-397.3960	-0.6687	-0.6952	0.6346
6	-1.6100	-1.4330	-1174.4230	-402.2210	0.2040	0.6516	0.7374
7	-0.8860	-0.3130	-1174.5690	-399.5870	-0.4741	0.0767	-0.8311
8	0.1880	1.6630	-1178.0780	-400.1840	0.3082	0.9923	-0.2004
9	1.8300	1.1690	-1175.4460	-402.9290	0.3784	-0.8436	-0.4803
10	1.8600	1.8380	-1180.2880	-400.9770	0.4963	-0.1146	0.6001

Table 4.3. Simulated values for reference object, i.e. 'nuisance', geometrical parameters at  $\alpha = 0^\circ$  rotation position.

Simulation $s$	$x_P$ /mm	$y_P$ /mm	$z_P$ /mm	$\rho_X$ /°	$\rho_Y$ /°	$\rho_Z$ /°
Nominal	0	0	-400	0	0	0
1	1.0051	1.3629	-400.5934	0.4121	-0.1225	-0.4479
2	-0.9796	-0.9829	-398.6767	-0.9363	-0.2369	0.3594
3	0.0238	1.2571	-399.6589	-0.4462	0.5310	0.3102
4	0.7963	-1.0259	-399.8011	-0.9077	0.5904	-0.6748
5	1.5636	1.7171	-398.3312	-0.8057	-0.6263	-0.7620
6	1.8372	-0.6001	-400.8566	0.6469	-0.0205	-0.0033
7	0.1889	-1.2136	-398.9712	0.3897	-0.1088	0.9195
8	-1.4455	-0.9957	-398.9851	-0.3658	0.2926	-0.3192
9	-1.4028	0.4642	-400.4782	0.9004	0.4187	0.1705
10	-0.9700	-0.1068	-399.7287	-0.9311	0.5094	-0.5524

### 4.3.1 Perturbation of sphere center coordinates

In experimental implementation, there is uncertainty in the calibrated sphere center coordinates. To account for this uncertainty, the actual center coordinates of the simulated spheres are perturbed from their nominal values in the local coordinate frame (equation 4.3). The perturbation is repeated separately for each simulation  $s$ .

$$(x, y, z)_{m,s}^{\text{local}} = (x, y, z)_{m,s}^{\text{nominal}} + (\Delta x, \Delta y, \Delta z)_{m,s} \quad (4.3)$$

where  $\Delta x, \Delta y$ , and  $\Delta z$  are randomly sampled coordinate perturbations from the normal distributions  $\delta_x, \delta_y$ , and  $\delta_z$  with zero mean and standard deviation  $\sigma = 0.603 \mu\text{m}$ . The uncertainty corresponds to the expected uncertainty in the calibration of sphere center coordinates by CMM.

### 4.3.2 Rotation stage error motions

Rotation stage error motions are applied as a combination of systematic and random perturbations to the sphere center coordinates in the simulated scans as a function of rotation stage position  $n$ . The modelled error motions are angular indexing error, axial error motion, radial error motion, and tilt error motion (see figure 3.15). The function and magnitude of each modelled error motion correspond to the observed error functions and acceptance limits reported in the manufacturer control report of a Newport RVS80CC rotation stage employed in the 225 kV CT instrument (Nikon XT H 225 M) at the National Physical Laboratory. The control report did not provide specifications for axial error motion; the specification value for radial error motion was therefore also applied to set the axial error motion interval. The characteristics of the modelled error motions are described in table 3.13. Random error motions are sampled from uniform (square) distributions symmetrical about zero; the magnitude of the distributions are defined by the interval boundaries. The center of rotation for tilt error motion is located 105 mm below the Y position of the local object origin and along the axis of rotation.

### 4.3.3 Blur and noise

Blur and noise were added to the radiographs after their generation by the simulation software using MATLAB built-in functions `imgaussfilt` [8] and `imnoise` [9], respectively. Blur was applied as a two-dimensional smoothing kernel with standard deviation of 1 pixel, chosen to correspond to blur observed in similar radiographs acquired on an experimental CT instrument. After blurring, Poisson noise was added to approximate the expected Poisson variation in the photon output of the X-ray source.

## 4.4 Analyzing the projection data

Analysis of the projection data consists of estimating the pixel coordinates of the center projections for all acquired radiographs. Three practical considerations are presented here, namely the definition of the center projection from the imaged sphere, automation of the analysis step by sphere tracking, and managing overlaps in the projected spheres.

### 4.4.1 Estimating center projection coordinates

Correctly determining the location of the center projection from the imaged sphere in the radiograph is not trivial and has been an ongoing topic of research [10-12]. In the absence of other objects in the field of view, a sphere is projected onto the detector as an elliptical disk [11]. Assuming a single-material sphere

with uniform density, the intensity recorded by each pixel within the elliptical disk is proportional to the path length of the corresponding X-ray trajectory through the sphere. The longest path through a perfect sphere is the path that contains the sphere center; therefore, the projection point of the sphere center  $P$  is theoretically the position on the projected elliptical disk with a minimum intensity, i.e. highest X-ray attenuation [12].

In practice, however, effects such as image blur, noise, and photon depletion (complete X-ray absorption by objects) result in low image gradients in the area of lowest intensity. It is therefore difficult to accurately locate the sphere center projection from the intensity minimum. An alternative to estimating the coordinate positions of the projected spheres consists of using the center  $e$  of an ellipse fit to the outer edge of the projected disk. Detailed investigations in the use of this alternative method of estimation are provided in [10,11]. It was found in [11] that the true sphere center projection  $P$  lies on the major axis of the projected elliptical disk, albeit closer to the orthogonal projection of the source onto the detector (also known as the principal point,  $O$ ) than  $e$  (figure 4.4).

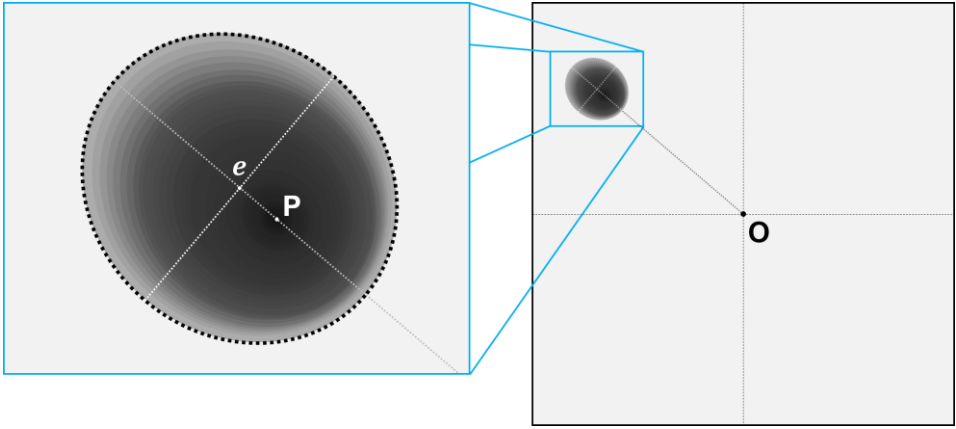


Figure 4.4. Comparison of the center of an ellipse fit to the outer edge of the projected sphere  $e$  to the actual pixel coordinate of the center projection  $P$ . The relative positions of  $e$  and  $P$  on the imaged elliptical disk in this figure are exaggerated for visualization.

Deng *et al.* [12] propose an enhanced estimate  $p$  of the sphere center projection coordinates  $P$  by applying a correction to the fit ellipse center  $e$  along the ellipse major axis in the direction of the principal point. The correction is calculated from the lengths of the major and minor axes of the fit ellipse  $L_{major}$  and  $L_{minor}$ , respectively, as shown in equation 4.4.

$$\mathbf{p} = \mathbf{e} - \frac{L_{major}^2 - L_{minor}^2}{4e} \quad (4.4)$$

where  $\mathbf{p}$  is the two-dimensional vector denoting the position of the corrected center projection coordinates on the detector,  $\mathbf{e}$  is the two-dimensional vector denoting the center coordinates of the fit ellipse, and  $L_{major}$  and  $L_{minor}$  are the scalar lengths of the major and minor axes, respectively, of the fit ellipse. The performance of the correction was validated by Deng *et al.* [12] through numerical simulations with varying levels of noise and various sphere characteristics. This estimate of the center projection coordinates is used in this study.

### 4.4.2 Tracking the spheres

Center projection coordinates are determined for all spheres  $M$  at all rotation positions  $N$ . The output of the image analysis step is therefore a set of  $M \times N$  observed pixel column and row coordinates ( $u_{\text{obs}}, v_{\text{obs}}$ ). Given the size of the dataset, a certain level of automation is needed to ensure the continued sanity of the user. A sphere projection tracking procedure is implemented to reduce user input. For each sphere, center projection coordinate gradients from radiograph  $n - 2$  to radiograph  $n - 1$  are used to predict the image location of the projected sphere in radiograph  $n$ . Furthermore, the size of the projected sphere at radiograph  $n - 1$  is used to generate an appropriately sized crop region for center projection estimation.

### 4.4.3 Projected sphere overlaps

Overlaps in the projected spheres introduce errors in the estimation of center projections. In the case of partial overlaps, circle-finding algorithms can be employed with appropriate modifications to the search parameters, for example by tightening the circle radius search range. Full overlaps of projected spheres, also known as projected sphere eclipsing, can be more difficult to overcome. If the eclipsing sphere, i.e. the second sphere covering the target sphere, completely absorbs the incoming X-rays, then circle-finding algorithms can provide little benefit in detecting the target sphere. For the purpose of simplicity, and due to the fact that overlaps only account for a few percent of all data points, those data points that correspond to sphere overlaps are not considered in the minimization objective function.

The sphere tracking algorithm is adapted to exclude these overlaps. For each sphere, the radiographs in which the sphere has overlaps are determined by manually scanning the set of radiographs. Overlap 'events' are clusters of sequential radiographs for which a sphere exhibits overlap. The projected sphere position after an overlap event is determined by multiplying the number of radiographs in the specific event  $\Delta n$  by the last image gradients prior to the event. The data points corresponding to overlap events are not included in the minimization procedure.

### 4.4.4 Error in observed center projection coordinates

The pixel coordinates assigned to each center projection deviate from the actual center projection position as a result of errors introduced by image blur, noise, and the image processing step. Furthermore, the presence of rotation stage error motions will also contribute to deviations of the projected sphere centers from the elliptical trajectories they would perform on the detector space under ideal rotation. To evaluate the magnitude of these errors, the set of observed center projection coordinates  $\{u_{\text{obs}}(\mathbf{m}, \mathbf{n}), v_{\text{obs}}(\mathbf{m}, \mathbf{n})\}$  is compared to the exact center projection coordinates  $\{u_{\text{exact}}(\mathbf{m}, \mathbf{n}), v_{\text{exact}}(\mathbf{m}, \mathbf{n})\}$ , which are calculated by performing forward projection on the known geometrical parameters of the simulation and under ideal rotation.

In figure 4.5, the errors in the estimated center projection coordinates  $\{\delta u_{\text{error}}(\mathbf{m}, \mathbf{n}), \delta v_{\text{error}}(\mathbf{m}, \mathbf{n})\}$  are plotted in histogram form for simulation  $s = 1$ . As a measure of dispersion, the 2.5 % and 97.5 % quantiles (corresponding to a 95 % coverage interval centered at the median error value) are indicated by dashed vertical lines and their values are shown adjacent to the lines. The shape and magnitudes of error distributions were similar for all simulated data sets. The 2.5 % and 97.5 % quantiles for all simulations are shown in table 4.4. Center projection errors were consistently within 0.3 pixels for all projected spheres in all radiographs.

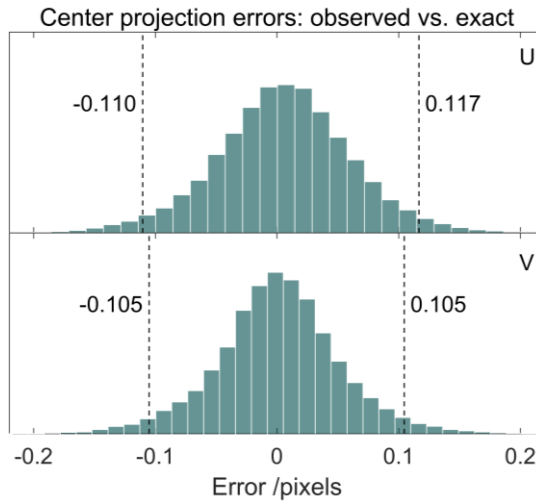


Figure 4.5. Histograms of error between exact and observed center projection coordinates for simulation 1. The vertical dashed lines correspond to the upper and lower boundaries of 95 % error interval.

Table 4.4. Lower and upper boundaries for 95 % of observed center projection errors designated by the 2.5 % and 97.5 % quantiles, respectively. All values are in pixels.

s	U coordinate quantiles		V coordinate quantiles	
	2.5 %	97.5 %	2.5 %	97.5 %
1	-0.1104	0.1167	-0.1051	0.1046
2	-0.1090	0.1166	-0.1014	0.1047
3	-0.1162	0.1095	-0.1027	0.1050
4	-0.1070	0.1148	-0.1031	0.1033
5	-0.1089	0.1136	-0.1029	0.1039
6	-0.1176	0.1063	-0.1048	0.1033
7	-0.1081	0.1195	-0.1039	0.1034
8	-0.1092	0.1171	-0.1029	0.1046
9	-0.1176	0.1117	-0.1054	0.1032
10	-0.1145	0.1041	-0.1025	0.1050

## 4.5 Convergence to a global solution and parameter identifiability

The measurement procedure was tested for convergence to the global minimum. Convergence testing comprises executing the minimization procedure using the exact (known) values of the input quantities, i.e. sphere center coordinates and center projection coordinates, while varying the initial values of the solvable parameters. The minimization for convergence testing is repeated 1000 times, each time randomly modifying the initial values of solvable parameters from corresponding uniform distributions (table 4.5) and ensuring that the solver search region (set as upper and lower solver search boundaries for each parameter) contains the corresponding simulated value. Differences in the results of convergence testing for more than 1000 repeated minimizations were observed to be negligible. The concept of convergence testing is illustrated in figure 4.6. Errors in solved parameters were observed to be larger when the true values were close to the corresponding search boundaries set in the *Global Search* function. It is therefore important to ensure that the search boundaries are large enough to avoid this shortfall.

Table 4.5. Perturbation of initial values of solvable parameters for convergence testing. Sampling distributions are uniform.

Parameter	Perturbation
$x_D$	$0 \pm 10$ mm
$y_D$	$0 \pm 10$ mm
$z_D$	$-1177 \pm 10$ mm
$\rho_X$	$0 \pm 10^\circ$
$\rho_Y$	$0 \pm 10^\circ$
$\rho_Z$	$0 \pm 10^\circ$
$x_P$	$0 \pm 10$ mm
$y_P$	$0 \pm 10$ mm
$z_P$	$-400 \pm 10$ mm
$z_R$	$-400 \pm 10$ mm
$\theta$	$0 \pm 10^\circ$
$\varphi$	$0 \pm 10^\circ$
$\eta$	$0 \pm 10^\circ$

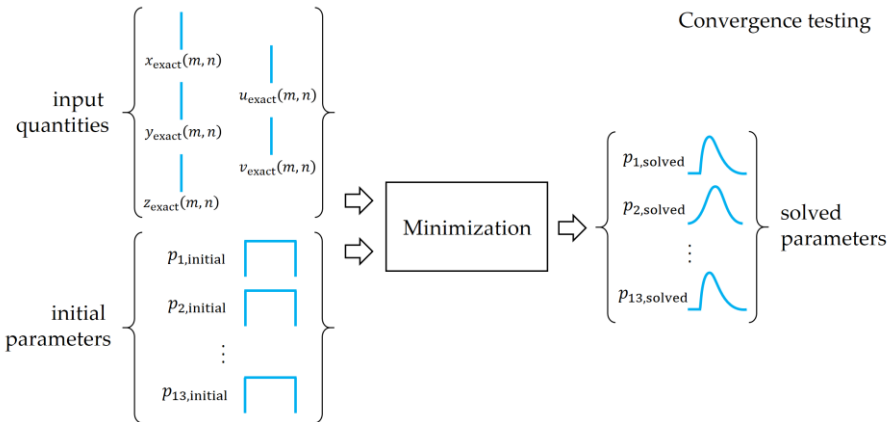


Figure 4.6. The global optimization technique is tested to ensure consistent convergence irrespective of initial values of the solvable parameters. The input quantities, i.e. sphere center coordinates and center projection coordinates, were set to their exact values for convergence testing.

Convergence testing was performed for all simulated data sets. Errors between the solved geometrical parameter values and the actual simulated values for simulation 1 are shown in histogram form in figure 4.7 and figure 4.8 for instrument geometrical parameters and in figure 4.9 and figure 4.10 for reference object geometrical parameters. Since the distributions of solved parameters were not normal in shape, the 2.5 % and 97.5 % quantiles corresponding to the 95 % spread of the respective result are denoted by the solid vertical lines [13]; their values are shown next to the solid lines. The simulated value is denoted by the dotted line, corresponding to an error of zero. Dashed lines correspond to the mean of the solved values. Some distributions were not symmetrical about the true values, which could be an indication of parameter coupling. Results for all simulated datasets are presented in figure 4.11 and figure 4.12, where the mean error is given by the circular marker and 95 % of the data points are contained within the associated error bars.

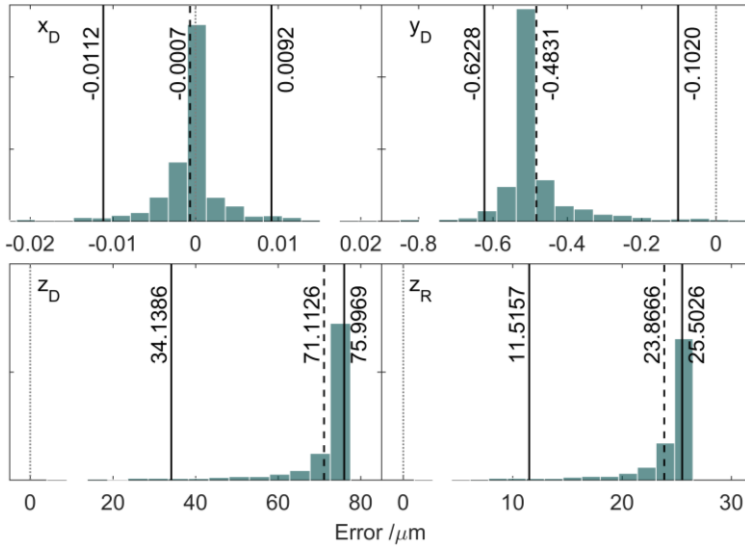


Figure 4.7. Histograms of solved instrument positional parameters from convergence testing for simulation 1. The dotted line corresponds to the actual simulated value (zero error) while the solid lines correspond to the lower and upper quantiles for 95 % of the solved parameter values. Dashed lines correspond to the mean of the solved values.

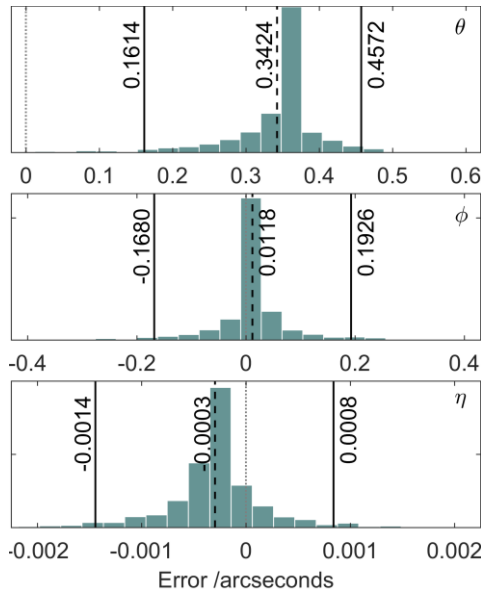


Figure 4.8. Histograms of solved instrument rotational parameters from convergence testing for simulation 1. The dotted line corresponds to the actual simulated value (zero error) while the solid lines correspond to the lower and upper quantiles for 95 % of the solved parameter values. Dashed lines correspond to the mean of the solved values.

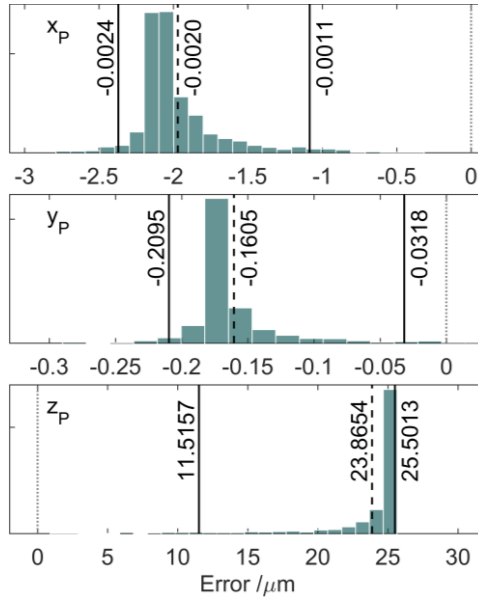


Figure 4.9. Histograms of solved reference object position from convergence testing for simulation 1. The dotted line corresponds to the actual simulated value (zero error) while the solid lines correspond to the lower and upper quantiles for 95 % of the solved parameter values. Dashed lines correspond to the mean of the solved values.

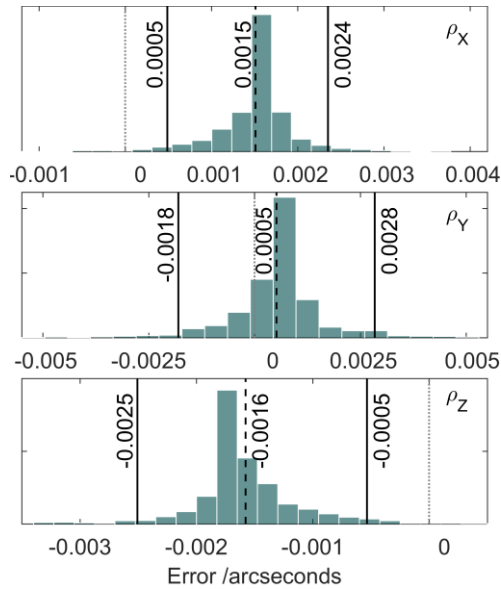


Figure 4.10. Histograms of solved reference object orientation from convergence testing for simulation 1. The dotted line corresponds to the actual simulated value (zero error) while the solid lines correspond to the lower and upper quantiles for 95 % of the solved parameter values. Dashed lines correspond to the mean of the solved values.

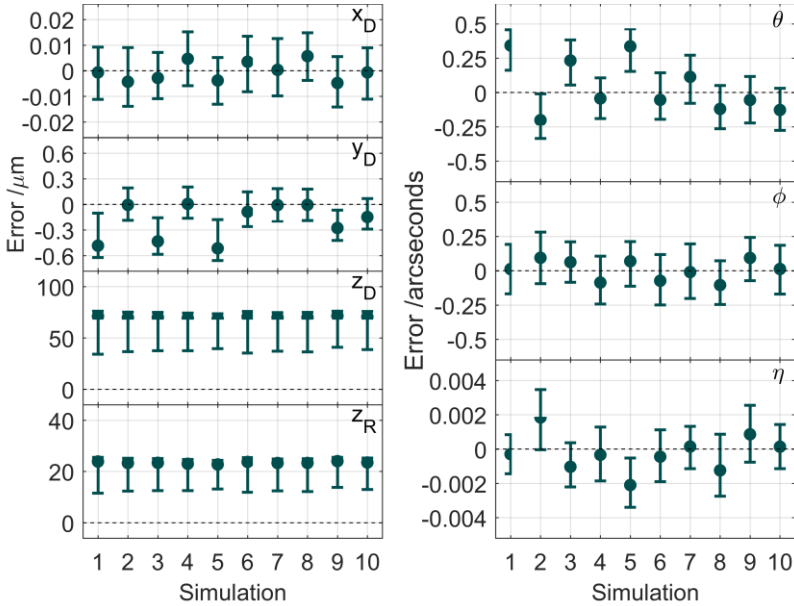


Figure 4.11. Errors in solved instrument geometrical parameters from convergence testing for all simulations. The circular marker denotes the mean error over 1000 repeat convergence runs, while the error bars correspond to 95 % of the solved parameter values, given by the 2.5 % (bottom) and 97.5 % (top) quantiles.

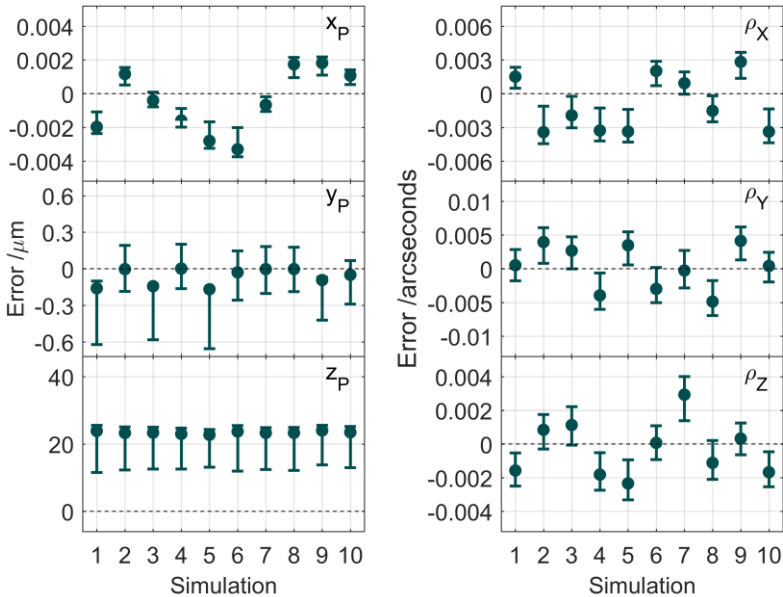


Figure 4.12. Errors in solved reference object geometrical parameters from convergence testing from all simulations. The circular marker denotes the mean error over 1000 repeat convergence runs, while the error bars correspond to 95 % of the solved parameter values, given by the 2.5 % (bottom) and 97.5 % (top) quantiles.

Convergence testing allows us to identify parameter coupling, which could influence parameter identifiability [14]. For example, the errors in solved Z positions of reference object, rotation axis, and detector are consistently offset in the same direction, i.e. closer to the source, and the magnitude of error in  $z_D$  is approximately the error in both  $z_R$  and  $z_P$  multiplied by the magnification factor of approximately 2.94. Convergence results indicate that, even in the presence of exact input quantities, the minimization procedure has intrinsic limitations in its ability to solve the geometrical parameters.

## 4.6 Measured geometrical parameters

The input quantities for the minimization procedure were the nominal (unperturbed) sphere center coordinates in the local object frame and the observed center projection coordinates ( $u_{obs}, v_{obs}$ ). Initial parameter values are set to their nominal values. Errors between solved parameter values and simulated values are shown for instrument geometrical parameters in figure 4.13 and for reference object geometrical parameters in figure 4.14. The solved values and corresponding errors are presented together with the simulated values in tables 4.10-4.14 in the appendix to this chapter. Errors in solved detector Z position were within 120  $\mu\text{m}$  for all simulations and errors in rotation axis and reference object Z positions were within 50  $\mu\text{m}$ . X and Y positions of detector and reference object were solved to within 5  $\mu\text{m}$  from their simulated values. Detector out-of-plane rotations  $\theta$  and  $\varphi$  solved to within 10 arcseconds and 3 arcseconds, respectively, while detector in-plane rotation  $\eta$  consistently solved to within 1 arcsecond. Coupling between the Z positions of rotation stage, reference object, and detector is evident.

Errors between observed center projection coordinates and minimized center projection coordinates, i.e. modelled after minimization, are analyzed. Histograms for these center projection coordinate errors from simulation 1 are shown in figure 4.15. 95 % of the data is indicated by dashed vertical lines corresponding to the 2.5 % and 97.5 % quantiles, respectively; their values are shown adjacent to the lines. The shape and magnitudes of error distributions were similar for all simulated data sets. The 2.5 % and 97.5 % quantiles for all simulations are shown in table 4.6. Comparison of the errors between minimized and observed center projection coordinates to the errors between exact and observed center projection coordinates from table 4.4 and figure 4.5 indicates that the two data sets are very similar.

Table 4.6. Lower and upper boundaries for 95 % of errors between observed and minimized center projection coordinates, designated by the 2.5 % and 97.5 % quantiles, respectively. All values are in pixels.

s	U coordinate quantiles		V coordinate quantiles	
	2.5 %	97.5 %	2.5 %	97.5 %
1	-0.1095	0.1144	-0.1039	0.1063
2	-0.1094	0.1090	-0.1046	0.1032
3	-0.1131	0.1118	-0.1040	0.1065
4	-0.1119	0.1096	-0.1033	0.1048
5	-0.1125	0.1095	-0.1055	0.1029
6	-0.1105	0.1111	-0.1059	0.1050
7	-0.1112	0.1117	-0.1027	0.1043
8	-0.1094	0.1121	-0.1025	0.1054
9	-0.1097	0.1113	-0.1038	0.1053
10	-0.1092	0.1088	-0.1055	0.1030

Geometrical measurement procedure with implementation on simulated data

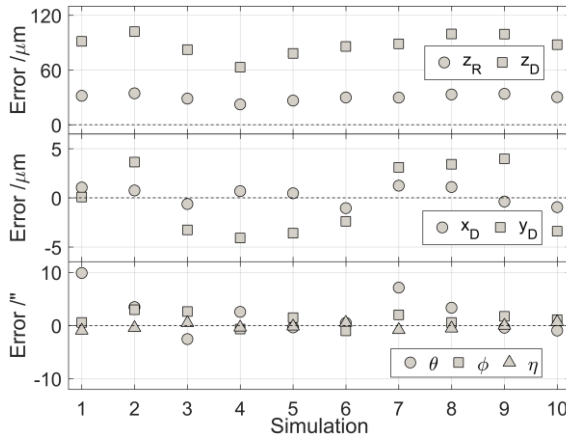


Figure 4.13. Errors in solved instrument geometrical parameters.

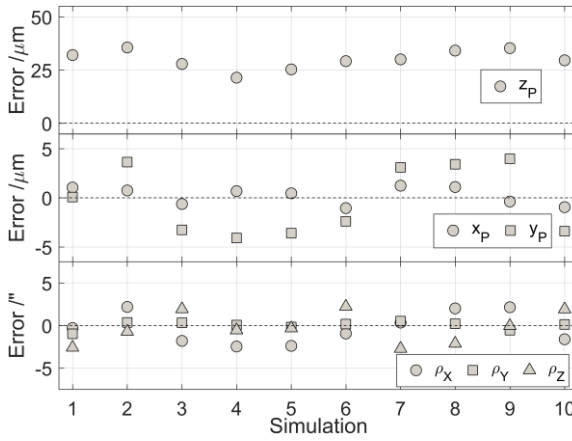


Figure 4.14. Errors in solved reference object geometrical parameters.

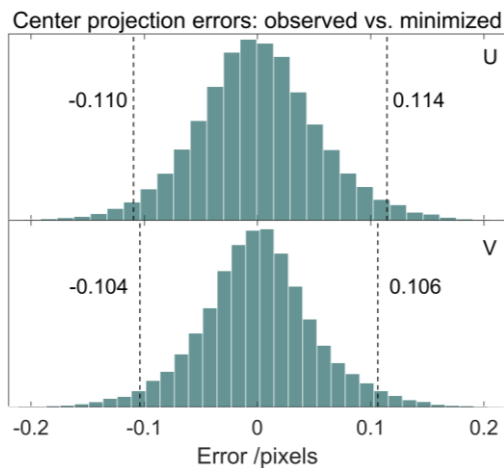


Figure 4.15. Histograms of error between observed and minimized center projection coordinates for one minimization run on the simulation 1 dataset. The data set is non-normal, as is shown by the superimposed dotted curve corresponding to a fit normal distribution. The vertical dashed lines correspond to the upper and lower boundaries of 95 % error interval.

## 4.7 Instrument adjustment

The output from the proposed geometrical measurement procedure is used to correct for instrument misalignments in the simulated CT measurement of a separate test object. The test object consists of a ball plate with 15 spheres of 2 mm diameter; 14 of these spheres form two crossing diagonal lines and one sphere is at a horizontal extremity of the plate (figure 4.16). Sphere center locations in a local coordinate system are provided in table 4.7. For simplicity, only the spheres are simulated.

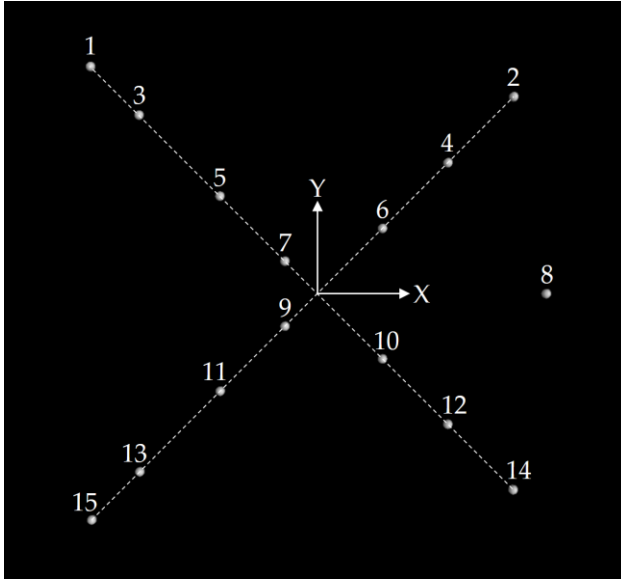


Figure 4.16. Test object for evaluating the correction of the CT instrument geometry from the output of the proposed geometrical measurement procedure.

Table 4.7. Sphere center coordinate positions for validation object. All values in mm.

Sphere	X	Y	Sphere	X	Y	Sphere	X	Y
1	-52.5	52.5	6	15	15	11	-22.5	-22.5
2	45	45	7	-7.5	7.5	12	30	-30
3	-41.25	41.25	8	52.5	0	13	-41.25	-41.25
4	30	30	9	-7.5	-7.5	14	45	-45
5	-22.5	22.5	10	15	-15	15	-52.5	-52.5

Some experimental CT instruments allow the detector position and orientation to be mechanically controlled, for example with kinematic axes or by re-mounting of the detector. In these instruments, detector lateral position  $x_D$ ,  $y_D$  and detector orientation  $\theta$ ,  $\varphi$ ,  $\eta$  can therefore be adjusted to zero using their measured values. SRD and SDD in the acquisition metafile (typically a text file containing relevant acquisition parameters used in tomographic reconstruction) are then adapted to the measured rotation axis position  $z_R$  and detector longitudinal position  $z_D$ ; the voxel size in the metafile is appropriately adjusted to reflect the new SRD and SDD. It should be noted that  $z_R$  and  $z_D$  only correspond to SRD and SDD when the detector out-of-plane rotations, i.e.  $\theta$  and  $\varphi$ , are zero. In experimental implementation, the geometrical measurement procedure should be repeated after physical adjustment of the detector

to confirm its correct adjustment. Furthermore, it is possible that the detector Z position can change during the physical adjustment. The repeated geometrical measurement will therefore provide an updated estimate for  $z_D$  and, consequently, SDD.

Differences between the set of solved and actual instrument geometrical parameters result in residual misalignments after correction. We evaluate the performance of correcting the instrument geometry from the set of measured geometrical parameters as follows. Radiographs of the test object are simulated under aligned instrument geometry, under 10 misaligned instrument geometries and under 10 adjusted instrument geometries, i.e. corrected for detector lateral position and orientation. Instrument geometrical parameters for nominal and misaligned acquisitions are provided in table 4.2, while the same parameters as identified and used for the adjusted acquisitions are shown in table 4.8. Note: Scorpius XLab® rounds linear positions to 3 decimal places and angular positions (in degrees) to four decimal places.

Table 4.8. Instrument parameters for adjusted geometry acquisitions. The values in this table are rounded to 4 decimal places to correspond to rounding of geometrical parameters in Scorpius XLab®.

s	Parameter						
	$x_D$ /mm	$y_D$ /mm	$z_D$ /mm	$z_R$ /mm	$\theta$ /°	$\varphi$ /°	$\eta$ /°
1	-0.001	0.000	-1175.443	-402.545	-0.0027	-0.0002	0.0003
2	-0.001	-0.004	-1181.643	-402.676	-0.0010	-0.0008	0.0001
3	0.001	0.003	-1173.509	-399.815	0.0007	-0.0007	-0.0001
4	-0.001	0.004	-1172.660	-398.325	-0.0007	0.0002	0.0001
5	0.000	0.004	-1175.213	-397.396	0.0001	-0.0004	0.0000
6	0.001	0.002	-1174.423	-402.221	-0.0001	0.0003	-0.0002
7	-0.001	-0.003	-1174.569	-399.587	-0.0020	-0.0006	0.0002
8	-0.001	-0.003	-1178.078	-400.184	-0.0009	-0.0002	0.0002
9	0.000	-0.004	-1175.446	-402.929	0.0001	-0.0005	0.0000
10	0.001	0.003	-1180.288	-400.977	0.0003	-0.0003	-0.0002

Tomographic reconstruction from the simulated radiographs is performed on Inspect-X (Nikon Metrology, UK). Reconstruction of the aligned and misaligned datasets is performed assuming nominal reconstruction geometry. Discrepancies in SRD and SDD between nominal reconstruction geometry and misaligned acquisition geometry can be partially corrected by implementing voxel rescaling. Voxel scaling factors for each misaligned acquisition of the ball plate are determined from center-to-center distance (C2C) measurements on the same misaligned acquisition of the CT<sup>2</sup> reference object (see figure 4.3). A linear regression curve is fit to CT measurements of sphere center-to-center distances plotted as a function of their respective simulated values. Voxel scaling factors applied to reconstructed volumes from each misaligned acquisition are as follows, in order of simulation number: (1) 1.0068, (2) 1.0016, (3) 1.0016, (4) 0.9983, (5) 0.9942, (6) 1.0065, (7) 1.0002, (8) 0.9984, (9) 1.0074, (10) 0.9985. Reconstruction of the adjusted datasets is performed under nominal detector lateral position and orientation. The values for SRD, SDD, and voxel size in the adjusted acquisition metafile for Inspect-X (.xtekt) are set to correspond to the measured  $z_R$  and  $z_D$  values, respectively from tables 4.10 and 4.12 in the appendix.

Dimensional measurements are performed on the reconstructed misaligned datasets without and with voxel scaling, henceforth 'misaligned' and 'rescaled', and on the adjusted datasets. Results are compared to equivalent measurements from aligned acquisition. Volumetric grey value models are imported into VGStudio MAX 3.0 (Volume Graphics, GmbH). Surfaces are generated from the volumetric models by

applying ‘advanced’ (local) surface determination to automatically evaluated initial grey value thresholds. The search distance for advanced surface determination is set to the default 4 voxels. The resulting surface model is converted to a three-dimensional coordinate point cloud by sampling at intervals of 1 voxel in all coordinate directions.

Point clouds are then processed in MATLAB. First, the point cloud is segmented such that the coordinate points corresponding to the surface of each sphere are separated from surface points of other spheres. Subsequently, spheres are least-squared fit [15] to each segmented set of coordinate points. Fit sphere centers are used to determine C2C between all combinations of spheres. Errors of misaligned, rescaled, and adjusted C2C relative to the same measurements from the aligned acquisition are plotted in figure 4.17. Results from all simulations are shown together. C2C errors in the misaligned dataset were as large as 1175  $\mu\text{m}$ . Voxel rescaling reduced these errors to below 220  $\mu\text{m}$ , while errors after adjustment were within 2  $\mu\text{m}$  of the aligned acquisition values.

Errors in sphere fit radii relative to aligned acquisition radii are shown in figure 4.18. Radius errors were mostly unchanged for misaligned and rescaled datasets; in both cases, the largest radius errors were approximately 100  $\mu\text{m}$ . After adjustment, radius errors were within 1  $\mu\text{m}$ . Sphere form is discerned from the residuals between sphere surface points and corresponding fit spheres for all spheres in a given dataset. The 2.5 % and 97.5 % quantiles, corresponding to the lower and upper boundaries covering 95 % of all residuals, are shown separately for misaligned, rescaled, and adjusted datasets in table 4.9. In the aligned acquisition the 2.5 % and 97.5 % quantiles are given by -4.9  $\mu\text{m}$  and 4.2  $\mu\text{m}$ , respectively. The sphere form results from misaligned and rescaled datasets did not differ substantially; 95 % of residuals in misaligned and rescaled datasets were as small as  $\pm 125 \mu\text{m}$  and as large as  $\pm 350 \mu\text{m}$ . The quantiles in adjusted datasets did not differ by more than 0.3  $\mu\text{m}$  from the same quantiles in the aligned dataset. Observed errors after adjustment are relatively small when compared to the effects of other error sources in the CT measurement procedure. These results therefore suggest that the geometrical measurement procedure provides a robust estimation of the instrument geometry.

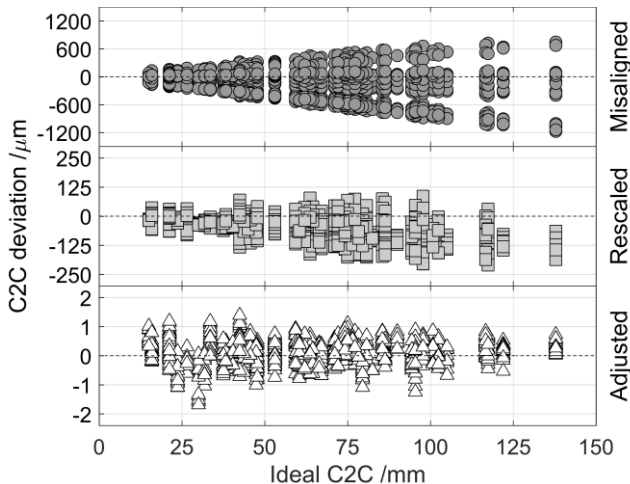


Figure 4.17. Center-to-center distance deviation from aligned acquisition for nominal, rescaled, and adjusted datasets.

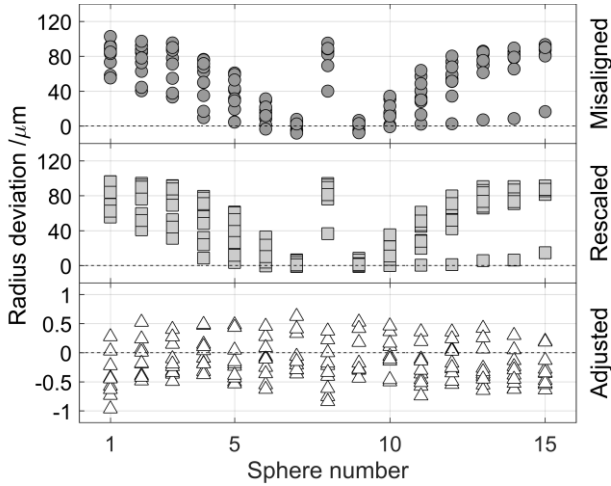


Figure 4.18. Radius deviation from aligned acquisition for nominal, rescaled, and adjusted datasets.

Table 4.9. Sphere form is indicated here by the 2.5 % and 97.5 % quantiles, corresponding to the lower and upper boundaries of 95 % of sphere fit residuals for all spheres in the test object. The equivalent 2.5 % and 97.5 % quantiles in the aligned acquisition were  $-4.9 \mu\text{m}$  and  $4.2 \mu\text{m}$ , respectively.

Quantiles / $\mu\text{m}$	Misaligned acquisition									
	1	2	3	4	5	6	7	8	9	10
2.5 %	-274.6	-322.7	-343.4	-215.6	-237.3	-262.2	-290.2	-127.4	-193.2	-223.8
97.5 %	241.5	310.5	348.3	182.6	201.8	228.5	253.0	85.4	159.8	189.6
Quantiles / $\mu\text{m}$	Rescaled acquisition									
	1	2	3	4	5	6	7	8	9	10
2.5 %	-277.2	-322.0	-340.9	-216.2	-236.0	-262.4	-289.0	-126.8	-192.7	-221.1
97.5 %	241.2	311.6	349.3	183.5	199.8	227.0	254.2	85.1	158.4	189.9
Quantiles / $\mu\text{m}$	Adjusted acquisition									
	1	2	3	4	5	6	7	8	9	10
2.5 %	-5.1	-4.9	-5.0	-5.1	-5.1	-4.9	-5.0	-5.0	-5.0	-5.2
97.5 %	4.3	4.5	4.4	4.4	4.3	4.3	4.5	4.5	4.3	4.3

## 4.8 Discussion

In this simulation study, we evaluate the performance of a procedure to measure the CT instrument geometry by minimization of reprojection errors from radiographs acquired of the CT<sup>2</sup> reference object. Realistic effects – such as rotation stage error motions, uncertainty in the reference object sphere center coordinates, and image blur and noise – were included in this simulation study to approximate the errors expected in experimental implementation. The proposed procedure is applied to measure 10 simulated acquisition geometries; the solved geometrical parameters are compared to the ‘true’ simulated parameters. Errors in solved parameters are relatively small. Detector X and Y positions are solved to within  $5 \mu\text{m}$  of the true value, while detector Z position is solved to within  $120 \mu\text{m}$ . Errors in detector out-of-plane rotations  $\theta$  and  $\varphi$  are within 10 arc seconds and 3 arc seconds, respectively, while errors in detector in-plane rotation  $\eta$  are within 1 arc second. The Z position of the axis of rotation is solved to within  $50 \mu\text{m}$  of the true value. The results from convergence testing (see section 6) indicate that coupling between Z positions of the rotation axis  $z_R$  and detector  $z_D$  resulted in systematic offsets of their solved values.

The solved geometrical parameters from the proposed measurement procedure can be used to correct the CT instrument, either by physical adjustment of the components or by software correction. Errors in the solved geometrical parameters will result in residual geometrical errors of the corrected instrument. The CT measurement of a separate ball plate is simulated under aligned, and misaligned (without and with voxel rescaling) and adjusted instrument geometries for each of the 10 simulated datasets. Dimensional measurements on the reconstructed datasets are compared. Center-to-center distance measurement errors were as large as 1175  $\mu\text{m}$  in the misaligned dataset without voxel rescaling. These errors were reduced to a maximum of 210  $\mu\text{m}$  after voxel rescaling and to within 2  $\mu\text{m}$  after adjustment. Radius errors as large as 100  $\mu\text{m}$  on 2 mm spheres in misaligned datasets were reduced to within 1  $\mu\text{m}$  after adjustment. Sphere form is given by the 2.5 % and 97.5 % quantiles of the sphere fit residuals from all spheres in the test object. In misaligned and rescaled datasets, 95 % of the observed residuals were as small as  $\pm 125 \mu\text{m}$  and as large as  $\pm 350 \mu\text{m}$ . Differences in the quantiles between aligned and corrected datasets were within 0.3  $\mu\text{m}$ . Errors in the reconstructed volume in the presence of residual geometrical misalignments are therefore relatively small, thereby validating the robustness of the geometrical measurement procedure.

## References

- [1] Hermanek P, Ferrucci M, Dewulf W, Carmignato S (2017) Optimized reference object for assessment of computed tomography instrument geometry. 7<sup>th</sup> Conference on Industrial Computed Tomography (Leuven, Belgium)
- [2] Ferrucci M, Leach RK, Giusca CL, Carmignato S, Dewulf W (2015) Towards geometrical calibration of X-ray computed tomography systems - A review. *Measurement Science and Technology* 26, 92003 doi:10.1088/0957-0233/26/9/092003
- [3] Ferrucci M (2017) Towards traceability of CT dimensional measurements. In: Carmignato S, Dewulf W, Leach RK, editors. *Industrial X-Ray Computed Tomography* (Springer-Verlag: Berlin, Germany)
- [4] Mathworks (2010) Global Search Class
- [5] Mathworks (2010) Multi Start Class
- [6] Cho Y, Moseley DJ, Siewerdsen JH, Jaffray DA (2005) Accurate technique for complete geometric calibration of cone-beam computed tomography systems. *Medical Physics* 32, 968–983 doi:10.1118/1.1869652
- [7] Claus BEH (2006) Geometry calibration phantom design for 3D imaging. *Proceedings of the SPIE* 6142, *Medical Imaging* doi:10.1117/12.652342
- [8] Mathworks. `imgaussfilt`, 2-D Gaussian filtering of images
- [9] Mathworks. `imnoise`, Add noise to image
- [10] Desbat L, Clackdoyle R, Grezes-Besset L, Mennessier C, Bricault I (2006) Cone-beam imaging of delta functions. *IEEE Nuclear Science Symposium Conference Record* 5, 2859–2863 doi:10.1109/NSSMIC.2006.356473
- [11] Clackdoyle R, Mennessier C (2011) Centers and centroids of the cone-beam projection of a ball. *Physics in Medicine and Biology* 56, 7371–7391 doi:10.1088/0031-9155/56/23/003

- [12] Deng L, Xi X, Li L, Han Y, Yan B (2015) A method to determine the detector locations of the cone-beam projection of the balls ' centers. *Physics in Medicine and Biology* 60, 9295–9311 doi:10.1088/0031-9155/60/24/9295
- [13] BIPM JCGM 101 (2008) Evaluation of measurement data — Supplement 1 to the “Guide to the expression of uncertainty in measurement” — Propagation of distributions using a Monte Carlo method (Geneva: International Organization for Standardization)
- [14] Doherty J, Hunt RJ (2009) Two statistics for evaluating parameter identifiability and error reduction. *Journal of Hydrology* 366, 119–127 doi:10.1016/j.jhydrol.2008.12.018
- [15] Hunyadi L (2014) Fitting quadratic curves and surfaces. MATLAB Central File Exchange



# Chapter 5

## Experimental validation of the geometrical measurement procedure

The reference object and geometrical measurement procedure described in chapter 4 are applied to the TORATOM (Twinned ORthogonal Adjustable TOMograph) experimental CT system at the Centre of Excellence Telč, Institute of Theoretical and Applied Mechanics, v.v.i, Czech Academy of Sciences (henceforth referred to by the abbreviation CET). Certain considerations in the practical implementation of this procedure, namely the number of acquired radiographic projection images and the way with which the reference object is rotated (i.e. stepped or continuous), are investigated to provide an indication of robustness for the geometrical measurement procedure. The geometry of the experimental system aligned roughly with an established TORATOM procedure (henceforth referred to as the 'initial' system geometry) is measured. Misalignments in the initial geometry are reduced by applying a series of physical adjustments to bring the instrument to its aligned state. CT measurements of a separate validation object are performed under initial and adjusted geometries. Dimensional measurements from both reconstructed datasets are compared to determine the efficacy of the geometrical measurement procedure to correctly inform the physical adjustment of the system to its aligned state. The content in this chapter is reproduced from [1].

### 5.1 Reference object

The reference object presented in [2] is used in this experimental study. The CT<sup>2</sup> reference object consists of 49 high X-ray absorption spheres of 2.5 mm diameter fixed to a hollow, cylindrical carbon fiber support (figure 5.1). Carbon fiber is chosen as the support material due its relatively low X-ray absorption, providing high contrast in the radiographic imaging of the spheres for visual detection. The spheres are arranged in 10 circular trajectories at various heights along the central axis of the cylindrical support. An additional marking sphere is included in the top circular trajectory to break the symmetry and facilitate sphere identification in the radiographs. Sphere locations were chosen to reduce the number of overlaps in their cone-beam projections at the highest magnification position of the reference object while ensuring the full inclusion of all spheres in the detector field of view. The three-dimensional  $(x, y, z)$  coordinate position of each sphere center  $m$  was measured on a tactile CMM system with a maximum permissible error (MPE) of  $2 + L/300 \mu\text{m}$ , where  $L$  is the measured length in millimeters. It should be noted that only  $M = 48$  spheres are used in the geometrical measurement procedure due to erroneous measurement of the center position of the marking sphere. The set of sphere center coordinates in the object's local frame  $(x_m, y_m, z_m)_{m=1,3,\dots,48}$  constitute the dimensional reference for measurement of the CT geometrical parameters.

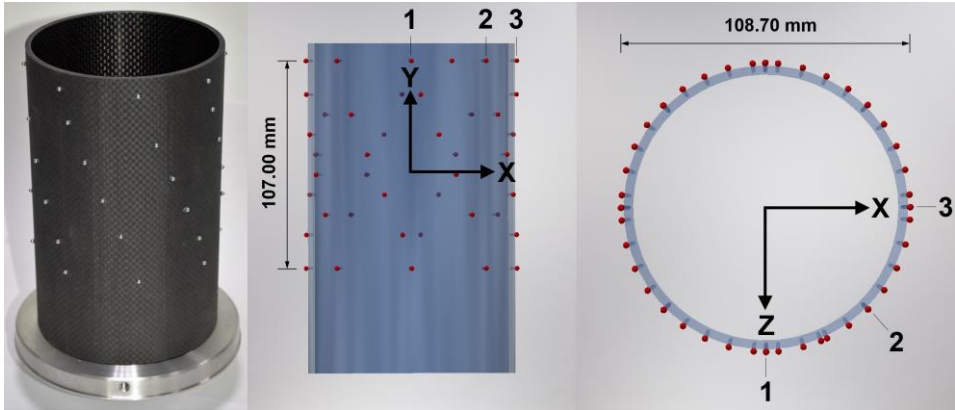


Figure 5.1. The Computed Tomography Calibration Tube ( $CT^2$ ) and local coordinate frame. The marking sphere is not included in the geometrical measurement procedure.

## 5.2 Experimental CT instrument

The TORATOM CT system at the CET (figure 5.2) is a patented, multi-purpose instrument comprising two orthogonal, independent X-ray imaging structures. Each structure consists of its own X-ray source and detector. An Aerotech APR150DR rotary stage (Aerotech Inc., USA) is shared by both structures. In this study, only one of the X-ray imaging structures was used, so only its technical specifications are provided. More information on the complete TORATOM CT system is given in [3]. The utilized X-ray imaging structure is equipped with an X-ray WorX XWT-240-SE (X-RAY WorX GmbH, Germany) X-ray source operated for all measurement tasks at 100 kV maximum tube acceleration voltage. Filament current was set to 400  $\mu$ A for the tests in section 5.3 and 380  $\mu$ A for the tests in section 5.4. A Perkin Elmer XRD1622 (Perkin Elmer Inc., USA) flat-panel detector with Gadolinium oxysulfide (Gadox) scintillator is used to acquire radiographic images. The detector consists of a 2048  $\times$  2048 array of square pixels, each 200  $\mu$ m in size (side lengths). For all measurements, radiographs were acquired with 1000 ms (1 s) exposures for the tests in section 5.3 and 1200 ms (1.2 s) exposures for the tests in section 5.4. Effects due to non-uniformities in the imaging system, for example in the intensity of the emitted beam and in the pixel response, and detector noise are reduced by flat-field correction (see, e.g. [4]), implemented after acquiring all projections.

Positioning of the instrument components is controlled by way of separate kinematic systems (figure 5.3). The positions of X-ray source and detector can be adapted along three directions in their local Cartesian coordinate axes, while the rotary stage can be positioned along the longitudinal axis between the source and detector and along its vertical  $Y_R$  direction. Note that, in the case of a misaligned system, the longitudinal axis does not coincide with the magnification axis. Transverse positioning of the detector, i.e. along  $X_D$  and  $Y_D$ , and X-ray source position along  $X_S$  can be adjusted in increments of 1  $\mu$ m, while positioning of the other axes can be adjusted in increments of < 10  $\mu$ m. The longitudinal ( $Z_R$ ) position of the rotary stage, approximately corresponding to the source-to-rotation axis distance (SRD), was chosen to maximize the coverage of the projected reference object in the detector field of view. The position of the rotary stage was kept fixed throughout the experiments in order to avoid positioning errors.

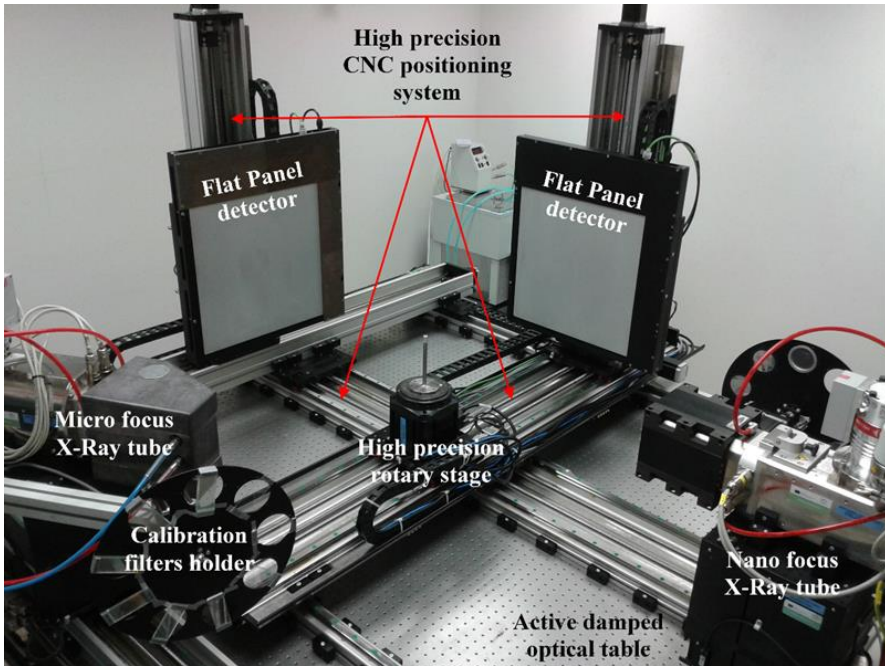


Figure 5.2. The TORATOM (Twinned Orthogonal Adjustable TOMograph) experimental CT system.

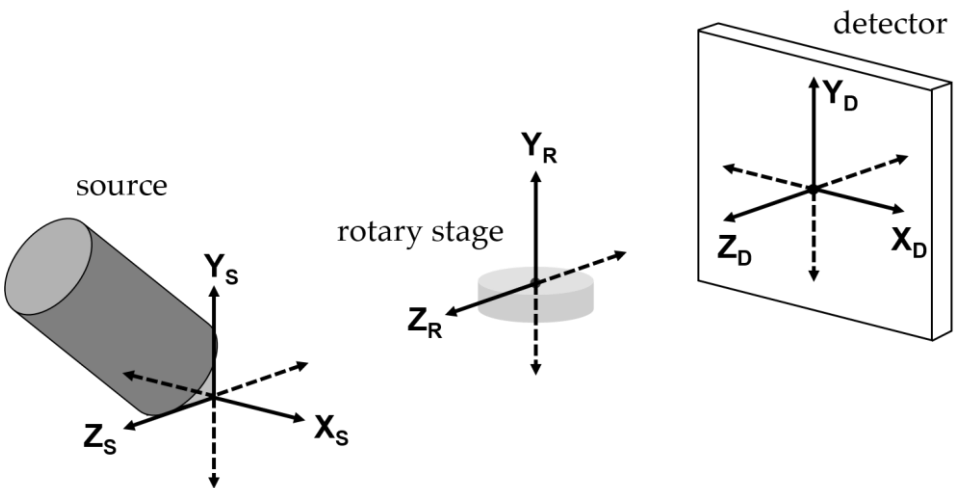


Figure 5.3. Kinematic positioning of the X-ray source, rotary stage, and flat-panel detector for the utilized X-ray imaging structure on the TORATOM CT system at CET.

While the in-plane rotation of the detector ( $\eta$ ) can be controlled by a stepper motor, the system does not have motorized units for controlling out-of-plane rotations of the detector ( $\varphi$  and  $\theta$ ). Therefore, in order to change the slant and tilt of the detector, metal washers of a specific thickness were placed between the detector and its mount at a certain distance from a pivot point. An example of modifying the detector tilt  $\theta$  is shown in figure 5.4.

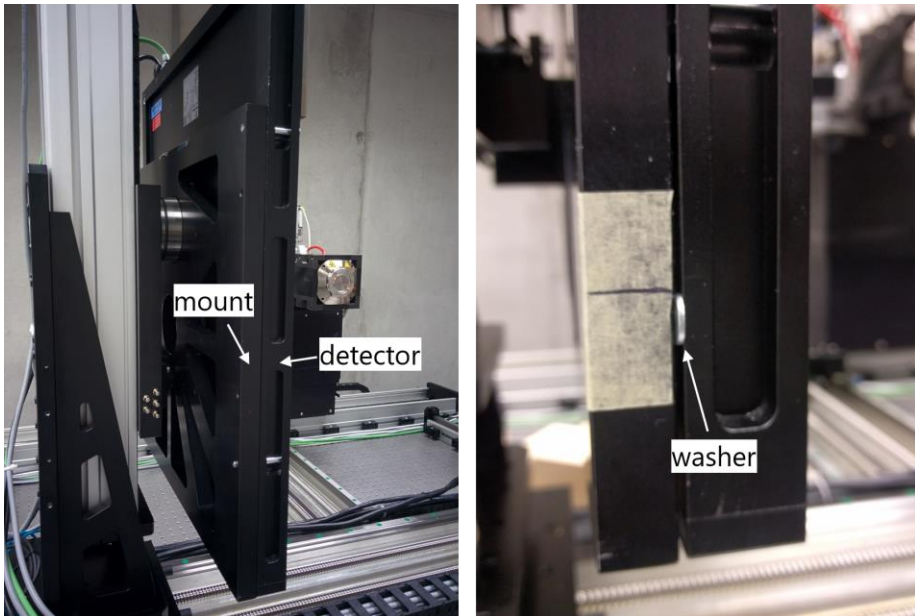


Figure 5.4. Modification of the detector orientation by inserting metal washers.

The alignment procedure currently implemented at CET consists of placing a metal rod of known diameter on the rotary stage and acquiring radiographic images. The rotary stage is then moved to a second position along the longitudinal direction and the procedure is repeated. Analysis of the acquired radiographs provides estimates for the CT instrument geometry, namely rotary stage position, detector position, and in-plane rotation of the detector.

### 5.3 Robustness testing

Generally, the robustness of a solution to a mathematical problem can be improved by increasing the number of input data points [5]. In this minimization problem, the number of data points can be increased by increasing the number of spheres in the reference object, decreasing the number of projected sphere overlaps, and increasing the number of rotation positions of the sample stage at which radiographic projections of the reference object are acquired. The number of spheres in the CT<sup>2</sup> reference object was maximized while also ensuring minimal occurrence of overlaps in the sphere projections. This means that, for the current reference object, only increasing the number of radiographic projections will provide a larger number of data points. However, the time required for acquisition and subsequent processing of radiographs will also increase with more radiographs.

Rotation of the reference object during radiographic acquisition can be either stepped or continuous. In stepped rotation, radiographs are acquired while the sample stage is stopped at the corresponding rotation angle. In continuous rotation, the stage is continuously rotating during data acquisition. Data acquisition by stepped rotation typically takes more time than the same data acquisition with continuous rotation. Furthermore, some rotation stages can exhibit larger angular indexing errors in stepped rotation than in continuous rotation. However, acquiring projections while the stage is continuously rotating can introduce blur in the imaged features, particularly when the rotation results in lateral motion of the feature with respect to the detector plane, i.e. not towards or away from the detector plane; these effects worsen

with longer exposures of the detector. In this section, the robustness of the geometrical measurement procedure is tested with respect to the number of acquired radiographs and to the rotation mode.

### 5.3.1 Number of projections

Saturation of data can occur for a “threshold” number of data points, above which the robustness of the solution is not improved, e.g. due to noise in the data. In this case, any additional projections of the reference object would not contribute to a more accurate estimation of geometrical parameters and would only increase time and effort for the user. Geometrical measurement was performed on the initial system geometry using various numbers of stepped angular positions of the reference object; a minimum of two projections is necessary to solve for rotary stage position  $z_R$ . The solved geometrical parameter values are presented for each acquisition in table 5.1 and in figure 5.5. Solved parameters for 5 or more projections were relatively consistent. The plots in figure 5.5 show that most results begin to diverge for acquisitions below 30 projections. Furthermore, the coupling between Z positions of rotation axis and detector discussed in [6] is also present in these experimental results, as shown by the simultaneous increase or decrease in solved values for both variables in figure 5.5, middle.

The distribution of reprojection errors, i.e. errors between modelled and observed sphere center projection coordinates, over all data points (all projected spheres at all projections) can also provide an indication of the robustness of the measurement procedure. In table 5.2, 95 % of the observed reprojection errors are presented by the 2.5 % and 97.5 % quantiles, corresponding to the lower and upper bounds of the coverage interval, for each acquisition. Reprojection errors are presented separately for each projected sphere center coordinate in figure 5.6:  $U_{2.5\%}$  and  $U_{97.5\%}$  correspond to the 2.5 % and 97.5 % quantiles, respectively, for the horizontal (U) coordinate, while  $V_{2.5\%}$  and  $V_{97.5\%}$  correspond to the 2.5 % and 97.5 % quantiles, respectively, for the vertical (V) coordinate. Histograms of the U and V coordinate reprojection errors from the 720 projection acquisition are presented in figure 5.7; this plot will serve as a reference for the reprojection error histograms from continuous rotation (figure 5.8). Dotted vertical lines in the histogram plots denote the lower and upper bounds corresponding to the 2.5 % and 97.5 % quantiles, respectively, containing 95 % of the reprojection error values.

Table 5.1. Solved instrument geometrical parameters for various numbers of stepped projections of the reference object.

#Proj.	$x_D$ /mm	$y_D$ /mm	$z_D$ /mm	$z_R$ /mm	$\theta$ /°	$\varphi$ /°	$\eta$ /°
2	0.0532	-0.5200	-1214.7514	-400.9991	0.2510	0.0850	-0.1079
5	0.0500	-0.4780	-1214.5483	-400.9489	0.2391	0.0821	-0.1070
10	0.0503	-0.4633	-1214.5484	-400.9518	0.2405	0.0814	-0.1069
15	0.0506	-0.4554	-1214.5575	-400.9550	0.2412	0.0810	-0.1068
30	0.0510	-0.4509	-1214.5439	-400.9513	0.2411	0.0803	-0.1068
45	0.0511	-0.4503	-1214.5441	-400.9514	0.2408	0.0801	-0.1068
90	0.0512	-0.4488	-1214.5418	-400.9507	0.2407	0.0800	-0.1068
180	0.0511	-0.4490	-1214.5489	-400.9531	0.2410	0.0795	-0.1068
360	0.0511	-0.4491	-1214.5482	-400.9531	0.2409	0.0795	-0.1068
720	0.0511	-0.4488	-1214.5480	-400.9530	0.2409	0.0793	-0.1068
1440	0.0512	-0.4483	-1214.5468	-400.9527	0.2410	0.0794	-0.1068
2880	0.0512	-0.4482	-1214.5464	-400.9526	0.2410	0.0793	-0.1068

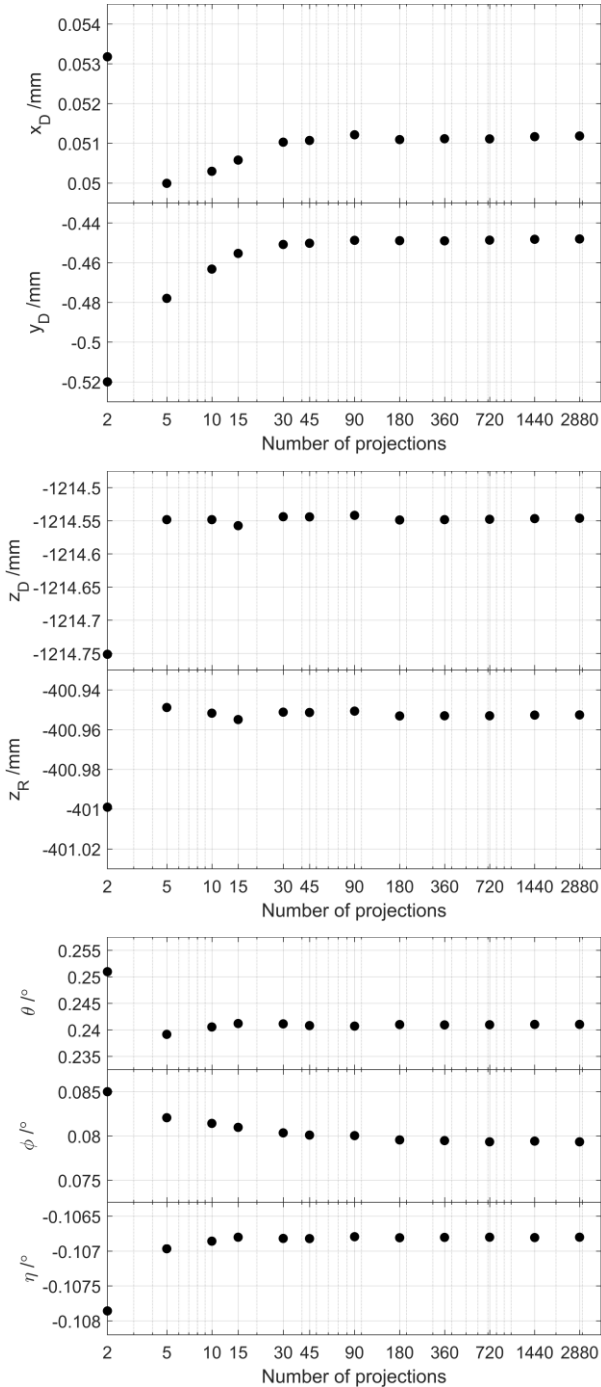


Figure 5.5. Comparison of solved instrument geometrical parameters for various numbers of stepped projections. Top: Detector lateral positions  $x_D$  and  $y_D$ . Center: Detector longitudinal position  $z_D$  and rotary stage position  $z_R$ . Bottom: Detector orientation  $\theta$ ,  $\phi$ , and  $\eta$ . Plot horizontal axes are logarithmic for better visualization of results.

Experimental validation of the geometrical measurement procedure

Table 5.2. Comparison of reprojection error 2.5 % quantiles ( $U_{2.5\%}$  and  $V_{2.5\%}$ ) and 97.5 % quantiles ( $U_{97.5\%}$  and  $V_{97.5\%}$ ) for various numbers of stepped projections. All values are in pixels.

# Proj.	$U_{2.5\%}$	$U_{97.5\%}$	$V_{2.5\%}$	$V_{97.5\%}$
2	-0.1254	0.1632	-0.0820	0.1269
5	-0.1763	0.1692	-0.1204	0.1381
10	-0.1801	0.1728	-0.1241	0.1334
15	-0.1760	0.1771	-0.1259	0.1313
30	-0.2051	0.1781	-0.1271	0.1237
45	-0.2049	0.1770	-0.1311	0.1300
90	-0.2094	0.1734	-0.1277	0.1251
180	-0.2110	0.1740	-0.1274	0.1245
360	-0.2095	0.1746	-0.1265	0.1234
720	-0.2104	0.1757	-0.1265	0.1243
1440	-0.2112	0.1762	-0.1266	0.1240
2880	-0.2116	0.1767	-0.1265	0.1243

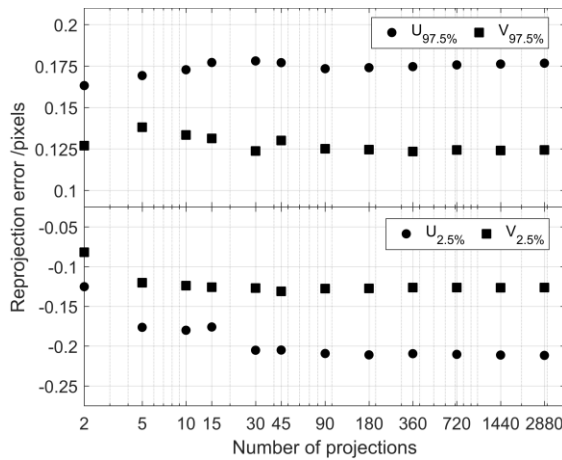


Figure 5.6. Reprojection error quantiles plotted as a function of number of stepped projections. Top: 2.5 % quantiles ( $U_{2.5\%}$ ) and 97.5 % quantiles ( $U_{97.5\%}$ ) for U coordinate reprojection error. Bottom: 2.5 % quantiles ( $V_{2.5\%}$ ) and 97.5 % quantiles ( $V_{97.5\%}$ ) for V coordinate reprojection error.

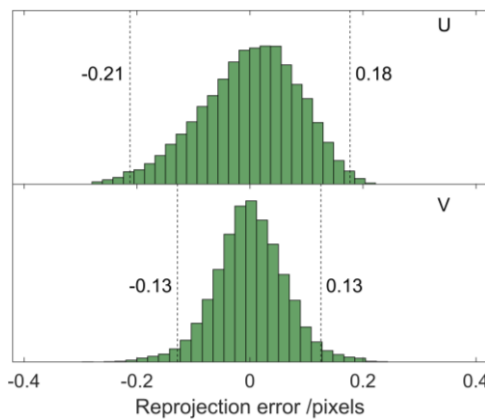


Figure 5.7. Reprojection error histograms for acquisition of 720 stepped projections of the reference object. Top: Reprojection errors in U coordinate. Bottom: Reprojection errors in V coordinate. The 95 % confidence intervals are shown by dotted lines, corresponding to the 2.5 % and 97.5 % quantiles.

Using at least 5 projections resulted in small differences of the solved parameters, indicating the robustness of the geometrical measurement procedure. Lower reprojection errors for fewer projections could be a result of the smaller sample size and not necessarily an indication that the corresponding solved parameters are more robust.

### 5.3.2 Continuous rotation

The effects of rotation mode are investigated for three speeds of continuous rotation: 0.125, 0.25, and 0.5 degrees per second. For each rotation speed, 720 projections of the reference object are acquired. Solved parameter values from minimization applied to the radiographs of the reference object acquired under continuous rotation are presented in table 5.3. The values from the 720-projection stepped acquisition are included for comparison. Change between continuous and stepped solved values is shown as percent in the parentheses. The largest relative deviations occur for  $x_D$  and  $\eta$ . No discernible trend, e.g. divergent parameter values, is observed as a function of rotation speed. Coupling between the Z positions of rotary axis and detector is present in the data from continuous rotation, as is indicated by the simultaneous increase or decrease in the solved values of both variables.

Table 5.3. Solved CT geometrical parameters from 720 projections of the reference object acquired with three continuous rotation speeds: 0.125, 0.250, 0.500 degrees per second. The solved parameters from stepped acquisition of 720 projections are provided for comparison and change from stepped is shown in percent within the parentheses. The range of solved parameters from continuous rotation is also shown.

Speed /°·s <sup>-1</sup>	$x_D$ /mm	$y_D$ /mm	$z_D$ /mm	$z_R$ /mm	$\theta$ /°	$\varphi$ /°	$\eta$ /°
<b>Stepped</b>	0.0511	-0.4488	-1214.5480	-400.9530	0.2409	0.0793	-0.1068
<b>0.125</b>	0.0711 (39.1 %)	-0.4576 (2.0 %)	-1214.5557 (< 0.1 %)	-400.9608 (< 0.1 %)	0.2425 (0.7 %)	0.0785 (1.0 %)	-0.1126 (5.4 %)
<b>0.250</b>	0.0606 (18.6 %)	-0.4553 (1.4 %)	-1214.6186 (< 0.1 %)	-400.9837 (< 0.1 %)	0.2420 (0.5 %)	0.0798 (0.6 %)	-0.1175 (10.0 %)
<b>0.500</b>	0.0687 (34.4 %)	-0.4496 (0.2 %)	-1214.5854 (< 0.1 %)	-400.9682 (< 0.1 %)	0.2418 (0.4 %)	0.0795 (0.3 %)	-0.1272 (19.1 %)
<b>Range</b>	0.0105	0.0080	0.0629	0.0228	0.0007	0.0014	0.0146

Histograms for the reprojection errors under continuous rotation of the reference object are presented in figure 5.8. Dotted vertical lines in the histogram plots denote the lower and upper bounds corresponding to the 2.5 % and 97.5 % quantiles, respectively, containing 95 % of the reprojection error values. Center projection errors are larger than the center projection errors in stepped acquisition and increase with speed of rotation, which is particularly noticeable for the horizontal (U) coordinate errors.

A systematic behavior is observed when plotting center projection errors for spheres 4 and 6 as a function of rotation angle for each continuous rotation speed (figure 5.9). The largest errors in horizontal U pixel coordinate occur when the sphere is closest to the source and, to a lesser extent, when the sphere is closest to the detector (figure 5.10, top). These locations correspond to the motion of the sphere being almost entirely horizontal with respect to the detector field of view. At the  $\alpha \approx 0^\circ$  position, movement on

the detector of sphere 6 is to the left (if facing the detector from the source), while the movement is to the right when the sphere is at the  $\alpha \approx 180^\circ$  position. The largest errors in vertical V pixel coordinate occur when the sphere movement is either towards or away from the detector, which nominally should correspond to the sphere 6 rotation positions  $\alpha \approx 90^\circ$  and  $\alpha \approx 270^\circ$ . However, at these rotation positions, sphere 6 also experiences center projection errors of similar magnitude due to the uneven background intensities from the carbon fiber support discussed in the previous section. Therefore, the maxima and minima of V pixel coordinate errors for sphere 6 are offset to correspond to the superposition of blurring from the continuous sphere movement during the radiographic exposure and errors due to uneven background intensities (figure 5.10, bottom). Similar behaviors are observed for other spheres in the reference object.

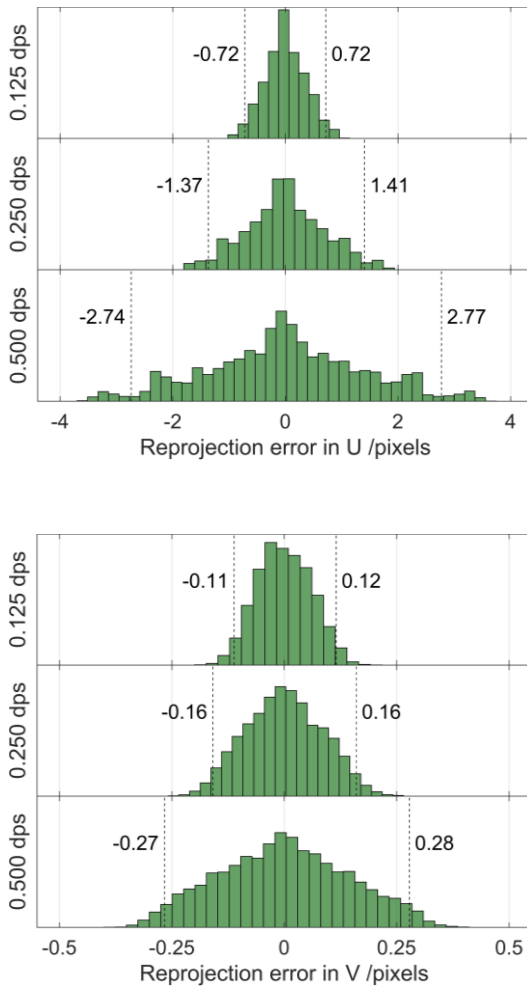


Figure 5.8. Histograms of reprojection errors for three continuous rotation speeds: 0.125, 0.25, and 0.5 degrees per second. Left: Reprojection errors in U coordinate. Right: Reprojection errors in V coordinate. The 95 % confidence intervals are shown by dotted lines, corresponding to the 2.5 % and 97.5 % quantiles.

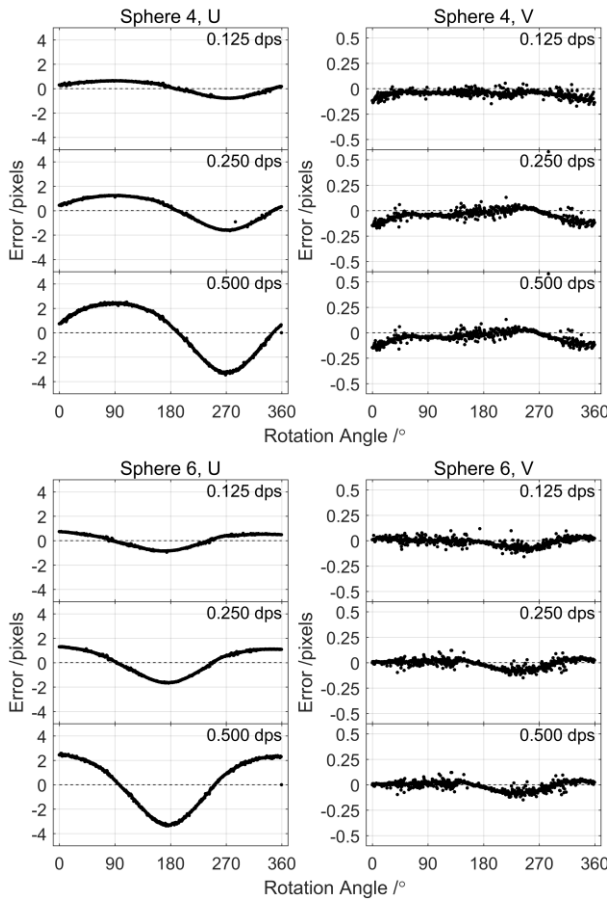


Figure 5.9. Error between minimized and observed center projection coordinates for sphere 4 (left) and sphere 6 (right) at three continuous rotation speeds: 0.125, 0.25, and 0.5 degrees per second. Sphere 4 is closest to the detector at rotation angle  $90^\circ$  and closest to the X-ray source at rotation angle  $270^\circ$ . Sphere 6 is closest to the detector at  $0^\circ$  and closest to the X-ray source at  $180^\circ$ .

The indexed rotation angle associated with a radiograph corresponds to the angle at the beginning of its exposure. Given a finite exposure, the acquired radiograph images the sphere as it moves from its position at the indexed rotation angle to its position at the end of the exposure. The acquired radiograph can therefore be considered an integral over many infinitesimally short exposures of the sphere as it moves away from its initial position at the beginning of the exposure, thereby resulting in a blurred image of the sphere (see figure 5.11, left for a magnified view of projected sphere 6 at its  $180^\circ$  position under each rotational speed). This blur is not symmetrical about the indexed angle associated with the exposure (figure 5.11, right), which results in an offset of the observed center projection coordinate from image analysis with respect to the modelled coordinate (which corresponds to the center projection at the beginning of the exposure). In fact, the discrepancy between the angle of rotation at the beginning of exposure and the continually moving sphere is indicated by the increase in solved reference object rotation position about the Y axis  $\rho_Y$  at the beginning of the scan, i.e.  $\alpha = 0^\circ$ , with increased rotation speed (table 5.4). Reducing the exposure time of the detector can theoretically reduce the effects of the moving sphere. However, the 1000 ms exposure time of the detector was not changed due to limitations in image buffering and transfer. Furthermore, shorter detector exposures reduce the signal-to-noise ratio.

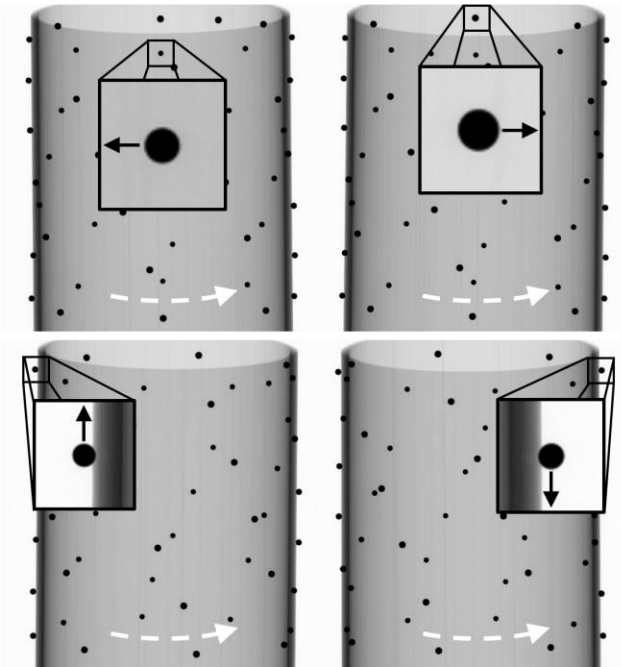


Figure 5.10. (Top) The largest errors in the U coordinate of the observed center projection occur when the sphere is closest to the source and, to a lesser extent, when the sphere is closest to the detector. (Bottom) The largest errors in the V coordinate of the observed center projection occur when the sphere motion is either towards or away from the detector, which corresponds to the sphere being at its furthest extent from the detector central column. Dashed arrows indicate direction of stage rotation.

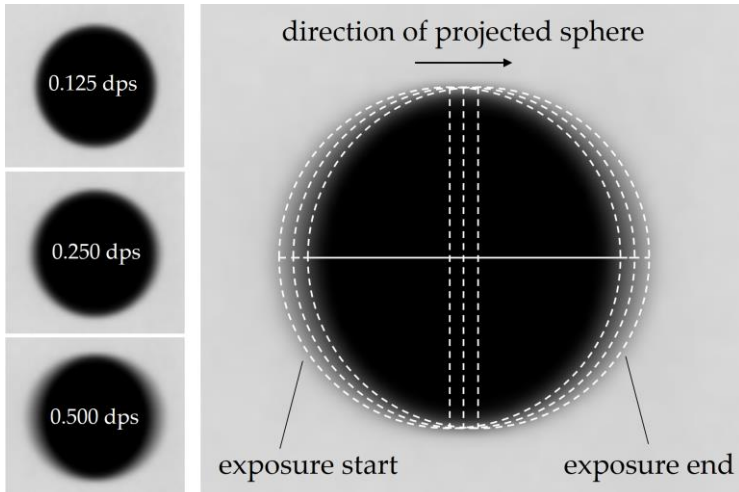


Figure 5.11. Under continuous rotation, the projected spheres exhibit increased blur, particularly when they are positioned closest to and furthest from the detector. At these locations, the lateral movement of the sphere with respect to the detector plane is highest. Left: magnified views of projected sphere 6 are shown for the three continuous rotation speeds. Right: the resulting offset between observed and modelled center projection coordinates is due to the continuous movement of the projected sphere from its indexed position in the model, which corresponds to the start of the exposure.

Table 5.4. Variation in solved initial (rotation position  $\alpha = 0^\circ$ ) orientation of the reference object about the Y axis  $\rho_Y$  due to changing speed of continuous rotation.

$\rho_Y / ^\circ$	Speed of continuous rotation		
	0.125 dps	0.250 dps	0.500 dps
	0.4453	0.7319	0.9553

## 5.4 Instrument adjustment

The output of the geometrical measurement procedure can be used to inform the re-alignment of the CT system by adjustment, i.e. mechanical re-positioning. Upon arrival on a second visit to CET, the geometry of the CT system was measured using 720 stepped projections of the CT<sup>2</sup> reference object. The output of this initial measurement is shown in table 5.5. Given the measured misalignments, adjustments were made to the out-of-plane detector orientation ( $\theta, \varphi$ ) and lateral position ( $x_D, y_D$ ) to bring the system to approximately ideal alignment. Lateral position were adjusted using the dedicated controllers, while detector out-of-plane rotations were adjusted by inserting washers between the detector frame and its mount (described in section 5.2). In-plane rotation was not intentionally adjusted since this misalignment is easily corrected in typical reconstruction software. Parameters  $z_D$  and  $z_R$  do not have dedicated aligned values, they need only be known accurately. The measured geometrical parameters after adjustment are also shown in table 5.5.

Table 5.5. Measured geometrical parameters upon arrival to CET ('initial') and after adjustment ('adjusted'). Ideal alignment is given when  $x_D, y_D, \theta, \varphi$ , and  $\eta$  are zero. The values for  $z_D$  and  $z_R$  do not have ideal values, yet their values in the backprojection step need to be consistent with their actual values. For this purpose, the accurate measurement of their quantity is critical.

System alignment	Geometrical parameters						
	$x_D$ /mm	$y_D$ /mm	$z_D$ /mm	$z_R$ /mm	$\theta$ /°	$\varphi$ /°	$\eta$ /°
Initial	-0.1116	0.1498	-1208.6387	-398.4272	0.2329	0.0798	0.0092
Adjusted	0.0011	-0.0055	-1207.5453	-398.4683	0.0019	-0.0080	0.0117

To validate the performance of the output from the geometrical measurement procedure to inform the adjustment of the CT instrument, the X-plate validation object (figure 5.12) is CT measured in the initial and adjusted geometries. The X-plate consists of 15 grade 20 [7] chrome steel spheres of 2.5 mm diameter arranged in a dedicated manner on a carbon fiber plate. Sphere center positions in a local coordinate frame were measured by Nikon Altera CMM with a MPE of  $2 + L/400 \mu\text{m}$ , where L is the measured length in millimeters. Acquisitions of 1440 projections of the X-plate are performed at the same sample stage position for which the instrument geometries were measured. The X-plate is reconstructed from initial and adjusted acquisitions with Inspect-X reconstruction software (Nikon Metrology). The values for SRD, source-to-detector distance (SDD), and voxel size in reconstruction of the initial dataset were set to the values estimated at CET using their procedure (see section 5.2). In the reconstruction of the adjusted dataset, SRD and SDD were set to the measured  $z_R$  and  $z_D$ , respectively, and the voxel size was calculated accordingly. Dual center of rotation estimation in Inspect-X is applied in reconstructions to estimate in-plane rotation and lateral position of the projected axis of rotation (approximately equivalent to the parameters  $\eta, x_D$ , and  $y_D$  in this study).

Discrepancies between SRD and SDD specified in the reconstruction metafile (used to define pre-weighting and backprojection geometry) and the effective SRD and SDD in the instrument can be partially corrected by implementing voxel rescaling [8]. Voxel rescaling factors are determined for each acquisition

from sphere center-to-center distance measurements on the nominally-reconstructed CT<sup>2</sup> reference object from the same acquisition geometry. The scaling factors are 0.993839 and 0.999987 for initial and adjusted geometries, respectively. Applying voxel rescaling to the adjusted dataset did not produce significant differences to the CT measurements; therefore, these results are not presented. CT measurements of the X-plate from initial acquisition without and with voxel rescaling (henceforth 'initial' and 'rescaled', respectively) are compared to the same CT measurements from the adjusted acquisition. The reconstructed three-dimensional grey value models are segmented into iso-surfaces by applying advanced local thresholding in VGStudio MAX 3.0 (Volume Graphics, GmbH). The iso-surfaces are converted to point clouds of three-dimensional surface coordinates by applying surface sampling at intervals of 1 voxel along each coordinate direction. The cloud of point coordinates is further analyzed in MATLAB (Mathworks, Inc). For each sphere in the reconstructed workpiece, a sphere is least-squares fit to the point coordinates belonging to the surface of that sphere. Sphere fit parameters are used to perform dimensional measurements on the reconstructed X-plate.

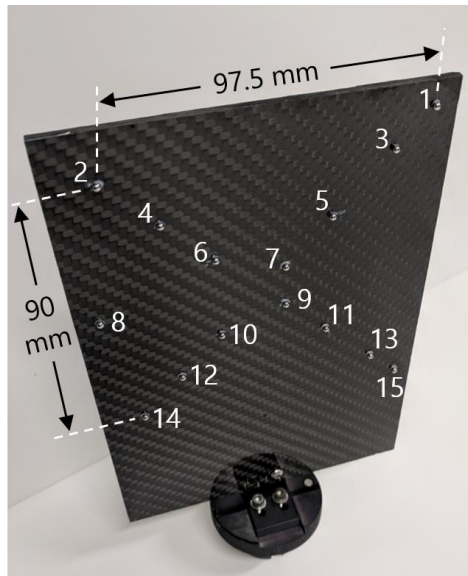


Figure 5.12. The X-plate validation object.

The distance between sphere fit centers is measured for all combinations of sphere pairs in nominal, rescaled, and adjusted reconstructed datasets and compared. Center-to-center distance (C2C) errors relative to the CMM measured reference distances are shown in figure 5.13 (top). As expected, rescaling removes length dependent errors, resulting in a reduction of maximum C2C errors from 843  $\mu\text{m}$  in the initial dataset to approximately 82  $\mu\text{m}$  in the rescaled dataset. Adjustment reduces the maximum C2C error to under 20  $\mu\text{m}$ . Sphere fit radius errors relative to the nominal radius are presented in figure 5.13 (middle). Rescaling reduces sphere fit radius errors from initial dataset by approximately 7  $\mu\text{m}$ , from approximately 20  $\mu\text{m}$  to approximately 13  $\mu\text{m}$ . While the magnitude of sphere fit radius errors were not significantly changed after adjustment, the variation in errors was reduced from 3.64  $\mu\text{m}$  and 3.73  $\mu\text{m}$  in initial and rescaled datasets, respectively, to 2.87  $\mu\text{m}$  in the adjusted dataset. Reconstructed sphere form is presented in figure 5.13 (bottom) as the distribution of sphere fit residuals over all spheres in histogram form. The vertical dashed lines are the 2.5 % and 97.5 % quantiles, corresponding to the lower and upper boundaries, respectively, of 95 % of the sphere fit residuals. Differences in sphere fit residuals are very small among datasets. This outcome is expected as it was shown in [9] that a tilt  $\theta$  of the detector (the largest angular misalignment in the initial instrument) does not significantly affect sphere form.

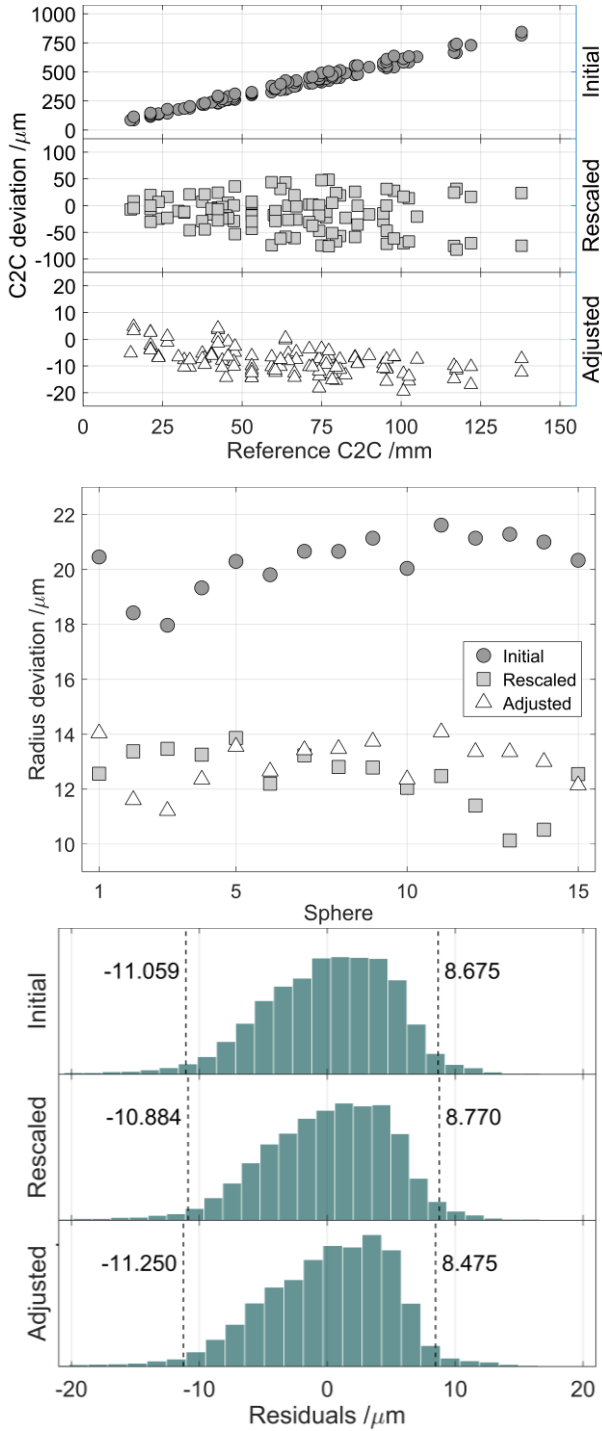


Figure 5.13. Errors in measurement of sphere C2C distances between all combinations of sphere pairs (top), sphere radius (middle), and sphere form error illustrated as histograms of sphere fit residuals (bottom) in the reconstructed X-plate under initial, rescaled, and adjusted instrument geometries.

## 5.5 Conclusion

In this study, we applied a procedure for CT geometry measurement on an experimental instrument. The measured geometry is only valid for the sample stage position in which the procedure is performed due to kinematic error motions in sample stage positioning. The development of an integrated geometrical mapping procedure for the entire CT measurement range is topic of future work. The robustness of the measurement procedure is tested with respect to the number of acquired projections and the mode with which the reference object is rotated, i.e. stepped or continuous rotation. The variances in solved parameter values from the various acquisitions of stepped projections were small. The largest deviations in solved parameter values occurred for acquisitions of less than 5 stepped projections. Reprojection errors from continuous rotation were overall larger than the reprojection errors from stepped rotation and increased with increasing rotation speed. Solved parameters from continuous rotation acquisition exhibited the largest relative deviations in detector horizontal position  $x_D$  and in-plane rotation  $\eta$ .

The output from the geometrical measurement procedure is used to inform the physical adjustment of the experimental CT system to the ideal alignment as defined for typical FDK-type reconstruction algorithms. Results from the reconstructed datasets after adjustment indicate an overall reduction of dimensional measurement errors for the X-plate validation object. Sphere center-to-center distances were reduced from a maximum of approximately 840  $\mu\text{m}$  and 82  $\mu\text{m}$  in initial and rescaled datasets, respectively, to less than 20  $\mu\text{m}$  after adjustment. These results shed light on the ineffectiveness of voxel rescaling in compensating geometrical misalignments of the CT instrument. Sphere radius errors were reduced by 7  $\mu\text{m}$  after voxel rescaling; adjustment did not provide significant improvements to the magnitude of these errors after rescaling. However, variation in sphere radius errors among all spheres was reduced from 3.73  $\mu\text{m}$  in the rescaled dataset to 2.87  $\mu\text{m}$  after adjustment. Sphere form, presented as the distribution of sphere fit residuals, was not significantly improved by either rescaling or adjustment. This observation is consistent with previous findings [9], which indicate that detector tilt  $\theta$  (the largest angular misalignment in the initial instrument geometry) does not significantly affect sphere form.

The results presented in this study indicate the robustness of the proposed procedure to measure the geometry of a CT instrument. The measured geometrical parameters were used to adjust the instrument to the ideal configuration as defined in the tomographic reconstruction algorithm. Reductions in observed dimensional errors on a separate validation object after adjustment serve as experimental validation of the effectiveness in the proposed procedure.

## References

- [1] Ferrucci M Petr Heřmánek, Evelina Ametova, Elia Sbettega, Michal Vopalensky, Ivana Kumpová, Daniel Vavřík, Simone Carmignato, Tom Craeghs, Wim Dewulf (2018) Measurement of the X-ray computed tomography instrument geometry by minimization of reprojection errors—implementation on experimental data. *Precision Engineering* 54, 107-117
- [2] Hermanek P, Ferrucci M, Dewulf W, Carmignato S (2017) Optimized reference object for assessment of computed tomography instrument geometry. 7<sup>th</sup> Conference on Industrial Computed Tomography (Leuven, Belgium)
- [3] Fíla T, Vavřík D (2016) EP 2835631 B1 A multi-axial apparatus for carrying out x-ray measurements, particularly computed tomography
- [4] Kwan ALC, Seibert JA, Boone JM (2006) An improved method for flat-field correction of flat panel x-ray detector. *Medical Physics* 33 (2), 391-393

## Chapter 5

- [5] Claus BEH (2006) Geometry calibration phantom design for 3D imaging. Proceedings of the SPIE 6142, Medical Imaging doi:10.1117/12.652342
- [6] Ferrucci M, Hermanek P, Ametova E, Carmignato S, Dewulf W (2018) Measurement of the X-ray computed tomography instrument geometry by minimization of reprojection errors—implementation on simulated data. Precision Engineering 54, 7-20
- [7] ISO 3290-1 (2014) Rolling bearings - Balls - Steel balls (Geneva: International Organization for Standardization)
- [8] Stolfi A, De Chiffre L (2016) 3D artefact for concurrent scale calibration in Computed Tomography. CIRP Annals - Manufacturing Technology 65, 499–502 doi:10.1016/j.cirp.2016.04.069
- [9] Ferrucci M, Ametova E, Carmignato S, Dewulf W (2015) Evaluating the effects of detector angular misalignments on simulated computed tomography data 45, 230-241 Precision Engineering. doi:10.1016/j.precisioneng.2016.03.001

# Chapter 6

## Uncertainty in the measured geometrical parameters

Effective correction of instrument geometrical misalignments demands calibration of the system geometry. Calibration is defined in the International Vocabulary of Metrology (VIM) [1] as the

“operation that, under specified conditions, in a first step, establishes a relation between the quantity values with measurement uncertainties provided by measurement standards and corresponding indications with associated measurement uncertainties”.

In other words, geometrical calibration consists of two steps: (1) measurement of the instrument geometry by comparison to a traceable reference and (2) assessment of uncertainty in the comparison. While the robust measurement of the instrument geometry by comparison to a traceable reference has been demonstrated (chapter 4), uncertainty in the measured parameters has yet to be assessed. Uncertainty in the measured misalignments will result in ‘residual’ uncertainty in CT measurements even after compensation. To determine this residual uncertainty, the uncertainty with which the instrument geometry is measured should be known. In this chapter, we present a statistical framework based on the Monte Carlo approach for assessing uncertainty in the measurement of instrument geometrical parameters. The framework is applied to radiographs generated under the same 10 misaligned instrument geometries presented in chapter 4, albeit without rotation stage errors. Correct implementation of the Monte Carlo approach relies on several conditions being met concerning the statistical nature of the input data. While these conditions are not met by the current estimates of center projection coordinates (from chapter 4), the proposal of such a framework for uncertainty assessment provides positive results for nominal inputs and catalyzes further research in this field.

### 6.1 Monte Carlo framework

Uncertainty in previous literature on estimation of geometrical parameters is solely calculated from uncertainty in the observed center projection coordinates [2] due to, e.g. detector noise. Other sources of error, such as uncertainty in the traceable reference features and rotation errors, are not considered. Assessment of uncertainty for quantities estimated by minimization (fitting) does not lend itself to analytical methods, such as the method described in the Joint Committee for Guides in Metrology (JCGM) 100 document [3]. A Monte Carlo approach for uncertainty assessment of the geometrical parameters solved by minimization is proposed here. Uncertainty estimation by the Monte Carlo is based on the observed distribution in the measured geometrical parameter values given a variation in the inputs (corresponding to their uncertainty intervals) for repeated measurements [4]. The Monte Carlo approach presented here is implemented on radiographs generated from the same 10 misaligned instrument geometries in chapter 4, which are revisited in table 6.1 for instrument geometrical parameters and table 6.2 for reference object geometrical parameters.

The diagram in figure 6.1 illustrates the proposed concept as it pertains to measurement of geometrical parameters by minimization. For each measurement iteration  $i = 1, 2, \dots, I$ , where  $I$  is the total number of repeated iterations of the geometrical measurement procedure, the values assigned to the input variables, i.e. local sphere center coordinates  $(x, y, z)_m$  and observed center projection coordinates  $u_{\text{obs}}(m, n), v_{\text{obs}}(m, n)$ , are sampled from distributions corresponding to the uncertainty in their values. The initial geometrical parameter values are kept constant for all Monte Carlo iterations, unlike in convergence testing (chapter 4). If rotation stage errors are considered, then their known behaviors

should be included in the modelled ray-tracing algorithm and any uncertainty in their values should also be varied according to their uncertainty, e.g. due to random components in the rotation stage errors and uncertainty in the procedure with which the systematic components were measured. Here, we do not consider rotation stage errors for simplicity.

Table 6.1. Simulated values for instrument geometrical parameters.

Simulation $s$	$x_D$ /mm	$y_D$ /mm	$z_D$ /mm	$z_R$ /mm	$\theta$ /°	$\varphi$ /°	$\eta$ /°
Nominal	0	0	-1177	-400	0	0	0
1	1.2590	-1.3700	-1175.4430	-402.5450	-0.6756	-0.0989	-0.7867
2	1.6230	1.8820	-1181.6430	-402.6760	0.5886	-0.8324	0.9238
3	-1.4920	1.8290	-1173.5090	-399.8150	-0.3776	-0.5420	-0.9907
4	1.6540	-0.0590	-1172.6600	-398.3250	0.0571	0.8267	0.5498
5	0.5290	1.2010	-1175.2130	-397.3960	-0.6687	-0.6952	0.6346
6	-1.6100	-1.4330	-1174.4230	-402.2210	0.2040	0.6516	0.7374
7	-0.8860	-0.3130	-1174.5690	-399.5870	-0.4741	0.0767	-0.8311
8	0.1880	1.6630	-1178.0780	-400.1840	0.3082	0.9923	-0.2004
9	1.8300	1.1690	-1175.4460	-402.9290	0.3784	-0.8436	-0.4803
10	1.8600	1.8380	-1180.2880	-400.9770	0.4963	-0.1146	0.6001

Table 6.2. Simulated values for reference object, i.e. 'nuisance', geometrical parameters at  $\alpha = 0^\circ$  rotation position.

Simulation $s$	$x_P$ /mm	$y_P$ /mm	$z_P$ /mm	$\rho_X$ /°	$\rho_Y$ /°	$\rho_Z$ /°
Nominal	0	0	-400	0	0	0
1	1.0051	1.3629	-400.5934	0.4121	-0.1225	-0.4479
2	-0.9796	-0.9829	-398.6767	-0.9363	-0.2369	0.3594
3	0.0238	1.2571	-399.6589	-0.4462	0.5310	0.3102
4	0.7963	-1.0259	-399.8011	-0.9077	0.5904	-0.6748
5	1.5636	1.7171	-398.3312	-0.8057	-0.6263	-0.7620
6	1.8372	-0.6001	-400.8566	0.6469	-0.0205	-0.0033
7	0.1889	-1.2136	-398.9712	0.3897	-0.1088	0.9195
8	-1.4455	-0.9957	-398.9851	-0.3658	0.2926	-0.3192
9	-1.4028	0.4642	-400.4782	0.9004	0.4187	0.1705
10	-0.9700	-0.1068	-399.7287	-0.9311	0.5094	-0.5524

The result of the Monte Carlo technique is a set of  $I$  solved values for each of the 13 geometrical parameters (7 instrument and 6 reference object parameters). The mean of the  $I$  solved values is the numerical quantity assigned to the measurement of the corresponding parameter. Uncertainty in the measured parameter values is expressed as the interval  $[a, b]$ , where  $a$  and  $b$  are the 2.5 % and 97.5 % quantiles, respectively, of the corresponding solved parameter distribution. The interval  $[a, b]$  contains 95 % of the  $I$  parameter values, and is used here instead of the commonly applied  $U = k\sigma$ , where  $\sigma$  is the standard deviation of the dataset and  $k$  is the coverage factor ( $k = 2$  corresponds to 95.45 % confidence interval), which is reserved for normally distributed datasets. In this study, the number of repeated iterations  $I$  was set to 10,000.

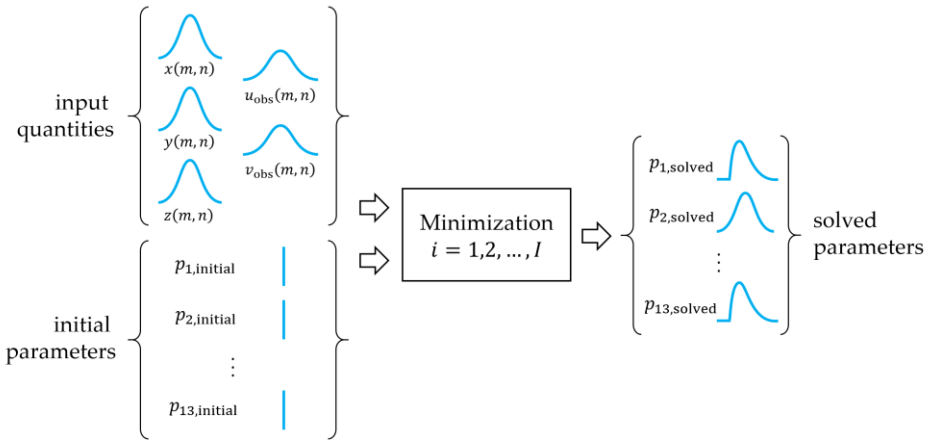


Figure 6.1. The Monte Carlo concept for evaluating uncertainty in geometrical parameters solved by minimization.

## 6.2 Input quantities

The values assigned to each input quantity for a given repeat measurement  $i$  are randomly sampled from a normal (Gaussian) distribution centered about a central value. These distributions can therefore be defined by the central value and a standard deviation  $\sigma$ . Table 6.3 outlines the distribution from which the input parameters are randomly sampled for this Monte Carlo implementation of the geometrical procedure.

Table 6.3. Uncertainty sources in Monte Carlo approach.

Uncertainty source	Mean value	Distribution	Magnitude
Sphere center coordinate	$x_{\text{nominal}}$	Gaussian	$\sigma_x = 0.603 \mu\text{m}$
	$y_{\text{nominal}}$	Gaussian	$\sigma_y = 0.603 \mu\text{m}$
	$z_{\text{nominal}}$	Gaussian	$\sigma_z = 0.603 \mu\text{m}$
Center projection coordinate	$u_{\text{exact}}$	Gaussian	$\sigma_u = 0.05 \text{ pixels}$
	$v_{\text{exact}}$	Gaussian	$\sigma_v = 0.05 \text{ pixels}$

### 6.2.1 Sphere center coordinate uncertainty

The combined uncertainty in sphere center coordinates is a result of uncertainty in the procedure with which the coordinates are measured, e.g. by tactile coordinate measuring machine (CMM). Here, the uncertainty applied in chapter 4 to perturb the simulated sphere center coordinates is used. The expanded uncertainty (Gaussian distribution with coverage factor  $k = 2$  for a 95.45 % confidence interval) expected for CMM calibration of the center-to-center length segments is  $U_{\text{CMM}}(k = 2) = 2.09 \mu\text{m}$ . The standard uncertainty value corresponding to a 68.3 % confidence interval ( $k = 1$ ), i.e.  $U_{\text{CMM}}(k = 1) = \frac{U_{\text{CMM}}(k=2)}{2}$ , is used. Calibration uncertainty corresponds to the distance from each sphere center to the origin of the reference object's local coordinate frame. This uncertainty is distributed equally to uncertainty in the individual coordinates and used to define the standard deviation of the corresponding sampling distributions.

$$U_{\text{CMM}}(k = 1) = \sqrt{\sigma_x^2 + \sigma_y^2 + \sigma_z^2}$$

$$\sigma_{x,y,z} = \sigma_x = \sigma_y = \sigma_z$$

$$U_{\text{CMM}}(k=1) = \sqrt{3\sigma_{x,y,z}^2}$$

$$\sigma_{x,y,z} = \frac{U_{\text{CMM}}(k=1)}{\sqrt{3}} = \frac{2.09 \mu\text{m}}{2\sqrt{3}} \approx 0.603 \mu\text{m}$$

### 6.2.2 Uncertainty in observed center projection coordinates

For each simulation  $i$ , the mean input center projection coordinates are given by  $\{u_{\text{exact}}(m, n), v_{\text{exact}}(m, n)\}$  for the corresponding instrument and reference object geometries. Uncertainty in each coordinate U and V can be a result of detector noise, blur, uncertainty due to ellipse fit algorithm, among others. This uncertainty contribution is defined by a Gaussian distribution with standard deviation  $\sigma_{U,V} = 0.05$  pixels. The magnitude of the uncertainty in observed center projection coordinates was defined from observations.

### 6.3 Estimation of uncertainty in geometrical parameter values

For each simulated data set  $s$ , the minimization was repeated  $I = 10,000$  times in the presence of random perturbations of the input quantities, providing a set of 10,000 values for each solved geometrical parameter. Histograms of solved parameter errors from their true simulated values for simulation 1 are shown in figures 6.2, 6.3, and 6.4 for instrument geometrical parameters and in figures 6.5 and 6.6 for reference object geometrical parameters. The dotted vertical line denotes zero error, i.e. the true simulated value. Dashed lines are the mean errors, while solid vertical lines denote the 2.5 % and 97.5 % quantiles, corresponding to the lower and upper limits, respectively, of 95 % of the observed errors. The errors in solved parameters are shown for all ten simulation data sets in figures 6.7 and 6.8; circular markers correspond to the mean solved values and the error bars contain 95 % of the observed errors (lower and upper ends of the error bars correspond to the 2.5 % and 97.5 % quantiles, respectively).

For most geometrical parameters, the distribution of  $I$  solved values was approximately symmetrical about their true simulated values and the true value was contained within the boundaries of the 95 % coverage intervals. This was not the case, however, for the Z positions of reference object  $z_p$ , axis of rotation  $z_R$ , and detector  $z_D$ ; coupling between these three parameters is present in all simulated datasets as indicated by the consistent offsets in the mean values of the solved distributions and the non-symmetrical 95 % confidence intervals about the mean values. These observations are consistent with the observations made in convergence testing (chapter 4).

The ratio of error in solved  $z_D$  and error in solved  $z_R$  from each of 10,000 repeat measurements was approximately equal to the ratio of the true simulated values of  $z_D$  and  $z_R$ . In figure 6.9, the ratios of errors in solved  $z_D$  and  $z_R$  from all 10,000 repeat measurements for simulation 1 are shown in histogram form. The dotted vertical line the ratio of the true simulated values of  $z_D$  and  $z_R$ . The dashed line is the mean ratio of solved errors in  $z_D$  and  $z_R$ , while solid vertical lines denote the 2.5 % and 97.5 % quantiles, corresponding to the lower and upper limits, respectively, of 95 % of the solved ratios. The same ratios are shown for all ten simulation data sets in figure 6.10; circular markers correspond to the mean solved errors ratio and the error bars contain 95 % of the ratios over 10,000 measurements (lower and upper ends of the error bars correspond to the 2.5 % and 97.5 % quantiles, respectively).

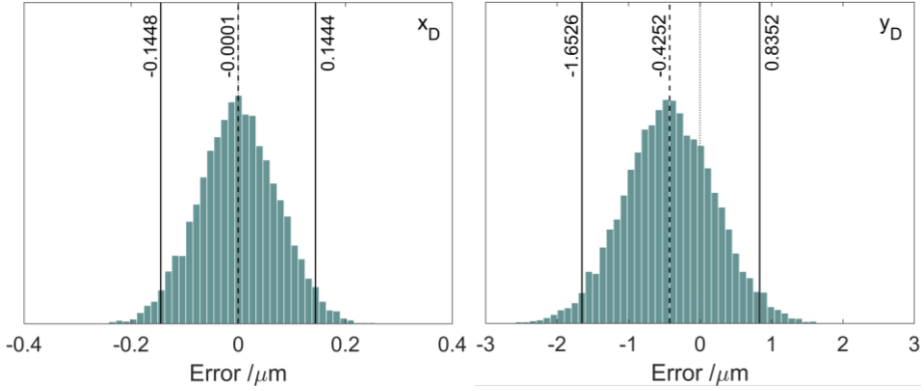


Figure 6.2. Error histograms for  $I = 10,000$  repeat measurements of detector lateral position for simulation 1. Dotted lines correspond to zero error, dashed lines correspond to the mean solved parameter value, and the solid lines correspond to the 2.5 % and 97.5 % quantiles.

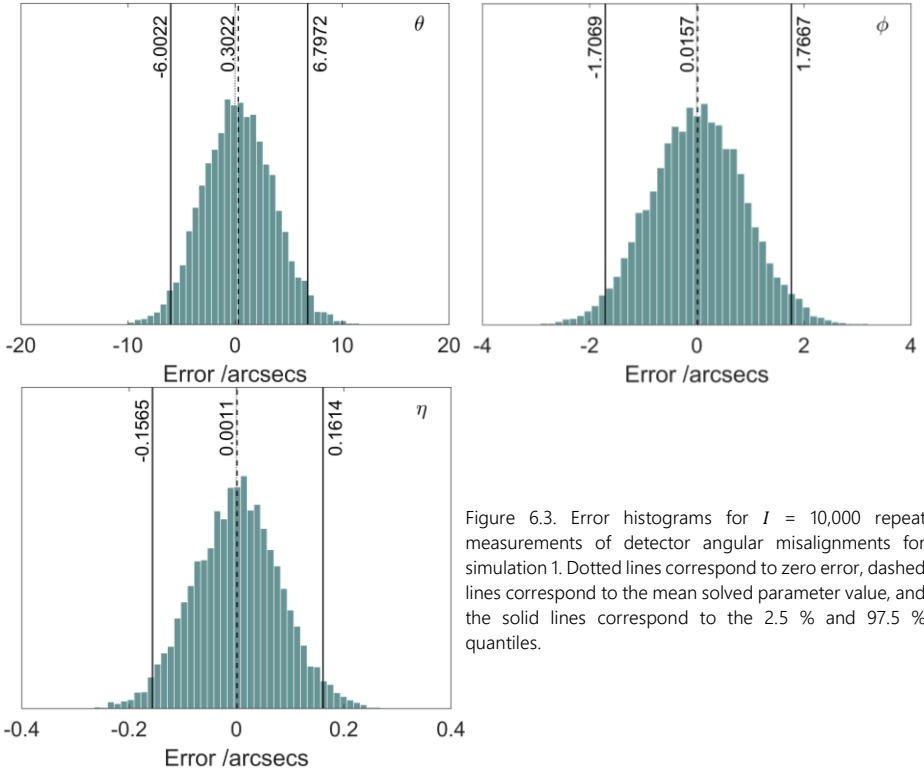


Figure 6.3. Error histograms for  $I = 10,000$  repeat measurements of detector angular misalignments for simulation 1. Dotted lines correspond to zero error, dashed lines correspond to the mean solved parameter value, and the solid lines correspond to the 2.5 % and 97.5 % quantiles.

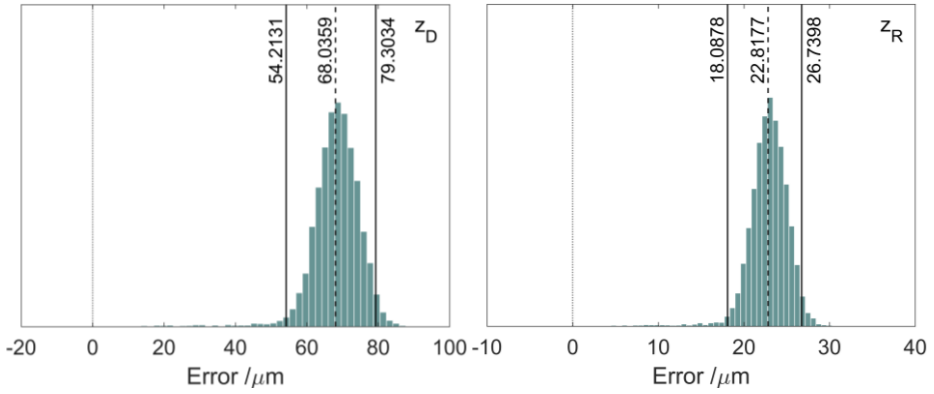


Figure 6.4. Error histograms for  $I = 10,000$  repeat measurements of detector and rotation axis longitudinal positions for simulation 1. Dotted lines correspond to zero error, dashed lines correspond to the mean solved parameter value, and the solid lines correspond to the 2.5 % and 97.5 % quantiles.

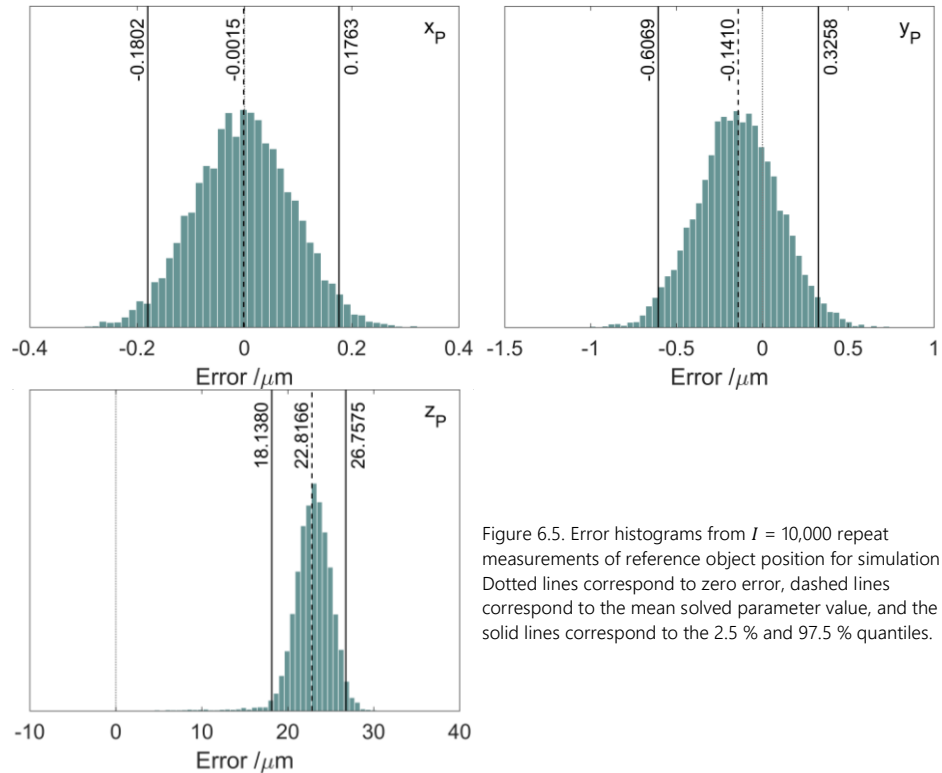


Figure 6.5. Error histograms from  $I = 10,000$  repeat measurements of reference object position for simulation 1. Dotted lines correspond to zero error, dashed lines correspond to the mean solved parameter value, and the solid lines correspond to the 2.5 % and 97.5 % quantiles.

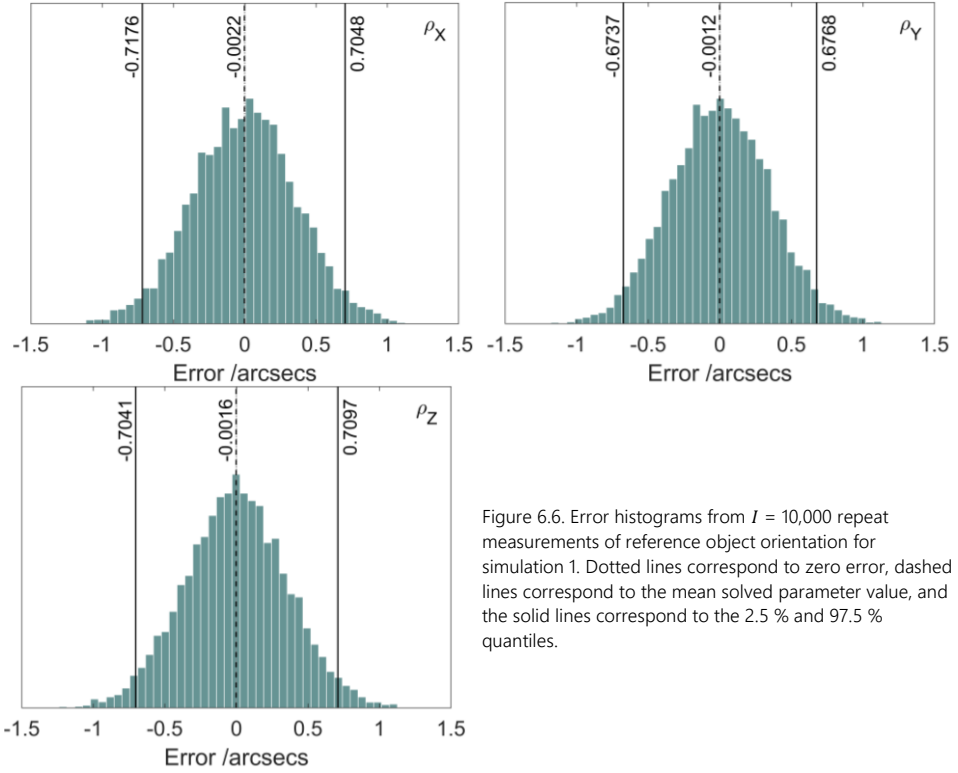


Figure 6.6. Error histograms from  $I = 10,000$  repeat measurements of reference object orientation for simulation 1. Dotted lines correspond to zero error, dashed lines correspond to the mean solved parameter value, and the solid lines correspond to the 2.5 % and 97.5 % quantiles.

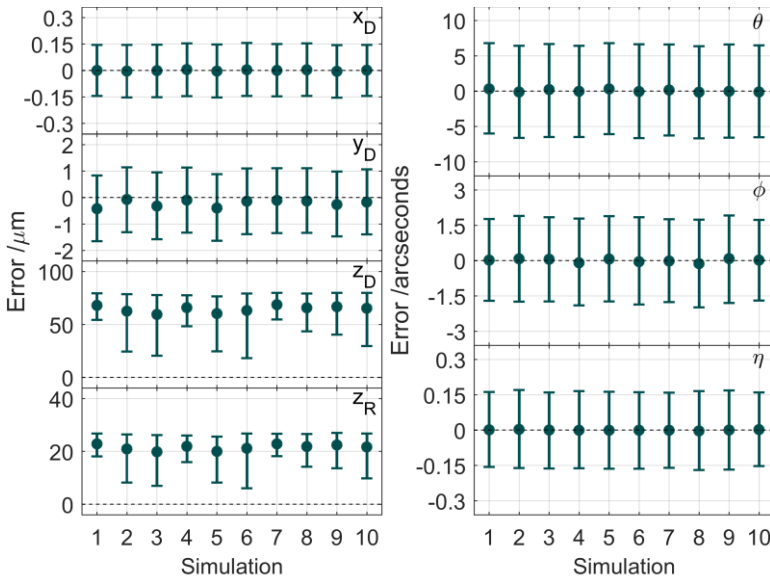


Figure 6.7. Errors in solved instrument geometrical parameters from  $I = 10,000$  repeat measurements for all simulations. The circular marker denotes the mean error, while the error bars correspond to 95 % of the solved parameter values, given by the 2.5 % (bottom) and 97.5 % (top) quantiles.

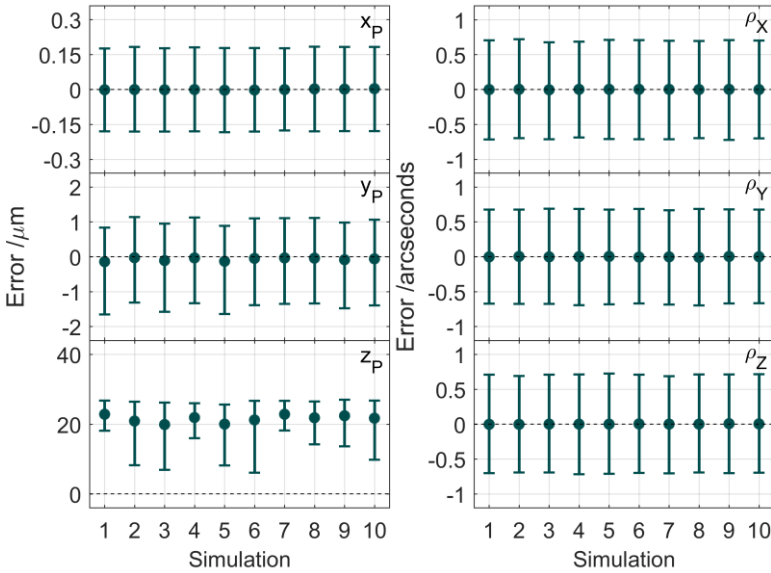


Figure 6.8. Errors in solved reference object geometrical parameters from  $I = 10,000$  repeat measurements for all simulations. The circular marker denotes the mean error, while the error bars correspond to 95 % of the solved parameter values, given by the 2.5 % (bottom) and 97.5 % (top) quantiles.

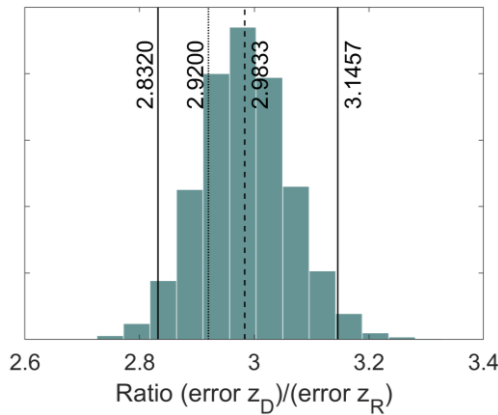


Figure 6.9. Histogram for ratios of errors in solved  $z_D$  and  $z_R$  from all 10,000 repeat measurements for simulation 1. The dotted vertical line the ratio of the true simulated values of  $z_D$  and  $z_R$ . The dashed line is the mean ratio of solved errors in  $z_D$  and  $z_R$ , while solid vertical lines denote the 2.5 % and 97.5 % quantiles, corresponding to the lower and upper limits, respectively, of 95 % of the solved ratios.

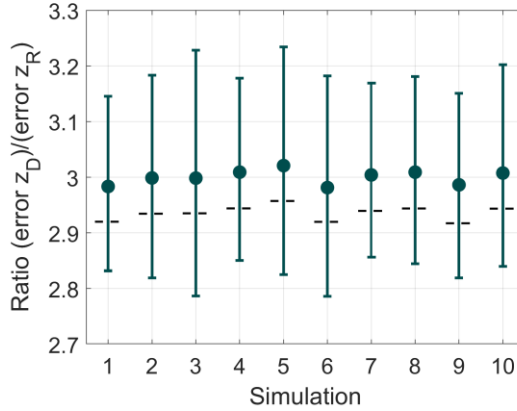


Figure 6.10. Ratios of errors in solved  $z_D$  and  $z_R$  from all 10,000 repeat measurements are shown for all ten simulation data sets. Circular markers correspond to the mean solved errors ratio, while the error bars contain 95 % of the ratios over 10,000 measurements, given by the 2.5 % (bottom) and 97.5 % (top) quantiles.

These observations provide further insight into the systematic nature of parameter coupling in the geometrical measurement procedure. Consistency in the ratio of errors to the true simulated values, which is approximately equivalent to the magnification factor, means that the effects of errors in one parameter is substantially compensated by the errors in the second parameter. This conclusion is supported by the magnitude of residual dimensional errors after adjustments observed in figure 4.17. Reprojection errors are mostly within 0.01 pixels, as shown by the histogram of reprojection errors for simulation 1 in figure 6.11 and the quantiles for all simulations in table 6.4.

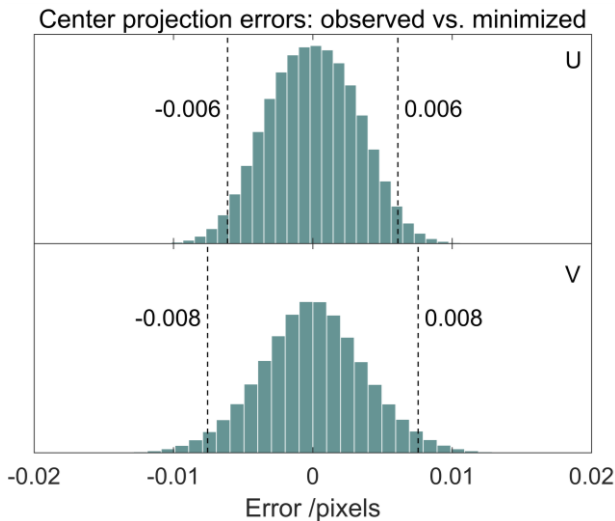


Figure 6.11. Histograms for center projection errors between observed (exact) and minimized center projection coordinates for simulation 1.

Table 6.4. Lower and upper boundaries for 95 % of reprojection errors from  $I = 10,000$  repeated minimizations, designated by the 2.5 % and 97.5 % quantiles, respectively. Results are presented for each simulation separately. All values are in pixels.

s	U coordinate quantiles		V coordinate quantiles	
	2.5 %	97.5 %	2.5 %	97.5 %
1	-0.0061	0.0061	-0.0075	0.0076
2	-0.0060	0.0060	-0.0073	0.0073
3	-0.0059	0.0059	-0.0072	0.0072
4	-0.0061	0.0061	-0.0075	0.0075
5	-0.0060	0.0060	-0.0073	0.0073
6	-0.0060	0.0060	-0.0074	0.0074
7	-0.0062	0.0062	-0.0076	0.0077
8	-0.0061	0.0061	-0.0075	0.0074
9	-0.0061	0.0061	-0.0075	0.0075
10	-0.0061	0.0061	-0.0075	0.0075

## 6.4 Discussion

In this chapter, a Monte Carlo approach has been presented for assessing uncertainty in the measured geometrical parameters of a CT scanner and applied to simulated CT data. The objective of the proposed framework is to ensure the true simulated geometrical parameter values are contained within the 95 % uncertainty intervals of the corresponding measured values. This was the case for most solved parameters except for the Z positions of reference object, axis of rotation, and detector due to known parameter coupling. The development of strategies for de-coupling these parameters should be the focus of future work. Furthermore, in this study the exact sphere center coordinates are used to define the central value of the input normal distributions. In experimental implementation, these exact coordinates are not known and the users are only equipped with the observed center projection coordinates (see chapter 4). Bias in the observed center projection coordinates will result in a bias of the solved distributions (in addition to bias introduced by parameter coupling). Therefore, investigation of systematic deviations in observed center projection coordinates or a method to incorporate the bias into the uncertainty of the solved geometrical parameters is necessary. Currently, for macro CT systems such as the ones studied here, the effects of other influence factors in CT, e.g. the finite size and drift of the X-ray focal spot, detector noise, scattering, among others, are relatively larger than the effects due to errors in the measured geometry after compensation. This statement is supported by the results of tomographic reconstruction in the presence of the residuals in chapter 4 of this doctoral thesis; more specifically, please refer to figure 4.17. Nevertheless, a detailed analysis of the limitations in the proposed Monte Carlo procedure is provided, paving the way for future development of the approach to reduce these limitations.

## References

- [1] BIPM JCGM 200 (2012) International vocabulary of metrology – Basic and general concepts and associated terms (VIM) 3rd edition (Geneva: International Organization for Standardization)
- [2] Ferrucci M, Leach RK, Giusca CL, Carmignato S, Dewulf W (2015) Towards geometrical calibration of X-ray computed tomography systems - A review. Measurement Science Technology 26, 92003 doi:10.1088/0957-0233/26/9/092003
- [3] BIPM JCGM 100 (2008) Evaluation of Measurement Data—Guide to the Expression of Uncertainty in Measurement (Geneva: International Organization for Standardization)

- [4] BIPM JCGM 101 (2008) Evaluation of measurement data — Supplement 1 to the “Guide to the expression of uncertainty in measurement” — Propagation of distributions using a Monte Carlo method (Geneva: International Organization for Standardization)



# Chapter 7

## Conclusions

This doctoral thesis addresses the issue of geometrical calibration of CT instruments. The term 'calibration' has a well-defined meaning in the field of metrology: measurement of a quantity by comparison to a traceable reference and assessment of uncertainty in that comparison. Therefore, instrument geometrical calibration refers to the measurement of the instrument geometry, given by the set of geometrical parameters, by comparison to a traceable reference and assessment of uncertainty in the measured values.

The question that this doctoral research has attempted to answer is the following.

"How can you calibrate the geometry of an X-ray computed tomography instrument?"

To answer the research question, the doctoral journey has followed a relatively common path in the quest for developing standardized methods to measure the geometry of a measuring instrument. After realizing that standardized methods do not exist (literature review, chapter 2), the sensitivity of measurements to various geometrical error sources is determined (chapter 3). The sensitivity analysis allows us to determine which error sources are negligible so that they may be put on the back burner of any research endeavor. Detector misalignments were found to have significant effects on the quality of reconstructed data, while rotation stage error motions as specified in a commercially-available rotation stage were found to have a negligible effect on CT measurements.

Dedicated procedures for the measurement of the CT instrument geometry by comparison to a traceable reference are developed and applied to simulated data (chapter 4). Implementation on simulated data provides us with ground truth, which we can use to evaluate the performance of the test procedures and tweak/adapt as necessary. The geometrical measurement procedure is applied to an experimental instrument (chapter 5). While ground truth is not available for the experimental implementation, i.e. we do not know the true instrument geometry, the efficacy of the developed procedures is validated by observing considerable reductions in measurement errors after compensation of the measured geometrical misalignments by instrument adjustment.

One of the two conditions for calibration per its definition in VIM has been achieved in this dissertation: the measurement of the geometrical parameters by comparison to a traceable reference. Uncertainty estimation is relatively straight forward if the relationship between measurement result(s) and input quantities can be described by one or more analytical equations. While analytical methods to determine the CT instrument geometry exist, their implementation demands accurate a priori knowledge of one or more input quantities and strict alignment of the reference object with respect to the instrument geometry. The development of a Monte Carlo framework for assessing uncertainty in CT instrument geometrical parameters solved by minimization is discussed in chapter 6. However, application of the Monte Carlo framework is currently limited as a result of bias in the input data and coupling of the solvable parameters. It should be noted that effects due to errors, with which the geometrical parameters are solved, are relatively small in comparison to effects from other error sources in the CT measurement procedure, e.g. finite focal spot size, focal spot drift, detector noise. Therefore, the assessment of uncertainty in the measured geometrical parameters is not yet critical. As these other sources of error are better characterized and methods for their compensation are developed, there will be an increasing need to know the uncertainty in the measurement of the instrument geometrical parameters. The Monte Carlo framework and the limitations outlined provide a path for such future research endeavors. Furthermore,

the Monte Carlo framework proposed here can be applied to evaluate uncertainty in any optimization-based measurement procedure.

## 7.1 Contributions and conclusions

The contributions in the dissertation are briefly summarized here. In **bold**, the conclusions from each contribution are provided.

### 7.1.1 Literature review

In the first chapter of this doctoral thesis, a thorough literature review of methods to measure the CT instrument geometry is provided. In the review, the role of measurement models to determine the sensitivity of CT measurements to various influence factors is introduced and several studies are presented in which such measurement models are applied. Then, analytical and numerical (minimization) methods based on imaging a reference object for determining the CT instrument geometry are reviewed. A discussion is provided on the nature of CT as both an imaging and a mechanical technology. A full geometrical mapping of the instrument relies on the combination of both imaging and mechanical methods. These concepts are considered in the discussion section of the literature review.

**The literature review compiled previous research on topics relevant to CT instrument geometry, including its measurement and understanding of the effects of misalignments on reconstructed data. The review highlighted the need for a metrological solution to the geometrical calibration of CT instruments, which had not been demonstrated.**

### 7.1.2 Sensitivity studies

Prior to the development of methods to quantify error sources, it is worthwhile to determine the sensitivity of measurements to each error source. If a measurement procedure can be described by an analytical function, the sensitivity study can simply consist of determining sensitivity coefficients by taking the partial derivative of the function with respect to each input parameter (assuming no covariance between input parameters). In the absence of an analytical function, numerical methods and simulation can be employed to determine the effects of error sources to a measurement result. In this chapter, the sensitivity of CT measurements to detector angular misalignments and to rotation stage errors is investigated by simulation.

#### *Detector angular misalignments*

CT measurement of a test object consisting of several sphere is simulated under various angular misalignments of the detector. Errors of the tomographically reconstructed test object are evaluated and compared for each simulated detector misalignment. It was shown that reconstructed sphere center positions were most sensitive to detector tilt  $\theta$  about the horizontal axis, while reconstructed sphere form was more strongly affected by detector slant  $\varphi$  and detector skew  $\eta$ .

A radiographic error map is developed to model pixel binning errors as a function of angular misalignments of the detector. The images acquired under the misaligned detector are corrected by applying re-binning maps based on the modelled pixel binning errors. Tomographic reconstruction is subsequently performed on the corrected X-ray images and CT measurements on the newly reconstructed volume. Significant reductions in observed sphere position and sphere form errors were observed for all simulated misalignments of the detector, thereby indicating the effective modelling of radiographic errors.

Detector angular misalignments are not readily noticeable by eye, although have an effect on the quality of the reconstructed volume, as shown in this sensitivity study. It is therefore imperative for users of CT who are concerned about measurement accuracy to determine whether their instrument detector has such misalignments and, if possible, to reduce their effects. One possible solution to reduce the effects of detector angular misalignments is proposed in this study and consists of re-binning the acquired radiographs prior to tomographic reconstruction. While practical limitations in this method exist, its implementation to the simulated data proved effective.

#### *Rotation stage errors*

Rotation stage errors are a result of imperfections in the manufacture of the rotation stage. Rotation stage errors include angular indexing error, radial and axial error motions, and tilt error motions. Methods to measure rotary stage error motions using reference instruments are well defined and are often applied by the stage manufacturer to ensure the product meets specified tolerances prior to making it commercially available. A control report indicating the measured rotation stage errors for the particular product is typically provided to the customer. The specified rotation stage error tolerances and observed error behaviors from the control report of a Newport RVS80CC rotation stage equipped in a 225 kV CT instrument are applied in the simulated CT measurement of a test object. Simulated scans of the test object are performed for various magnification positions; the size of the test object is scaled to preserve the object size to voxel size ratio. The objective of this sensitivity study is to determine the measurement domain within which the specified rotation stage errors have a significant effect on CT measurements (sphere center-to-center distances, sphere radius, and sphere form) of the test object. The results from the simulation study indicate that the specified rotation stage errors significantly affect CT measurements for magnifications above 50. At these magnifications, the effects of focal spot size and focal spot drift are larger than the effects of rotation stage error motions. As a result, rotation stage error motions are considered negligible for the more common "macro" CT instruments.

**Rotation stage errors as specified by the control report of a commercially-available rotation stage equipped in a 225 kV CT instrument are shown to have negligible effects on dimensional measurements. In fact, significant deviations in dimensional measurements were observed for magnification positions above 50; in this measurement domain, the effects of focal spot size and focal spot drift are significantly larger than the observed effects of rotation stage errors.**

### 7.1.3 Development of geometrical measurement procedure

In practice, the geometry of a CT instrument can be determined by imaging an object consisting of  $M$  spheres with known center positions in a local coordinate frame.  $N$  radiographs of the reference object are acquired at various angular positions of the object. The three-dimensional coordinate positions of the sphere centers are perturbed from their nominal values to reflect uncertainty in CMM measurement of sphere center positions in experimental implementation. Rotation stage errors and image noise and blur were included to approximate expected experimental conditions. Analysis of the acquired radiographs consists of identifying the image coordinates of projected sphere centers for all projections, resulting in a set of  $M \times N$  observed center projection coordinates. A ray-tracing algorithm is used to generate a set of corresponding modelled center projection coordinates given the local sphere center positions and an initial set of instrument and reference object geometrical parameters. The modelled reference object and instrument geometrical parameters in the ray-tracing algorithm are least-squares fit to minimize the reprojection error. The reprojection error is given by the sum of squared residuals between modelled and observed center projection coordinates. The proposed procedure has been applied to the measurement of 10 simulated misaligned instrument geometries.

The ability for the minimization procedure to converge to the correct instrument geometry is determined by way of convergence testing. In these tests, the geometrical measurement procedure is applied to solve for the instrument geometry given exact sphere center coordinates and exact center projection coordinates while varying the initial values of the solvable instrument and reference object geometrical

parameters. Results from convergence testing indicate correlation between the Z coordinate positions of stage rotation axis and detector. The regular geometrical measurement procedure, i.e. using nominal sphere center coordinates positions and observed center projection coordinates, is implemented on the 10 simulated misaligned instrument geometries. Regular implementation consistently solved detector Z position to within 105  $\mu\text{m}$  from the 'true' simulated value and stage rotation axis Z position to within 35  $\mu\text{m}$ ; detector lateral (X and Y) positions were solved to within 5  $\mu\text{m}$ . Detector tilt  $\theta$  was solved to within 10 arcseconds, detector slant  $\varphi$  was solved to within 3 arcseconds, and detector skew  $\eta$  was solved to within 1 arcsecond.

The simulated acquisitions were repeated for the CT measurement of a validation object under 'adjusted' acquisition geometries, i.e. the simulated instrument misalignments corresponded to the residuals between true and measured values of the misalignment parameters. Reductions in dimensional measurement errors on the subsequently reconstructed object to less than a voxel size indicate the robustness of the measurement procedure to effectively solve the instrument geometry. It is important to emphasize that the developed geometrical measurement procedure is not limited to the reference object described in chapter 4.

**The proposed geometrical measurement procedure was proven effective in correctly determining the simulated instrument geometry. Detector angular misalignments  $\theta$ ,  $\varphi$ , and  $\eta$  were consistently solved to within 10 arcseconds, 3 arcseconds, and 1 arcsecond, respectively. Detector lateral positions were solved to within 5  $\mu\text{m}$ . Parameter coupling was observed between longitudinal (Z) positions of the detector and rotation axis, albeit both parameters were consistently solved to within 1 part in  $10^4$ . The observed CT measurement errors in the presence of residual misalignments, i.e. after adjustment, are negligible compared to much more influential error sources such as X-ray source focal spot size and drift. Therefore,**

#### 7.1.4 Experimental validation

The geometrical measurement procedure is applied to data acquired from an experimental CT instrument at the Center of Excellence Telč (CET), in the Czech Republic. In a first visit, the geometrical measurement procedure was implemented for various numbers of stepped rotation positions of the reference object. Results indicate that the geometrical measurement procedure is robust when using projection information from 30 or more stepped rotation positions of the object. The procedure was also implemented for 720 projections of the reference object acquired under various speeds of continuous rotation. While continuous rotation of the reference object did provide solved geometrical parameters that differed from those acquired under stepped rotation (with equivalent number of projections), the differences are relatively small, further supporting the robustness of the method.

During a second visit to CET, the geometrical measurement procedure was used to inform the adjustment of the CT instrument components from their state upon arrival ('initial', aligned per CET procedure) to their ideal alignment as defined for conventional tomographic reconstruction algorithms. A separate calibrated validation object was CT measured under initial instrument geometry and again under the adjusted instrument geometry. Significant reductions were observed in dimensional measurement errors of the validation object performed on the adjusted geometry acquired dataset when compared to the dataset acquired under the initial instrument alignment. For example, the maximum sphere center-to-center distance error in the measured validation object was reduced from 843  $\mu\text{m}$  to under 20  $\mu\text{m}$ . Furthermore, variation in sphere fit radii over the 15 spheres in the validation object after adjustment was reduced to 2.87  $\mu\text{m}$  from 3.64  $\mu\text{m}$  in the initial scan geometry.

**The proposed geometrical measurement procedure was experimentally shown to be robust to various acquisition conditions (number of projections and rotation mode). Solved measured geometrical parameter values were consistent for acquisitions of at least 30 projections of the reference object. Solved parameter values were also consistent for various rotation speeds of the**

stage. The efficacy of the measurement procedure to correctly determine the geometrical parameters was demonstrated in the reduction of measurement errors after adjustment of the instrument components given the previously measured misalignments.

Users of CT can use the geometrical measurement procedure to inform the adjustment of their instruments, thereby reducing measurement errors. Users of commercial instruments, for which physical adjustment of the components may compromise warranty or service contracts with the instrument manufacturer, can use the output of the geometrical measurement procedure to modify the backprojection geometry in tomographic reconstruction, i.e. software correction. The development of such a modified tomographic reconstruction algorithm was the focus of concurrent work (see reference [15] in chapter 1). Implementation of an in-house procedure for correction of misalignments can provide cost benefits over, for example, paid calibration services by instrument manufacturers or third parties.

Due to known kinematic errors in the sample stage manipulator, the output of the geometrical measurement procedure is only valid for a given position of the sample stage. Therefore, the geometrical measurement procedure must be repeated after movement of the sample stage. Future work should consider the inclusion of measured kinematic errors of the manipulator into an 'instrument geometry map', whereby a lookup table of instrument geometries can be accessed for any sample stage position in its kinematic domain.

### 7.1.5 Estimation of uncertainty in geometrical parameters

Chapter 6 introduced a statistical framework for estimating uncertainty in the measured geometrical parameters. The proposed framework is based on the Monte Carlo approach, which consists of repeating the measurement procedure while varying the values of the measurement inputs, i.e. sphere center coordinates and center projection coordinates. The result is a distribution of solved values for each parameter. The value assigned to the parameter measurement is the mean of the corresponding distribution and the 95 % confidence uncertainty interval is given by the 2.5 % and 97.5 % quantiles of the solved distribution. Most solved parameter distributions were approximately centered on the true simulated value of the respective parameter, which is contained within the respective 95 % uncertainty interval. Coupling in the Z positions of reference object, axis of rotation, and detector (as seen in convergence testing in chapter 4) is still present and is indicated by a consistent offset in the mean of the solved distributions from the true simulated value. Furthermore, the 95 % uncertainty interval for these three parameters do not contain the true simulated values.

Despite the limitations in the implementation for assessment of uncertainty in the measurement of CT instrument geometry, the Monte Carlo framework paves the way for uncertainty assessment in other measurement procedures based on optimization. The task of solving bias in the inputs and overcoming parameter coupling is an opportunity for future research.



# Appendix A

When performing optimization, the mathematical nature of the objective function can have significant effects on the quality of the results. The results presented in chapters 4, 5, and 6 were solved using the sum of squared residuals (SSR) between modelled and observed center projection coordinates as the objective function. The formula for SSR is revisited in equation A.1.

$$SSR = \sum_{n=1}^N \sum_{m=1}^M \left( \sqrt{(u_{\text{mod}}(m, n) - u_{\text{obs}}(m, n))^2 + (v_{\text{mod}}(m, n) - v_{\text{obs}}(m, n))^2} \right)^2 \quad (\text{A.1})$$

Towards the end of the doctoral research, a short study was performed to understand how adapting the objective function in the minimization step of the geometrical measurement procedure would affect the solved parameter values. Due to the summation in quadrature of the two components, the sensitivity of the geometrical measurement procedure to the individual  $u$  and  $v$  components of the reprojection error is significantly reduced. Therefore, two new objective functions are tested on the geometrical measurement of the ten simulated datasets from chapter 4 (see tables 4.2 and 4.3 for the simulated geometrical parameter values of the instrument and reference object, respectively).

A modification of the SSR, in which the summation of the squared residuals is performed individually to the  $u$  and  $v$  components prior to taking the square root, is applied. The formula for this modification is given in equation A.2. Henceforth, this objective function is referred to as 'mSSR' (short for 'modified SSR').

$$mSSR = \sqrt{\sum_{n=1}^N \sum_{m=1}^M (u_{\text{mod}}(m, n) - u_{\text{obs}}(m, n))^2 + \sum_{n=1}^N \sum_{m=1}^M (v_{\text{mod}}(m, n) - v_{\text{obs}}(m, n))^2} \quad (\text{A.2})$$

Similarly to the SSR, mSSR is a single-value objective function and is applied using MATLAB built-in constrained minimization function *fmincon*. A third measurement of the simulated geometries is performed with multiple objective minimization, henceforth referred to as multi-objective minimization. In this third test of the geometrical measurement procedure, the set of  $M \times N$  individual column reprojection errors  $du(m, n) = u_{\text{mod}}(m, n) - u_{\text{obs}}(m, n)$  and  $M \times N$  individual row reprojection errors  $dv(m, n) = v_{\text{mod}}(m, n) - v_{\text{obs}}(m, n)$  are minimized separately, yet simultaneously. MATLAB built-in non-linear least squares fitting function *lsqnonlin* is used for multi-objective minimization.

Errors between solved and simulated instrument geometrical parameter values are shown for each objective function (SSR, mSSR, and multi-objective) in figures A.1, A.2, and A.3. Errors in the solved detector angular misalignments  $\theta$ ,  $\varphi$ , and  $\eta$ ; and solved detector lateral positions  $x_D$  and  $y_D$  did not change significantly with objective function. Errors in the solved detector and rotation axis longitudinal positions  $z_D$  and  $z_R$ , respectively, were reduced with respect to SSR when applying mSSR and multi-objective minimization. The lowest errors are observed for multi-objective minimization. Despite the reduced errors, coupling between  $z_D$  and  $z_R$  is still present.

Appendix A

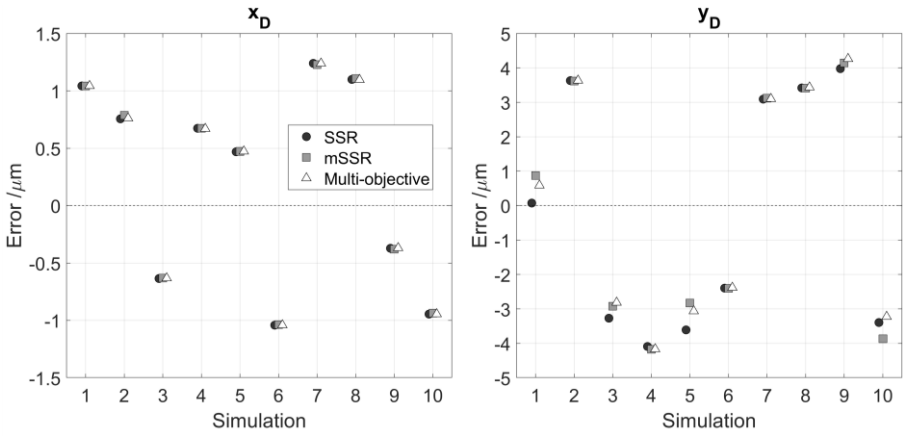


Figure A.1. Error between simulated and solved detector lateral position from minimization using SSR, mSSR, and multi-objective functions.

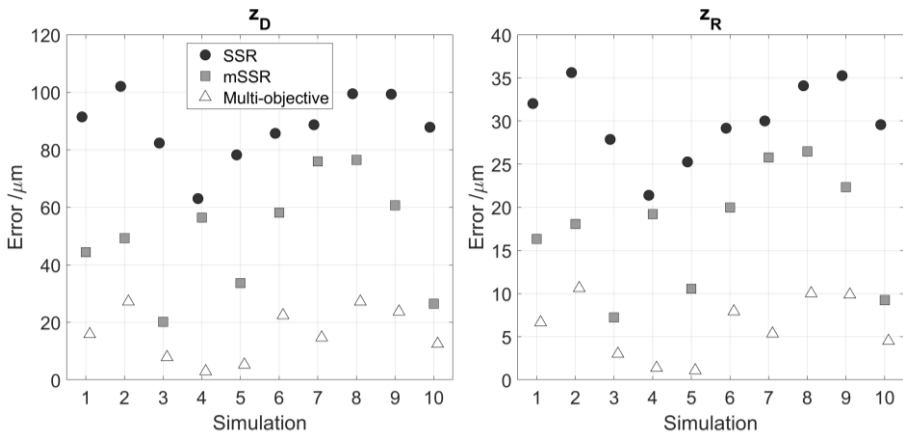


Figure A.2. Error between simulated and solved detector longitudinal position from minimization using SSR, mSSR, and multi-objective functions.

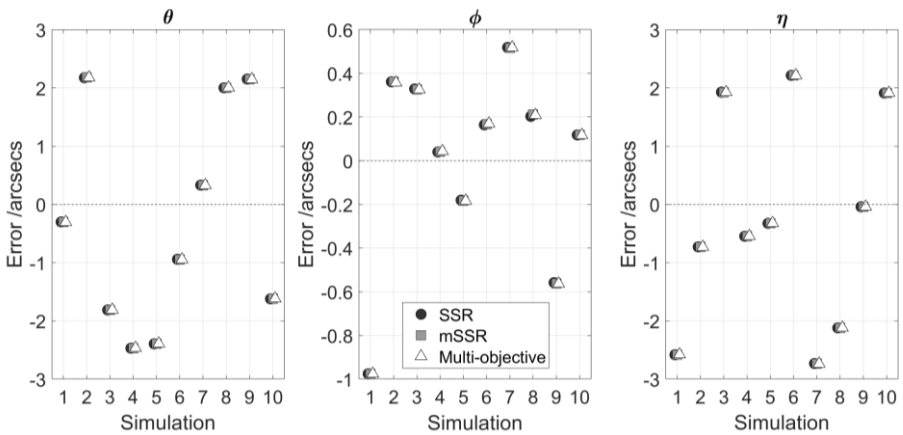


Figure A.3. Error between simulated and solved detector angular misalignments from minimization using SSR, mSSR, and multi-objective functions.

# Appendix B

Table 4.10. Comparison of solved detector position after minimization of reprojection errors to true simulated values for each simulation. True and solved values are in mm, while errors are in  $\mu\text{m}$ .

$s$	$x_D$			$y_D$			$z_D$		
	True /mm	Solved /mm	Error / $\mu\text{m}$	True /mm	Solved /mm	Error / $\mu\text{m}$	True /mm	Solved /mm	Error / $\mu\text{m}$
1	1.2590	1.2600	1.0427	-1.3700	-1.3699	0.0739	-1175.4430	-1175.3516	91.4167
2	1.6230	1.6238	0.7558	1.8820	1.8856	3.6289	-1181.6430	-1181.5410	102.0365
3	-1.4920	-1.4926	-0.6351	1.8290	1.8257	-3.2696	-1173.5090	-1173.4267	82.3333
4	1.6540	1.6547	0.6736	-0.0590	-0.0631	-4.0903	-1172.6600	-1172.5970	63.0269
5	0.5290	0.5295	0.4689	1.2010	1.1974	-3.6089	-1175.2130	-1175.1348	78.2149
6	-1.6100	-1.6110	-1.0414	-1.4330	-1.4354	-2.3963	-1174.4230	-1174.3373	85.6979
7	-0.8860	-0.8848	1.2391	-0.3130	-0.3099	3.0915	-1174.5690	-1174.4803	88.6874
8	0.1880	0.1891	1.0990	1.6630	1.6664	3.4178	-1178.0780	-1177.9785	99.4698
9	1.8300	1.8296	-0.3719	1.1690	1.1730	3.9766	-1175.4460	-1175.3467	99.3094
10	1.8600	1.8591	-0.9451	1.8380	1.8346	-3.3946	-1180.2880	-1180.2002	87.8361

Table 4.11. Comparison of solved detector orientation after minimization of reprojection errors to true simulated values for each simulation. True and solved values are in degrees ( $^\circ$ ), while errors are in arcseconds ( $1/3600^\circ$ ).

$s$	$\theta$			$\varphi$			$\eta$		
	True / $^\circ$	Solved / $^\circ$	Error /arcsecs	True / $^\circ$	Solved / $^\circ$	Error /arcsecs	True / $^\circ$	Solved / $^\circ$	Error /arcsecs
1	-0.6756	-0.6729	9.8741	-0.0989	-0.0987	0.5852	-0.7867	-0.7870	-0.9400
2	0.5886	0.5896	3.4445	-0.8324	-0.8316	2.9650	0.9238	0.9237	-0.4427
3	-0.3776	-0.3783	-2.5576	-0.5420	-0.5413	2.6222	-0.9907	-0.9906	0.4905
4	0.0571	0.0578	2.5552	0.8267	0.8265	-0.6820	0.5498	0.5497	-0.3554
5	-0.6687	-0.6688	-0.3608	-0.6952	-0.6948	1.4780	0.6346	0.6346	-0.1787
6	0.2040	0.2041	0.4834	0.6516	0.6513	-1.0173	0.7374	0.7376	0.5548
7	-0.4741	-0.4721	7.1076	0.0767	0.0773	2.0130	-0.8311	-0.8313	-0.8109
8	0.3082	0.3091	3.3472	0.9923	0.9925	0.5815	-0.2004	-0.2006	-0.5417
9	0.3784	0.3783	-0.4235	-0.8436	-0.8431	1.7183	-0.4803	-0.4803	-0.0220
10	0.4963	0.4960	-0.9362	-0.1146	-0.1143	1.1016	0.6001	0.6003	0.6440

Appendix B

Table 4.12. Comparison of solved rotation axis position after minimization of reprojection errors to true simulated values for each simulation. True and solved values are in mm, while errors are in  $\mu\text{m}$ .

$s$	$z_R$		
	True /mm	Solved /mm	Error / $\mu\text{m}$
1	-402.5450	-402.5133	31.7315
2	-402.6760	-402.6415	34.4909
3	-399.8150	-399.7863	28.7070
4	-398.3250	-398.3028	22.2407
5	-397.3960	-397.3696	26.4214
6	-402.2210	-402.1912	29.8046
7	-399.5870	-399.5573	29.6724
8	-400.1840	-400.1508	33.1642
9	-402.9290	-402.8952	33.8073
10	-400.9770	-400.9468	30.2234

Table 4.13. Comparison of solved reference object position after minimization of reprojection errors to true simulated values for each simulation. True and solved values are in mm, while errors are in  $\mu\text{m}$ .

$s$	$x_P$			$y_P$			$z_P$		
	True /mm	Solved /mm	Error / $\mu\text{m}$	True /mm	Solved /mm	Error / $\mu\text{m}$	True /mm	Solved /mm	Error / $\mu\text{m}$
1	1.0051	1.0061	1.0260	1.3629	1.3632	0.2826	-400.5934	-400.5614	32.0206
2	-0.9796	-0.9791	0.4860	-0.9829	-0.9815	1.3863	-398.6767	-398.6411	35.6076
3	0.0238	0.0233	-0.5026	1.2571	1.2562	-0.8926	-399.6589	-399.6310	27.8658
4	0.7963	0.7966	0.3135	-1.0259	-1.0273	-1.4259	-399.8011	-399.7797	21.3906
5	1.5636	1.5638	0.2218	1.7171	1.7160	-1.0979	-398.3312	-398.3059	25.2578
6	1.8372	1.8362	-1.0487	-0.6001	-0.6009	-0.7714	-400.8566	-400.8274	29.1669
7	0.1889	0.1900	1.1174	-1.2136	-1.2123	1.2633	-398.9712	-398.9412	30.0043
8	-1.4455	-1.4446	0.9163	-0.9957	-0.9943	1.3517	-398.9851	-398.9510	34.0834
9	-1.4028	-1.4029	-0.1128	0.4642	0.4654	1.2131	-400.4782	-400.4430	35.2490
10	-0.9700	-0.9708	-0.7862	-0.1068	-0.1080	-1.1630	-399.7287	-399.6991	29.5716

Table 4.14. Comparison of solved reference object orientation after minimization of reprojection errors to true simulated values for each simulation. True and solved values are in degrees ( $^\circ$ ), while errors are in arcseconds ( $1/3600^\circ$ ).

$s$	$\rho_X$			$\rho_Y$			$\rho_Z$		
	True / $^\circ$	Solved / $^\circ$	Error /arcsecs	True / $^\circ$	Solved / $^\circ$	Error /arcsecs	True / $^\circ$	Solved / $^\circ$	Error /arcsecs
1	0.4121	0.4120	-0.3017	-0.1225	-0.1228	-0.9755	-0.4479	-0.4486	-2.5806
2	-0.9363	-0.9357	2.1737	-0.2369	-0.2368	0.3612	0.3594	0.3592	-0.7298
3	-0.4462	-0.4467	-1.8134	0.5310	0.5311	0.3284	0.3102	0.3107	1.9268
4	-0.9077	-0.9084	-2.4691	0.5904	0.5904	0.0398	-0.6748	-0.6750	-0.5476
5	-0.8057	-0.8064	-2.3942	-0.6263	-0.6264	-0.1808	-0.7620	-0.7621	-0.3257
6	0.6469	0.6466	-0.9431	-0.0205	-0.0205	0.1642	-0.0033	-0.0027	2.2132
7	0.3897	0.3898	0.3295	-0.1088	-0.1087	0.5184	0.9195	0.9187	-2.7323
8	-0.3658	-0.3652	2.0001	0.2926	0.2927	0.2028	-0.3192	-0.3198	-2.1207
9	0.9004	0.9010	2.1504	0.4187	0.4185	-0.5584	0.1705	0.1705	-0.0414
10	-0.9311	-0.9316	-1.6217	0.5094	0.5094	0.1178	-0.5524	-0.5519	1.9108

# Doctoral publications

In the time frame of the doctoral research, the following first and second author publications were published or accepted. The list within each category is in chronological order.

## Journal publications:

- J1. Ferrucci M et al. (2015) Towards geometrical calibration of X-ray computed tomography systems—a review *Measurement Science and Technology* 26 92003
- J2. Ferrucci M et al. (2016) Evaluating the effects of detector angular misalignments on simulated computed tomography data *Precision Engineering* 45, 230–241
- J3. Dewulf W, Ferrucci M, et al. (2018) Enhanced dimensional measurement by fast determination and compensation of geometrical misalignments of X-ray computed tomography instruments. *CIRP Annals – Manufacturing Technology* 67, 523–526
- J4. Ametova E, Ferrucci M, et al. (2018) A computationally inexpensive model for estimating dimensional measurement uncertainty due to X-ray computed tomography instrument misalignments. *Measurement Science and Technology* 29 (6), 065007
- J5. Ametova E, Ferrucci M, et al. (2018) Software-based compensation of instrument misalignments for X-ray computed tomography dimensional metrology. *Precision Engineering* 54, 233–242
- J6. Ferrucci M et al. (2018) Measurement of the X-ray computed tomography instrument geometry by minimization of reprojection errors—implementation on simulated data. *Precision Engineering* 54, 7–20
- J7. Ferrucci M et al. (2018) Measurement of the X-ray computed tomography instrument geometry by minimization of reprojection errors—implementation on experimental data. *Precision Engineering* 54, 107–117

## Conference proceedings:

- C1. Ferrucci M et al. (2016) Development of a geometrical error model for coordinate measurements made by industrial X-ray computed tomography. *Proceedings of the 16<sup>th</sup> EUSPEN International Conference and Exhibition* (Nottingham, UK)
- C2. Buratti A, Ferrucci M et al. (2016) An analytical method for optimizing imaging parameters in industrial X-ray computed tomography for dimensional measurements on multimaterial workpieces. *Proceedings of SPIE 9967 Developments in X-Ray Tomography X* doi: 10.1117/12.2240566
- C3. Ametova E, Ferrucci M et al. (2016) Uncertainty quantification in dimensional measurements by computed tomography due to uncertainty in data acquisition geometrical parameters. *Proceedings of the 31st Annual Meeting of ASPE* (Portland, USA)
- C4. Ametova E, Ferrucci M et al. (2017) A tool for reducing cone-beam artifacts in computed tomography data. *7<sup>th</sup> Conference on Industrial Computed Tomography* (Leuven, Belgium)
- C5. Hermanek P, Ferrucci M *et al.* (2017) Optimized reference object for assessment of computed tomography instrument geometry. *7<sup>th</sup> Conference on Industrial Computed Tomography* (Leuven, Belgium)
- C6. Ferrucci M et al. (2018) Sensitivity of CT dimensional measurements to rotation stage errors. *8<sup>th</sup> Conference on Industrial Computed Tomography* (Wels, Austria)

Doctoral publications

**Book chapters:**

B1. Ferrucci M (2017) Towards traceability of CT dimensional measurements (Book chapter) Industrial X-ray Computed Tomography Editors: Simone Carmignato, Wim Dewulf, Richard Leach Springer-Verlag (Berlin, Germany)

B2. Ferrucci M et al. (2018) Dimensional Metrology (Book chapter) Basics of Precision Engineering Editors: Richard Leach and Stuart Smith CRC Press (Boca Raton, USA)

# Curriculum Vitae

**Name:** Massimiliano Ferrucci  
**Date of birth:** 27 December 1985  
**Place of birth:** Siena, Italy

## Work Experience

---

**Research Engineer** Since December 2017  
Research and Development  
Materialise NV  
Leuven, Belgium

**Graduate Research Fellow** December 2016 – December 2017  
Faculty of Engineering Technology  
Katholieke Universiteit Leuven  
Leuven, Belgium

**Research Scientist** November 2013 – November 2016  
Mass and Dimensional Group  
National Physical Laboratory  
Teddington, United Kingdom

**Physicist** September 2008 – November 2013  
Dimensional Metrology Group  
National Institute of Standards and Technology  
Gaithersburg, Maryland (USA)

**Intern and Student Director** September 2007 – September 2008  
DEVELOP Program  
NASA Goodard Space Flight Center  
Greenbelt, Maryland (USA)

**Research Assistant** October 2006 – December 2007  
Center for Nanophysics and Advanced Materials  
University of Maryland  
College Park, Maryland (USA)

## Academic Experience

---

**PhD Engineering Technology** November 2013 – November 2018  
Katholieke Universiteit Leuven (Belgium)

**MSc Applied Physics** January 2009 – May 2012  
The Johns Hopkins University (USA)

## Scientific Publications

---

- Ferrucci M et al. (2018) Measurement of the X-ray computed tomography instrument geometry by minimization of reprojection errors—implementation on experimental data. *Precision Engineering* 54, 107-117
- Ferrucci M et al. (2018) Measurement of the X-ray computed tomography instrument geometry by minimization of reprojection errors—implementation on simulated data. *Precision Engineering* 54, 7-20
- Ametova E, Ferrucci M, et al. (2018) Software-based compensation of instrument misalignments for X-ray computed tomography dimensional metrology. *Precision Engineering* 54, 233-242
- Dewulf W, Ferrucci M, et al. (2018) Enhanced dimensional measurement by fast determination and compensation of geometrical misalignments of X-ray computed tomography instruments. *CIRP Annals – Manufacturing Technology* 67, 523–526
- Ametova E, Ferrucci M, et al. (2018) A computationally inexpensive model for estimating dimensional measurement uncertainty due to X-ray computed tomography instrument misalignments. *Measurement Science and Technology* 29 (6), 065007
- Ferrucci M et al. (2018) Sensitivity of CT dimensional measurements to rotation stage errors. 8<sup>th</sup> Conference on Industrial Computed Tomography (Wels, Austria)
- Ferrucci M et al. (2018) Dimensional Metrology (Book Chapter). *Basics of Precision Engineering* Editors: Richard Leach and Stuart T. Smith. (CRC Press: Boca Raton, USA), ISBN 9781498760850
- Ferrucci M (2018) Towards traceability of CT dimensional measurements (Book Chapter). *Industrial X-ray Computed Tomography*. Editors: Simone Carmignato, Wim Dewulf, and Richard Leach (Springer-Verlag: Berlin, Germany), ISBN 978-3-319-59573-3
- Ametova E, Ferrucci M, et al. (2017) A tool for reducing cone-beam artifacts in computed tomography data. 7<sup>th</sup> Conference on Industrial Computed Tomography (Leuven, Belgium)
- Heřmànek P, Ferrucci M et al. (2017) Optimized reference object for assessment of computed tomography instrument geometry. 7<sup>th</sup> Conference on Industrial Computed Tomography (Leuven, Belgium)
- Ametova E, Ferrucci M et al. (2016) Uncertainty quantification in dimensional measurements by computed tomography due to uncertainty in data acquisition geometrical parameters. *Proceedings of the 31st Annual Meeting of ASPE* (Portland, USA)
- Buratti A, Ferrucci M et al. (2016) An analytical method for optimizing imaging parameters in industrial X-ray computed tomography for dimensional measurements on multimaterial workpieces. *Proceedings of SPIE 9967 Developments in X-Ray Tomography X* doi: 10.1117/12.2240566
- Ferrucci M et al. (2016) Development of a geometrical error model for coordinate measurements made by industrial X-ray computed tomography. *Proceedings of the 16th euspen International Conference & Exhibition* (Nottingham, UK)
- Ferrucci M et al. (2016) Evaluating the effects of detector angular misalignments on simulated computed tomography data. *Precision Engineering* 45, 230-241 doi:10.1016/j.precisioneng.2016.03.001

- Ferrucci M et al. (2015) Towards geometrical calibration of X-ray computed tomography systems—a review. *Measurement Science and Technology* 26 092003 doi:10.1088/0957-0233/26/9/092003
- Ferrucci M, Doiron T, et al. (2015) Dimensional review of scales for forensic photography. *Journal of Forensic Science* 61 (2), 509-519 doi: 10.1111/1556-4029.12976
- Hughes EB, Ferrucci M, et al. (2015) Preliminary investigation into the use of a network-based technique for calibration of 3D laser scanners. NPL Report ENG 59
- Muralikrishnan B, Ferrucci M, et al. (2014) Volumetric performance evaluation of a laser scanner based on geometric error model. *Precision Engineering* 40, 139-150 doi:10.1016/j.precisioneng.2014.11.002
- Ferrucci M, Muralikrishnan B, et al. (2014) Evaluation of a laser scanner for large volume coordinate metrology: a comparison of results before and after factory calibration. *Measurement Science and Technology* 25 105010 doi:10.1088/0957-0233/25/10/105010
- Muralikrishnan B, Ferrucci M, et al. (2013) Volumetric performance evaluation of a laser scanner. *Proceedings of the 28th Annual Meeting of ASPE (St. Paul, USA)*
- Ferrucci M, Muralikrishnan B, et al. (2013) Ranging performance evaluation of a laser scanner. *Proceedings of the 28th Annual Meeting of ASPE (St. Paul, USA)*